THE UNIVERSITY OF CHICAGO

CELLULOSE NANOCRYSTALS BASED FUNCTIONAL POLYMER NANOMATERIALS

A DISSERTATION SUBMITTED TO
THE FACULTY OF THE PRITZKER SCHOOL OF MOLECULAR ENGINEERING
IN CANDIDACY FOR THE DEGREE OF
DOCTOR OF PHILOSOPHY

BY
YEFEI ZHANG

CHICAGO, ILLINOIS
AUGUST 2020

Table of Contents

List of Figures

List of Schemes

List of Tables

Acknowledgement

I would like to thank my advisor, Dr. Stuart Rowan, for his guidance and continuous support during my PhD study. In addition to his great ideas, his hard work and dedication to science has been truly inspirational to me. I certainly would not be the scientist I am today without him. I would also like to take this opportunity to thank Prof. Paul Nealey and Prof. Aaron Esser-Kahn for serving on my dissertation committee.

I would like to thank all the past and present members in the Rowan group, as well as all the people who helped and encouraged me during my PhD study. In particular, I would like to thank Dr. Reza Foudazi for teaching me a lot during my early PhD study, thank Dr. Han Yang and Dr. Ryo Kato for their assistance in the lab and many help discussions, thank Nanetta Pon for her contribution to the squid beak project and thank Dr. Philip Griffin for his help with the instruments.

Finally, I am truly grateful for the endless love, encouragement and support from my parents and especially my wife, Ruotian Gao. Without them, none of this work would have been possible.

Abstract

Cellulose nanocrystals (CNC) are rod like polymer nanoparticles that can be extracted from a wide variety of biosources. CNCs have been investigated extensively in the past decade as important building blocks for the development of novel functional materials. This growing interest in CNC based materials is not only related to CNCs' sustainability and bioavailability, but also their inherent properties, such as high elastic modulus, high aspect ratio, high surface area and low density. With the presence of a large number of hydroxyl groups on the surface, CNCs provide a platform for various surface functionalization with the goal of tuning their surface properties or introducing new functionalities which further extends their use in highly sophisticated applications.

This dissertation focuses on the fabrication and characterization of functionalized CNC based polymer nanomaterials with the goal of understanding how the surface functionalities impact the macroscopic properties of the materials.

In the first part of the work (Chapter 2 and 3), CNCs were covalently functionalized with alkylamines of different alkyl chain length to increase their hydrophobicity, and the resulting alkyl-functionalized CNCs have been investigated as particle stabilizers for oil-in-water Pickering emulsion. The results have shown that the hydrophobic/hydrophilic balance of the functionalized CNCs is critical to lower the interfacial tension between the oil and water phase, which allowed access to stable emulsions with droplet sizes of only a few hundred nanometers. The CNC stabilized nano-emulsions can be polymerized into latex nanoparticles, which were further fabricated into latex nanocomposite films. Microscopy analysis of the latex nanocomposites revealed a unique CNC network structure formed by excluded volume effect of the latex particles. The excluded volume lead to the formation of percolation networks at a much lower CNC concentration. As a result, the latex nanocomposites containing functionalized CNCs demonstrated

a higher plateau modulus. When this percolating CNC-rich network was disrupted by melt pressing, a significant decrease in mechanical properties of the films was observed.

The second part of the work (Chapter 4-6) focus on the preparation of CNC based polymer nanocomposites with water enhanced mechanical gradient properties inspired by the squid beak biomodel. The first-generation bio-inspired nanocomposite was fabrication based on allyl-functionalized CNCs embedded into a polyvinyl acetate matrix. The functionalized CNC fillers can be covalently crosslinked using UV initiated thiol-ene chemistry to yield composite films with tunable mechanical properties with a modulus contrast of 7 ($E'_{stiff}/E'_{soft}=7$) when swelled in water. With the goal of further improving the modulus contrast, polymer containing alkene functionalities were employed as matrix for the preparation of second-generation bio-inspired nanocomposite. Through crosslinking both the CNC fillers and the polymer matrix, it is possible to access larger wet mechanical contrasts upon crosslinking (E'_{stiff}/E'_{soft}=ca. 20). Finally, the third-generation nanocomposite was prepared based on carboxylic acid functionalized CNCs embedded into a partially hydrolyzed poly(vinyl acetate-co-vinyl alcohol) matrix with covalent crosslinking formed between the hydroxyl groups from both the CNC filler and polymer matrix. Owing to the strong hydrophilic nature of the material which effectively decreases the modulus of soft uncrosslinked materials (E'_{soft}), the third-generation nanocomposites demonstrated a wet modulus contrast over 2 order of magnitude ($E'_{stiff}/E'_{soft}>400$) upon swelling in water.

Chapter 1. Introduction.

1.1 Cellulose

Cellulose, which is the most abundant biopolymer on earth with an annual production of ca. 75 billion tons, has been widely studied as renewable materials.[1,2] As a type of polysaccharide, cellulose is mainly present in wood, cotton and other plant-based materials, although it can also be found in sea animals (tunicate), marine plants (algae), and bacteria.[3–6] The polymeric structure of cellulose consists of repeating cellobiose of two anhydroglucose units (AGU) connected through a covalent β-1,4-glycosidic bond between the C1 anomeric carbon and the C4 oxygen atom.[7] Every second AGU ring is rotated at 180 degree in the plane as opposed to the adjacent AGU unit in order to form a sterically stable structure.[8] The cellulose chain is also directionally asymmetric, with a hemiacetal unit on one end of the chain (also called reducing end) and a pendant hydroxyl group on the other end (also called non-reducing end) (Figure 1.1).[7] The hydroxyl groups on the equatorial positions of the ring lead to the formation of strong intramolecular and intermolecular hydron bonding interactions which effectively pack the cellulose chains into highly crystalline structure that is no longer soluble in water and most other common solvents.[9]

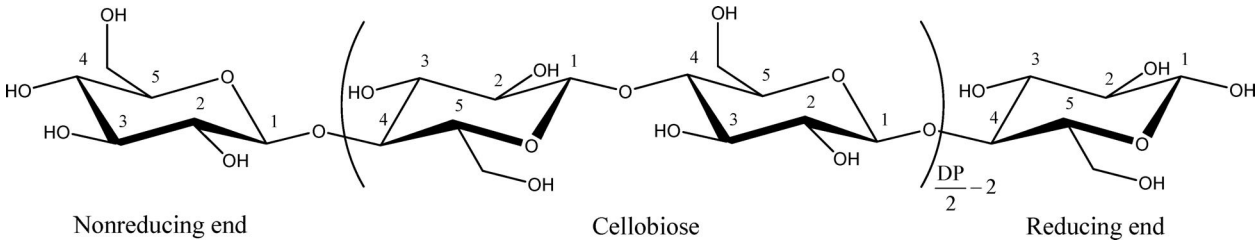

Figure 1.1 The chemical structure of cellulose.[7]

In nature, cellulose chains organize themselves into a multi-level fibrillar bundles with a hierarchical structure, which consists of cellulose fibers (diameter 20-50 μm), microfibrils (diameter 4-35 nm) and elementary fibrils (diameter 2-20 nm). The elementary fibrils are the basic building blocks in plants and typically consists of 20-40 cellulose chains assembled into highly ordered crystalline domains and disordered domains (also called amorphous domains).[10,11] The amorphous domains are distributed along the fibrils as a result of the dislocations of cellulose chains which is known to cause distortion and twist of the fibrils.[9] While the crystalline domains are resulting from tightly packed cellulose chains. The hydrogen-bonding network and molecular orientation in cellulose varies widely with the source and isolation method.[12] The crystal structures in native cellulose, which is called cellulose I, are consisting of cellulose chains that are orientated parallel to each other.[13] This is in contrast to cellulose II structure which exists in regenerated or derivatized cellulose where an anti-parallel chain orientation is adopted.[14] Cellulose I comprise two polymorphs, namely cellulose Iα with triclinic unit cell and cellulose Iβ with a monoclinic unit cell.[15] Cellulose Iα mainly exists in algae and bacteria,[16–18] while cellulose Iβ is dominant in plant cell walls such as cotton and in tunicates.[6]

Natural cellulose has been used in the form of wood and plant fibers as energy source, building materials and clothing for thousands of years.[19] During the past 200 years, materials based on cellulose and its derivatives have been industrialized in large scale and utilized in a wide range of applications including food, coatings, films, membranes, pharmaceuticals.[20] Some of the most widely known cellulose materials include celluloid (base on nitrocellulose, discovered in 1870), cellophane (based on regenerated cellulose, discovered in 1900) as well as carboxymethyl cellulose (used as food additives).

1.2 Cellulose nanomaterials

Cellulose nanomaterials (CNM), or nanocellulose (NC), refers to cellulose particles with at least one dimension in the nanometer range (1-100 nm).[21] Cellulose nanomaterials combine the excellent properties of cellulose, such as high specific strength, low density, hydrophilicity and available surface hydroxyl groups for functionalization, with specific properties of nanoscale materials, such as high aspect ratio and high surface areas. Therefore, the use of cellulose nanomaterials as building blocks in modern material design offers countless opportunities for the development of high-performance materials.[21–25] Besides, with the worldwide demands for renewable and non-petroleum based materials, cellulose nanomaterials have received a considerable amount of interests as a result of their availability, sustainability and biodegradability.[26,27] Cellulose nanomaterials can be isolated from a wide range of bio-sources via both top-down methods including chemical/physical/enzymatic process, as well as bottom-up approaches using certain type of bacteria.[28] Based on their dimensions and preparation methods, cellulose nanomaterials can be classified into two major categories, cellulose nanocrystals (CNC) and cellulose nanofibers (CNF).

1.2.1 Cellulose nanofibers (CNF)

Cellulose nanofibers (CNF) are flexible nano-scale fibers with a high aspect ratio, which contain both crystalline and amorphous regions distributed along the long axis.[29,30] CNF can be extract from plant cell walls under mechanical treatments, including high-pressure homogenization, grinding or high intensity ultrasonication which can break down the cellulose microfibrils into individual nanofibers.[31–35] However, the isolation of CNF using pure mechanical treatment requires significant amount of energy input and results in materials which still contains a lot of

aggregated fiber bundles. Therefore, different pretreatment methods are applied prior to the mechanical disintegration to facilitate the isolation process, which includes chemical treatments and enzymatic degradation.[36,37] One of the most commonly used chemical treatments is 2,2,6,6-tetramethylpiperidine-1-oxyl (TEMPO)-mediated oxidation, which introduces negatively charged carboxylate groups to the surface of the fibers to aid the delamination process.[38–40] The resulting nanofibers have a typical dimension between 3-20 nm in width, with lengths from hundreds of nanometers to a few micrometers, and form a highly viscous suspension in water even at low solid content (1-2 wt%) due to high aspect ratio and flexibility of the nanofibers (Figure 1.2).[40] As such, CNF has been investigated as rheological modifiers and can be potentially utilized in food, cosmetic, pharmaceutical and mining industry.[41] In the dry state, transparent films with high mechanical integrity and excellent oxygen barrier properties can be prepared with pure CNF.[42–44] Besides, CNF can be used as reinforcing agent in polymer composites which significantly enhance the mechanical properties of the materials. [27,29,30]

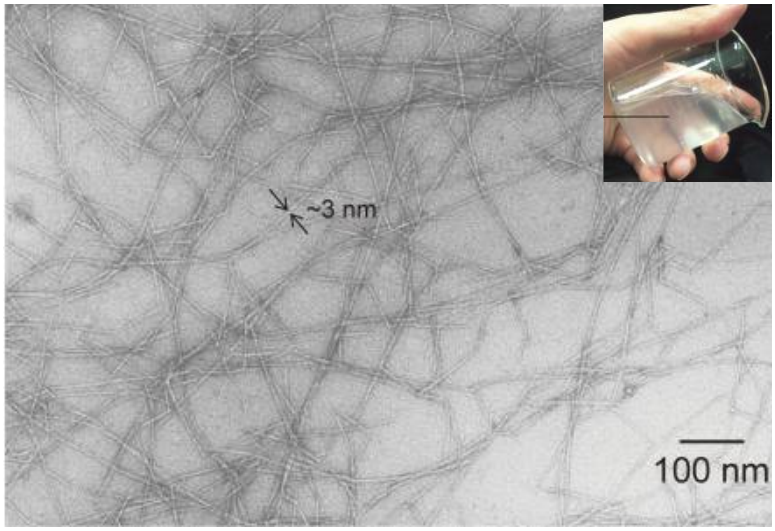

Figure 1.2 TEM image of TEMPO oxidized cellulose nanofibers. Insert: typical aqueous dispersion of the oxidized CNF. (Figure reproduced from ref[45])

1.2.2 Cellulose nanocrystals (CNC)

Cellulose nanocrystals (CNC) are rod like nanoparticles, which are reminiscent of the crystalline regions within the elementary nanofibrils of cellulose. In 1947, Nickerson and Habrle reported the first hydrolysis of cellulose fibers using aqueous hydrochloric acid or sulfuric acid, where they found out that the disordered intercrystalline regions appeared to be dissolved first as opposed to the crystalline sections.[46] This observation lead to the first successful isolation of the crystalline particles as a colloid suspension by Ranby in 1949.[47] The nanocrystals were later visualized by electron microscope, and their crystal structure was confirmed by X-ray diffraction to be the same as the cellulose fibers.[48,49] Various types of aqueous inorganic acid have been utilized for the hydrolysis of CNCs which yields nanocrystals with different surface functionalities. Nanocrystals prepared by sulfuric acid hydrolysis display a good colloid dispersibility in water as a result of the more negatively charged sulfate ester groups introduced onto the surface during hydrolysis.[50] Whereas hydrochloric acid[51] or hydrobromic acid[52] hydrolysis yields CNC with uncharged surfaces and poor dispersibility in water. Phosphoric acid has also been used for the hydrolysis reaction, and the resulting CNCs show a good dispersity in polar solvents due to the negative charged phosphate groups, as well as a much higher thermal stability as compared to the sulfonated CNCs.[53]

CNCs can be isolated from a wide range of biosources, including wood pulp,[54] cotton,[55] ramie,[56] sisal,[57] tunicates,[58] bacteria,[59] etc. The dimension of the nanocrystals is approximately 5 to 25 nm in cross-section, and hundreds of nanometers to microns in length, which varies widely depending on the source that they are isolated from and the isolation methods.[60,61] For example, CNCs from wood are 3-5 nm in width and 100-200 nm in length, while cotton CNCs are 5-10 nm in width and 100-300 in length. CNCs isolated from tunicates and bacteria are much longer, with a width of 10-

20 nm in length and 500-2000 nm in length for tunicate CNCs, and a width between 10-50 nm and 100 a length between 100-2000 nm for bacteria CNCs (Figure 1.3). The most important property of the CNCs isolated from different sources is their aspect ratio (defined by the ratio of crystals length and the width) which can affect the reinforcing potential in composite materials.

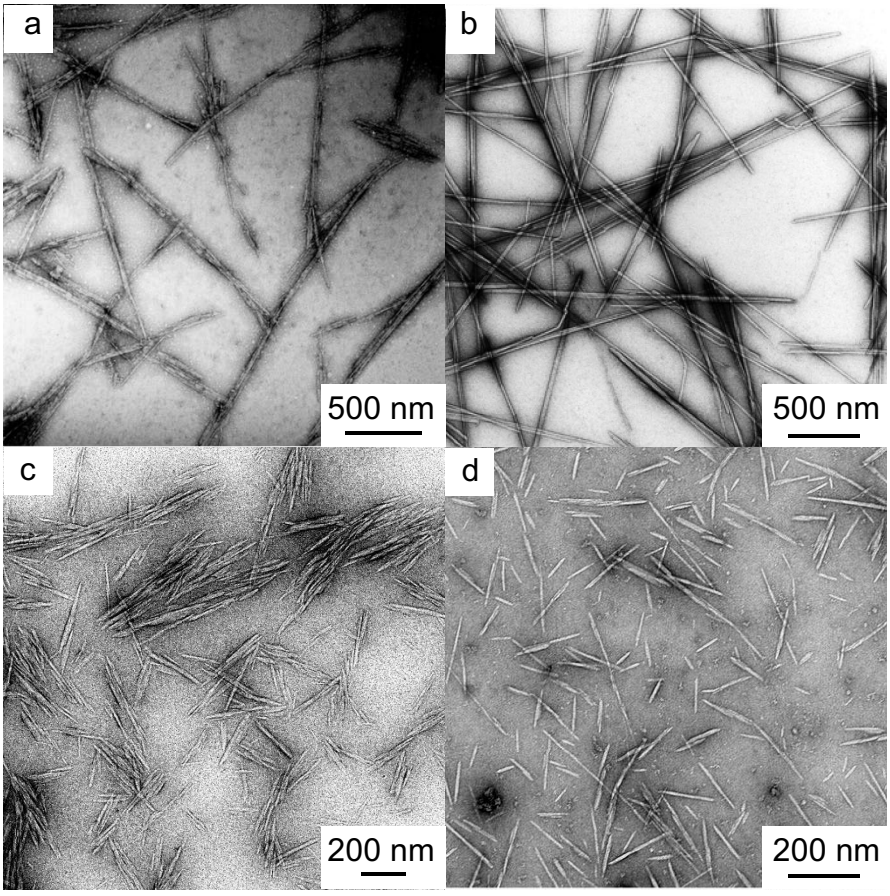

Figure 1.3 TEM images of CNCs isolated from a) bacteria,[59] b) tunicate,[61] c) cotton[62] and d) wood (USDA Forest Lab, WI).

The main benefits attributed to CNCs are their high aspect ratio, low density, and high tensile strength (with a theoretical predicted elastic modulus of about 150 GPa that is comparable to steel).[63] Therefore, the most significant efforts have been focused on the application of CNCs as

reinforcing materials in polymer nanocomposites to significantly improve the mechanical property of the materials.[64–66] By carefully tuning the functionalities on the surface for the nanocrystals, their applications in catalyst, energy storage devices, membranes, Pickering emulsions and biomedical materials have also been explored.[67,68]

1.3 Surface functionalization of Cellulose Nanocrystals

Due to the abundance of surface hydroxyl groups, chemical modifications have been carried out to control the surface properties of the nanocrystals with the goal of increasing colloid stability, improving compatibility between CNC and polymer in composite materials, or introducing specific functionality for the development of functional materials. A wide range of chemistries have been attempted, including oxidation, amidation, esterification, etherification, silylation, polymer grafting, etc. Noncovalent functionalization, such as electrostatic interactions, absorption of surfactants and polymers, have also been explored. The surface functionalization of CNCs have been review extensively in several publications.[24,69,70] The main challenge for the surface functionalization of CNCs is to only react the surface hydroxyl groups without affecting the integrity of the crystal structure. It should also be noted that the majority of the hydroxyl groups on the cellulose chains are buried inside the crystals and do not participate in the surface functionalization reaction.

1.3.1 Noncovalent functionalization

The first report of a noncovalent functionalization of CNC was done by Heux et al. who mixed CNC aqueous suspension with surfactants containing alkylphenol tails.[71] The surfactants were shown to form a thin layer of 15 Å at the surface of the CNCs, and the surfactant-modified CNCs

can be dispersed in nonpolar solvents.[71,72] Cationic surfactants are commonly used in literatures, since the surface charges of CNCs are generally negative (after sulfuric acid hydrolysis or TEMPO-mediated oxidation) so the positive charges from surfactants could form electrostatic interaction with the CNCs.[73–75] Uncharged polymers were also shown to be able to selectively absorb at the surface of CNCs.[76–79] For example, Ben Azouz reported that adding CNCs to an aqueous solution of polyethylene oxide (PEO) could decrease the viscosity of the suspension which indicates there is an interaction between the PEO chains and the surface of the nanocrystals.[79] The PEO-coated CNCs were then used to reinforce low density polyethylene, and the nanocomposites showed good dispersity of nanofillers as well as an improved thermal stability compared to neat CNC-based nanocomposites.

1.3.2 TEMPO-mediated oxidation

Oxidation remains one of the most commonly used surface modification techniques which introduces aldehyde or carboxylic acid groups.[7,69,70,80] Two of the most widely performed oxidation reactions on CNCs include periodate oxidation which cleaves C2-C3 bonds of glucose rings and selectively oxidizes C-2 and C-3 vicinal hydroxyl groups into 2, 3-dialdehyde,[81] and 2,2,6,6-tetramethylpiperidine-1-oxyl (TEMPO)-mediated oxidation which selectively oxidizes the primary C6 hydroxyl groups into carboxylic acid groups.[82]

TEMPO oxidation was first reported by Nooy et al.,[83] the process generally required a catalytic amount of stable nitroxyl racial (TEMPO) in the presence of sodium hypochlorite (NaOCl) and sodium bromide (NaBr), at pH 10-11 where the reactions showed good selectivity for primary alcohols (Figure 1.4).[82] This process had been applied to CNCs isolated using HCl hydrolysis by Araki et al.,[84] where negatively charged carboxylic acid groups can be introduced to the surface of

CNCs which increases the stability in aqueous suspension through electrostatic repulsion. Report by Habibi et al. showed that the morphological integrity and crystallinity of the HCl hydrolyzed tunicate CNCs were not affected by TEMPO oxidation reaction.[85] The results in both works also indicate that the degree of oxidation can be controlled by the concentration of primary oxidant, NaOCl.[84,85] In addition to promoting the dispersibility of CNCs in water and other polar organic solvent (DMF, DMSO, NMP), the surface carboxylic acid moieties also served as reactive sites that can be used for further surface functionalization.[86]

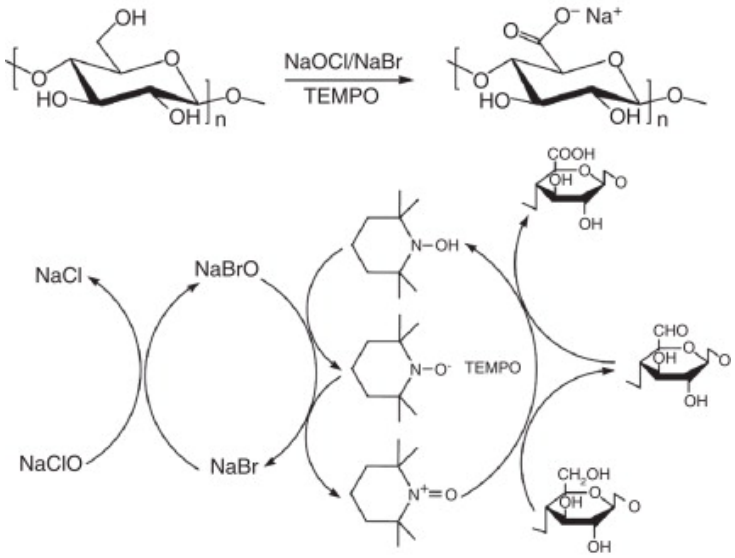

Figure 1.4 Schematics of TEMPO-mediated oxidation mechanism of primary alcohols.87

1.3.3 Amidation

The carboxylic acid groups obtained after TEMPO oxidation allows subsequent coupling reaction using amine derivatives to synthesis CNCs with new functionalities. The amidation reaction involves the activation of the carboxylic acid group using a carbodiimide compound in the presence of N-hydroxysuccinimide (NHS) through the formation of stable N-hydroxysuccinimidyl ester intermediate, followed by reaction with primary amine to yield the final

product (Figure 1.5).[88] Araki et al. first reported the amidation reaction on TEMPO oxidized CNCs with a primary amine terminated polyethylene glycol (PEG-NH_2) using 1-ethyl-3-(3-dimethylaminopropyl)carbodiimide hydrochloride (EDC) and N-hydroxysuccinimide (NHS) to prepare PEG-grafted CNCs.[84] Various amine derivatives such as hexylamine, ethylene diamine, Jeffamine, amine terminated poly(oligo(ethylene glycol)monomethyl ether (meth)acrylates) (POEG(M)A) were attached to the CNCs.[89–92] It is worth pointing out that the carbodiimide-mediated amidation can be carried both in water and in polar solvent such as DMF. It is reported that the favorable pH range is 7.5-8.0 for the amidation reaction of CNCs in water, while the pH is less important for reactions proceeded in DMF. Azzam et al. conducted amidation reactions of TEMPO-oxidized cotton CNC with Jeffamine in both water and DMF, and reported that the reaction is favored in DMF with a higher degree of coupling.[92] The result is believed to be a limited competition between solvent and polymer with the surface of CNC in DMF compared to water.[93]

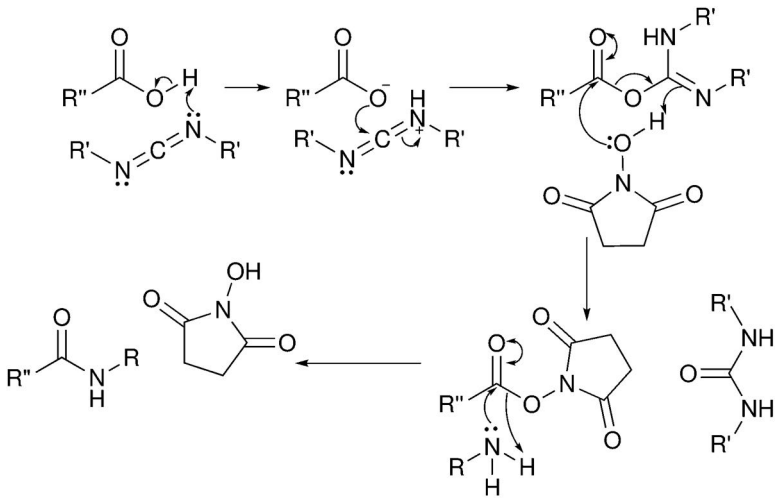

Figure 1.5 Mechanism for carbodiimide mediated amidation reaction.[70]

Although the carbodiimide coupling agent is popular and effective, the carbodiimide-mediated amidation reaction of CNCs is still suffering from a relatively low coupling efficiency and difficulty in byproduct removal. Recently, a promising coupling agent, 4-(4,6-Dimethoxy-1,3,5-triazin-2-yl)-4-methylmorpholinium chloride (DMTMM), has been reported as coupling agent for the amidation reaction of alginate oligosaccharides (AOS) with amino acid.[94] DMTMM was shown to have a higher reactivity which lead to a higher coupling efficiency, the byproduct is also fully soluble in water and easy to remove.[95,96] DMTMM can potentially be used for the amidation reaction of CNCs to further improve the degree of amine coupling.

1.4 CNC stabilized Pickering emulsions

1.4.1 Pickering emulsions

An emulsion is a mixture of two immiscible liquids with one dispersed in another continuous liquid phase that is usually stabilized by a surface active compound (surfactant). Conventional surfactants are low molar mass molecules or polymers that contain a balance of both hydrophilic and hydrophobic groups. The surface tension between the two liquid phase is decreased by the surfactant so the emulsion can be stabilized without phase separation. A different class of emulsions are the Pickering emulsions which are stabilized by solid colloid particles. Pickering emulsion was discovered in the early 1900's,[97,98] but the research on the subject only starts to regain interest in the past two decades due to its excellent properties in food, pharmaceutical and cosmetic applications.[99]

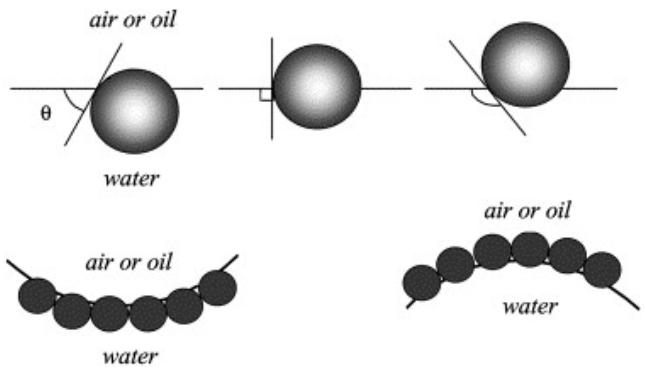

Figure 1.6 Schematic illustration of the effect of particles contact angle on the result emulsion.[100]

Unlike traditional surfactants which have to be amphiphilic to absorb at the oil-water interface, colloid particles in Pickering emulsion that have partial wettability in both immiscible liquid phases will preferentially orientate at the interface.[101,102] The wettability at the solid/oil/water interface is evaluated by the three-phase contact angle θ_{ow} (Figure 1.6).[100] Particles that have a better affinity to the water phase will show a θ_{ow} lower than 90° when absorbed at the interface. Therefore, the curvature of the interface will change such that the phase where the particles resides (water) become continuous phase, which leads to an oil-in-water emulsion. On the other hand, water-in-oil emulsion can be achieved using particle that have a better affinity to the oil phase where the three-phase contact angle θ_{ow} is greater than 90°. The particles adsorption at the interface tends to be irreversible as indicated by the relatively large energy (on the order of 10^5 k_BT for a 100 nm particle) required to remove them from the interface.[103] Therefore, Pickering emulsion demonstrate better stability against coalescence with the particle layer act as a mechanical barrier.

1.4.2 Pickering emulsions stabilized by unfunctionalized CNCs

Most of the work on particle stabilized emulsions are based on inorganic and organic spherical particles.[104,105] While emulsions are of great interests for their application in food, pharmaceuticals,

and cosmetics, colloid particles derived from biomass, such as starch, chitin and cellulose-based particles, are preferred. The first report of an emulsion stabilized with solid cellulose particles were published by Oza and Frank, who showed that heavy mineral oil-in-water emulsions could be stabilized with microcrystalline cellulose.[106] Various microfibrillated cellulose (MFC) and bacteria cellulose nanofibrils have been successfully used as emulsifiers.[107] However, these high aspect ratio fibers do not efficiently pack the interface which leads to the formation of bigger emulsion droplet sizes, and poor long term stability since a large portion of the interface are left unprotected.

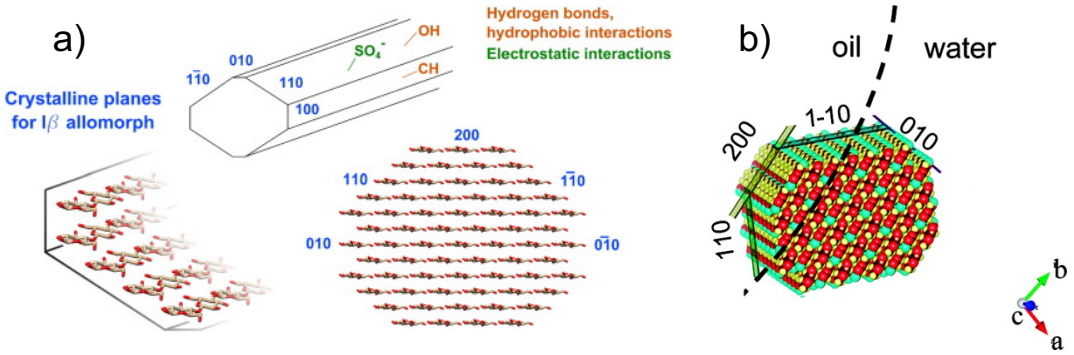

Figure 1.7 Schematic representation of a) the crystal planes of CNCs and b) the orientation of CNCs at the oil/water interfaces. (Figure reproduced from ref[108] and ref[109])

Therefore, the shorter and well-defined cellulose nanoparticles are good potential candidates for interfacial stabilization. Capron group has pioneered the work on using unmodified/sulfated CNCs as solid stabilizers to access stable oil-in-water Pickering emulsions.[109–111] Studies on the crystal structures suggests that the CNCs are inherently amphiphilic with one of the crystal planes (200) being more hydrophobic (on account of the axial C-H methine groups) and others being hydrophilic.[112] The Capron group suggests that the sulfated CNCs can be preferentially absorbed at the interface with the (200) plane orientated towards the oil phase and stabilize the emulsion though Pickering emulsion mechanism (Figure 1.7).[109] This was further proved by a recent study

using neutron scattering where they also found the nanocrystals have little-to-no change to the interface.[113] The result also implies that the wetting behavior at the interface tend to bend the rigid crystals in order to accommodate the curvature of the droplet.

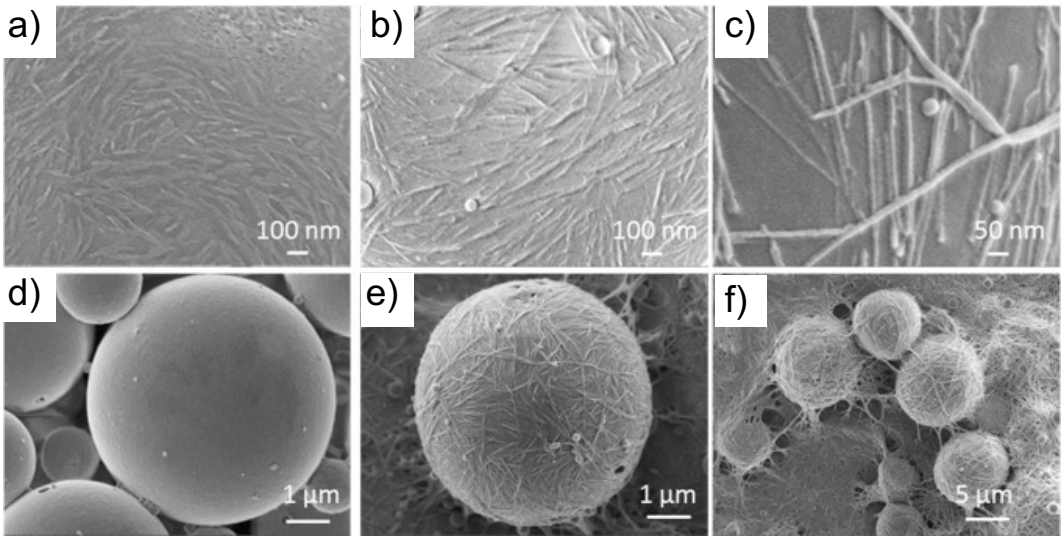

Figure 1.8 SEM images of polymerizes styrene-in-water emulsions stabilized by cotton CNC (a, d), bacterial CNC (b, e), and Cladophora algae CNC (c, f) revealing the coverage variation as a function of aspect ratio. (Figure reproduced from ref[114])

The surface charge density of CNCs were also shown to significantly impact the stability of the emulsions. CNCs with a surface charge density (sulfate half ester) above 0.03 e/nm^2 were not able to stabilize the interface, presumably because higher charges will promote electrostatic repulsion at the interface which destabilized the emulsions.[109] The Capron group also showed that the aspect ratio of CNCs directly affects the coverage behavior of CNCs at the interface (Figure 1.8). Cotton CNCs with lower aspect ratio could more densely pack the surface with a coverage of 84%, while Cladophora CNCs with higher aspect ratio tend to span between droplets and only a minimum of 44% coverage is needed to access stable emulsions.[111]

1.4.3 Pickering emulsions stabilized by functionalized CNCs

Owing to the strong hydrophilic nature of the cellulose nanocrystals, only oil-in-water emulsions can be stabilized by unfunctionalized CNCs. However, the surface of the crystals can be functionalized to increase the hydrophobicity which makes them suitable to stabilize water-in-oil emulsions. Limousin et al. functionalized the surface of CNCs with long hydrophobic alkyl chains using lauroyl chloride and showed that water-in-oil emulsion can be obtained as a result of the increased hydrophobicity of the CNCs.[115] The functionalization can be done in a simple manner by physical adsorption of surfactant molecules or polymers to alter the surface properties of the CNCs. Saidane et al. mixed TEMPO oxidized CNCs with quaternary ammonium salts solution and showed that the resulting noncovalently modified CNCs could be used to stabilized water-in-oil emulsions.[116] Cranston and co-workers have reported the use of surface active polymers (hydroxyethyl cellulose, methyl cellulose) or cationic surfactants, didecyldimethylammonium bromide (DMAB) and cetyltrimethylammonium (CTAB), to functionalized the CNCs.[117,118] They reported these polymer or surfactant functionalized CNC can reduce the interfacial tension between the oil and water phase as a result of the surface active molecules absorbed at the surface, which resulted in an enhanced emulsion stability.

1.5 CNC based polymer nanocomposites

Polymer nanocomposites are multiphase system, where one of the phases has at least one dimension less than 100 nm. Polymer nanocomposites usually consist of nanosized fillers distributed into a polymer matrix. The properties of the polymer nanocomposites are noticeably different from the matrix polymer, which can be affected by a number of factors, such as the inherent properties of both the filler and the matrix, the size, shape, aspect ratio, and distribution

of the filler, as well as the filler-filler and fill-matrix interactions.[119] On account of the high elastic modulus, low density, high aspect ratio, high surface area, as well as available surface for further functionalization, CNCs have been widely explored as filler materials to reinforce a number of polymer matrices. Adding CNCs have been shown to dramatically alter the thermomechanical and dynamic mechanical properties of the materials. The first report of using CNC as fillers to fabricate polymer nanocomposites was performed by Favier et al., who mixed aqueous suspensions of sulfuric acid-hydrolyzed tunicate CNCs with a commercial aqueous poly(styrene-co-butyl acrylate) latex.[120] The resulting polymer nanocomposites demonstrated a significant enhancement in mechanical properties, which is attributed to the formation of a percolating CNC filler network. Much of the work to date has been extensively reviewed.[121–123] It is important to note that optimal reinforcement requires the nanocrystals to be uniformly dispersed within the polymer matrix. It remains a challenge to disperse unfunctionalized CNCs that are hydrophilic into some hydrophobic polymers.

1.5.1 Bio-inspired stimuli-responsive mechanically dynamic nanocomposite

Polymer nanocomposites are frequently used by nature to create biological materials with a wide range of exceptional properties. Adoption of nature's design strategy allows for the development of novel polymer nanocomposites that either mimic the excellent properties of the biological materials or improve the performance of the current synthetic materials. The inner dermis of the sea cucumber is an interesting example of a biological composites with stimuli-responsive behavior.[124] The dermis of the sea cucumber transitions from a soft to stiff state within millisecond when the animal is threatened (Figure 1.9). Several studies have shown that the defense mechanism of the dermis is enable by a nanocomposite structure consisting of rigid, high-aspect ratio collagen

fibrils embedded into a low modulus fibrillin matrix. The sea cucumber releases glycipriteins when threatened, which chemically crosslink the rigid collagen fibrils and form a percolating network to reinforce its soft matrix. The process is fully reversible through proteinases.

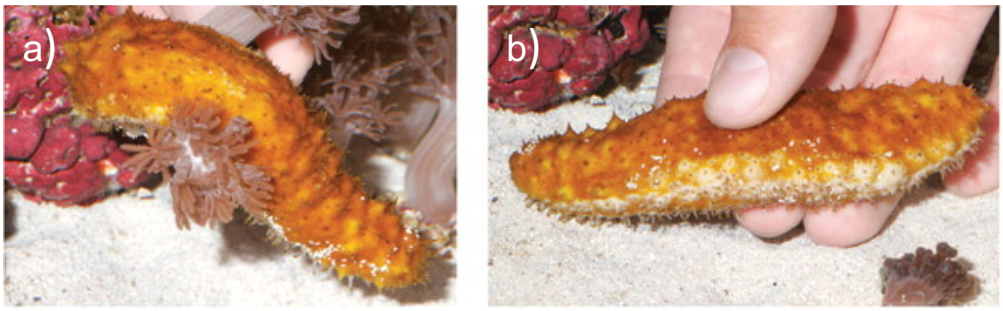

Figure 1.9 Photos of sea cucumber in the a) relaxed and b) stiff state.[125]

Inspired by the stimuli-responsive behavior of the sea cucumber dermis, Capadona et al. reported the preparation of the first synthetic polymer nanocomposite that mimic the mechanically switchable behavior by embedding rigid tunicate CNCs into a soft EO-EPI (ethyleneoxide/epichlorohydrin) copolymer matrix.[125] In the dry state, the strong hydron-bonding interaction between the CNC fillers (may also aid by CNC-matrix interactions) lead to the formation of a reinforcing, percolating network, resulting in stiff materials. Dynamic mechanical analysis (DMA) results demonstrated an increase in the tensile storage modulus as the volume fraction of CNCs increased (Figure 1.10). The data fits nicely with the percolation model, which is used to predict the storage modulus of the nanocomposites, assuming strong interactions between the rigid fillers.[126] The result is consistent with the formation of rigid filler networks. Exposing the nanocomposite to water will lead to a mechanical softening of the materials, on account of the disengagement of the CNC interactions (and presumably also reduction of CNC-matrix interactions) via competitive hydrogen bonding between the CNCs and water molecules.

As a result, the modulus decreases from ca. 800 MPa to 20 MPa for 19 vol.% CNC nanocomposites. The modulus of the wet films fit to the Halpon-Kardos model,[127] which is used to describe the modulus of nanocomposites in which the filler is homogeneously dispersed but do not display filler-filler interactions. Using the same design strategy, Rowan and co-workers have fabricated mechanically dynamic nanocomposites using a wide range of polymer matrices.[128–130]

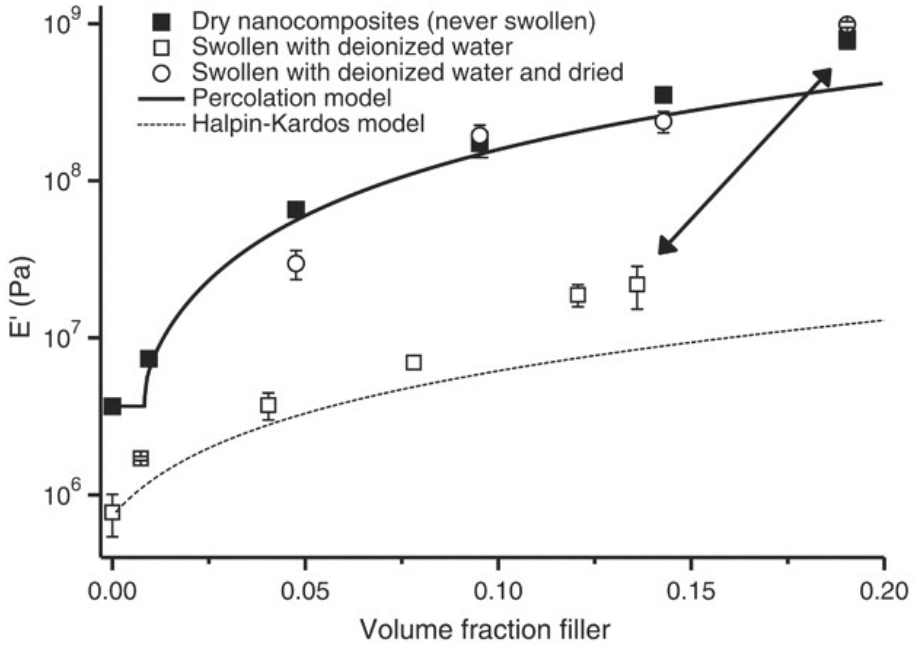

Figure 1.10 Tensile storage moduli (E') versus volume fraction of CNC filler in EO-EPI nanocomposites in the dry and wet state. Dry state data was fit to the Percolation model (solid line) and wet state data was fit to the Halpin-Kardos model (dotted line).[125]

1.5.2 Bio-inspired water-enhance mechanical gradient nanocomposite

The squid beak is another interesting natural nanocomposite which displays a water-enhanced mechanical gradient property that bridges between the stiff tip of the beak (rostrum) to the squid's soft muscle tissues (buccal) (Figure 1.11).[131] In order to protect the soft buccal tissue (elastic modulus 50 MPa) from damaging by the high interfacial stresses generated at the stiff rostrum

(elastic modulus 5 GPa) during feeding, a mechanical gradient that spans two orders of magnitude in stiffness is required. Research performed by Waite, Zok, Miserez and coworkers have shown that the squid beak is consist of chitin, proteins and water.[131,132] The excellent mechanical gradient property of the beak is achieved by varying the degree of covalent crosslinking within the protein matrix and the degree of hydration along the structure.[133,134]

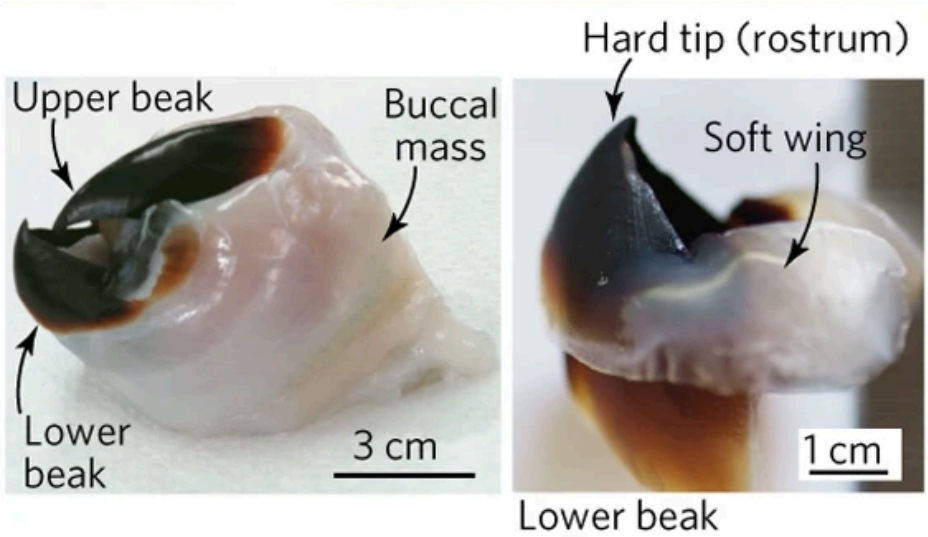

Figure 1.11 Photos of a dissected beak embedded within its soft buccal mass (left) and a lower beak (right).[134]

Fox et al. have reported the preparation of polymer nanocomposites that mimic the water-enhanced mechanical gradient property of the squid beak biomodel.[135] By embedding allyl-functionalized tunicate CNCs into a polyvinyl acetate matrix along with a tetra thiol crosslinker (pentaerythritol tetrakis(3-mercaptopropionate), PETMP) and photoinitiator, the CNC fillers can be covalent crosslinked via photo-induced thiol-ene chemistry. The amount of UV exposure can be used to control the degree of crosslinking which allows access to materials with tunable mechanical properties. In the dry state, the original hydrogen bonding interactions between the CNC fillers can be augmented with covalent crosslinks which results in a slight increase in storage

modulus. However, in the wet state, the covalent crosslinks between CNCs will be permanently "switch-on" and as such can greatly reduce the mechanical softening effect of the nanocomposites. As a result, films with a storage modulus of over 100 MPa in the wet state can be achieved, as compared to ca. 30 MPa for unexposed composites that only contain noncovalent interactions which can be easily disrupted by the presence of water. By carefully controlling the UV exposure along the composite films, materials with a gradient in stiffness can be achieved (Figure 1.12). These materials can be potentially used in biomedical applications where a stiff therapeutic implant device is in immediate contact with soft biological tissues, such as intracortical microelectrodes.

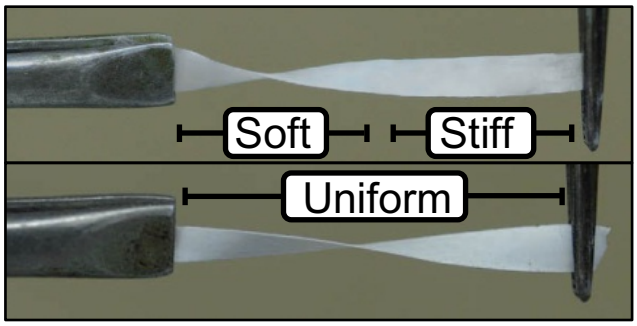

Figure 1.12 Photos of wet nanocomposite samples twisted by half turn. Top: gradient exposed film. Bottom: uniform crosslinked film.[135]

1.6 Dissertation Scope

The aim of this dissertation is to incorporate surface functionalized CNCs into different polymer matrices and investigate the relationship between the CNC surface functionalities and the macroscopic material properties of the nanocomposites.

Chapter 2 will focus on CNCs functionalized with alkylamines of different alkyl chain length to increase the hydrophobicity. The resulting alkyl-functionalized CNCs have been investigated as solid particle surfactants to stabilize oil-in-water emulsion. The relationship between the

hydrophobic/hydrophilic properties of the CNCs and the stability and size of the emulsion is investigated.

Chapter 3 will focus on the properties of the latex nanocomposites fabricated by polymer latex nanoparticles stabilized with hydrophobically functionalized CNCs. The thermomechanical properties and microstructures of the films are studied and related to the type and amount of stabilizers as well as the processing conditions.

Chapter 4 will focus on the effect of processing conditions on the mechanical properties of bio-inspired nanocomposite based on allyl-functionalized CNCs embedded into polyvinyl acetate matrix. The effects of UV crosslinking conditions, films processing conditions as well as film thickness on final mechanical properties of the films are studied.

Chapter 5 will focus on the mechanical properties of the nanocomposites fabricated by alkene-containing polymer, poly(vinyl acetate-co-vinyl pentenoate), with either carboxylic- or ally-functionalized CNCs. The effect of the placement of the covalent crosslinks (i.e. within matrix only or also between the matrix and filler) on the wet mechanical properties of the films are evaluated.

Chapter 6 will focus on the preparation of bio-inspired nanocomposites based on carboxylic acid functionalized CNCs and partially hydrolyzed poly(vinyl acetate-co-vinyl alcohol) matrix. The effect of UV initiated covalent crosslinking between the hydroxyl groups on the wet mechanical properties as well as the water swelling behavior of the films are investigated.

1.7 Reference

(1) French, A. D.; Bertoniere, N. R.; Battiste, O. A.; Cuculo, J. A.; Gray, D. L. *Cellulose Kirk-Othmer Encyclopedia of Chemical Technology, Vol. 5*; 1993.

(2) Kaplan, D. L. Introduction to Biopolymers from Renewable Resources. In *Biopolymers from Renewable Resources*; Springer Berlin Heidelberg: Berlin, Heidelberg, 1998; pp 1–29.

(3) Rosli, N. A.; Ahmad, I.; Abdullah, I. Isolation and Characterization of Cellulose Nanocrystals from Agave Angustifolia Fibre. *BioResources* **2013**, *8* (2), 93–97.

(4) Nobles, D. R.; Romanovicz, D. K.; Brown, R. M. Cellulose in Cyanobacteria. Origin of Vascular Plant Cellulose Synthase? *Plant Physiol.* **2001**, *127* (2), 529–542.

(5) Ross, P.; Mayer, R.; Benziman, M. Cellulose Biosynthesis and Function in Bacteria. *Microbiol. Rev.* **1991**, *55* (1), 35–58.

(6) Belton, P. S.; Tanner, S. F.; Cartier, N.; Chanzy, H. High-Resolution Solid-State Carbon-13 Nuclear Magnetic Resonance Spectroscopy of Tunicin, an Animal Cellulose. *Macromolecules* **1989**, *22* (4), 1615–1617.

(7) Habibi, Y.; Lucia, L. A.; Rojas, O. J. Cellulose Nanocrystals: Chemistry, Self-Assembly, and Applications. *Chem. Rev.* **2010**, *110* (6), 3479–3500.

(8) Hon, D. N.-S. Cellulose: A Random Walk along Its Historical Path. *Cellulose* **1994**, *1* (1), 1–25.

(9) Rowland, S. P.; Roberts, E. J. The Nature of Accessible Surfaces in the Microstructure of Cotton Cellulose. *J. Polym. Sci. Part A-1 Polym. Chem.* **1972**, *10* (8), 2447–2461.

(10) Gibson, L. J. The Hierarchical Structure and Mechanics of Plant Materials. *Journal of the Royal Society Interface*. Royal Society November 7, 2012, pp 2749–2766.

(11) Isogai, A.; Saito, T.; Fukuzumi, H. TEMPO-Oxidized Cellulose Nanofibers. *Nanoscale* **2011**, *3* (1), 71–85.

(12) A., S. Recent X-Ray Crystallographic Studies of Celluloses. In *Cellulose: Structure, Modification and Hydrolysis*; John Wiley & Sons, 1986.

(13) Nishiyama, Y.; Langan, P.; Chanzy, H. Crystal Structure and Hydrogen-Bonding System in Cellulose Iβ from Synchrotron X-Ray and Neutron Fiber Diffraction. *J. Am. Chem. Soc.* **2002**, *124* (31), 9074–9082.

(14) Kolpak, F. J.; Blackwell, J. Determination of the Structure of Cellulose II. *Macromolecules* **1976**, *9* (2), 273–278.

(15) ATALLA, R. H.; VANDERHART, D. L. Native Cellulose: A Composite of Two Distinct Crystalline Forms. *Science (80-.).* **1984**, *223* (4633), 283–285.

(16) Eichhorn, S. J.; Dufresne, A.; Aranguren, M.; Marcovich, N. E.; Capadona, J. R.; Rowan, S. J.; Weder, C.; Thielemans, W.; Roman, M.; Renneckar, S.; Gindl, W.; Veigel, S.; Keckes, J.; Yano, H.; Abe, K.; Nogi, M.; Nakagaito, A. N.; Mangalam, A.; Simonsen, J.; Benight, A. S.; Bismarck, A.; Berglund, L. A.; Peijs, T. Review: Current International Research into Cellulose Nanofibres and Nanocomposites. *Journal of Materials Science*. Springer January 1, 2010, pp 1–33.

(17) Yamamoto, H.; Horii, F. CPMAS Carbon-13 NMR Analysis of the Crystal Transformation Induced for Valonia Cellulose by Annealing at High Temperatures. *Macromolecules* **1993**, *26* (6), 1313–1317.

(18) Yamamoto, H.; Horii, F.; Hirai, A. In Situ Crystallization of Bacterial Cellulose II. Influences of Different Polymeric Additives on the Formation of Celluloses Iα and Iβ at the Early Stage of Incubation. *Cellulose* **1996**, *3* (1), 229–242.

(19) Klemm, D.; Heublein, B.; Fink, H.-P.; Bohn, A. Cellulose: Fascinating Biopolymer and Sustainable Raw Material. *Angew. Chemie Int. Ed.* **2005**, *44* (22), 3358–3393.

(20) Kamide, K. *Cellulose and Cellulose Derivatives*; 2005

(21) Klemm, D.; Kramer, F.; Moritz, S.; Lindström, T.; Ankerfors, M.; Gray, D.; Dorris, A. Nanocelluloses: A New Family of Nature-Based Materials. *Angew. Chemie Int. Ed.* **2011**, *50* (24), 5438–5466.

(22) Eichhorn, S. J. Cellulose Nanowhiskers: Promising Materials for Advanced Applications. *Soft Matter* **2011**, *7* (2), 303–315.

(23) Wicklein, B.; Salazar-Alvarez, G. Functional Hybrids Based on Biogenic Nanofibrils and Inorganic Nanomaterials. *J. Mater. Chem. A* **2013**, *1* (18), 5469.

(24) Moon, R. J.; Martini, A.; Nairn, J.; Simonsen, J.; Youngblood, J. Cellulose Nanomaterials Review: Structure, Properties and Nanocomposites. *Chemical Society Reviews*. Royal Society of Chemistry July 20, 2011, pp 3941–3994.

(25) Eichhorn, S. J. 1000 at 1000: Reflecting on "Review: Current International Research into Cellulose Nanofibres and Nanocomposites." *J. Mater. Sci.* **2020**, *55* (27), 12637–12641.

(26) Plackett, D.; Letchford, K.; Jackson, J.; Burt, H. A Review of Nanocellulose as a Novel Vehicle for Drug Delivery. *Nord. Pulp Pap. Res. J.* **2014**, *29* (1), 105–118.

(27) Dufresne, A. Cellulose Nanomaterial Reinforced Polymer Nanocomposites. *Curr. Opin. Colloid Interface Sci.* **2017**, *29*, 1–8.

(28) Su, Y.; Burger, C.; Hsiao, B. S.; Chu, B. Characterization of TEMPO-Oxidized Cellulose Nanofibers in Aqueous Suspension by Small-Angle X-Ray Scattering. *J. Appl. Crystallogr.* **2014**, *47* (2), 788–798.

(29) Nakagaito, A. N.; Yano, H. Novel High-Strength Biocomposites Based on Microfibrillated Cellulose Having Nano-Order-Unit Web-like Network Structure. *Appl. Phys. A* **2005**, *80* (1), 155–159.

(30) Abdul Khalil, H. P. S.; Bhat, A. H.; Ireana Yusra, A. F. Green Composites from Sustainable Cellulose Nanofibrils: A Review. *Carbohydr. Polym.* **2012**, *87* (2), 963–979.

(31) He, W.; Jiang, X.; Sun, F.; Xu, X. Extraction and Characterization of Cellulose Nanofibers from Phyllostachys Nidularia Munro via a Combination of Acid Treatment and Ultrasonication. *BioResources* **2014**, *9* (4), 6876–6887.

(32) Li, M.; Wang, L. J.; Li, D.; Cheng, Y. L.; Adhikari, B. Preparation and Characterization of Cellulose Nanofibers from De-Pectinated Sugar Beet Pulp. *Carbohydr. Polym.* **2014**, *102* (1), 136–143.

(33) Kargarzadeh, H.; Mariano, M.; Gopakumar, D.; Ahmad, I.; Thomas, S.; Dufresne, A.; Huang, J.; Lin, N. Advances in Cellulose Nanomaterials. *Cellulose*. Springer Netherlands April 1, 2018, pp 2151–2189.

(34) Chirayil, C. J.; Joy, J.; Mathew, L.; Mozetic, M.; Koetz, J.; Thomas, S. Isolation and Characterization of Cellulose Nanofibrils from Helicteres Isora Plant. *Ind. Crops Prod.* **2014**, *59*, 27–34.

(35) Abe, K.; Iwamoto, S.; Yano, H. Obtaining Cellulose Nanofibers with a Uniform Width of 15 Nm from Wood. *Biomacromolecules* **2007**, *8* (10), 3276–3278.

(36) Boldizar, A.; Klason, C.; Kubát, J.; Näslund, P.; Sáha, P. Prehydrolyzed Cellulose as Reinforcing Filler for Thermoplastics. *Int. J. Polym. Mater.* **1987**, *11* (4), 229–262.

(37) Pääkkö, M.; Ankerfors, M.; Kosonen, H.; Nykänen, A.; Ahola, S.; Österberg, M.; Ruokolainen, J.; Laine, J.; Larsson, P. T.; Ikkala, O.; Lindström, T. Enzymatic Hydrolysis Combined with Mechanical Shearing and High-Pressure Homogenization for Nanoscale Cellulose Fibrils and Strong Gels. *Biomacromolecules* **2007**, *8* (6), 1934–1941.

(38) Saito, T.; Nishiyama, Y.; Putaux, J.-L.; Vignon, M.; Isogai, A. Homogeneous Suspensions of Individualized Microfibrils from TEMPO-Catalyzed Oxidation of Native Cellulose. *Biomacromolecules* **2006**, *7* (6), 1687–1691.

(39) Isogai, A.; Saito, T.; Fukuzumi, H. TEMPO-Oxidized Cellulose Nanofibers. *Nanoscale* **2011**, *3* (1), 71–85.

(40) Saito, T.; Hirota, M.; Tamura, N.; Kimura, S.; Fukuzumi, H.; Heux, L.; Isogai, A.

Individualization of Nano-Sized Plant Cellulose Fibrils by Direct Surface Carboxylation Using TEMPO Catalyst under Neutral Conditions. *Biomacromolecules* **2009**, *10* (7), 1992–1996.

(41) Li, M.-C.; Wu, Q.; Song, K.; Lee, S.; Qing, Y.; Wu, Y. Cellulose Nanoparticles: Structure–Morphology–Rheology Relationships. *ACS Sustain. Chem. Eng.* **2015**, *3* (5), 821–832.

(42) Wang, J.; Gardner, D. J.; Stark, N. M.; Bousfield, D. W.; Tajvidi, M.; Cai, Z. Moisture and Oxygen Barrier Properties of Cellulose Nanomaterial-Based Films. *ACS Sustain. Chem. Eng.* **2018**, *6* (1), 49–70.

(43) Syverud, K.; Stenius, P. Strength and Barrier Properties of MFC Films. *Cellulose* **2009**, *16* (1), 75–85.

(44) Henriksson, M.; Berglund, L. A.; Isaksson, P.; Lindström, T.; Nishino, T. Cellulose Nanopaper Structures of High Toughness. *Biomacromolecules* **2008**, *9* (6), 1579–1585.

(45) ISOGAI, A. Development of Completely Dispersed Cellulose Nanofibers. *Proc. Japan Acad. Ser. B* **2018**, *94* (4), 161–179.

(46) Nickerson, R. F.; Habrle, J. A. Cellulose Intercrystalline Structure. *Ind. Eng. Chem.* **1947**, *39* (11), 1507–1512.

(47) Rånby, B. G.; Banderet, A.; Sillén, L. G. Aqueous Colloidal Solutions of Cellulose Micelles. *Acta Chem. Scand.* **1949**, *3*, 649–650.

(48) Mukherjee, S. M.; Woods, H. J. X-Ray and Electron Microscope Studies of the Degradation of Cellulose by Sulphuric Acid. *Biochim. Biophys. Acta* **1953**, *10* (C), 499–511. https://doi.org/10.1016/0006-3002(53)90295-9.

(49) Emerton, H. W.; Wrist, P. E.; Sikorski, J.; Woods, H. J. Electron-Microscopy of Degraded Cellulose Fibres. *J. Text. Inst. Trans.* **1952**, *43* (11), T563–T564.

(50) Beck-Candanedo, S.; Roman, M.; Gray, D. G. Effect of Reaction Conditions on the Properties and Behavior of Wood Cellulose Nanocrystal Suspensions. *Biomacromolecules* **2005**, *6* (2), 1048–1054.

(51) Yu, H.; Qin, Z.; Liang, B.; Liu, N.; Zhou, Z.; Chen, L. Facile Extraction of Thermally Stable Cellulose Nanocrystals with a High Yield of 93% through Hydrochloric Acid Hydrolysis under Hydrothermal Conditions. *J. Mater. Chem. A* **2013**, *1* (12), 3938.

(52) Sadeghifar, H.; Filpponen, I.; Clarke, S. P.; Brougham, D. F.; Argyropoulos, D. S. Production of Cellulose Nanocrystals Using Hydrobromic Acid and Click Reactions on Their Surface. *J. Mater. Sci.* **2011**, *46* (22), 7344–7355.

(53) Camarero Espinosa, S.; Kuhnt, T.; Foster, E. J.; Weder, C. Isolation of Thermally Stable

Cellulose Nanocrystals by Phosphoric Acid Hydrolysis. *Biomacromolecules* **2013**, *14* (4), 1223–1230.

(54) Araki, J.; Wada, M.; Kuga, S.; Okano, T. Influence of Surface Charge on Viscosity Behavior of Cellulose Microcrystal Suspension. *J. Wood Sci.* **1999**, *45* (3), 258–261.

(55) Dong, X. M.; Revol, J. F.; Gray, D. G. Effect of Microcrystallite Preparation Conditions on the Formation of Colloid Crystals of Cellulose. *Cellulose* **1998**, *5* (1), 19–32.

(56) Habibi, Y.; Goffin, A.-L.; Schiltz, N.; Duquesne, E.; Dubois, P.; Dufresne, A. Bionanocomposites Based on Poly(ε-Caprolactone)-Grafted Cellulose Nanocrystals by Ring-Opening Polymerization. *J. Mater. Chem.* **2008**, *18* (41), 5002.

(57) Garcia de Rodriguez, N. L.; Thielemans, W.; Dufresne, A. Sisal Cellulose Whiskers Reinforced Polyvinyl Acetate Nanocomposites. *Cellulose* **2006**, *13* (3), 261–270.

(58) Zhao, Y.; Zhang, Y.; Lindström, M. E.; Li, J. Tunicate Cellulose Nanocrystals: Preparation, Neat Films and Nanocomposite Films with Glucomannans. *Carbohydr. Polym.* **2015**, *117*, 286–296.

(59) Roman, M.; Winter, W. T. Effect of Sulfate Groups from Sulfuric Acid Hydrolysis on the Thermal Degradation Behavior of Bacterial Cellulose. *Biomacromolecules* **2004**, *5* (5), 1671–1677.

(60) Sacui, I. A.; Nieuwendaal, R. C.; Burnett, D. J.; Stranick, S. J.; Jorfi, M.; Weder, C.; Foster, E. J.; Olsson, R. T.; Gilman, J. W. Comparison of the Properties of Cellulose Nanocrystals and Cellulose Nanofibrils Isolated from Bacteria, Tunicate, and Wood Processed Using Acid, Enzymatic, Mechanical, and Oxidative Methods. *ACS Appl. Mater. Interfaces* **2014**, *6* (9), 6127–6138.

(61) Elazzouzi-Hafraoui, S.; Nishiyama, Y.; Putaux, J.-L.; Heux, L.; Dubreuil, F.; Rochas, C. The Shape and Size Distribution of Crystalline Nanoparticles Prepared by Acid Hydrolysis of Native Cellulose. *Biomacromolecules* **2008**, *9* (1), 57–65.

(62) Kaushik, M.; Fraschini, C.; Chauve, G.; Putaux, J.-L.; Moores, A. Transmission Electron Microscopy for the Characterization of Cellulose Nanocrystals. In *The Transmission Electron Microscope - Theory and Applications*; InTech, 2015.

(63) Nishino, T.; Takano, K.; Nakamae, K. Elastic Modulus of the Crystalline Regions of Cellulose Polymorphs. *J. Polym. Sci. Part B Polym. Phys.* **1995**, *33* (11), 1647–1651.

(64) Favier, V.; Chanzy, H.; Cavaille, J. Y. Polymer Nanocomposites Reinforced by Cellulose Whiskers. *Macromolecules* **1995**, *28* (18), 6365–6367.

(65) Moon, R. J.; Schueneman, G. T.; Simonsen, J. Overview of Cellulose Nanomaterials, Their Capabilities and Applications. *JOM*. Minerals, Metals and Materials Society September 26,

2016, pp 2383–2394.

(66) Dufresne, A. Cellulose Nanomaterials as Green Nanoreinforcements for Polymer Nanocomposites. *Philos. Trans. R. Soc. A Math. Phys. Eng. Sci.* **2018**, *376* (2112), 20170040.

(67) Calvino, C.; Macke, N.; Kato, R.; Rowan, S. J. Development, Processing and Applications of Bio-Sourced Cellulose Nanocrystal Composites. *Prog. Polym. Sci.* **2020**, *103*, 101221.

(68) Mokhena, T. C.; John, M. J. Cellulose Nanomaterials: New Generation Materials for Solving Global Issues. *Cellulose*. Springer February 1, 2020, pp 1149–1194.

(69) Habibi, Y. Key Advances in the Chemical Modification of Nanocelluloses. *Chemical Society Reviews*. Royal Society of Chemistry March 7, 2014, pp 1519–1542.

(70) Eyley, S.; Thielemans, W. Surface Modification of Cellulose Nanocrystals. *Nanoscale* **2014**, *6* (14), 7764–7779.

(71) Heux, L.; Chauve, G.; Bonini, C. Nonflocculating and Chiral-Nematic Self-Ordering of Cellulose Microcrystals Suspensions in Nonpolar Solvents. *Langmuir* **2000**, *16* (21), 8210–8212.

(72) Bonini, C.; Heux, L.; Cavaillé, J.-Y.; Lindner, P.; Dewhurst, C.; Terech, P. Rodlike Cellulose Whiskers Coated with Surfactant: A Small-Angle Neutron Scattering Characterization. *Langmuir* **2002**, *18* (8), 3311–3314.

(73) Salajková, M.; Berglund, L. A.; Zhou, Q. Hydrophobic Cellulose Nanocrystals Modified with Quaternary Ammonium Salts. *J. Mater. Chem.* **2012**, *22* (37), 19798.

(74) Syverud, K.; Xhanari, K.; Chinga-Carrasco, G.; Yu, Y.; Stenius, P. Films Made of Cellulose Nanofibrils: Surface Modification by Adsorption of a Cationic Surfactant and Characterization by Computer-Assisted Electron Microscopy. *J. Nanoparticle Res.* **2011**, *13* (2), 773–782.

(75) Xhanari, K.; Syverud, K.; Chinga-Carrasco, G.; Paso, K.; Stenius, P. Reduction of Water Wettability of Nanofibrillated Cellulose by Adsorption of Cationic Surfactants. *Cellulose* **2011**, *18* (2), 257–270.

(76) Zhou, Q.; Brumer, H.; Teeri, T. T. Self-Organization of Cellulose Nanocrystals Adsorbed with Xyloglucan Oligosaccharide−Poly(Ethylene Glycol)−Polystyrene Triblock Copolymer. *Macromolecules* **2009**, *42* (15), 5430–5432.

(77) Zhou, Q.; Malm, E.; Nilsson, H.; Larsson, P. T.; Iversen, T.; Berglund, L. A.; Bulone, V. Nanostructured Biocomposites Based on Bacterial Cellulosic Nanofibers Compartmentalized by a Soft Hydroxyethylcellulose Matrix Coating. *Soft Matter* **2009**, *5* (21), 4124.

(78) Brown, E. E.; Laborie, M.-P. G. Bioengineering Bacterial Cellulose/Poly(Ethylene Oxide) Nanocomposites. *Biomacromolecules* **2007**, *8* (10), 3074–3081.

(79) Ben Azouz, K.; Ramires, E. C.; Van den Fonteyne, W.; El Kissi, N.; Dufresne, A. Simple Method for the Melt Extrusion of a Cellulose Nanocrystal Reinforced Hydrophobic Polymer. *ACS Macro Lett.* **2012**, *1* (1), 236–240.

(80) Coseri, S.; Biliuta, G.; Simionescu, B. C.; Stana-Kleinschek, K.; Ribitsch, V.; Harabagiu, V. Oxidized Cellulose—Survey of the Most Recent Achievements. *Carbohydr. Polym.* **2013**, *93* (1), 207–215.

(81) Yang, H.; Tejado, A.; Alam, N.; Antal, M.; van de Ven, T. G. M. Films Prepared from Electrosterically Stabilized Nanocrystalline Cellulose. *Langmuir* **2012**, *28* (20), 7834–7842.

(82) Bragd, P. L.; van Bekkum, H.; Besemer, A. C. TEMPO-Mediated Oxidation of Polysaccharides: Survey of Methods and Applications. *Top. Catal.* **2004**, *27* (1–4), 49–66.

(83) de Nooy, A. E. J.; Besemer, A. C.; van Bekkum, H. Highly Selective Nitroxyl Radical-Mediated Oxidation of Primary Alcohol Groups in Water-Soluble Glucans. *Carbohydr. Res.* **1995**, *269* (1), 89–98.

(84) Araki, J.; Wada, M.; Kuga, S. Steric Stabilization of a Cellulose Microcrystal Suspension by Poly(Ethylene Glycol) Grafting. *Langmuir* **2001**, *17* (1), 21–27.

(85) Habibi, Y.; Chanzy, H.; Vignon, M. R. TEMPO-Mediated Surface Oxidation of Cellulose Whiskers. *Cellulose* **2006**, *13* (6), 679–687.

(86) Okita, Y.; Fujisawa, S.; Saito, T.; Isogai, A. TEMPO-Oxidized Cellulose Nanofibrils Dispersed in Organic Solvents. *Biomacromolecules* **2011**, *12* (2), 518–522.

(87) Pérez, S.; Samain, D. Structure and Engineering of Celluloses. In *Advances in Carbohydrate Chemistry and Biochemistry*; Academic Press Inc., 2010; Vol. 64, pp 25–116.

(88) Bulpitt, P.; Aeschlimann, D. New Strategy for Chemical Modification of Hyaluronic Acid: Preparation of Functionalized Derivatives and Their Use in the Formation of Novel Biocompatible Hydrogels. *J. Biomed. Mater. Res.* **1999**, *47* (2), 152–169.

(89) Way, A. E.; Hsu, L.; Shanmuganathan, K.; Weder, C.; Rowan, S. J. PH-Responsive Cellulose Nanocrystal Gels and Nanocomposites. *ACS Macro Lett.* **2012**, *1* (8), 1001–1006.

(90) Cudjoe, E.; Khani, S.; Way, A. E.; Hore, M. J. A.; Maia, J.; Rowan, S. J. Biomimetic Reversible Heat-Stiffening Polymer Nanocomposites. *ACS Cent. Sci.* **2017**, *3* (8), 886–894.

(91) Lin, N.; Dufresne, A. Physical and/or Chemical Compatibilization of Extruded Cellulose Nanocrystal Reinforced Polystyrene Nanocomposites. *Macromolecules* **2013**, *46* (14), 5570–5583.

(92) Azzam, F.; Heux, L.; Putaux, J.-L.; Jean, B. Preparation By Grafting Onto, Characterization, and Properties of Thermally Responsive Polymer-Decorated Cellulose Nanocrystals. *Biomacromolecules* **2010**, *11* (12), 3652–3659.

(93) C˘er˘ovský, V.; Jakubke, H.-D. Peptide Synthesis Catalyzed by Crosslinked α-Chymotrypsin in Water/Dimethylformamide Solvent System. *Biocatalysis* **1994**, *11* (3), 233–240.

(94) Labre, F.; Mathieu, S.; Chaud, P.; Morvan, P.-Y.; Vallée, R.; Helbert, W.; Fort, S. DMTMM-Mediated Amidation of Alginate Oligosaccharides Aimed at Modulating Their Interaction with Proteins. *Carbohydr. Polym.* **2018**, *184*, 427–434.

(95) Montalbetti, C. A. G. N.; Falque, V. Amide Bond Formation and Peptide Coupling. *Tetrahedron* **2005**, *61* (46), 10827–10852.

(96) Falchi, A.; Giacomelli, G.; Porcheddu, A.; Taddei, M. 4-(4,6-Dimethoxy[1,3,5]Triazin-2-Yl)-4-Methyl-Morpholinium Chloride (DMTMM): A Valuable Alternative to PyBOP for Solid Phase Peptide Synthesis. *Synlett* **2000**, *2000* (2), 275–277.

(97) Ramsden, W. Separation of Solids in the Surface-Layers of Solutions and 'Suspensions' (Observations on Surface-Membranes, Bubbles, Emulsions, and Mechanical Coagulation).—Preliminary Account. *Proc. R. Soc. London* **1904**, *72* (477–486), 156–164.

(98) Pickering, S. U. CXCVI.—Emulsions. *J. Chem. Soc., Trans.* **1907**, *91*, 2001–2021.

(99) Chevalier, Y.; Bolzinger, M.-A. Emulsions Stabilized with Solid Nanoparticles: Pickering Emulsions. *Colloids Surfaces A Physicochem. Eng. Asp.* **2013**, *439*, 23–34.

(100) Binks, B. P. Particles as Surfactants - Similarities and Differences. *Curr. Opin. Colloid Interface Sci.* **2002**, *7* (1–2), 21–41. https://doi.org/10.1016/S1359-0294(02)00008-0.

(101) Binks, B. P.; Lumsdon, S. O. Influence of Particle Wettability on the Type and Stability of Surfactant-Free Emulsions †. *Langmuir* **2000**, *16* (23), 8622–8631.

(102) Aveyard, R.; Binks, B. P.; Clint, J. H. Emulsions Stabilised Solely by Colloidal Particles. *Adv. Colloid Interface Sci.* **2003**, *100–102* (SUPPL.), 503–546.

(103) Vignati, E.; Piazza, R.; Lockhart, T. P. Pickering Emulsions: Interfacial Tension, Colloidal Layer Morphology, and Trapped-Particle Motion. *Langmuir* **2003**, *19* (17), 6650–6656.

(104) Binks, B. P.; Philip, J.; Rodrigues, J. A. Inversion of Silica-Stabilized Emulsions Induced by Particle Concentration. *Langmuir* **2005**, *21* (8), 3296–3302.

(105) Ashby, N. P.; Binks, B. P. Pickering Emulsions Stabilised by Laponite Clay Particles. *Phys. Chem. Chem. Phys.* **2000**, *2* (24), 5640–5646.

(106) Oza, K. P.; Frank, S. G. MICROCRYSTALLINE CELLULOSE STABILIZEDEMULSIONS. *J. Dispers. Sci. Technol.* **1986**, *7* (5), 543–561.

(107) Ougiya, H.; Watanabe, K.; Morinaga, Y.; Yoshinaga, F. Emulsion-Stabilizing Effect of Bacterial Cellulose. *Biosci. Biotechnol. Biochem.* **1997**, *61* (9), 1541–1545.

(108) Capron, I.; Rojas, O. J.; Bordes, R. Behavior of Nanocelluloses at Interfaces. *Current Opinion in Colloid and Interface Science*. Elsevier Ltd May 1, 2017, pp 83–95.

(109) Kalashnikova, I.; Bizot, H.; Cathala, B.; Capron, I. Modulation of Cellulose Nanocrystals Amphiphilic Properties to Stabilize Oil/Water Interface. *Biomacromolecules* **2012**, *13* (1), 267–275.

(110) Kalashnikova, I.; Bizot, H.; Cathala, B.; Capron, I. New Pickering Emulsions Stabilized by Bacterial Cellulose Nanocrystals. *Langmuir* **2011**, *27* (12), 7471–7479.

(111) Kalashnikova, I.; Bizot, H.; Bertoncini, P.; Cathala, B.; Capron, I. Cellulosic Nanorods of Various Aspect Ratios for Oil in Water Pickering Emulsions. *Soft Matter* **2013**, *9* (3), 952–959.

(112) Helbert, W.; Nishiyama, Y.; Okano, T.; Sugiyama, J. Molecular Imaging of Halocynthia Papillosa Cellulose. *J. Struct. Biol.* **1998**, *124* (1), 42–50.

(113) Cherhal, F.; Cousin, F.; Capron, I. Structural Description of the Interface of Pickering Emulsions Stabilized by Cellulose Nanocrystals. *Biomacromolecules* **2016**, *17* (2), 496–502.

(114) Moreau, C.; Villares, A.; Capron, I.; Cathala, B. Tuning Supramolecular Interactions of Cellulose Nanocrystals to Design Innovative Functional Materials. *Ind. Crops Prod.* **2016**, *93*, 96–107.

(115) Cunha, A. G.; Mougel, J. B.; Cathala, B.; Berglund, L. A.; Capron, I. Preparation of Double Pickering Emulsions Stabilized by Chemically Tailored Nanocelluloses. *Langmuir* **2014**, *30* (31), 9327–9335.

(116) Saidane, D.; Perrin, E.; Cherhal, F.; Guellec, F.; Capron, I. Some Modification of Cellulose Nanocrystals for Functional Pickering Emulsions. *Philos. Trans. R. Soc. A Math. Phys. Eng. Sci.* **2016**, *374* (2072), 374.

(117) Hu, Z.; Ballinger, S.; Pelton, R.; Cranston, E. D. Surfactant-Enhanced Cellulose Nanocrystal Pickering Emulsions. *J. Colloid Interface Sci.* **2015**, *439*, 139–148.

(118) Hu, Z.; Patten, T.; Pelton, R.; Cranston, E. D. Synergistic Stabilization of Emulsions and Emulsion Gels with Water-Soluble Polymers and Cellulose Nanocrystals. *ACS Sustain. Chem. Eng.* **2015**, *3* (5), 1023–1031.

(119) Ahmed, S.; Jones, F. R. A Review of Particulate Reinforcement Theories for Polymer Composites. *J. Mater. Sci.* **1990**, *25* (12), 4933–4942.

(120) Favier, V.; Canova, G. R.; Cavaillé, J. Y.; Chanzy, H.; Dufresne, A.; Gauthier, C. Nanocomposite Materials from Latex and Cellulose Whiskers. *Polym. Adv. Technol.* **1995**, *6* (5), 351–355.

(121) Dufresne, A. Cellulose Nanomaterials as Green Nanoreinforcements for Polymer Nanocomposites. *Philosophical Transactions of the Royal Society A: Mathematical, Physical and Engineering Sciences*. Royal Society Publishing February 13, 2018.

(122) Dufresne, A. Cellulose Nanomaterial Reinforced Polymer Nanocomposites. *Current Opinion in Colloid and Interface Science*. Elsevier Ltd May 1, 2017, pp 1–8.

(123) Kargarzadeh, H.; Mariano, M.; Huang, J.; Lin, N.; Ahmad, I.; Dufresne, A.; Thomas, S. Recent Developments on Nanocellulose Reinforced Polymer Nanocomposites: A Review. *Polymer*. Elsevier Ltd December 6, 2017, pp 368–393.

(124) Trotter, J. A.; Tipper, J.; Lyons-Levy, G.; Chino, K.; Heuer, A. H.; Liu, Z.; Mrksich, M.; Hodneland, C.; Dillmore, W. S.; Koob, T. J.; Koob-Emunds, M. M.; Kadler, K.; Holmes, D. Towards a Fibrous Composite with Dynamically Controlled Stiffness: Lessons from Echinoderms. *Biochem. Soc. Trans.* **2000**, *28* (4), 357–362.

(125) Capadona, J. R.; Shanmuganathan, K.; Tyler, D. J.; Rowan, S. J.; Weder, C. Stimuli-Responsive Polymer Nanocomposites Inspired by the Sea Cucumber Dermis. *Science (80-.).* **2008**, *319* (5868), 1370–1374. https://doi.org/10.1126/science.1153307.

(126) Favier, V.; Cavaille, J. Y.; Canova, G. R.; Shrivastava, S. C. Mechanical Percolation in Cellulose Whisker Nanocomposites. *Polym. Eng. Sci.* **1997**, *37* (10), 1732–1739.

(127) Halpin, J. C.; Kardos, J. L. Moduli of Crystalline Polymers Employing Composite Theory. *J. Appl. Phys.* **1972**, *43* (5), 2235–2241.

(128) Annamalai, P. K.; Dagnon, K. L.; Monemian, S.; Foster, E. J.; Rowan, S. J.; Weder, C. Water-Responsive Mechanically Adaptive Nanocomposites Based on Styrene–Butadiene Rubber and Cellulose Nanocrystals—Processing Matters. *ACS Appl. Mater. Interfaces* **2014**, *6* (2), 967–976.

(129) Jorfi, M.; Roberts, M. N.; Foster, E. J.; Weder, C. Physiologically Responsive, Mechanically Adaptive Bio-Nanocomposites for Biomedical Applications. *ACS Appl. Mater. Interfaces* **2013**, *5* (4), 1517–1526.

(130) Shanmuganathan, K.; Capadona, J. R.; Rowan, S. J.; Weder, C. Biomimetic Mechanically Adaptive Nanocomposites. *Prog. Polym. Sci.* **2010**, *35* (1–2), 212–222.

(131) Miserez, A.; Schneberk, T.; Sun, C.; Zok, F. W.; Waite, J. H. The Transition from Stiff to

Compliant Materials in Squid Beaks. *Science (80-.).* **2008**, *319* (5871), 1816–1819.

(132) Miserez, A.; Li, Y.; Waite, J. H.; Zok, F. Jumbo Squid Beaks: Inspiration for Design of Robust Organic Composites. *Acta Biomater.* **2007**, *3* (1), 139–149.

(133) Miserez, A.; Rubin, D.; Waite, J. H. Cross-Linking Chemistry of Squid Beak. *J. Biol. Chem.* **2010**, *285* (49), 38115–38124.

(134) Tan, Y.; Hoon, S.; Guerette, P. A.; Wei, W.; Ghadban, A.; Hao, C.; Miserez, A.; Waite, J. H. Infiltration of Chitin by Protein Coacervates Defines the Squid Beak Mechanical Gradient. *Nat. Chem. Biol.* **2015**, *11* (7), 488–495.

(135) Fox, J. D.; Capadona, J. R.; Marasco, P. D.; Rowan, S. J. Bioinspired Water-Enhanced Mechanical Gradient Nanocomposite Films That Mimic the Architecture and Properties of the Squid Beak. *J. Am. Chem. Soc.* **2013**, *135* (13), 5167–5174.

Chapter 2. Nano-emulsions and Nano-latexes Stabilized by Hydrophobically Functionalized Cellulose Nanocrystals.*

2.1 Abstract

Carboxylic acid cellulose nanocrystals (CNC-COOHs) that have been covalently functionalized (via peptide coupling chemistry) with a range of different hydrophobic groups have been investigated as nanoparticle surfactants to stabilize styrene-in-water nanoemulsions. It is shown that the size and stability of these nanoemulsions depend on both the amount of surface carboxylic acid groups as well as the amount and type of hydrophobic alkyl groups on the CNC surface. Two different biosources for the CNCs, microcrystalline cellulose (MCC) and Miscanthus x. Giganteus (MxG), were investigated to see the effect that the CNC aspect ratio has on these nanoemulsions. Stable oil-in-water (o/w) Pickering emulsions with particle diameters of only a few hundred nanometers can be accessed using these hydrophobic functionalized CNCs, and the resulting emulsion can be further polymerized to access nanometer sized latexes. The hydrophobic/hydrophilic balance of the functionalized CNCs was found to be critical to lower the interfacial tension between oil and water, allowed access to stable emulsions with droplet diameters < 1 μm. The ability to stabilized nano-sized emulsions and latexes extends the potential of CNCs as green surfactants for numerous technological applications, such as food, cosmetics, drug delivery systems and coatings.

* This chapter is adapted from: **Zhang, Y.**; Karimkhani, V.; Makowski, B. T.; Samaranayake, G.; Rowan, S. J. *Macromolecules* **2017**, *50* (16), 6032–6042

2.2 Introduction

An emulsion is a mixture of two immiscible liquids with one liquid dispersed in another, that is usually stabilize by a surface-active compound (surfactant). Conventional surfactants are small molecules or polymers that contain a balance of both hydrophilic and hydrophobic groups. A different class of emulsions are the Pickering emulsions in which solid colloidal particles are the surface-active stabilizer.[1,2] Studies have shown that if the solid nanoparticles have partial wettability in both phases, they will preferentially assemble at the interface to form a (densely) packed particle layer. The particle adsorption at the interface tends to be irreversible and as such the resulting Pickering emulsions can show enhanced stability against coalescence and require a reduced amount of the stabilizer.[3–5] Various inorganic and organic materials have been utilized to access stable Pickering emulsions, including silica,[6] Laponite,[7] calcium carbonate,[8] carbon nanotubes,[9] polystyrene latex,[10] polymeric microgel particles,[11] and cellulose nanocrystals.[12] Emulsions are of great interests for their application in food, pharmaceuticals, cosmetics and coatings, and a lot of effort has been made to develop environmental friendly, biobased-materials in particular for these applications.[13–15] As such, cellulose-based particles are good potential candidates on account of their sustainability, nontoxicity and biodegradability.[16]

Cellulose is the most abundant biopolymer on earth, and it can be isolated from a variety of different plant and animal sources, such as wood, cotton, bacteria, tunicate, etc.[17] It occurs naturally as fiber bundles which contain highly ordered crystalline regions connected by less ordered regions. Through selective mechanical and chemical processing it is possible to obtain a range of different types of micron and nano-sized cellulose particles, including microcrystalline cellulose, microfibrillated cellulose, nanofibrillated cellulose, cellulose nanofibers and cellulose nanocrystals.[18] The first study on using a solid cellulose particle as a surfactant was reported by

Oza and Frank, who showed that heavy mineral oil-in-water emulsions could be stabilized by food grade microcrystalline cellulose.[19] Other types of cellulose particles have also been investigated, such as microfibrillated cellulose (MFC) and bacteria cellulose nanofibrils.[20] As a consequence of the hydrophilic nature of the cellulose materials, only oil-in-water emulsions can be stabilized by unmodified cellulose, therefore studies on hydrophobic modification of cellulose have been carried out in order to access water-in-oil emulsion. Studies involving silylation of cellulose fibrils,[21–23] esterification of bacteria cellulose nanofibrils,[24] acetylation of cellulose nanofibrils,[25] carboxymethylation of cellulose fibers,[26] and cellulose nanofibrils modified with octadecylamine and poly(styrene-*co*-maleic anhydride).[27] One feature of all these cellulose particles is the long length of the fibers, which can limit their ability to efficiently pack at the droplet surface, resulting in the formation of bigger emulsion droplet sizes (in the range from 10-500 μm), hindering their utility for some applications.

Conceptually, in order to better pack at the droplet surface, cellulose particles should be prepared in shorter and more uniform size. It is known that acid hydrolysis of cellulose fibers will selectively dissolve the less ordered/amorphous regions and leave only highly crystalline particles known as the cellulose nanocrystals (CNC). CNCs are rod-like crystals, which have a rough dimension of 5 to 25 nm in cross-section, and hundred nanometers to microns in length, depending on the biosource it is isolated from.[28] In some very elegant work the Capron group have studied the ability of using unmodified/sulfated CNCs as the surface-active particle to access stable o/w Pickering emulsions.[12,29–31] Studies on crystal structures of CNCs have shown that after the acid hydrolysis process they are inherently amphiphilic with one of the crystal faces (200) being hydrophobic (on account of the axial C-H of the six-membered ring) and the other crystal faces being hydrophilic.[32,33] The Capron group suggest that sulfated CNCs can be preferentially absorbed at

the o/w interface and as such can stabilize oil-in-water microemulsions, presumably with the hydrophobic 200 edge orientated towards the oil phase.[34] They also showed that the surface (sulfate half ester) charge density significantly affects the stability of the emulsion, presumably because higher charges on the CNC surface will cause electrostatic repulsion between neighboring CNCs, destabilizing the interface. In a separate study using CNCs with different aspect ratios, the Capron group showed that the CNCs with lower aspect ratio (cotton CNCs) could more densely pack the surface with an estimate coverage of 84%, while higher aspect ratio Cladophora CNCs tended to span between different emulsion droplets and only a minimum of approximately 44% coverage is needed to access stable emulsions.[29] However, it is important to note that the smallest emulsion diameters reported in this work is around 4 μm, irrespective of the aspect ratio and surface charge density of the CNC used.

The use of chemically modified CNCs to stabilize emulsions has also been studied, and by introducing different functionalities to the surface of CNCs, the properties of emulsions can be adjusted. Capron and co-workers functionalized CNC with lauroyl chloride to introduce relatively long hydrophobic alkyl chains, and showed that instead of accessing o/w emulsions, that w/o emulsions could be obtained as a result of the increased hydrophobicity of the CNCs, and a o/w/o double emulsion could also be formed by combing the modified and unmodified CNCs.[35] In other work published by the Capron group, TEMPO oxidation of the CNCs to access carboxylic acid functionalized CNCs followed by mixing with stearyltrimethylammonium chloride surfactant solution showed that the resulting non-covalently modified CNCs could be used to access stable w/o micron-sized emulsions.[36] Rojas and co-workers functionalized the CNCs with the thermally responsive polymer, poly(N-isopropylacrylamide) (PNIPAM), and showed that the micron-sized o/w emulsions (40 μm) stabilized by PNIPAM-g-CNCs exhibited a temperature responsive

behavior; the emulsions where destabilized when the temperature was raised above the lower critical solution temperature (LCST) of PNIPAM.[37] In related work Tam and co-workers, used poly[2-(dimethylamine) ethyl methacrylate] (PDMAEMA) grafted CNCs to allow access to o/w emulsions, with droplet size between 8 to 20 μm, that are responsive to both pH and temperature.[38] Cranston and co-workers have used physical adsorption of surface active water soluble polymers (hydroxyethyl cellulose, methyl cellulose) or commercial low molecular weight cationic surfactants didecyldimethylammonium bromide (DMAB) and cetyltrimethylammonium bromide (CTAB) to modify the CNCs, and showed that the interfacial tension could be significantly reduced by these non-covalently modified CNCs with the help of either the hydrophobic part of the surfactant or the surface active polymers, which leads to an enhanced emulsion stability.[39,40] As a result, droplet sizes as small as 1.9 μm was obtained for dodecane-in-water emulsions stabilized by the CNC-methyl cellulose system, and a double phase inversion from o/w to w/o and then back to o/w was observed for the CNC-DMAB system with increasing concentration of DMAB. In other work, Fe_3O_4 modified CNCs were prepared by heating a CNC solution with iron chloride, and the resulting CNCs were shown to stabilize palm olein-in-water emulsions with droplet sizes ranging from 11.9 μm to 109 μm, depending on the pH of the environment.[41] Lingyu and co-workers also modified the oxidized cellulose nanocrystals surface with phenyltrimethylammonium chloride through electrostatic interactions, and these charged surfactant modified CNCs can stabilize hexadecane-in-water emulsions with droplet diameters of ca. 2.4 μm.[42]

A critical factor in numerous applications of emulsions and latexes is the resulting particle size. In fact, nanoemulsions with size in the 20-500 nm range offer unique properties and open the door to different applications, compared to microemulsions.[43,44] O/W nanoemulsions have been utilized

in the food industry, where a reduction in droplet size has been shown to enhance the bioavailability of the encapsulated flavor/ingredients during digestion.[45] Furthermore, researchers have also shown that nanoemulsions can serve as a more efficient delivery vehicle for hydrophobic drugs on account of their small sizes.[46,47] In cosmetic products, nanosized emulsion droplets have been shown to facilitate absorption through the skin.[48] In addition, nanosized emulsion droplets can be polymerized (mini-emulsion polymerization) and utilized as building blocks for polymer synthesis and nanoparticle fabrication.[49] The prior work (*vide supra*) has shown that it is possible to access particle sizes only above 1 μm using CNCs as the only droplet stabilizing agent. There are reports of nanosized emulsions that contain CNCs but in all cases additional low molecular weight surfactant (such as sodium dodecylsulfate, SDS) is employed.[50,51] A key aspect in determining the droplet size of an emulsion is the design of the particle stabilizer which should exhibit good wettability at the interface, i.e. both surface active and amphiphilic.[52] Such systems have been investigated using Janus particles (JPs), which possess two different polarity sides.[53] Binks et. al. proposed that the desorption energies increase three times compared to homogeneous particles, when the amphiphilicity of a JP is optimized, resulting in a better wettability at the interface.[54] The use of JPs to stabilize emulsions has been reported, including w/o emulsions stabilized by gold/iron oxide JP,[55] amphiphilic silica JP,[56] and o/w emulsions stabilized by PLGA JP,[57] and PS-PMMA JP.[58] The experiments show that amphiphilic JPs can lower the interfacial tension between the two immiscible phases and result in a higher emulsion stabilization. The goal of this work is to see if changing the CNC hydrophobic/hydrophilic balance by covalent surface functionalization of the hydrophilic faces of the CNC particles would allow access to emulsions and latexes with particle diameters <500 nm.

2.3 Experimental Section

Materials

Microcrystalline cellulose (MCC) (trade name: Lattice® NT) was received from FMC Corporation (Newark, DE). *Miscanthus x. Giganteus* (MxG) stalks were donated by Aloterra Energy LLC (Conneaut, OH). Styrene monomer was purified by passing through a basic alumina packed column to remove the 4-tert-butylcatechol inhibitor. NaOCl was received from Alfa Aesar with 14.5% available chlorine. All other reagents were purchased from Sigma-Aldrich and used as received.

Synthesis of mCNC-COOH via TEMPO oxidation of MCC

TEMPO oxidation was carried out following the previous published procedure with minor modifications.[59] 5 g of MCC was stirred in 250 mL of DI water overnight and then ultrasonicated for 4 hrs in an ice bath using a Q500 QSonica Ultrasonic Processor at 40% amplitude. The MCC suspension was then diluted by adding an additional 250 mL DI water and transferred to a 3-neck flask equipped with an overhead stirrer. TEMPO (4 g, 25.6 mmol), NaBr (40 g, 388.7 mmol) and NaOCl (30 g, 403 mmol) were added into the solution while stirring, and an additional NaOCl (10 g, 134.3 mmol) was added in order to maintain the pH at 10-11. The pH of the solution was monitored, and 10 M NaOH solution was added to keep the pH above 10. The reaction was finished when the pH did not change during a 15-minute period, and 25 mL of methanol was then added to eliminate the residual NaOCl. The final CNCs aqueous dispersion was centrifuged and the supernatant, which contains the water-soluble oxidized CNCs, was precipitated in excess methanol and centrifuged again to yield the mCNC-COOH as a white precipitate. The product was further washed with methanol and DI water using successive centrifugation before being dialyzed against

DI water for 2 days. The oxidized CNCs were recovered (yield 60%) through lyophilization for 4 days using a VirTis benchtop K lyophilizer.

Isolation and oxidation of MxG-CNCs

MxG-CNC-OH was isolated from *Miscanthus x. Giganteus* stalks and hydrolyzed using hydrochloric acid according to previously published methods.[60] TEMPO oxidation was performed using the same procedure in the literature to yield MxG-CNC-COOH. The yield for HCl hydrolysis and TEMPO oxidation of MxG are 85% and 90%, respectively.

Conductometric titration

The amount of surface carboxylic groups was determined through conductomeric titrations for all the functionalized CNCs. In a typical titration experiment, between 25-50 mg of either CNC-COOH or CNC-alkyl-COOH was dispersed in 80 ml of DI water via overnight sonication in a Branson CPX sonication bath. Then 15 μL of concentrated (33%) HCl was added under stirring to drop the pH of the dispersion below 3 and the titration was performed using 0.01 M NaOH solution under a Accumet XL benchtop pH/conductivity meter (Fisher Scientific). The conductivity was plotted against the volume of NaOH consumed, and the difference in NaOH volume between the start and the end of the plateau region was determined from where the trend lines intersect, which represents the volume of NaOH used to neutralize the carboxylic acid groups. The results can be calculated using the following equation:

$$Carboxylic\ acid\ density\ (\frac{mmol}{kg}) = \frac{\Delta V \times C_{NaOH}}{m} \qquad (1)$$

where ΔV is the difference in NaOH volume for the plateau region, C_{NaOH} is the concentration of NaOH and m is the mass of the CNCs used in the titration.

Functionalization of CNCs with alkyl groups

The oxidized CNC-COOH were reacted with different alkyl amines (propylamine, n-butylamine, amylamine, hexylamine and heptylamine) using the previously published related peptide coupling methods with a few slight modifications.[61–63] *Sample procedure for the synthesis of mCNC-hexyl-COOH:* mCNC-$COOH_{520}$ (200 mg, 0.104 mmol of carboxylic acid moieties) was dispersed in DMF via overnight sonication. 1-Ethyl-3-(3-(dimethylamino)propyl) carbodiimide hydrochloride (EDC) (299.0 mg, 1.56 mmol, 15 equiv.) was added and the reaction was allowed to stir for 5 min. Then N-hydroxysuccinimide (NHS) (179.7 mg, 1.56 mmol, 15 equiv.) was added and the reaction was stirred for a further 30 min. Hexylamine (210.8 mg, 2.08 mmol, 20 equiv.) was then slowly added and the reaction was allowed to stir at room temperature for 16 hrs. The reaction mixture was precipitate in excess methanol and then centrifuged. The residual was washed with methanol (three times) and DI water (three times) under successive centrifuge, dialyzed against DI water and finally lyophilized to yield mCNC-hexyl-COOH. The sample was titrated again to determine the residual amount of carboxylic acid groups, and the amount of hexyl groups was calculated by the difference in the number of carboxylic acid before and after the reaction. Same reaction procedure was adopted for the synthesis of the other alkyl amine functionalized CNCs.

Transmission electron microscopy (TEM)

All the CNC samples for TEM measurement were dispersed in water at a concentration of 1 mg/mL. About 10 μL of CNC sample was drop cast on an ultrathin holey carbon coated copper grid, and stained with 2wt% uranyl acetate solution. The stained sample was allowed to dry in vacuum oven overnight and imaged using a FEI Technai F30 TEM.

Emulsion preparation

mCNCs and MxG-CNCs with different surface functional groups were dispersed in water at the desired concentrations via ultrasonication prior to making the emulsions and used as the aqueous phase. 3.5 g of styrene monomer was added as the oil phase to 6.5 g of the CNC aqueous dispersion, to make an oil/water ratio of 35/65, and the mixture was shaken by hand before being ultrasonicated (using a QSonica Q500 ultrasonicator equipped with a 12.7 mm probe) for 60 s under pulse mode (3 s on, 3 s off), at 40% amplitude by positioning the tip 2 mm below the surface. The average droplet size was measured by dynamic light scattering (DLS) using either a Brookhaven 90 plus particle size analyzer or a WYATT Mobiüs DLS detector. To make the sample for DLS, 40 μL of emulsions sample was diluted in 3 mL of 0.1wt% SDS aqueous solution to prevent agglomeration. The use of SDS has been reported to facilitate the measurement of individual particles without changing the average diameter, since the SDS was added after the emulsion or latex was formed.[29]

Latex particles preparation

10 g of styrene-in-water emulsion with 35/65 ratio was ultrasonicated first and purged with nitrogen for 10 min, and then immediately sealed and stirred in an oil bath set at 40 °C. Ammonium persulfate (11.41 mg, 0.0625 mmol), sodium metabisulfide (23.86 mg, 0.125 mmol) were dissolved in 0.5 mL of water, and added into the emulsion dropwise as initiators. The polymerization was carried out at 40 °C for 2 hrs and then the temperature was ramped up to 65 °C and left for another hour. After polymerization, the reaction was allowed to cool down to room temperature. 40 μL of the resulting polystyrene particle suspension was diluted in 3 mL of 0.1wt%

SDS aqueous solution, and drop cast on carbon tape for scanning electron microscopy (SEM) measurement. The sample was sputter coated with 5 nm of Pd/Pt, and then characterized using a Zeiss Merlin SEM at 5 kV acceleration voltage.

Interfacial tension measurement

The interfacial tension between the CNC aqueous phase and styrene phase was measured with a Kruss DSA15 drop shape analyzer using the pendant drop method.[64] 3 mL of neat styrene was added into a quartz cuvette, then a pendant drop (10 μL) of the CNC aqueous dispersion at 10mg/mL was formed at the end of a needle that was immersed into the styrene. The oil/water interface was allowed to equilibrate for 20 min, and the interfacial tension data then calculated by fitting the shape of the droplet using the Young-Laplace model.

2.4 Result and Discussions

2.4.1 Isolation and functionalization of the Cellulose Nanocrystals

Two types of CNCs with different aspect ratios were isolated and oxidized in order to study how aspect ratio as well as surface functionalization impacts the size and stability of the resulting oil-in-water (O/W) CNC Pickering emulsions. Microcrystalline cellulose (MCC) is partially depolymerized cellulose synthesized from an alpha-cellulose precursor, and the raw MCC is a white dry powder consisting of large agglomerates ranging from 5-80 μm. Mechanical treatment (ultrasonication) followed by TEMPO oxidation, to introduced charged carboxylate groups to the surface (Scheme 2.1), was carried out to access the cellulose nanocrystals (mCNC-COOH). The dimensions of the crystals were measured using AFM height images, and found to have an average size of 100 nm in length, 5.3 nm in height and therefore an aspect ratio of ca. 19 (

Figure A2.1). Conductometric titrations on these carboxylic acid functionalized CNCs show a –COOH density of 520 mmol/kg (mCNC-$COOH_{520}$, the functional group density in mmol/kg is shown in subscript).

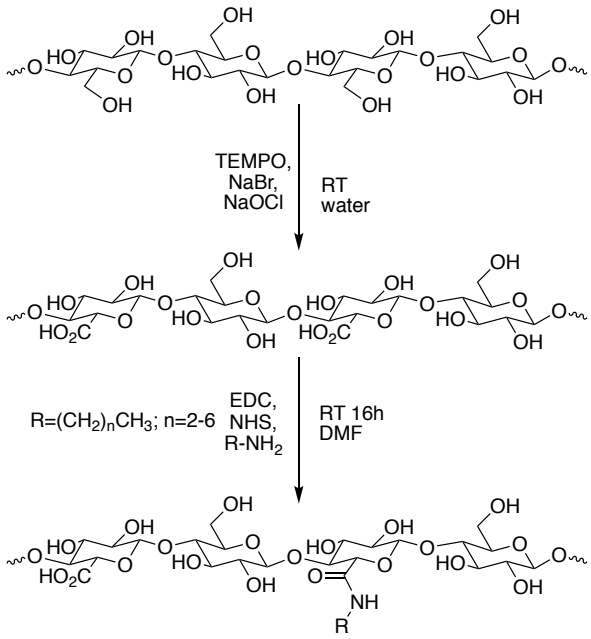

Scheme 2.1 Chemistry used to access the functionalized CNCs.

Recently, we have reported a procedure to isolate CNCs from *Miscanthus x. Giganteus* (MxG) stalks in good yield.[60] MxG is a fast growing, non-invasive plant which is a potential commercially-viable biosource for producing CNCs in large quantities at relatively low cost. Of interest for this study is that MxG-CNCs have a higher aspect ratio than mCNCs. These MxG-CNCs were converted into carboxylic acid CNCs (MxG-CNC-COOH) through standard TEMPO oxidation procedures (**Error! Reference source not found.**). The size of the MxG-CNC-COOHs used in this study were estimated from AFM images (

Figure A2.1c), to be around 300 nm in length, and an average 3.4 nm in height (Note: SANS data suggests that MxG-CNC have a more rectangular/ribbon-like cross section with a width of 8.5 nm and height of 2.8 nm), it is possible that the wider edge of the crystals are in contact with the mica substrate and as such the height measured by AFM is the size of the shorter edge. Conductometric titrations showed that these CNCs have a surface carboxylic acid density of 920 mmol/kg (MxG-CNC-$COOH_{920}$).

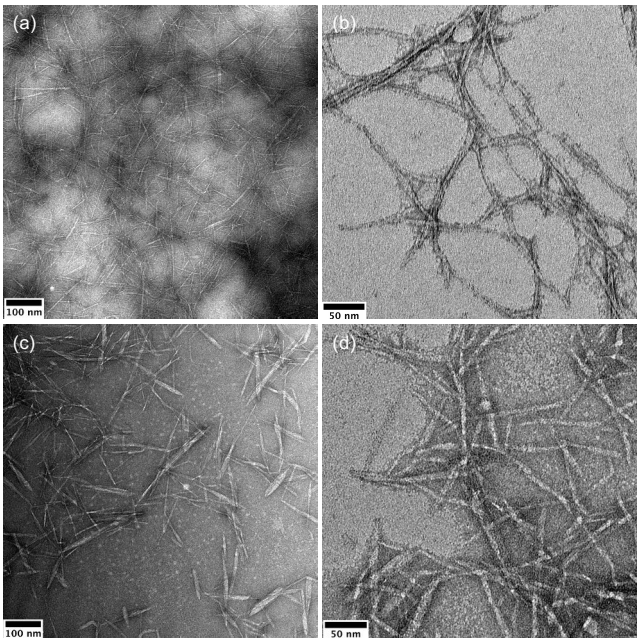

Figure 2.1 TEM images of a) mCNC-$COOH_{520}$, b) MxG-CNC-$COOH_{920}$, c) mCNC-$hexyl_{320}$-$COOH_{200}$ and d) MxG-CNC-$hexyl_{411}$-$COOH_{509}$.

With the goal of tailoring the hydrophobicity of the CNCs the CNC-COOHs were functionalized with different alkyl amines using standard peptide coupling chemistry (Scheme 2.1). The amount of hydrophobic alkyl groups attached was then calculated by the difference between the amount of carboxylic acid groups before and after functionalization, as measured via

conductometric titration. TEM and AFM characterization of the functionalized mCNC-alkyl$_x$-COOH$_y$ and MxG-CNC-alkyl$_x$-COOH$_y$ (Figure 2.1c and d, Figure A2.1b and c) show that approximate length of both the CNCs remain unchanged after the reaction, although some of the crystals appear to be thicker which maybe on account of reduced water dispersibility. As such the coupling reaction does not significantly change the dimensions of the crystals and the modified CNCs are still hydrophilic enough to be dispersible in water as primarily individual crystals. In fact, the modified CNCs were stable in aqueous suspension at least for several days without any visible precipitation. Table 2.1 summarizes the samples prepared using the different alkyl amines (n =2-6, **Error! Reference source not found.**). The subscripts x and y refer to the density of those functional groups in mmol/kg (based on the amount of –COOH measured by conductometric titrations). To further prove that the alkyl amines were covalently attached to the surface of the CNCs, a Kaiser test was performed on all the functionalized CNC (detailed procedure in the supporting information). The Kaiser test is a widely-utilized technique that is very sensitive to the presence of primary amines; if primary amines are present in a sample the test solution will turn blue.[65] The results for all the functionalized CNCs show no color change (e.g. Figure A2.2a). For comparison, hexyl amine was mixed with 1 wt.% dispersion of both mCNC-COOH$_{520}$ and MxG-CNC-COOH$_{920}$ in water at a level that would be the equivalent to 20 mmol/kg w.r.t. the CNCs (i.e. about 10% of what is measured to be covalently attached to the mCNCs). Kaiser test of these mixed samples showed a blue color (Figure A2.2b), confirming that this method is able to detect free alkyl amines in the presence of the CNC-COOHs and confirming that there is little-to-no non-covalently attached alkyl amines present in the modified CNCs.

The degree of crystallinity of the oxidized CNCs as well as the hydrophobic functionalized CNCs were also measured and the X-ray diffraction patterns are shown in the supporting

information (Figure A2.3). The percent crystallinity was calculated using the amorphous subtraction method.[66] For mCNCs, the percent crystallinity dropped from 78% for mCNC-$COOH_{520}$ to 73% for mCNC-$hexyl_{320}$-$COOH_{200}$, while the MxG-CNC samples have almost the same percent crystallinity before (83% for MxG-CNC-$COOH_{920}$) and after functionalization (82% for MxG-CNC-$hexyl_{411}$-$COOH_{509}$). The results also confirm that the oxidation and hydrophobic functionalization do not significantly change the crystalline nature of the materials.

Table 2.1 Summary of the hydrophobic functionalized CNC samples

Sample	Original COOH density (mmol/kg)	Residual COOH density (mmol/kg)	Alkyl group density (mmol/kg)	Ratio of CH_2/CH_3 to COOH
mCNC-$propyl_{290}$-$COOH_{230}$	520	230	290	3.78
mCNC-$butyl_{380}$-$COOH_{170}$	520	170	380	8.94
mCNC-$amyl_{300}$-$COOH_{220}$	520	220	300	6.82
mCNC-$hexyl_{320}$-$COOH_{200}$	520	200	320	9.6
mCNC-$heptyl_{315}$-$COOH_{205}$	520	205	315	10.76
mCNC-$butyl_{309}$-$COOH_{311}$	620	311	309	3.97
MxG-CNC-$hexyl_{455}$-$COOH_{335}$	790	335	455	8.15
MxG-CNC-$propyl_{381}$-$COOH_{539}$	920	539	381	2.12
MxG-CNC-$butyl_{449}$-$COOH_{471}$	920	471	449	3.81
MxG-CNC-$amyl_{428}$-$COOH_{492}$	920	492	428	4.35
MxG-CNC-$amyl_{657}$-$COOH_{263}$	920	263	657	12.49
MxG-CNC-$hexyl_{411}$-$COOH_{509}$	920	509	411	4.84
MxG-CNC-$heptyl_{435}$-$COOH_{485}$	920	485	435	6.28

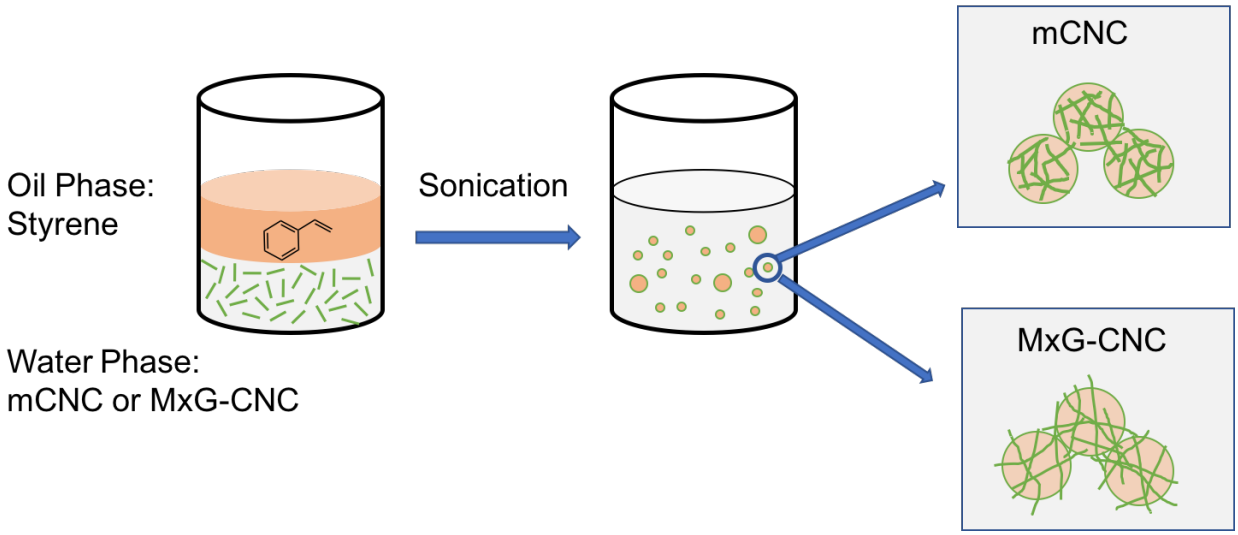

Figure 2.2 Schematic representation of the styrene-in-water emulsion stabilizing process using modified mCNCs or MxG-CNCs as the surfactant.

2.4.2 Oil-in-water emulsions stabilized by CNC-COOH

Most of the literature reports using CNCs to access stable o/w Pickering emulsions employ sulfated CNCs, which have half ester sulfate groups on the CNC surface. Thus, initial experiments were carried out to see if the carboxylic acid CNC (mCNC-$COOH_{520}$ or MxG-CNC-$COOH_{920}$) would allow access to stable emulsions. For all the emulsions studied here, styrene is employed as the oil component, and the aqueous component consists of either mCNC-$COOH_{520}$ or MxG-CNC-$COOH_{920}$ dispersed in DI water at the desired concentrations (supporting information). After mixing the styrene and the CNC aqueous dispersion at a 35/65 ratio the emulsions were ultrasonicated. Figure 2.3a and c shows pictures of the o/w emulsions stabilized by mCNC-$COOH_{520}$ and MxG-CNC-$COOH_{920}$, respectively at concentrations ranging from 0.5 mg/mL to 15 mg/mL and show that with these CNC-COOHs stable o/w emulsions are formed at all the concentrations.

The average diameter of the emulsion droplets was then determined by Dynamic Light Scattering (DLS) and the results are plotted against the concentration of CNC-COOH dispersed in the aqueous phase in Figure 2.4. For the o/w emulsions stabilized by both mCNC-$COOH_{520}$ or MxG-CNC-$COOH_{920}$, the average diameters decrease as the concentration of CNCs in the aqueous phase is increased until it reaches a plateau value of around 3.5 μm at 7.5 mg/mL for mCNC-$COOH_{520}$ and 10 mg/mL for MxG-CNC-$COOH_{920}$. These size limitations are in accordance with the results that Capron and coworkers found for the sulfated CNCs, which they assumed is related to the characteristic of CNCs based on the limited coalescence theory.[Error! Bookmark not defined.] It is worthwhile noting that at the same concentration, the size of the emulsion droplets stabilized by mCNC-$COOH_{520}$ is smaller (especially at lower concentrations) than the droplets stabilized by MxG-CNC-$COOH_{920}$. Previous studies have proposed that different crystal dimensions have no impact on the bending capacities of the crystals at the interface, but the higher aspect ratio of MxG-CNC-$COOH_{920}$, as well as the enhanced electrostatic repulsion on account of the higher COOH density, may make it more difficult for them to pack efficiently at the droplet interface, resulting in lower coverage than the mCNC-$COOH_{520}$s.[Error! Bookmark not defined.] Moreover, the high density of carboxylic acid moieties on the MxG-CNC-$COOH_{920}$ surface will make them more water soluble, which presumably also reduces the amount of MxG-CNC-$COOH_{920}$ at the interface.

In order to confirm that the CNCs were absorbed at the interface, the resulting emulsions were examined using polarized optical microscopy (POM) and confocal microscopy with the addition of a fluorescence dye that adsorbs onto the cellulose (supporting information). A birefringence pattern can be seen around the larger droplets under POM (Figure A2.5a) which, along with the high fluorescence intensity at the droplet surface under confocal microscopy (Figure A2.5b), is consistent with the majority of CNCs being selectively orientated/adsorbed at the o/w interface.

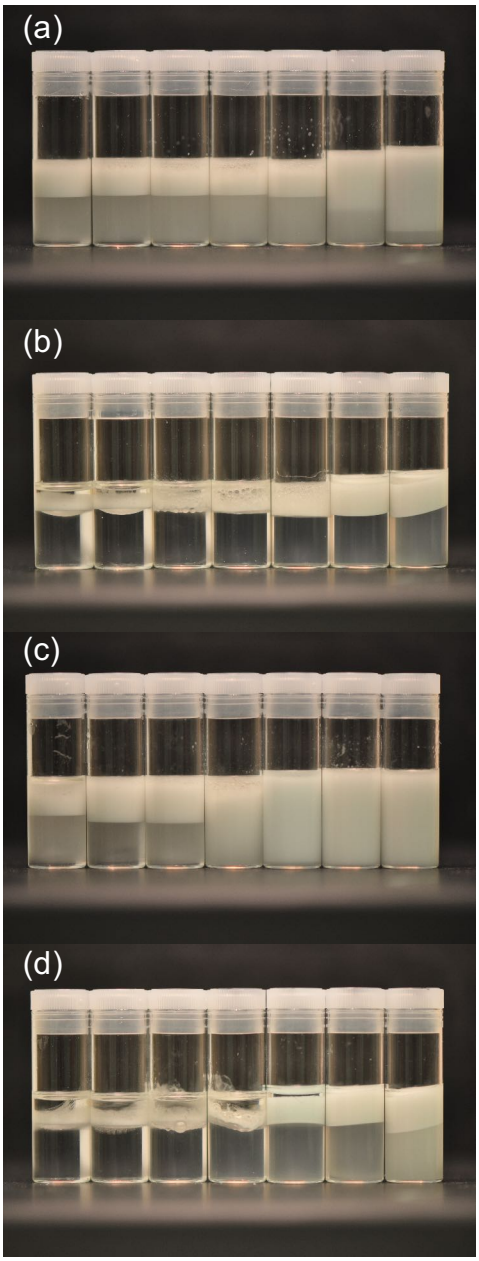

Figure 2.3 Styrene-in-water emulsions stabilized by mCNC-$COOH_{520}$ (a, b) and MxG-CNC-$COOH_{920}$ (c, d) at different CNC/aqueous concentrations (from left to right, 0.5, 1.0. 2.5, 5.0, 7.5, 10.0 and 15.0 mg/mL), before (a, c) and after (b, d) centrifugation.

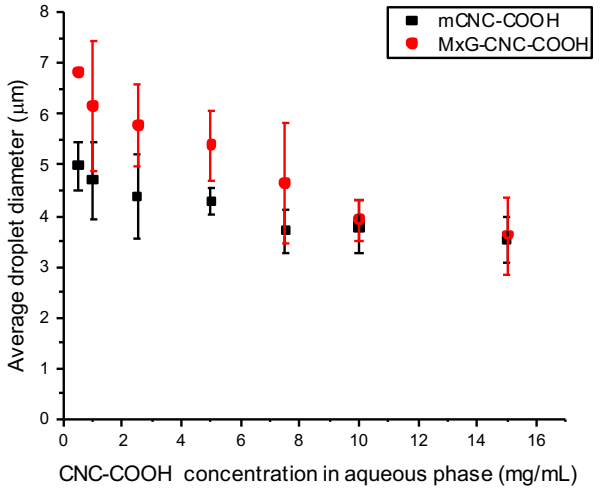

Figure 2.4 DLS results of the average diameters of the o/w emulsion droplets stabilized by mCNC-$COOH_{520}$ and MxG-CNC-$COOH_{920}$ at different concentrations.

To test the stability of the CNC-COOH stabilized emulsions they were subjected to a 10-min centrifuge at 4000g and the emulsions were visually evaluated. The strong centrifugation force accelerates the creaming process of the emulsions, and coalescence will happen if the emulsions are less stable. As can be seen from Figure 2.3b, the emulsions stabilized by 0.5, 1.0, 2.5 and 5.0 mg/mL of mCNC-$COOH_{520}$ all showed phase separation of the styrene and the water layer, while the 7.5, 10 and 15 mg/mL samples remained stable with the emulsion layer creamed on top of the water layer, but no phase separation was observed. A similar trend was also observed for the emulsions stabilized by MxG-CNC-$COOH_{920}$. Thus, a concentration of 7.5 mg/mL of either carboxylic acid functionalized mCNC or MxG-CNC in the aqueous phase is required to obtain stable o/w emulsions.

It is worthwhile pointing out that in the emulsion samples after centrifugation the bottom aqueous layers are semi-transparent in the sample containing a higher wt% CNC. As there exists

a distribution in the size and charge density of the CNCs, then it is certainly possible that some of the longer/highly charged CNCs are too hydrophilic to go to the o/w interface. If this is true, then subtracting the amount of water dispersed CNCs from the original CNC batch would result in a more accurate determination of the amount of CNCs that are absorbed at the o/w interface. Therefore, the bottom aqueous layers (after centrifugation) were separated from the emulsion layer and dried in the vacuum oven allowing the residual amount of CNCs in the water phase to be determined. The amount of wt.% CNCs obtained by this method was between 46-74 wt.% for mCNC-$COOH_{520}$ and 55-77 wt% MxG-CNC-$COOH_{920}$ (see supporting information for details) suggesting that a significant amount of these CNC-COOHs are not involved in stabilizing the interface. None-the-less the results of particle size vs. the effective amount of CNC at the interface are shown in the supporting information (Figure A2.6) and a similar trend in observed, i.e. the m-CNCs showed smaller particle diameters at lower concentrations (relative to the MxG-CNCs), which maybe a result of high charged MxG-CNC-$COOH_{920}$ de-stabilizing the interface.

It is possible to get an estimation of the theoretical coverage of the CNCs at the droplet interface by using equation (2):

$$\text{coverage} = \frac{m_p D}{6h\rho V} \qquad (2)$$

where m_p is the effective amount of CNCs that were absorbed at the interface, D is the average diameter of the emulsions measured by DLS, h is the height of the CNCs, ρ is the density of the CNCs (1.49 g/cm^3 for both CNCs) and V is the volume of the styrene phase stabilized by CNCs.[67] The results can then be plotted against the effective amount of CNCs per mL of styrene stabilized (m_p/V) (see supporting information Figure A2.7). It is worth pointing out that the height and width of the cross-section of mCNC-$COOH_{520}$ crystals are similar, so the 5.3nm obtained from AFM height image was used as the height in the calculation. The calculated coverage for mCNC-

$COOH_{520}$ increase linearly with the concentration of nanocrystals used as the surfactant, with the highest percentage coverage approaching 80%.The data suggests that stable emulsions are obtained if the mCNC-$COOH_{520}$ surpasses 40% coverage, which is consistent with the results discussed in Capron's work.[29] It is harder to get good, reliable coverage data for the MxG-CNC-$COOH_{920}$ as our prior work had shown that the cross-section of these CNCs is more ribbon shaped, with dimensions of 2.8 nm x 8.5 nm (as measured by small angle neutron scattering).[60] At the moment it is not known how the MxG-CNCs are orientated at the o/w interface. Figure A2.7 does show the calculated theoretical coverage using both 2.8 nm and 8.5 nm as the height of the CNCs as two possible extremes. Not surprisingly, the calculated coverage data is very different depending on which height data used in the calculation and it is certainly possible that the orientation of the CNCs at the interface changes with CNC concentration. As such using this approach it is not possible to get a good indication of the surface coverage with the available current data. However, as can been seen in Figure A2.7, even taking the lowest calculated coverage data, it appears that the MxG-CNCs also require about 40% coverage to form stable emulsions.

2.4.3 Oil-in-water emulsions stabilized by CNC-alkyl-COOH

Emulsion samples with the same 35/65 o/w ratio were prepared using aqueous solutions that consisted of 10 mg/mL of the CNC-alkyl-COOHs. Gratifyingly, all the emulsions showed good stability and the average diameters of the emulsions were measure by DLS and plotted against the length of alkyl groups for both mCNC-alkyl-COOH and MxG-CNC-alkyl-COOH (Figure 2.5a). As can be seen all the emulsions stabilized with the alkyl functionalized CNCs show droplet diameters much less than one micron, with the emulsions stabilized with mCNC-$butyl_{380}$-$COOH_{170}$, showing an average diameter as low as 250 nm, significantly smaller than the 3.5 μm stabilized

by the oxidized mCNCs. A centrifuge test was also performed on the emulsion stabilized by mCNC-hexyl$_{320}$-COOH$_{200}$ and no free oil layer was observed confirming the stability of the emulsion (Figure A2.8). Although it has been shown that no free alkyl amines were present in the modified CNCs, additional control studies were carried to examine if the alkyl amines themselves could stabilize styrene-in-water emulsions. To this end hexyl amine was dissolved in water at 1wt%. After addition of styrene and sonication, the water phase did appear cloudy (Figure A2.9a), but phase separation of the oil (styrene) phase can be clearly observed consistent with little-to-no emulsion formed (DLS did not show the presence of any stable droplets). Furthermore, after centrifugation the oil phase completely separated from the aqueous phase (Figure A2.9b) confirming that alkyl amines do not have the ability to form stable o/w (nano)emulsions under these conditions.

There will be numerous factors that impact the stability and size of these CNC Pickering emulsions, including the increased hydrophobicity from the alkyl chains and the reduced density of charged groups on the surface of the CNCs. However, it is hard to draw any direct conclusions as to the relative importance of these effects from the data in Figure 2.5a since each set of CNCs has different alkyl chain lengths, different amounts of alkyl chains, as well as different amounts of residual charged (carboxylate) groups. In order to better see if the hydrophobic/hydrophilic balance impacts the size of the emulsions, the average droplet diameter was plotted against the ratio of the grafted CH_2/CH_3 groups to the residual carboxylic acid groups (Figure 2.5b). Doing this analysis, it appears that increasing the CH_2/CH_3:COOH ratio from 0 to 8 results in the average droplet diameter decreasing irrespective of the aspect ratio of the CNCs used. Interestingly, however, the average droplet diameter starts to increase again when the CH_2/CH_3:COOH ratio is greater than 9. Given the nature of the synthetic protocol it can be expected that there will be a distribution in the

degree of functionalization (of both carboxylic acid and hydrophobic moieties) within each of the samples. Thus, at higher CH_2/CH_3:COOH ratios there will be a larger fraction of the CNC that are too hydrophobic to disperse in the aqueous phase (or are too soluble in the oil phase), which consequently reduces the amount of CNCs at the interface, resulting in larger droplet sizes. Therefore, a critical hydrophobic/hydrophilic ratio is important in designing the modified CNC system to access nanosized emulsions droplets (as would be expected). This result is in accordance with the well-known Bancroft rule, which states that the emulsifier should be more soluble in the continuous phase.[68] It is also worth pointing out that this critical ratio will presumably change for different oil phases. When comparing the mCNC and MxG-CNC samples, even though they show the same trend, the droplets stabilized by mCNCs are always smaller than those of MxG-CNCs at the same CH_2/CH_3:COOH ratio, which is consistent with the hypothesis of the packing behavior of the different aspect ratio nanoparticles at the interface. To the best of our knowledge, this is the first report of utilizing the CNCs alone as a surfactant to make stable oil-in-water Pickering emulsions with sizes in the hundreds of nanometer range.

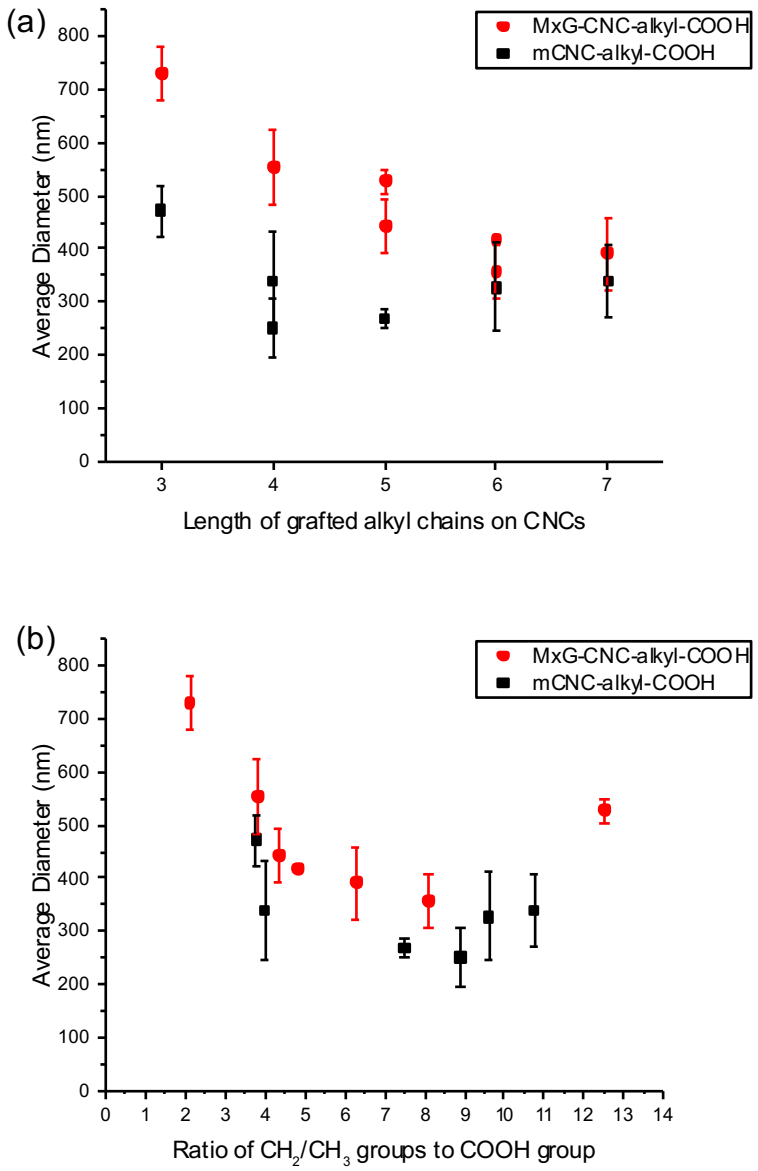

Figure 2.5 Dynamic light scattering (DLS) results of the average diameter of the emulsions stabilized by mCNC-alkyl-COOH and MxG-CNC-alkyl-COOH verse (a) the length of the alkyl chain grafted to the CNC and (b) the ratio of CH_2/CH_3 groups to the residual COOH groups on the surface of the CNCs.

As mentioned in the introduction researchers have increased the hydrophobicity of the CNCs by either reacting very long alkyl chains or absorbing low molecular weight surfactants/or polymers onto the surface of the CNCs, however usually water-in-oil emulsions or o/w/o double emulsions

are obtained.[Error! Bookmark not defined.,Error! Bookmark not defined.] Here, we show that by using relatively short alky chains (< seven carbons) and by keeping the amount of alkyl functionalization relatively low (through only partial reaction of one position of the anhydroglucose repeat unit), it is possible to access stable submicron-sized o/w emulsions. The theoretical coverage of the CNC-alkyl-COOHs on the emulsion droplet surfaces were calculated using equation (1) and values between 13-23% are obtained (for the mCNCs), which is about half of the minimum average coverage observed in the stable emulsions using the CNC-COOHs. It is worthwhile pointing out that stable Pickering emulsions with a calculated average surface coverage of less than 10% have been reported in the literature before.[67,69,] None-the-less it became of interest to investigate if there were possibility additional mechanisms at play that aided in the stabilization of nano-sized emulsions with the alkyl-modified CNCs. In the case of spherical Janus particles (JP), the mechanism in stabilizing emulsion is a combination of the Pickering effect (the formation of a densely packed particle layer at the interface to prevent coalescence) and reduction of the surface tension-similar to a small molecule surfactant. This raises the question, do the rodlike CNC-alkyl-COOHs impact the interfacial tension, which in turn would play a role in stabilization of these nanoemulsions? Thus, interfacial tension measurements were undertaken between styrene and an aqueous phase that contained 10 mg/mL of the CNCs used in this study (oxidized mCNC-COOH or MxG-CNC-COOH as well as the hydrophobically-modified mCNC-alkyl-COOHs or MxG-CNC-alkyl-COOHs) using the pendent drop method.[Error! Bookmark not defined.] The interfacial tension was measure over a period of 20min with the assumption that the kinetics for these rodlike crystals to diffuse to the interface may well be slower than for small molecule surfactants. From the results shown in Figure 2.6a and b, most CNC samples equilibrated within 5 min, and, as expected, both the mCNC-COOH and MxG-CNC-COOH did not significantly lower the interfacial tension. However, the

interfacial tensions drop significantly with either set of the alkyl functionalized CNCs (mCNC-alkyl-COOH and MxG-CNC-alkyl-COOH). Interestingly, there is a good correlation of the interfacial tension data with the DLS data, and a general trend can be seen that a lower interfacial tension will lead to a smaller droplet diameter for the styrene-in-water emulsions (Figure 2.6c). For example, the smallest particle sizes (ca. 250 nm) are obtained using mCNC-butyl$_{380}$-COOH$_{170}$ which also reduces the interfacial tension most effectively, from 33 mN/m to around 18 mN/m. Thus is appears that energy output from the ultrasonication method used here is sufficient to break the oil phase into nanosized droplets, however coalescence between neighboring droplets takes place immediately to minimize the surface area until it can be stabilized by the CNCs. By using the alkyl functionalized CNCs as stabilizers, the reduced interfacial tension indicates that the hydrophobically-modified CNCs have better wettability at the interface, therefore smaller size droplets with larger surface area can be stabilized against further coalescence.

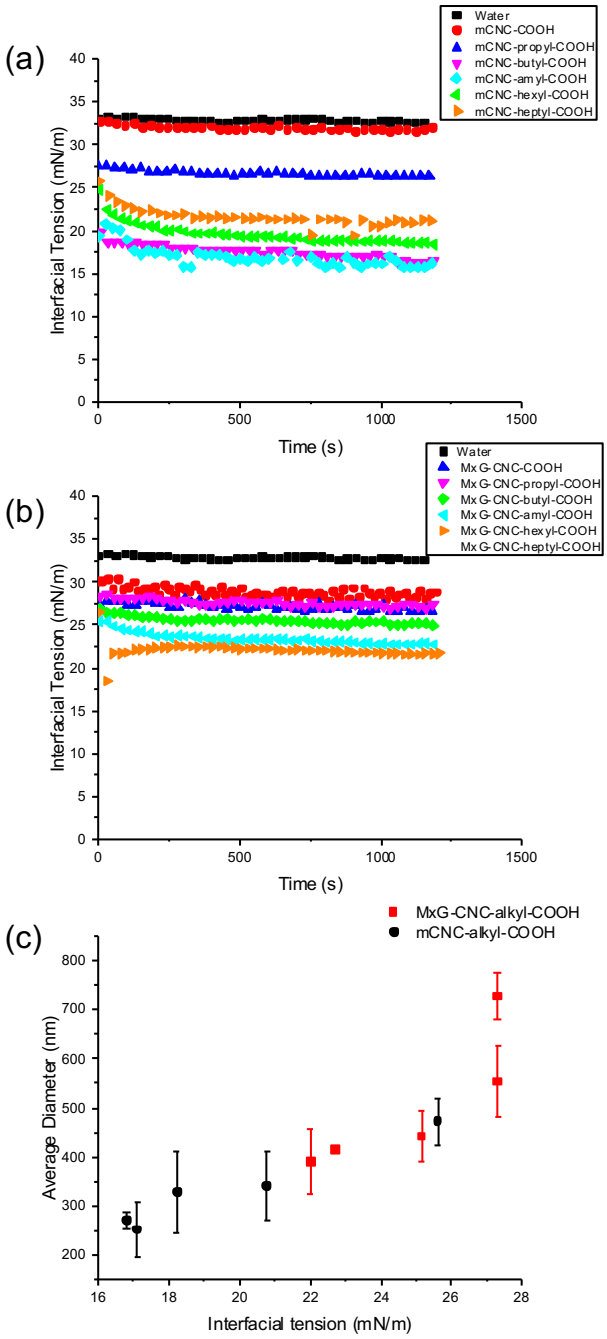

Figure 2.6 Interfacial tension between styrene and hydrophobically-modified (a) m-CNC or (b) MxG-CNC aqueous dispersions and (c) the interfacial tension vs. average diameter of the styrene droplet size (as measured by DLS).

Unlike sulfate groups, carboxylate groups are sensitive to the pH of the environment, and exist as both carboxylic acid and negatively charged carboxylate anions in DI water at neutral pH. All

the previous studies on the CNC-COOH and CNC-alkyl-COOH are done in DI water without adjusting the pH (~6), so the actual amount of charge is presumably slightly smaller than the number determined from the titration. Thus, it was decided to study how the pH of the environment would affect the size of the o/w emulsion. MxG-CNC-butyl$_{449}$-COOH$_{471}$ were dispersed in 20mM buffer solutions at pH 3, 4, 5, 6 and 7 (the ionic strength of the buffer were kept the same by adding additional NaCl), and these were used as the water phase for the o/w emulsions. DLS studies of the styrene:MxG-CNC-butyl$_{449}$-COOH$_{471}$ (35:65) emulsions show average diameters of the droplets decreased slightly from 479 nm at pH 3 to 438 nm at pH 4, but then started to increase to 700nm as the pH of the buffer changed from 4 to 7 (Figure A2.10). It is worth mentioning here that the pKa of the surface COOH groups on wood CNCs is ca. 4.5,[70] therefore the overall negative charge of the CNCs decrease at lower pH as a consequence of the protonation of carboxylate groups and increases at higher pH when the carboxylic acid moieties are deprotonated, while the amount of alkyl groups remains unaffected. This result is consistent with prior work that the size of the emulsion droplets can be affected by the nature of the charge on the CNCs and (at least to a point) lower charge favors smaller droplet sizes. Thus, it is possible to "fine tune" the droplet size of the emulsions stabilized by CNC-alkyl-COOH by simply changing the pH of the environment.

2.4.4 Nanolatexes via the polymerization of the oil phase

One important application of oil-in-water emulsions is as a route to access particle suspensions, or latexes, which have uses in numerous applications (e.g. food, cosmetics, coatings etc.). As the oil phase used in this study is styrene it was of interest to see if these nanoemulsions could be converted into nano-sized latexes. The styrene-in-water emulsions stabilized by mCNC-hexyl$_{320}$-COOH$_{200}$ and MxG-CNC-hexyl$_{455}$-COOH$_{335}$ were therefore thermally polymerized using

ammonium persulfate and sodium metabisulfide. The resulting latex particles can be clearly visualized under SEM (Figure 2.7), and the average diameters estimated from SEM images (248 nm with mCNC-hexyl$_{320}$-COOH$_{200}$ and 230 nm with MxG-CNC-hexyl$_{455}$-COOH$_{335}$) match up with the latex particle size measured by DLS (280 nm with mCNC-hexyl$_{320}$-COOH$_{200}$ and 270 nm with MxG-CNC-hexyl$_{455}$-COOH$_{335}$). The DLS data of the emulsion droplets (i.e. before polymerization) were also compared with the size of the latex particles (Figure A2.11), which confirms that the droplets were stable during the polymerization process without significant coalescence. The CNCs are clearly visible on the surface of the polystyrene particles by SEM confirming that they are absorbed at the interface and act as particle stabilizers. Zeta potential of the latex particles were also measured, with values of -50.8±0.9 mV and -44.4±1.5 mV being obtained for the latex stabilized by mCNC-hexyl$_{320}$-COOH$_{200}$ and MxG-CNC-hexyl$_{455}$-COOH$_{335}$ respectively, consistent with both latexes exhibiting good stability as a result of the electrostatic repulsion through the negatively charge CNCs at the surface of the particles.

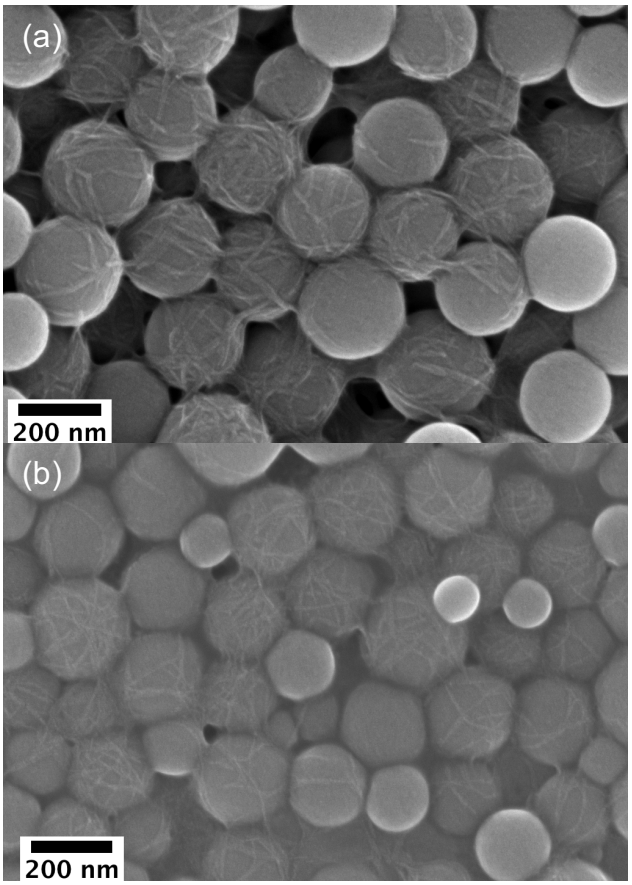

Figure 2.7 SEM images of the polystyrene latex particles stabilized by (a) mCNC-hexyl$_{320}$-COOH$_{200}$ and (b) MxG-CNC-hexyl$_{455}$-COOH$_{335}$.

2.5 Conclusion

Styrene-in-water emulsions stabilized by carboxylic acid and alkyl modified CNCs have been prepared using CNCs from two different biosources. Both the carboxylic acid functionalized mCNC-COOHs and MxG-COOHs can be used as nanoparticle surfactants and the resulting o/w emulsions are stable at CNC aqueous concentrations higher than 7.5 mg/mL. After partial modification of the carboxylic acid groups with alkylamines of different alkyl chain length to increase the hydrophobicity of the CNCs, the resulting mCNC-alkyl-COOH and MxG-CNC-alkyl-COOH were able to reduce the interfacial tension between the styrene and the water phase, and allow access to stabilized emulsions with droplet sizes of only a few hundred nanometers. The

ratio CH_2/CH_3 groups to residual COOH groups was found to be critical for the wettability of CNCs at the o/w interface, and an CH_2/CH_3:COOH ratio of ca. 9 for the butyl functionalized mCNC-butyl$_{380}$-COOH$_{170}$, accessed emulsions with the smallest diameters (ca. 250 nm). The polymerization of the styrene-in-water emulsions to form nanosized latexes was also successfully achieved, and the emulsions showed good stability during the polymerization process with the size of the latex particles consistent with those of the emulsion droplets. The ability of using hydrophobically-modified CNCs alone as a surfactant to access nanosized emulsions and latexes opens the door to these being used as novel green stabilizers for making e.g. coatings products.

2.6 Appendix

Atomic Force Microscopy (AFM)

The dimensions of CNC-COOHs as well as the CNC-alkyl-COOHs were measures by AFM using a Bruker Multimode 8 instrument equipped with a Nanoscope 5 controller. CNCs were dispersed in water and dilute to 0.1 mg/mL, then a drop of CNC aqueous dispersion was placed on a freshly cleaved mica surface, and excess liquid was rinsed off with water. The images were acquired using scan assist mode, and the length and thickness of the CNCs were analyzed using the height image by Gwyddion software.

Kaiser Test

A Kaiser test was performed on finalized CNCs to further prove no free amine was left in the samples after coupling reaction. The Kaiser test reagents were purchased from Sigma Aldrich, which consists of three solutions. Functionalized CNCs were dispersed in water at 1wt% via sonication. One drop of the CNC aqueous dispersed was added into a small vial, then three drops

of each of the three Kaiser test solution were added. The solution was mixed well before heating at 120 °C for 5 min. The solution turns dark blue when free primary amine is present, and the it stays yellow if no free primary amine is present. To test the sensitivity of the Kaiser reagents, oxidized mCNC-$COOH_{520}$ and MxG-CNC-$COOH_{920}$ were first dispersed in water at 1wt%, then hexyl amine was mixed with the CNC aqueous dispersion at a ratio of ca. 20 mmol /kg compared to the total amount of CNCs in the solution. The whole solution was sonicated and then analyzed using the Kaiser test reagents.

X-ray diffraction (XRD)

The XRD measurement was performed using a Bruker D8 Discover GADDS with Vantec-2000 2-demension detector, with cupper K-alpha source at a voltage of 40 kV and a 40 mA power. The degree of crystallinity was calculated using the amorphous subtraction method. The crystalline peaks were masked using Origin software, and the rest of the spectrum was fitted using a Gaussian function with X mas set at 20º to be the amorphous region. Then the amorphous region was subtracted from the original spectrum to yield the crystalline region. The amorphous region and the crystalline region were both integrated, and the area under the curve was used to calculate the percent crystallinity using the following equation:

$$\%\ Crystallinity = \frac{Crystalline\ area}{Crystalline\ area + Amorphous\ area} \times 100$$

Polarized optical microscopy (POM)

mCNC-$COOH_{520}$ was dispersed in water at 5 mg/mL (0.5wt%) and used as the aqueous component. Styrene was used as oil component, and the two components were mixed at 35/65

ratio. After ultrasonacating for 60 s, the resulting emulsion was characterized using a Leica DM 2700P polarization microscope under transmittance light.

Confocal microscopy

mCNC-$COOH_{520}$ was dispersed in water at 5mg/mL (0.5wt%) with 1wt% (compared to CNCs) of Calcofluor White fluorescence dye. The CNC/aqueous dispersion was mixed with styrene at 35/65 ratio, and ultrasonicated to form emulsion. The resulting emulsion was characterized using a Leica TCS SPE confocal microscope.

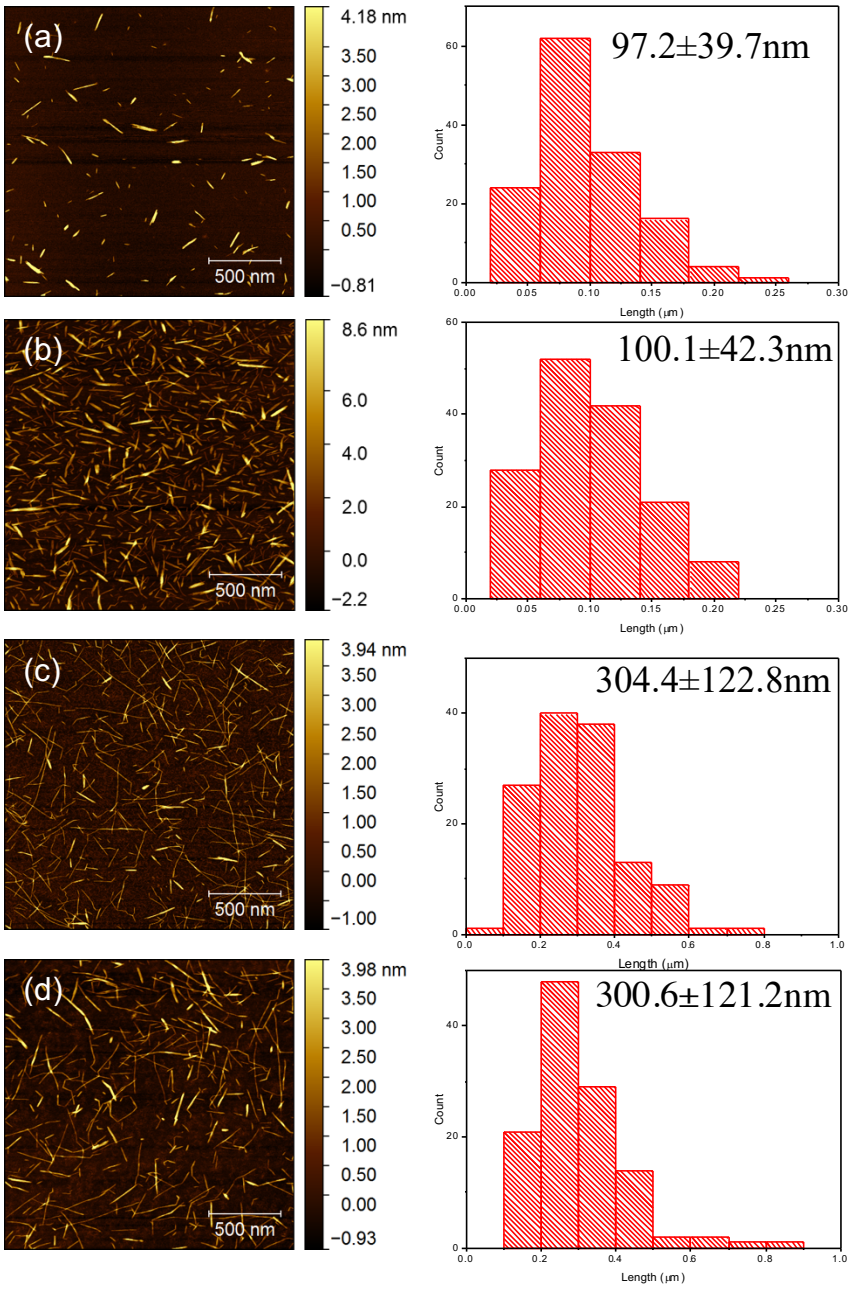

Figure A2.1 AFM height image of (a) mCNC-$COOH_{520}$, (b) mCNC-$hexyl_{320}$-$COOH_{200}$, (c) MxG-CNC-$COOH_{920}$ and (d) MxG-CNC-$hexyl_{411}$-$COOH_{509}$. The average length of each samples measured directly using the image were shown in histogram next to the AFM image.

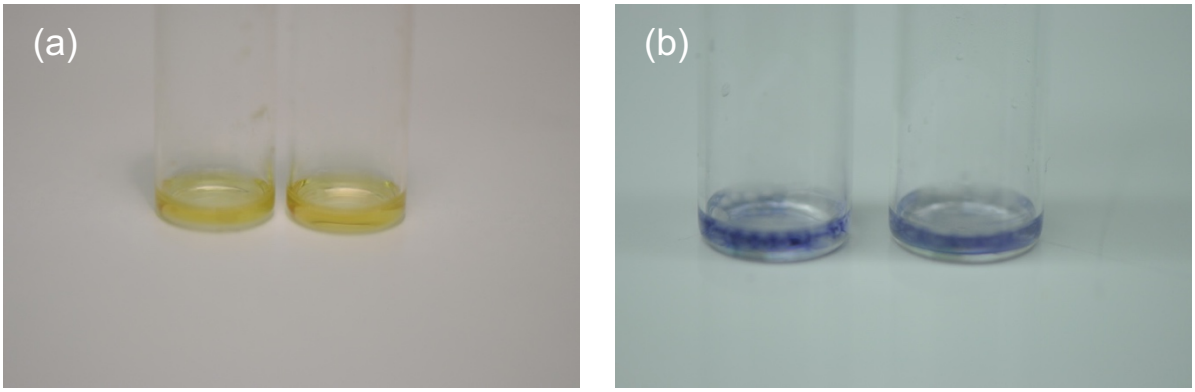

Figure A2.2 Photos of the Kaiser test of (a) mCNC-hexyl$_{320}$-COOH$_{200}$ (left) and MxG-CNC-hexyl$_{411}$-COOH$_{509}$ (right) and (b) mixed sample with hexyl amine and mCNC-COOH$_{520}$ (left) and MxG-CNC-COOH$_{920}$ (right).

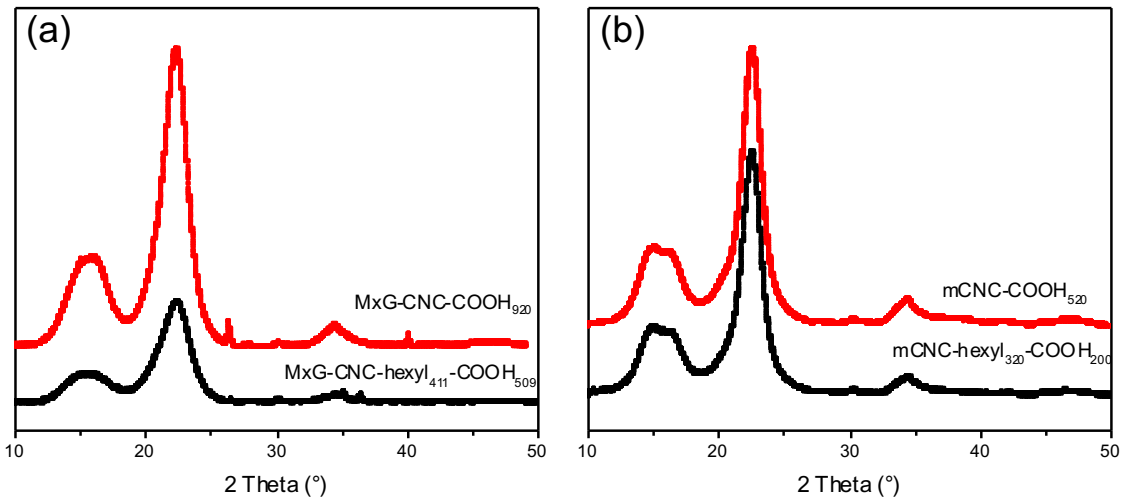

Figure A2.3 X-ray diffraction pattern of (a) mCNC and (b) MxG-CNC after oxidation (red) and after hydrophobic functionalization with hexyl amine (black).

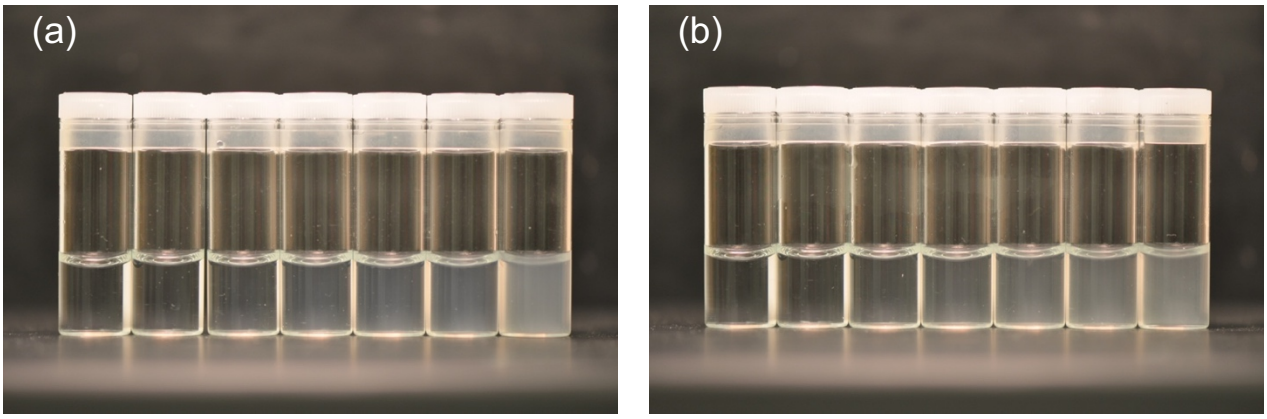

Figure A2.4 CNC/aqueous dispersion at different concentrations (from left to right, 0.5, 1.0. 2.5, 5.0, 7.5, 10.0 and 15.0 mg/mL) for (a) mCNC-$COOH_{520}$ and (b) MxG-CNC-$COOH_{920}$.

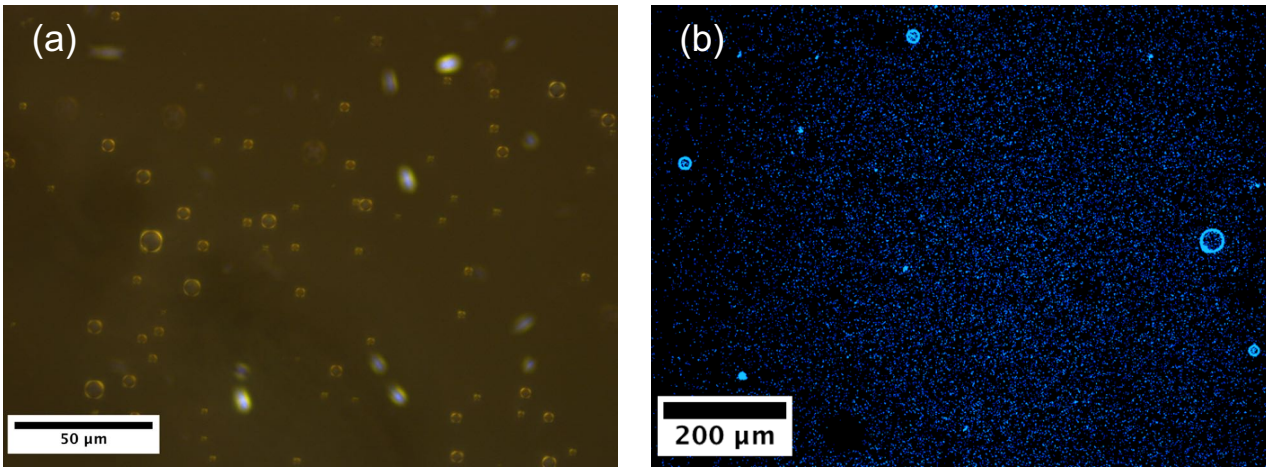

Figure A2.5 (a) Polarized optical microscope (POM) image and (b) confocal microscope image (with Calcofluor White fluorescence dye added) of the styrene-in-water emulsion stabilized by mCNC-$COOH_{520}$.

Calculation of effective amount of CNCs at the interface

mCNC-$COOH_{520}$ and MxG-CNC-$COOH_{920}$ were dispersed in water at 0.5, 1.0. 2.5, 5.0, 7.5, 10.0 and 15.0 mg/mL. The initial amount of CNCs in the water phase were calculated based on concentration and amount of water. After the emulsion was formed, a brief centrifugation was

performed and emulsion was separated into two layers, a condensed emulsion layer on top (free oil layer if emulsion is unstable) and a water layer at the bottom. The water layer at the bottom may contain residual amount of CNCs that were not stabilize at the interfaces. Therefore, the bottom water layer was collected and dried in vac oven to determine the amount of residual CNCs, and the effective amount of CNCs at the interface was calculated by subtracting the residual amount from the initial amount dispersed in water phase. The results are summarized in Table A2.1 and Table A2.2**Error! Reference source not found.**.

Table A2.1 Calculation of effective amount of mCNC-$COOH_{520}$ at the o/w interface

Concentration (mg/mL)	Amount of Water g	Initial CNC amount (mg)	Residual CNC amount in water (mg)	Effective CNC amount at interface (mg)
0.5	4.3	2.2	1	1.2
1	4.3	4.3	3	1.3
2.5	4.3	10.8	8	2.8
5	4.3	21.5	15	6.5
7.5	4.3	32.3	19	13.3
10	4.3	43.0	28	15.0
15	4.3	64.5	39	25.5

Table A2.2 Calculation of effective amount of MxG-CNC-$COOH_{920}$ at the o/w interface

Concentration (mg/mL)	Amount of Water g	Initial CNC amount (mg)	Residual CNC amount in water (mg)	Effective CNC amount at interface (mg)
0.5	5.2	2.6	2	0.6
1	5.2	5.2	4	1.2
2.5	5.2	13.0	8	5.0
5	5.2	26.0	14	12.0
7.5	5.2	39.0	21	18.0
10	5.2	52.0	29	23.0
15	5.2	78.0	45	33.0

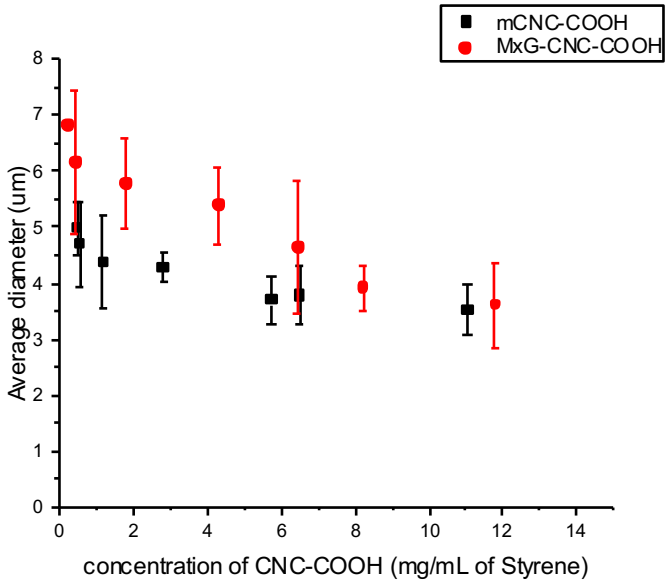

Figure A2.6 DLS results of the average diameters of the o/w emulsion droplets stabilized by mCNC-COOH$_{520}$ and MxG-CNC-COOH$_{920}$ versus the effective concentration of CNC-COOH at the interface (i.e. after subtraction of water soluble fraction) per mL of styrene.

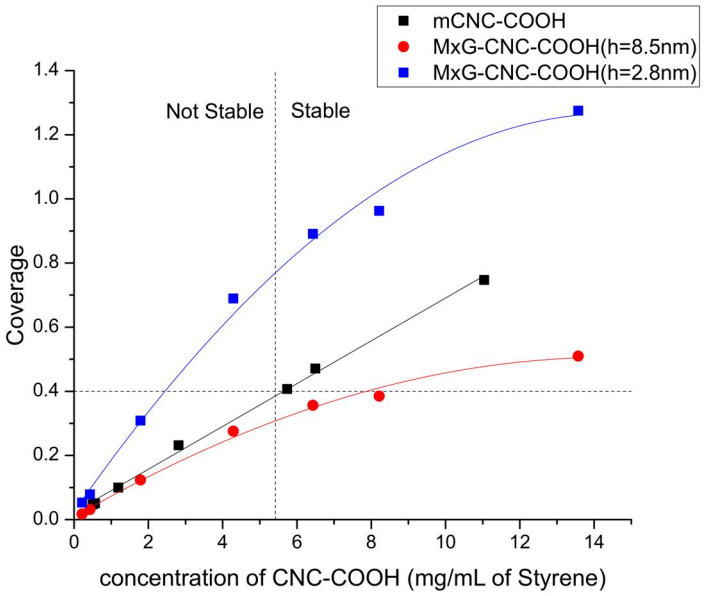

Figure A2.7 Theoretical coverage versus the effective concentration of CNC-COOH at the interface (i.e. after subtraction of water soluble fraction) per mL of styrene.

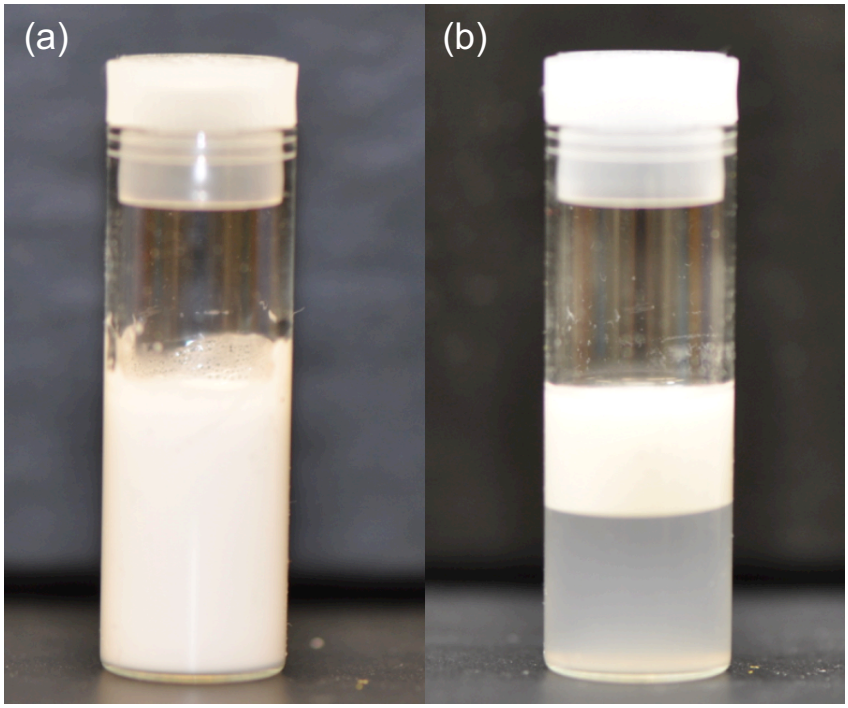

Figure A2.8 Styrene-in-water emulsions stabilized by mCNC-hexyl$_{320}$-COOH$_{200}$ (a) before and (b) after centrifugation.

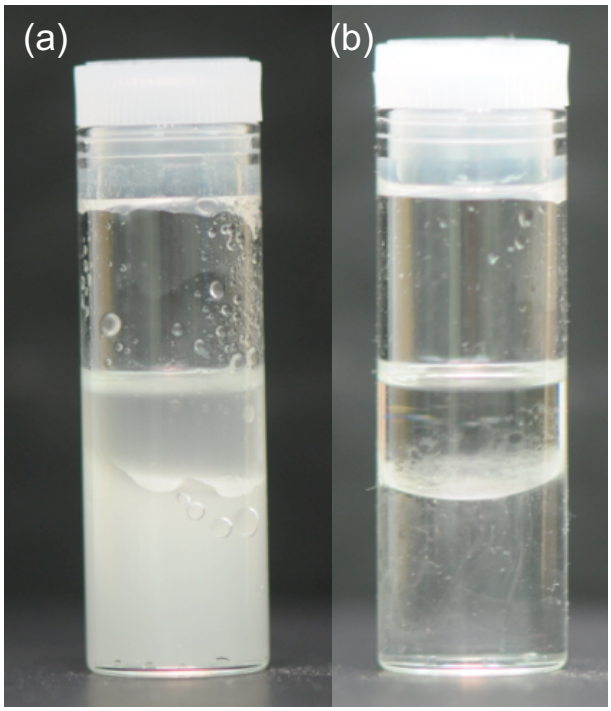

Figure A2.9 Styrene-in-water emulsions stabilized by 1wt% hexyl amine (a) before and (b) after centrifugation.

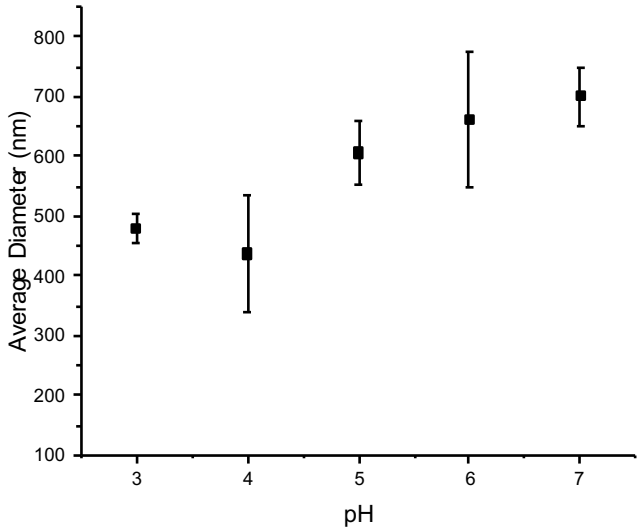

Figure A2.10 DLS results of the average diameters of the o/w emulsions stabilized by dispersed MxG-CNC-butyl$_{449}$-COOH$_{471}$ in phosphate buffer at different pH (the ionic strength of all buffers was set to 50mM by adding additional NaCl).

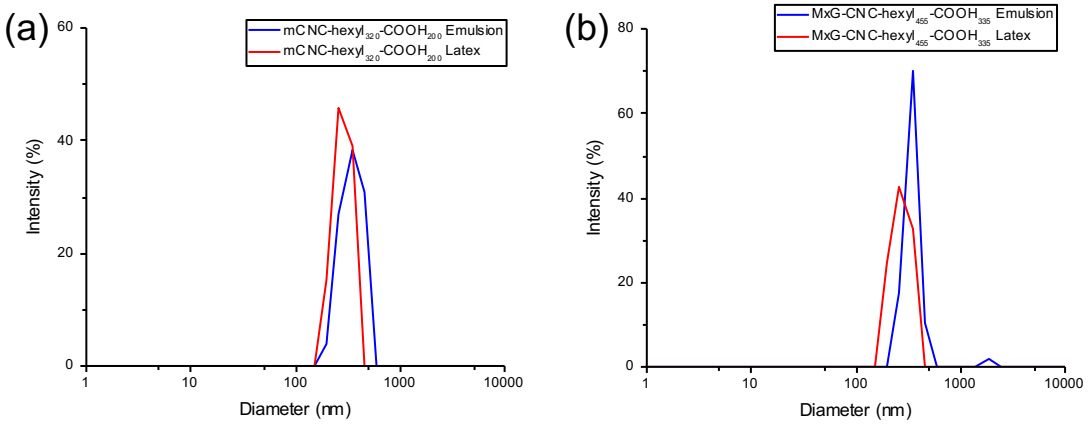

Figure A2.11 DLS results of the average diameters of the o/w emulsions after sonication and the average diameters of the latex particles after polymerization for (a) mCNC-hexyl$_{320}$-COOH$_{200}$ and (b) MxG-CNC-hexyl$_{455}$-COOH$_{335}$.

2.7 Reference

(1) Ramsden, W. Separation of Solids in the Surface-Layers of Solutions and 'Suspensions' (Observations on Surface-Membranes, Bubbles, Emulsions, and Mechanical Coagulation).—Preliminary Account. *Proc. R. Soc. London* **1904**, *72* (477–486), 156–164.

(2) Pickering, S. U. CXCVI.—Emulsions. *J. Chem. Soc., Trans.* **1907**, *91*, 2001–2021.

(3) Binks, B. P.; Lumsdon, S. O. Influence of Particle Wettability on the Type and Stability of Surfactant-Free Emulsions †. *Langmuir* **2000**, *16* (23), 8622–8631.

(4) Binks, B. P. Particles as Surfactants - Similarities and Differences. *Curr. Opin. Colloid Interface Sci.* **2002**, *7* (1–2), 21–41.

(5) Aveyard, R.; Binks, B. P.; Clint, J. H. Emulsions Stabilised Solely by Colloidal Particles. *Adv. Colloid Interface Sci.* **2003**, *100–102* (SUPPL.), 503–546.

(6) Binks, B. P.; Philip, J.; Rodrigues, J. A. Inversion of Silica-Stabilized Emulsions Induced by Particle Concentration. *Langmuir* **2005**, *21* (8), 3296–3302.

(7) Ashby, N. P.; Binks, B. P. Pickering Emulsions Stabilised by Laponite Clay Particles. *Phys. Chem. Chem. Phys.* **2000**, *2* (24), 5640–5646.

(8) Cui, Z. G.; Shi, K. Z.; Cui, Y. Z.; Binks, B. P. Double Phase Inversion of Emulsions Stabilized by a Mixture of CaCO3 Nanoparticles and Sodium Dodecyl Sulphate. *Colloids Surfaces A Physicochem. Eng. Asp.* **2008**, *329* (1–2), 67–74.

(9) Shen, M.; Resasco, D. E. Emulsions Stabilized by Carbon Nanotube-Silica Nanohybrids. *AIChE Annu. Meet. Conf. Proc.* **2009**, *25*, 10843–10851.

(10) Binks, B. P.; Lumsdon, S. O. Pickering Emulsions Stabilized by Monodisperse Latex Particles: Effects of Particle Size. *Langmuir* **2001**, *17* (15), 4540–4547.

(11) Ngai, T.; Behrens, S. H.; Auweter, H. Novel Emulsions Stabilized by PH and Temperature Sensitive Microgels. *Chem. Commun.* **2005**, No. 3, 331–333.

(12) Kalashnikova, I.; Bizot, H.; Cathala, B.; Capron, I. New Pickering Emulsions Stabilized by Bacterial Cellulose Nanocrystals. *Langmuir* **2011**, *27* (12), 7471–7479.

(13) Fernandez, A. M.; Held, U.; Willing, A.; Breuer, W. H. New Green Surfactants for Emulsion Polymerization. *Prog. Org. Coatings* **2005**, *53* (4), 246–255.

(14) Rayner, M.; Marku, D.; Eriksson, M.; Sjöö, M.; Dejmek, P.; Wahlgren, M. Biomass-Based Particles for the Formulation of Pickering Type Emulsions in Food and Topical Applications. *Colloids Surfaces A Physicochem. Eng. Asp.* **2014**, *458* (1), 48–62.

(15) Lam, S.; Velikov, K. P.; Velev, O. D. Pickering Stabilization of Foams and Emulsions with Particles of Biological Origin. *Curr. Opin. Colloid Interface Sci.* **2014**, *19* (5), 490–500.

(16) VanGinkel, C. G.; Gayton, S. The Biodegradability and Nontoxicity of Carboxymethyl Cellulose (DS 0.7) and Intermediates. *Environ. Toxicol. Chem.* **1996**, *15* (3), 270–274.

(17) Eichhorn, S. J.; Dufresne, A.; Aranguren, M.; Marcovich, N. E.; Capadona, J. R.; Rowan, S. J.; Weder, C.; Thielemans, W.; Roman, M.; Renneckar, S.; Gindl, W.; Veigel, S.; Keckes, J.; Yano, H.; Abe, K.; Nogi, M.; Nakagaito, A. N.; Mangalam, A.; Simonsen, J.; Benight, A. S.; Bismarck, A.; Berglund, L. A.; Peijs, T. Review: Current International Research into Cellulose Nanofibres and Nanocomposites. *J. Mater. Sci.* **2010**, *45* (1), 1–33.

(18) Moon, R. J.; Martini, A.; Nairn, J.; Simonsen, J.; Youngblood, J. Cellulose Nanomaterials Review: Structure, Properties and Nanocomposites. *Chem. Soc. Rev.* **2011**, *40* (7), 3941.

(19) Oza, K. P.; Frank, S. G. Microcrystalline Stabilized Emulsions. *J. Dispers. Sci. Technol.* **1986**, *7* (5), 543–561..

(20) Ougiya, H.; Watanabe, K.; Morinaga, Y.; Yoshinaga, F. Emulsion-Stabilizing Effect of Bacterial Cellulose. *Biosci. Biotechnol. Biochem.* **1997**, *61* (9), 1541–1545.

(21) Andresen, M.; Stenius, P. Water-in-Oil Emulsions Stabilized by Hydrophobized Microfibrillated Cellulose. *J. Dispers. Sci. Technol.* **2007**, *28* (6), 837–844.

(22) Blaker, J. J.; Lee, K. Y.; Li, X.; Menner, A.; Bismarck, A. Renewable Nanocomposite Polymer Foams Synthesized from Pickering Emulsion Templates. *Green Chemistry*. **2009**, *11*, 1321–1326.

(23) Xhanari, K.; Syverud, K.; Stenius, P. Emulsions Stabilized by Microfibrillated Cellulose: The Effect of Hydrophobization, Concentration and O/W Ratio. *J. Dispers. Sci. Technol.* **2011**, *32* (3), 447–452

(24) Lee, K. Y.; Blaker, J. J.; Murakami, R.; Heng, J. Y. Y.; Bismarck, A. Phase Behavior of Medium and High Internal Phase Water-in-Oil Emulsions Stabilized Solely by Hydrophobized Bacterial Cellulose Nanofibrils. *Langmuir* **2014**, *30* (2), 452–460.

(25) Jonoobi, M.; Harun, J.; Mathew, A. P.; Hussein, M. Z. B.; Oksman, K. Preparation of Cellulose Nanofibers with Hydrophobic Surface Characteristics. *Cellulose* **2010**, *17* (2), 299–307.

(26) Wågberg, L.; Decher, G.; Norgren, M.; Lindström, T.; Ankerfors, M.; Axnäs, K. The Build-Up of Polyelectrolyte Multilayers of Microfibrillated Cellulose and Cationic Polyelectrolytes. *Langmuir* **2008**, *24* (3), 784–795.

(27) Lif, A.; Stenstad, P.; Syverud, K.; Nydén, M.; Holmberg, K. Fischer-Tropsch Diesel Emulsions Stabilised by Microfibrillated Cellulose and Nonionic Surfactants. *J. Colloid*

Interface Sci. **2010**, *352* (2), 585–592.

(28) Habibi, Y.; Lucia, L. A.; Rojas, O. J. Cellulose Nanocrystals: Chemistry, Self-Assembly, and Applications. *Chem. Rev.* **2010**, *110* (6), 3479–3500.

(29) Kalashnikova, I.; Bizot, H.; Bertoncini, P.; Cathala, B.; Capron, I. Cellulosic Nanorods of Various Aspect Ratios for Oil in Water Pickering Emulsions. *Soft Matter* **2013**, *9* (3), 952–959.

(30) Kalashnikova, I.; Bizot, H.; Cathala, B.; Capron, I. Modulation of Cellulose Nanocrystals Amphiphilic Properties to Stabilize Oil/Water Interface. *Biomacromolecules* **2012**, *13* (1), 267–275.

(31) Capron, I.; Cathala, B. Surfactant-Free High Internal Phase Emulsions Stabilized by Cellulose Nanocrystals. *Biomacromolecules* **2013**, *14* (2), 291–296.

(32) Lehtiö, J.; Sugiyama, J.; Gustavsson, M.; Fransson, L.; Linder, M.; Teeri, T. T. The Binding Specificity and Affinity Determinants of Family 1 and Family 3 Cellulose Binding Modules. *Proc. Natl. Acad. Sci. U. S. A.* **2003**, *100* (2), 484–489.

(33) Helbert, W.; Nishiyama, Y.; Okano, T.; Sugiyama, J. Molecular Imaging of Halocynthia Papillosa Cellulose. *J. Struct. Biol.* **1998**, *124* (1), 42–50.

(34) Cherhal, F.; Cousin, F.; Capron, I. Structural Description of the Interface of Pickering Emulsions Stabilized by Cellulose Nanocrystals. *Biomacromolecules* **2016**, *17* (2), 496–502.

(35) Cunha, A. G.; Mougel, J. B.; Cathala, B.; Berglund, L. A.; Capron, I. Preparation of Double Pickering Emulsions Stabilized by Chemically Tailored Nanocelluloses. *Langmuir* **2014**, *30* (31), 9327–9335.

(36) Saidane, D.; Perrin, E.; Cherhal, F.; Guellec, F.; Capron, I. Some Modification of Cellulose Nanocrystals for Functional Pickering Emulsions. *Philos. Trans. R. Soc. A Math. Phys. Eng. Sci.* **2016**, *374* (2072), 374.

(37) Zoppe, J. O.; Venditti, R. A.; Rojas, O. J. Pickering Emulsions Stabilized by Cellulose Nanocrystals Grafted with Thermo-Responsive Polymer Brushes. *J. Colloid Interface Sci.* **2012**, *369* (1), 202–209.

(38) Tang, J.; Lee, M. F. X.; Zhang, W.; Zhao, B.; Berry, R. M.; Tam, K. C. Dual Responsive Pickering Emulsion Stabilized by Poly[2-(Dimethylamino) Ethyl Methacrylate] Grafted Cellulose Nanocrystals. *Biomacromolecules* **2014**, *15* (8), 3052–3060.

(39) Hu, Z.; Patten, T.; Pelton, R.; Cranston, E. D. Synergistic Stabilization of Emulsions and Emulsion Gels with Water-Soluble Polymers and Cellulose Nanocrystals. *ACS Sustain. Chem. Eng.* **2015**, *3* (5), 1023–1031.

(40) Hu, Z.; Ballinger, S.; Pelton, R.; Cranston, E. D. Surfactant-Enhanced Cellulose Nanocrystal Pickering Emulsions. *J. Colloid Interface Sci.* **2015**, *439*, 139–148.

(41) Low, L. E.; Tey, B. T.; Ong, B. H.; Chan, E. S.; Tang, S. Y. Palm Olein-in-Water Pickering Emulsion Stabilized by Fe3O4-Cellulose Nanocrystal Nanocomposites and Their Responses to PH. *Carbohydr. Polym.* **2017**, *155*, 391–399.

(42) Gong, X.; Wang, Y.; Chen, L. Enhanced Emulsifying Properties of Wood-Based Cellulose Nanocrystals as Pickering Emulsion Stabilizer. *Carbohydr. Polym.* **2017**, *169* (Supplement C), 295–303.

(43) Gupta, A.; Eral, H. B.; Hatton, T. A.; Doyle, P. S. Nanoemulsions: Formation, Properties and Applications. *Soft Matter* **2016**, *12* (11), 2826–2841.

(44) Fryd, M. M.; Mason, T. G. Advanced Nanoemulsions. *Annu. Rev. Phys. Chem.* **2012**, *63* (1), 493–518.

(45) Arancibia, C.; Navarro-Lisboa, R.; Zúñiga, R. N.; Matiacevich, S. Application of CMC as Thickener on Nanoemulsions Based on Olive Oil: Physical Properties and Stability. *Int. J. Polym. Sci.* **2016**, *2016*, 6280581.

(46) Tagne, J.-B.; Kakumanu, S.; Nicolosi, R. J. Nanoemulsion Preparations of the Anticancer Drug Dacarbazine Significantly Increase Its Efficacy in a Xenograft Mouse Melanoma Model. *Mol. Pharm.* **2008**, *5* (6), 1055–1063.

(47) Tagne, J. B.; Kakumanu, S.; Ortiz, D.; Shea, T.; Nicolosi, R. J. A Nanoemulsion Formulation of Tamoxifen Increases Its Efficacy in a Breast Cancer Cell Line. *Mol. Pharm.* **2008**, *5* (2), 280–286.

(48) Sonneville-Aubrun, O.; Simonnet, J. T.; L'Alloret, F. Nanoemulsions: A New Vehicle for Skincare Products. *Adv. Colloid Interface Sci.* **2004**, *108–109*, 145–149.

(49) Asua, J. M. Miniemulsion Polymerization. *Prog. Polym. Sci.* **2002**, *27* (7), 1283–1346.

(50) Elmabrouk, A. Ben; Wim, T.; Dufresne, A.; Boufi, S. Preparation of Poly(Styrene- Co -Hexylacrylate)/Cellulose Whiskers Nanocomposites via Miniemulsion Polymerization. *J. Appl. Polym. Sci.* **2009**, *114* (5), 2946–2955.

(51) Kedzior, S. A.; Marway, H. S.; Cranston, E. D. Tailoring Cellulose Nanocrystal and Surfactant Behavior in Miniemulsion Polymerization. *Macromolecules* **2017**, *50* (7),

(52) Wu, J.; Ma, G. H. Pickering Emulsions: Recent Studies of Pickering Emulsions: Particles Make the Difference (Small 34/2016). *Small* **2016**, *12* (34), 4582.

(53) Lattuada, M.; Hatton, T. A. Synthesis, Properties and Applications of Janus Nanoparticles.

(54) Binks, B. P.; Fletcher, P. D. I. Particles Adsorbed at the Oil-Water Interface: A Theoretical Comparison between Spheres of Uniform Wettability and "Janus" Particles. *Langmuir* **2001**, *17* (16), 4708–4710.

(55) Glaser, N.; Adams, D. J.; Böker, A.; Krausch, G. Janus Particles at Liquid-Liquid Interfaces. *Langmuir* **2006**, *22* (12), 5227–5229.

(56) Cao, W.; Huang, R.; Qi, W.; Su, R.; He, Z. Self-Assembly of Amphiphilic Janus Particles into Monolayer Capsules for Enhanced Enzyme Catalysis in Organic Media. *ACS Appl. Mater. Interfaces* **2015**, *7* (1), 465–473.

(57) Qi, F.; Wu, J.; Sun, G.; Nan, F.; Ngai, T.; Ma, G. Systematic Studies of Pickering Emulsions Stabilized by Uniform-Sized PLGA Particles: Preparation and Stabilization Mechanism. *J. Mater. Chem. B* **2014**, *2* (43), 7605–7611.

(58) Walther, A.; Hoffmann, M.; Müller, A. H. E. Emulsion Polymerization Using Janus Particles as Stabilizers. *Angew. Chemie - Int. Ed.* **2008**, *47* (4), 711–714.

(59) da Silva Perez, D.; Montanari, S.; Vignon, M. R. TEMPO-Mediated Oxidation of Cellulose III. *Biomacromolecules* **2003**, *4* (5), 1417–1425.

(60) Cudjoe, E.; Hunsen, M.; Xue, Z.; Way, A. E.; Barrios, E.; Olson, R. A.; Hore, M. J. A.; Rowan, S. J. Miscanthus Giganteus: A Commercially Viable Sustainable Source of Cellulose Nanocrystals. *Carbohydr. Polym.* **2017**, *155*, 230–241.

(61) Fox, J. D.; Capadona, J. R.; Marasco, P. D.; Rowan, S. J. Bioinspired Water-Enhanced Mechanical Gradient Nanocomposite Films That Mimic the Architecture and Properties of the Squid Beak. *J. Am. Chem. Soc.* **2013**, *135* (13), 5167–5174.

(62) Dagnon, K. L.; Way, A. E.; Carson, S. O.; Silva, J.; Maia, J.; Rowan, S. J. Controlling the Rate of Water-Induced Switching in Mechanically Dynamic Cellulose Nanocrystal Composites. *Macromolecules* **2013**, *46* (20), 8203–8212.

(63) Way, A. E.; Hsu, L.; Shanmuganathan, K.; Weder, C.; Rowan, S. J. PH-Responsive Cellulose Nanocrystal Gels and Nanocomposites. *ACS Macro Lett.* **2012**, *1* (8), 1001–1006.

(64) Berry, J. D.; Neeson, M. J.; Dagastine, R. R.; Chan, D. Y. C.; Tabor, R. F. Measurement of Surface and Interfacial Tension Using Pendant Drop Tensiometry. *J. Colloid Interface Sci.* **2015**, *454*, 226–237.

(65) Kaiser, E.; Colescott, R. L.; Bossinger, C. D.; Cook, P. I. Color Test for Detection of Free Terminal Amino Groups in the Solid-Phase Synthesis of Peptides. *Anal. Biochem.* **1970**, *34* (2), 595–598.

(66) Park, S.; Baker, J. O.; Himmel, M. E.; Parilla, P. A.; Johnson, D. K. Cellulose Crystallinity Index: Measurement Techniques and Their Impact on Interpreting Cellulase Performance.

Biotechnol. Biofuels **2010**, *3* (1), 10.

(67) Gautier, F.; Destribats, M.; Perrier-Cornet, R.; Dechézelles, J.-F.; Giermanska, J.; Héroguez, V.; Ravaine, S.; Leal-Calderon, F.; Schmitt, V. Pickering Emulsions with Stimulable Particles: From Highly- to Weakly-Covered Interfaces. *Phys. Chem. Chem. Phys.* **2007**, *9* (48), 6455.

(68) Bancroft, W. D. The Theory of Emulsification, V. *J. Phys. Chem.* **1913**, *17* (6), 501–519.

(69) Vignati, E.; Piazza, R.; Lockhart, T. P. Pickering Emulsions: Interfacial Tension, Colloidal Layer Morphology, and Trapped-Particle Motion. *Langmuir* **2003**, *19* (17), 6650–6656.

(70) Pu, Q.; Sarkanen, K. Donnan Equilibria in Wood-Alkali Interactions. Part I. Quantitative Determination of Carboxyl-, Carboxyl Ester and Phenolic Hydroxyl Groups. *J. Wood Chem. Technol.* **1989**, *9* (3), 293–312.

Chapter 3. Surfactant-Free Latex Nanocomposites Stabilized and Reinforced by Hydrophobically Functionalized Cellulose Nanocrystals.*

3.1 Abstract

Stable poly(styrene-*co*-2-ethylhexyl acrylate) latex particles with diameter less than 600 nm were prepared by the miniemulsion polymerization of Pickering emulsions stabilized with hexyl-functionalized cellulose nanocrystals (CNC-hexyl-COOHs). Polymer nanocomposites were fabricated by casting of the CNC stabilized latex particles, and the thermomechanical properties and microstructures of the films were studied and related to the type and amount of stabilizer as well as the processing conditions. Compared to the latex films stabilized with low molecular weight sodium dodecyl sulfate (SDS) surfactant, or using a combination of SDS and carboxylic acid CNC-COOHs, films stabilized solely with the alky-functionalized CNC-hexyl-COOHs showed much higher storage moduli in the rubbery regime and lower water uptake. Scanning electron microscopy (SEM) revealed a CNC network structure that is formed by excluded volume effects of the latex particles which concentrates the CNC-hexyl-COOHs into the interstitial space during solvent evaporation. This effect results in the formation of a percolation network at lower CNC concentration within the latex composite films. The network can be further reinforced by increasing the concentration of CNCs through an "ex-situ" process where CNC-hexyl-COOHs stabilized latex particles were mixed with CNC-COOH aqueous dispersions before film casting. The ability to replace low molecular weight surfactants in water-based latexes with alkyl-functionalized CNCs that are not only biosourced but also act to reinforcing agents, offers

* This chapter is adapted from: **Zhang, Y.**; Yang, H.; Naren, N.; Rowan, S. J. *ACS Appl. Polym. Mater.* **2020**, *2* (6), 2291–2302

opportunity to expand the property profile of a variety of commercial products, such as paints, coatings and adhesives.

3.2 Introduction

Polymer latexes consist of microscopic polymer particles dispersed in a continuous liquid media (commonly water) and are used in a wide range of applications, such as additives, cosmetics, adhesives, paints and coatings.[1] They can be formed by the polymerization of an emulsion in which the non-continuous phase contains monomers. If the latexes are composed of relatively low glass transition (T_g) (co)polymers then it is possible to form a uniform film upon evaporation of the continuous phase.[2,3] As such, water-based latexes have been studied and used extensively in commercial coating and adhesive products to replace solvent-based materials with the goal of reducing environmental impact. However, latex-based coating films generally suffer from relatively low mechanical properties as a consequence of the low T_g polymer in the formulation and the presence of the low molecular weight surfactant that is used to stabilize the emulsion/latex. One strategy that can be used to improve the performance of a latex film is the introduction of nanofillers into the latex dispersion, such as various inorganic nanoparticles (ZnO, TiO_2, Al_2O_3, SiO_2),[4–7] nanoclays,[8] carbon nanotubes,[9] as well as cellulose nanocrystals (CNCs).[10–14] These latex nanocomposites showed enhanced thermal, mechanical and adhesive properties which further broaden their applications in commercial products.[15]

Among all the potential nanofillers, cellulose nanocrystals (CNCs) have gained a considerable amount of attention for the preparation of more environmentally friendly polymer nanocomposites.[16] CNCs are rod-like organic nanoparticles which can be isolated from a variety of renewable bio-sources through selective mechanical and chemical treatment.[17–19] On account of

their sustainability, excellent mechanical properties and low density, CNCs have been widely explored as a green filler to reinforce a number of polymer matrices.[20–25] The significant enhancement in mechanical properties of the nanocomposites is attributed to the formation of a percolating CNC filler network within the polymer matrix through strong hydrogen-bonding interactions between the nanocrystals and/or between the matrix and filler.[26,27] Optimal reinforcement requires the nanocrystals to be uniformly dispersed within the polymer matrix, but it remains a challenge to mix unfunctionalized CNCs that are primarily hydrophilic with some hydrophobic polymers. The incompatibility between CNCs and such polymers can lead to phase separation and result in poor mechanical reinforcement.

To better disperse CNCs into a hydrophobic polymer matrix, nanocomposites can be prepared by mixing pre-synthesized polymer latexes with aqueous dispersions of CNCs, or by incorporating CNCs *in-situ* during the polymerization to yield the latex, followed by casting and drying. Early work by Favier et al. showed it was possible to access polymer nanocomposites by mixing aqueous suspensions of sulfuric acid hydrolyzed tunicate CNCs with a commercial aqueous poly(styrene-*co*-butyl acrylate) latex stabilized with surfactants.[26] An increase in thermal stability and mechanical properties above the glass transition temperature T_g were observed as a result of the incorporation of the CNCs.[27,28] The effect of different processing methods on the mechanical properties of the latex-based nanocomposites has also been investigated in follow-up studies.[29–33] For example, results showed that composites fabricated by casting, as opposed to freeze drying followed by melt processing, gave the highest mechanical reinforcement.[29–31] Similar results were observed in a study by Annamalai et al., where CNCs were added to a commercial low molecular weight surfactant-stabilized styrene-butadiene rubber (SBR) latex and the resulting CNC reinforced SBR composites prepared by casting demonstrated higher storage moduli than the

composites prepared by compression molding.[33] The higher reinforcement observed in both works suggested there is a different CNC network structure within the latex nanocomposites. It was hypothesized in both studies that the excluded volume of the latex particles concentrates all the CNCs into the interstitial areas during water evaporation, which leads to the formation of a robust percolation network as well as a decrease in percolation threshold relative to the case where CNCs are uniformly dispersed in the polymer matrix.[32,33] However, no clear microscopic evidence for such CNCs network structures were shown. Koning and co-workers reported the fabrication of conductive polymer nanocomposites by mixing PEDOT:PSS coated CNCs with pre-synthesized polystyrene latex particles that were stabilized with SDS, and demonstration the percolation threshold of PEDOT:PSS conducting polymer decreased from 2.2 wt% to only 0.4 wt% with the addition of 0.8 wt% of CNCs.[34] The author attributed the low threshold to the CNC network formed in the interstitial areas by PS latex templating effects which was observed by SEM. More recently, Ballard and coworkers showed that a honeycomb microstructure can be observed after mixing and drying negatively charged CNCs (length ca. 120 nm) with positively charged latex particles (size 530 nm, stabilized with cationic surfactant) on account of electrostatic interactions and latex templating.[35] Such film structure leads to a significantly higher Young's modulus and ultimate tensile strength, consistent with the mechanical properties being heavily affected by the composite microstructure. It is worth pointing out that in the mixing approach to fabricate latex nanocomposites, low molecular weight surfactants are required to help stabilize the latex particles from aggregation. However, such surfactants are less favorable for film applications since they can lead to an increasing sensitivity to water and a decrease in gloss or adhesion properties by migrating to the interface or by forming aggregates.[36–38]

As an alternative to the mixing approach utilized in these prior studies (which has been termed *ex-situ*), composite films prepared from latexes that were synthesized with the CNCs present during the polymerization of the emulsion show enhanced mechanical properties.[10,11] This *in-situ* method appears to promote better interactions between the CNCs and the polymer matrix through either better physical absorption or covalent grafting of the polymer from the surface of the CNCs.[39,40] The presence of CNCs at the interface also helps in stabilizing the monomer droplets by acting as a mechanical barrier to prevent particles from coalescing. In fact, it has been reported that sulfated CNCs can be used as solid stabilizers to access stable oil-in-water Pickering emulsions as a consequence of the amphiphilic character of the nanocrystals (one of the crystal faces (200) is hydrophobic).[41–47] However, to achieve nano-sized emulsions with enhanced stability, covalent or noncovalent surface modification of CNCs is generally required.[48–57] Electrostatic interactions between charged surfactants and negatively charged CNCs has been shown to be an effective way to non-covalently modify the CNCs resulting in enhanced wettability at the o/w interface. For example, Dubé and co-workers successfully synthesized CNC/poly(n-butyl acrylate-*co*-methyl methacrylate) latex nanocomposites for pressure sensitive adhesive (PSA) applications by using CNCs and the anionic surfactant sodium dodecyl sulfate (SDS) as co-stabilizers during emulsion polymerization.[58,59] They observed an improved mechanical performance (tack, peel strength and shear strength) of the composite PSA films by increasing CNC concentration from 0 to 1 wt.%, and the level of reinforcement is better relative to nanocomposites prepared by simply mixing the CNCs with pre-synthesized P(BA-*co*-MMA) latex particles in water and drying (i.e. the *ex-situ* approach).[59] The better reinforcement was attributed to the possible polymer grafting of the CNCs during *in-situ* emulsion polymerization as indicated by a high gel content of the nanocomposites (61.6 wt.%). It is worth mentioning that in this case

the latex interface will be stabilized by both the surfactant molecules as well as the CNCs. In other work reported by Boufi and co-workers, comonomers such as γ-methacryloxypropyl trimethoxysilane (MPS)[14,60] and low molecular weight poly(ethylene glycol) methacrylate (MPEG)[11,61] were added to the oil phase in order to facilitate the absorption of CNC to the surface of droplet during *in-situ* polymerizations. A 2-fold increase in storage modulus in rubbery regime and a 230% increase in adhesive strength of poly(vinyl acetate) nanocomposites (with 8 wt% of CNCs and 5 wt% of MPEG) were observed.[11] However, no details of the how the microstructure of the composite films impacted their properties was discussed.

Although the above research shows that hydrophobic polymers can be reinforced with CNCs through a latex approach, in all cases low molecular weight surfactants are still required to help stabilize the formation of nanoemulsions. However, being surface active low molecular weight surfactants tend to migrate to the surface or to the substrate interface during the drying of the films. The aggregation of surfactants at the surface leads to leaching, discoloration of the coatings, and a reduction in water resistance properties, barrier properties as well as adhesion behavior.[36] Therefore, it would be of interest to synthesize surfactant-free polymer latex composites that are stabilized only by functionalized CNCs. Thus, the specific goal of this research is to build upon our prior work which showed that alkyl-modified CNCs can be used to replace low molecular weight surfactants in o/w emulsions.[50] The alkyl-CNCs help to stabilize the emulsion by not only acting as Pickering stabilizers but also by dropping the interfacial energy between the oil phase and aqueous phase. However, these prior studies did not investigate how the use of these alkyl-CNCs as the only stabilizing agent impacts film properties. Thus, reported herein is the preparation of low-molecular weight surfactant-free stabile oil-in-water emulsions and latexes using styrene and 2-ethylhexyl acrylate (and 1 wt.% methacrylic acid) as the oil phase, and hexyl

modified CNCs as both the emulsion/latex stabilizer and reinforcing agent. Latex nanocomposite films were fabricated by simple casting from CNC-stabilized latex particle dispersions and their mechanical properties as well as microstructures were investigated. The microstructures formed by *in-situ* polymerization of the latexes stabilized with hexyl modified CNCs were found to be critical for the strong mechanical reinforcement effect. In addition, these results are compared to the mechanical properties of low molecular weight surfactant (in this case sodium dodecyl sulfate, SDS) stabilized latexes as well as SDS/CNC stabilized latexes to evaluate the effect that removing the low molecular surfactant has on the properties of these latex films.

3.3 Experimental Section

Materials

Styrene and 2-ethylhexyl acrylate monomers were purchased from Sigma-Aldrich and purified by passing through a basic alumina packed column to remove inhibitors. Methacrylic acid, *N*-(3-dimethylaminopropyl)-*N′*-ethylcarbodiimide hydrochloride (EDC), *N*-hydroxysuccinimide (NHS), hexylamine, sodium metabisulfite, tert-butyl hydroperoxide solution (70% in H_2O), D-(-)-Isoascorbic acid, sodium dodecyl sulfate (SDS) and dialysis membranes (14 kDa molecular weight cutoff) were all purchased from Sigma-Aldrich and used as received. Hydrochloric acid, sodium hydroxide (NaOH), potassium persulfate (KPS) were purchased from Fisher Scientific and used without further purification. Microcrystalline cellulose (MCC) (trade name: Lattice® NT) was received from FMC Corporation (Newark, DE). Miscanthus x. Giganteus (MxG) stalks were donated by Aloterra Energy LLC (Conneaut, OH).

Synthesis of m-CNC-COOH via TEMPO oxidation of MCC

Oxidation of MCC was performed by adapting the previous published procedure.[50] 5 g of MCC was dispersed in 500 mL of DI water via sonication for 4 hrs using a Q500 QSonica Ultrasonic Processor at 40% amplitude. TEMPO (4 g, 25.6 mmol), NaBr (40 g, 388.7 mmol) and NaOCl (30 g, 403 mmol) were added into the dispersion while stirring. An additional NaOCl (10 g, 134.3 mmol) was added in order to maintain the pH of the reaction between 10-11. After the addition of NaOCl, 10 M NaOH was used to maintain the pH above 10. The pH of the solution was closely monitored and the reaction was quenched by adding 25 mL of methanol when the pH stayed unchanged during a 15-minute period. The CNC dispersion was centrifuged, and the supernatant was precipitated in excess methanol and collected via centrifugation. The product was further washed with methanol and DI water using successive centrifugation before being dialyzed against DI water for 2 days. Finally, m-CNC-COOH was recovered through lyophilization for 4 days using a VirTis benchtop K lyophilizer.

Isolation and oxidation of MxG-CNCs

MxG-CNC-OH was isolated from *Miscanthus x. Giganteus* stalks and oxidized according to previous published methods.[62] Ground up MxG powder (8 g) was soaked in 250 mL of 2 wt% sodium hydroxide solution for 24 hrs. The base treatment was repeated twice in the same concentration of sodium hydroxide solution at 100 °C for 24 hrs. The solid was filtered and washed thoroughly with DI water after each treatment. The remaining solid was re-dispersed into 180 mL of 2 wt% sodium chlorite solution with 12 mL of glacial acetic acid, and the dispersion was allowed to heat to 70 °C for 2 hrs under stirring before being filtered and washed. The white MxG pulp was further hydrolyzed in 100 mL of 1 M HCl solution at 75 °C for 15 hrs. The resulting pulp was thoroughly washed with DI water until neutral pH. The product was subjected to dialysis against

DI water and collected via lyophilization. 1 g of hydrolyzed MxG-CNC-OH was dispersed in 150 mL of DI water via ultrasonication before TEMPO (0.123 g), NaBr (1.23 g) and NaOCl (1.23 g) was added. The reaction was stirred at room temperature for 4.5 hrs while the pH of the solution was maintained above 10 with the addition of 1 M NaOH solution. The reaction was quenched by adding excess methanol and the oxidized product MxG-CNC-COOH was recovered as white precipitate after centrifugation of the solution. Finally, the product was subjected to dialysis against DI water and collected via lyophilization.

Functionalization of CNCs with hexyl amine

m-CNC-COOH (1 g, 0.72 mmol of carboxylic acid moieties) was dispersed in 200 mL of DMF via overnight sonication. EDC (0.60 g, 3.6 mmol, 5 equiv) was added and the reaction was allowed to stir for 5 min. Then NHS (0.414 g, 3.6 mmol, 5 equiv) was added and the reaction was allowed to stir for another 30 min. Hexylamine (0.364 g, 3.6 mmol, 5 equiv) was slowly added, and the reaction was allowed to stir at room temperature for 16 hrs. The reaction was stopped by adding 100 mL of methanol and the white precipitate was collected by centrifugation. The product was further washed with methanol (three times) and DI water (three times) under successive centrifugation, dialysis against DI water, and finally lyophilized to yield m-CNC-hexyl-COOH. The same reaction was adopted on MxG-CNC-COOH (1g, 0.92 mmol of carboxylic acid moieties) for the synthesis of MxG-CNC-hexyl-COOH. Kaiser test was performed on the functionalized CNCs to make sure that free amine had been completely washed out.

Characterization of hexyl-functionalized CNCs

Conductometric Titration. The content of surface carboxylic groups of CNC-COOH and CNC-hexyl-COOH was determined through conductometric titrations. Around 25 mg of CNC-COOH or 50 mg of CNC-hexyl-COOH was dispersed in 80 mL of DI water via overnight sonication in a Branson CPX sonication bath before titration. The pH of the dispersion was adjusted to below 3 by adding 15 μL of concentrated HCl (33%) and the titration was performed by adding 0.01 M NaOH solution using an Accumet XL benchtop pH/conductivity meter (Fisher Scientific). The conductivity was plotted against the volume of NaOH consumed, and plateau region was used to determine the volume of NaOH used to neutralize the carboxylic acid groups, which then can be further used to calculate the content of carboxylic groups. The amount of hexyl groups was calculated by the difference in the number of carboxylic acid groups before and after functionalization.

Fourier Transform Infrared Spectroscopy (FTIR). FTIR studies of CNCs were performed using a Shimadzu IRTracer-100 FTIR spectrometer. Freeze dried CNC-hexyl-COOHs were placed directly on the ATR crystal, and the spectra were averaged from 45 scans between 400 to 4000 cm^{-1} with a resolution of 4 cm^{-1}.

Atomic Force Microscopy (AFM). Suspensions of CNCs at a concentration of 0.01 wt.% were drop-casted on freshly cleaved mica surfaces which has been pretreated with polylysine solutions. The samples were imaged using a Bruker Multimode 8 AFM instrument using ScanAsyst mode. The AFM images were processed by Gwyddion software.

Emulsion and latex particle preparation

m-CNC-hexyl-COOH or MxG-CNC-hexyl-COOH were dispersed in 7 g of DI water at desired concentrations (1wt.%, 2wt.% and 3wt.% based on monomers) via ultrasonication. 2 g of acrylate

monomer mixtures which consist of styrene, 2-ethylhexyl acrylate and methacrylic acid at a weight ratio of 54:45:1 were added to the CNC/aqueous dispersion, and the mixture was ultrasonicated (Branson Sonifier SFX 550) for 60 s under pulse mode (3 s on, 3 s off) to form emulsion. The emulsion was purged with nitrogen for 10 min, and then sealed and heated up to 40 °C. Potassium persulfate (20 mg) and sodium metabisulfite (20 mg) were dissolved in 0.5 mL of DI water separately and injected dropwise as initiators. The polymerization was carried out at 40 °C for 2 hrs and then the temperature was ramped up to 65 °C and left for 4 hrs. Tert-butyl hydroperoxide solution (2 mg, 70% aqueous solution) was diluted in 0.2 mL of DI water, added into the reaction and stirred for 30 min. This was followed by the addition of 0.2 mL of D-(-)-Isoascorbic acid aqueous solution (1 mg) and the polymerization was allowed to continue for another 30 min. Finally, the reaction was cooled down to room temperature.

Characterization of Latex Particles

Dynamic Light Scattering (DLS) and Zeta Potential. The average diameter of the polymer latex particles was measured by dynamic light scattering. Samples were prepared by diluting 10 μL of latex particle suspension after polymerization in 2 mL of DI water. DLS, electrophoretic mobility and zeta potential measurements were carried simultaneously using a WYATT Mobiüs DLS detector.

Conversion. The conversion of the miniemulsion polymerization was measured gravimetrically. An aliquot of latex samples after polymerization was weighted and the weight percent (wt.%) of polymer were calculated after drying the sample in vacuum oven for 24 hrs at 100 °C. The conversion was calculated as the ratio between the wt.% of polymer vs the theoretical wt.% of monomer according to the formulation.

Latex films preparation

Solution Casting of Latex Films. As-cast latex films were prepared by directly casting the polymerized latex aqueous dispersion into PTFE dishes (diameter ca. 10 cm). Latexes were first dried in fume hood for 24 hrs to evaporate most of the water, and then furthered dried at 90 °C in a vacuum oven for another 24 hrs to fully remove water and unreacted monomers. Homogeneous films with thickness between 200-300 nm were formed.

Melt processing of latex films. The as-cast films were also compression molded between two PTFE support films at 90 °C and 4000 psi for 10 min using a Carver laboratory press.

Characterization of Latex Films

Scanning Electron Microscopy (SEM). The cross-section of the latex films was imaged by SEM. Films were first frozen in liquid nitrogen for 30 s and fractured to expose the cross-section areas. The fractured surfaces were then sputter-coated with 5 nm of Pd/Pt and imaged under a Carl Zeiss Merlin SEM.

Mechanical Properties. Latex films were cut into rectangular samples with an approximate dimension of 30 mm by 4 mm. The viscoelastic properties of the latex films were then analyzed using an RSA-G2 solid analyzer (TA Instrument, DE) equipped with a tension clamp. The modulus of the samples was analyzed using a temperature sweep method from -20 °C to 80 °C at a heating rate of 3 °C /min, with a fixed frequency of 1 Hz and a strain of 0.1%. All the DMA tests were performed in triplicate and the standard deviations were reported as error bars.

Swelling Test. Latex film samples were first weighted to obtain the dry mass before placing in vials filled with DI water. After 48 hrs the samples were removed from water, gently blotted using filter paper and weighted to obtain the wet mass. The degree of water uptake can be calculated by

$$\%Swelling = \frac{Wet\ mass - Dry\ mass}{Dry\ mass} \times 100$$

3.4 Result and Discussion

3.4.1 Acrylate emulsions and latexes stabilized by hydrophobically functionalized CNCs

In prior work it has been shown that alkyl-modified CNCs better stabilize the o/w interface relative to carboxylic acid-functionalized CNCs.[50] Therefore, carboxylic acid-functionalized CNCs from both microcrystalline cellulose (MCC) (m-CNC-COOH) and *Miscanthus x. Giganteus* (MxG-CNC-COOH) were functionalized with hexyl groups to increase the hydrophobicity of the nanocrystals. Both m-CNC-COOH (length ca. 100 nm, height 5.3 nm by AFM) and MxG-CNC-COOH (length ca. 300 nm, height 3.4 nm by AFM) (Figure A3.1) were selected here with the goal of studying the effect of aspect ratio of the nanofillers on the mechanical reinforcement of latex nanocomposites. Reaction of hexylamine with the CNC-COOHs using standard peptide coupling conditions (EDC/NHS) results in the formation of the hexyl functionalization CNCs (CNC-hexyl-COOH). FTIR (Figure A3.2) of the oxidized CNC-COOHs shows a peak at 1600 cm^{-1} which is consistent with the formation of carboxylate moieties on the CNC surface. A new peak at 1645 cm^{-1} showed up after hydrophobic modification which is consistent with the formation of the amide bond, while the peak at 1720 cm^{-1} corresponds to the carbonyl peak of the residual carboxylic acid moieties. The formation of the amide bond is further confirmed by an increase in the nitrogen content (0.75% for m-CNC-hexyl-COOH, 1.40% for MxG-CNC-hexyl-COOH) as determined by elemental analysis after functionalization (Table A3.1). Conductometric titrations

showed that the carboxylic acid CNCs have a surface carboxylic acid density of 725 and 920 mmol/kg for m-CNC-COOH and MxG-CNC-COOH, respectively. After reaction with hexyl amine the residual carboxylic acid density dropped to ca. 270 mmol/kg for m-CNC-hexyl-COOH and 360 mmol/kg for MxG-CNC-hexyl-COOH, consistent with a hexyl group density of ca. 455 mmol/kg and 560 mmol/kg for m-CNC and MxG-CNC, respectively. This corresponds to a CH_2/CH_3 (from the alkyl units) to COOH ratio of ca. 10.1 (m-CNC-hexyl-COOH) and 9.3 (MxG-CNC-hexyl-COOH), which is close the optimum ratio (ca. 9) that was found to give the smallest droplet sizes in the prior study.[50]

A mixture of styrene, 2-ethylhexyl acrylate and methacrylic acid at a weight ratio of 54:45:1 was employed as the oil phase with the goal of synthesizing low T_g copolymer latexes that are similar to those used in water-based paints and coating applications (Scheme 3.1). The small percent of methacrylic acid was included in the monomer phase as it is commonly used in coating formulations to further aid latex stability. In this study, the oil/water ratio is kept at 20/80 (w/w) and the amount of hexyl-modified CNCs in the aqueous phase was varied between 1, 2 and 3 wt.% based on the mass of monomers. In addition, emulsions stabilized with MxG-CNC-COOH and/or low molecular surfactant SDS were prepared for comparison. Miniemulsion polymerization reactions were carried out with the different types and concentration of stabilizers, and the properties of the final latex particles (sizes, conversion, zeta potential) are summarized in Table 3.1.

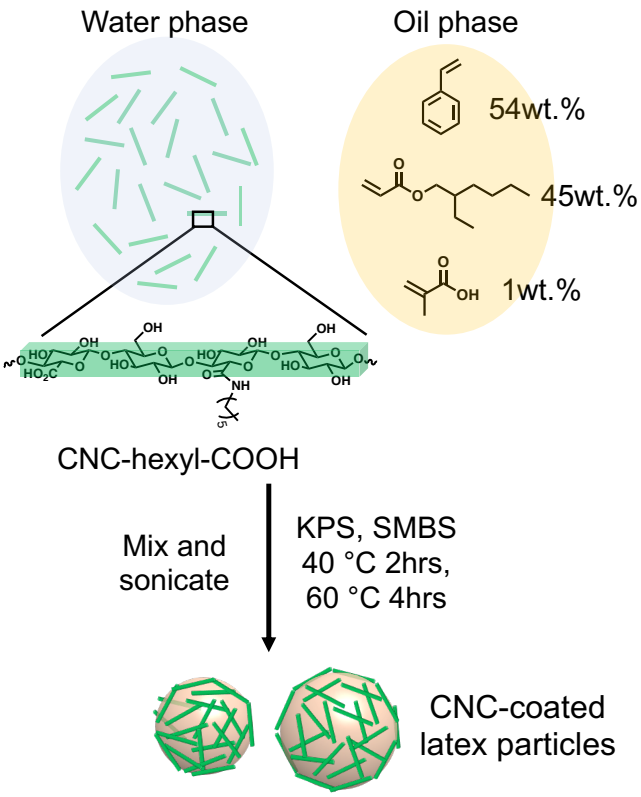

Scheme 3.1 Synthesis of poly(styrene-*co*-2-ethylhexyl acrylate) latex particles via in-situ miniemulsion polymerization stabilized using CNC-hexyl-COOH.

The poly(styrene-co-2-ethylhexyl acrylate) latexes stabilized by m-CNC-hexyl-COOH or MxG-CNC-hexyl-COOH at different concentration are formed in good yield (>80%), except for the latex polymerized with the presence of 1wt.% of MxG-CNC-hexyl-COOH which has a conversion of ca. 76%. A small amount of coagulation is observed which decreases the overall yield of the stable emulsion, and is attributed to unoptimized stirring conditions in the small sample vials. The particle sizes of the latex stabilized with CNCs are all in the 100's of nanometer range. While there is no clear correlation between the concentration of CNC-hexyl-COOH and the particles sizes, the yield of latex obtained did increase with increasing CNC concentration. It is worth pointing out that the theoretical CNC coverage of the particles can be roughly estimated by the average size of the latex particles and the dimension of the CNCs assuming that all CNCs in the aqueous phase

are absorbed at the interfaces (see Appendix). For m-CNC (h=5.3 nm), the calculated coverage for the 1, 2 and 3 wt% latexes based on the average particle size from DLS are ca. 10, 27 and 34%, respectively, while the calculated coverage for the MxG-CNC (h=3.4 nm) latexes, are ca. 19, 38 and 53% (for 1, 2 and 3 wt% respectively). The absorption of more CNCs at the surface of latex particles can be further demonstrated by their higher negative zeta potential with increasing CNC concentration, on account of the negatively charged COO- ions on the surface of CNCs (Table A3.1). It should be noted that particularly at low CNC wt.% these coverage numbers are lower than has been suggested to stabilize similar CNC-stabilize latex particles (ca. 40%). The main difference here is the inclusion of 1wt.% methacrylic acid in the oil formulation which presumably helps to stabilize the particles even at low CNC coverages. These results are consistent with the hexyl-functionalized CNCs acting as a stabilizer at the oil/water interface preventing significant coalescence during polymerization.

In the case where MxG-CNC-COOH was used as stabilizer, the emulsion immediately showed phase separation after ultrasonication with a clear oil phase forming on top of the aqueous phase. Moreover, the latex was obtained in a relatively low yield (ca. 55%) after polymerization which is consistent with the reduced stability of the emulsion. None-the-less, latex particles with an average size of ca. 440 nm are obtained which are presumably stabilized by the negative charges from the methacrylate acid monomer and the decomposed persulfate (KPS) initiators.[63] To test out the hypothesis, the same monomer mixture was mixed with water without using any surfactant (CNC or otherwise), and the emulsion showed same phase separation behavior, particle size and emulsion yield as observed with the MxG-CNC-COOH experiments. This result indicates that the size and stability of these methacrylic acid-containing latexes are not significantly impacted by the presence of the MxG-CNC-COOH. This is consistent with results from a previous study that shows that

these alkyl-modified CNCs can reduce the interfacial tension between the oil and aqueous phase, while carboxylic acid CNCs have little-to-no effect on the interfacial energy.[50] It is important to note that the inclusion of the methacrylic acid monomer (1 wt.%) and the use of persulfate initiator will help to prevent coalescence of the oil droplets, but the concentrations used in these experiments is not sufficient to stabilize the entire monomer phase which is required to achieve high yielding formation of the latex. Tuning the hydrophobic/hydrophilic balance of the CNCs (through reaction with hexyl amine) allows the CNC-hexyl-COOHs to better stabilize the monomer/water interface and act as mechanical barriers to prevent further coalescence which result in the formation of stable emulsions and latexes with an increase in yield of 20-30%. As a final control an emulsion stabilized with the low molecular weight surfactant SDS was also polymerized and as expected resulted in much smaller particles sizes and higher conversion relative to the functionalized-CNCs.

Table 3.1 Summary of the P(St-co-EHA) latexes stabilized with different type of stabilizers.

	Concentration	Size (nm)	Conversion （%）	Zeta Potential (mV)
m-CNC-hexyl-COOH	1wt.%	443.7±5.8	82.1	--
m-CNC-hexyl-COOH	2wt.%	590.4±25.3	83.7	-21.4±0.9
m-CNC-hexyl-COOH	3wt.%	517.8±16.1	86.5	-33.5±0.3
MxG-CNC-hexyl-COOH	1wt.%	490.5±14.3	75.5	--
MxG-CNC-hexyl-COOH	2wt.%	541.0±7.2	84	-28.5±1.1
MxG-CNC-hexyl-COOH	3wt.%	522.6±8.9	87.8	-33.0±0.5
SDS	2wt.%	98.8±0.3	97.4	-21.6±0.7

Table 3.1 Summary of the P(St-co-EHA) latexes stabilized with different type of stabilizers.

MxG-CNC-COOH	2wt.%	444.2±4.8	55.5	-38.1±1.7
No surfactant	0	426.3±4.8	53.3	--

--: not measured

3.4.2 Mechanical properties of latex films

Latexes stabilized with different concentrations of the hexyl-functionalized CNCs were cast from their water dispersions, to yield mechanically robust latex composite films after evaporation of the continuous phase. Figure 3.1 shows the images of the CNC stabilized latex nanocomposites at different loadings of CNCs. The films become less transparent as the concentration of nanocrystals increases from 1 to 3 wt.% for both m-CNC-hexyl-COOH and MxG-CNC-hexyl-COOH. The temperature dependency of the storage modulus (*E′*) of the latex nanocomposites containing the various types and concentration of stabilizers was measured by dynamic mechanical analysis (DMA) studies (Figure 3.2). The storage modulus (*E′*) shows a transition between 20-40 °C, which is attributed to the glass transition of the P(St-*co*-EHA) matrix (glass transition temperature, T_g varied between 26-31 °C, Table 3.). At temperatures lower than 20 °C (i.e. below the T_g), all latex films showed a similar storage modulus, regardless of the type and concentration of the stabilizers used, indicating that the mechanical properties are dominated by the stiff polymer matrix. However, at temperatures above T_g, the latex films containing the hexyl-functionalized CNCs exhibited a much higher plateau storage modulus relative to the latex films stabilized only with low molecular weight SDS surfactant. The plateau modulus also increases as the CNC concentration increases from 1 to 3 wt.% for both m-CNC-hexyl-COOH and MxG-CNC-hexyl-COOH containing films. The mechanical reinforcement is consistent with the formation of a

percolating CNC network akin to what has been reported in other CNC/polymer nanocomposites.[27,28,64]

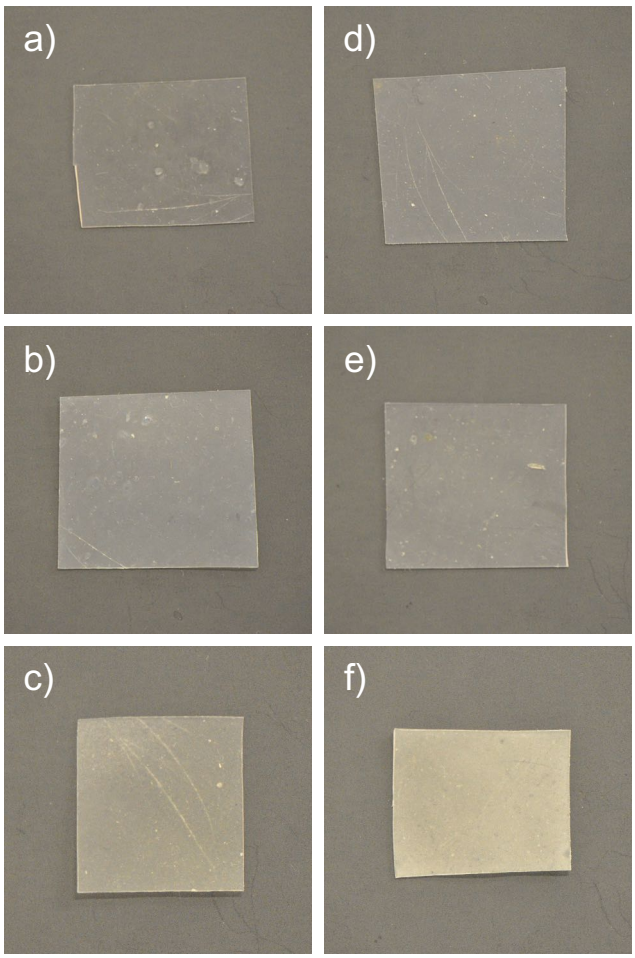

Figure 3.1 As-cast latex nanocomposites stabilized by a) 1 wt.%, b) 2wt.%, c) 3wt.% of m-CNC-hexyl-COOH and d) 1 wt.%, e) 2 wt.%, f) 3 wt.% of MxG-CNC-hexyl-COOH (dimension of films: ca. 40 mm by 40 mm).

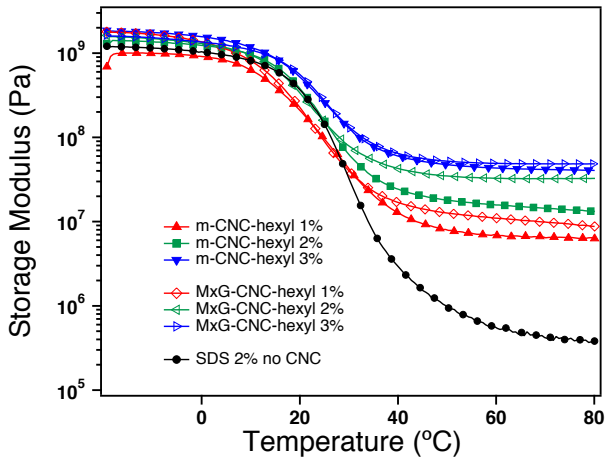

Figure 3.2 DMA temperature sweep study of the storage modulus (E') of the latex composite films stabilized with different type and concentration of stabilizers (heating rate 3 °C/min, frequency 1 Hz, strain 0.1 %). Loss modulus (E'') and tan δ peak are shown in Appendix (Figure A3.3).

For latex composite films containing the same amount of alkyl-CNCs isolated from two different biosources, the plateau storage modulus is slightly higher for films stabilized with MxG-CNC-hexyl-COOH than the films stabilized with m-CNC-hexyl-COOH. The CNCs isolated from MCC have an aspect ratio of ca. 19 while the MxG-CNCs have an aspect ratio of ca. 65.[50,65] Therefore the enhanced reinforcement effect of MxG-CNC-hexyl-COOHs may be attributed to the higher aspect ratio of the MxG nanocrystals, as is predicted by the percolation model for fiber composites (see Appendix).[28,66] However, comparing the plateau modulus between the films containing alkyl-CNCs and SDS, the mechanical reinforcement effect by the alkyl-CNCs results in a modulus increase by up to two orders of magnitude (for the 3 wt% MxG-CNC-hexyl-COOH). Even in the case when the amount of CNCs in the latex is less than the percolation threshold (as predicted by the aspect ratio of the filler) significant reinforcement is still observed. For example, the percolation threshold for the m-CNC is ca. 3.7 vol.% (see Appendix for details), and as such no significant mechanical reinforcement is expected below 3.7 vol.% (or ca. 5.4 wt.% for the P(St-*co*-EHA) nanocomposites). However, the latex film stabilized with only 1 wt.% of m-CNC-hexyl-

COOH demonstrated a mechanical reinforcement with a storage modulus (E') of 7.0 ± 0.2 MPa at 60 °C that is ca. 15 times higher than the storage modulus of SDS stabilized latex film at the same temperature (E' =0.48 ± 0.05 MPa). Of course, the higher aspect ratio of MxG-CNCs means they have a lower percolation threshold (1.1 vol.% or ca. 1.6 wt.%) and the percolation model predicts a storage modulus at 60 °C of ca. 4.4 MPa and 9.7 MPa for nanocomposites containing 2 and 3 wt.% of MxG-CNC, respectively (see Supporting Information for details). However, the MxG-CNC-hexyl-COOHs latex films show enhanced reinforcement relative to the model (E' = 25.9 ± 8.3 MPa and 44.5 ± 4.1 MPa for 2 and 3 wt.% respectively), suggesting that there is something else going on other than a simple homogeneously distributed CNC network that is assumed in the model.

With the goal of better understanding this reinforcement effect, the internal microstructures of the latex nanocomposites were characterized by SEM (Figure 3.3). From SEM images of the cross-sectional areas, a clear interconnected network structure can be observed within the films stabilized by either m-CNC and MxG-CNC. As the CNCs are predominately organized at the surface of the latex particles, the polymer particles act as an excluded volume where no CNCs are present. The deformation of low T_g latex particles concentrates the CNCs into the interstitial space between the particles resulting in the formation of an interconnected network. It is important to note that given its dimensions the “honeycomb” network observed in the SEMs presumably consists of a mixture of CNCs and polymer with the darker regions being predominantly a polymer only phase. Similar honeycomb-like network structures have also been observed before with Laponite and silica stabilized latex films.[67,68] Such excluded volume effect allows the CNCs to form percolating network structures at a much lower concentration than would be predicated in a composite where the filler is well dispersed and as such have an enhanced reinforcement effect. It is important to

note that the structures that the SEM image of the cross-sectional area of the latex films stabilized with SDS does not reveal any such network structures (Figure A3.4).

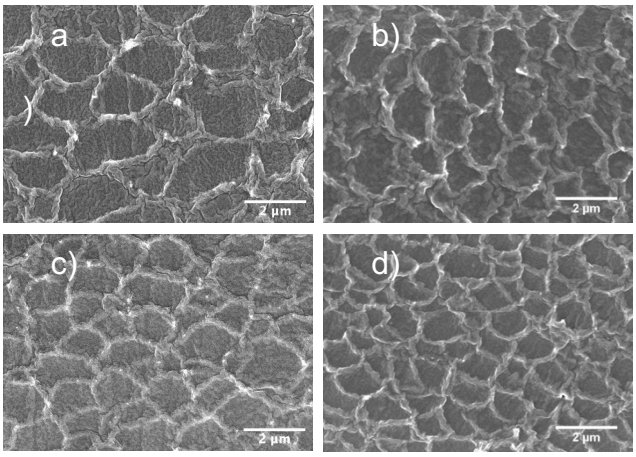

Figure 3.3 SEM images of the cross-sectional areas of latex composite films stabilized using a) 2 wt.%, b) 3 wt.% of m-CNC-hexyl-COOH and c) 2 wt.%, d) 3wt.% of MxG-CNC-hexyl-COOH.

Table 3.2 Summary of the storage modulus (E') and glass transition temperature (T_g) of the latex composite films stabilized with different type and concentration of stabilizers.

Stabilizer type	Concentration	As-cast		Melt-pressed	
		E' at 60 °C (MPa)	T_g	E' at 60 °C (MPa)	T_g
m-CNC-hexyl-COOH	1wt%	7.0±0.2	30.5	1.0±0.1	31.5
m-CNC-hexyl-COOH	2wt%	17.1±1.7	28	1.2±0.1	31.4
m-CNC-hexyl-COOH	3wt%	32.9±10.8	28.3	1.5±0.4	31.8
MxG-CNC-hexyl-COOH	1wt%	14.5±2.4	27	1.0±0.1	28.4
MxG-CNC-hexyl-COOH	2wt%	25.9±8.3	26.3	1.5±0.1	30.3
MxG-CNC-hexyl-COOH	3wt%	44.5±4.1	27.9	2.2±0.3	33.2

Table 3.2 Summary of the storage modulus (E') and glass transition temperature (Tg) of the latex composite films stabilized with different type and concentration of stabilizers.

SDS	2wt%	0.48±0.05	29.5	0.76	32.6
m-CNC-COOH/SDS	2wt%	11.1±1.8	29.1	--	--
MxG-CNC-COOH/SDS	2wt%	12.7±1.6	30.8	--	--

T_g determined from the peak of tan δ.

A number of reports in the literature[48,58,59,69] have focused on accessing latex/CNC nanocomposites by taking advantage of non-covalent interactions between the CNCs and traditional surfactants, and utilized surfactant and/or surfactant coated CNCs as the stabilizers to access stable oil-in-water emulsions. As such latexes with the same monomer mixture but stabilized by a combination of CNC-COOH and SDS were prepared in order to compare their film properties to those of the alkyl-CNCs latex films. To this end, 2 wt.% of m-CNC-COOH or MxG-CNC-COOH (with respect to monomer) were dispersed in water along with SDS (10 mM, above CMC).[48] The monomer phase was then added, and the polymerization of emulsions was carried out using the same initiator systems to yield stable polymer latex particles with diameters of 172 ± 10.5 nm (m-CNC-COOH/SDS) and 166 ± 8.0 nm (MxG-CNC-COOH/SDS) (Table A3.2). Nanocomposite films formed from the latexes stabilized with CNC-COOH/SDS (Figure A3.5) showed a lower storage modulus in the rubber regime compared to CNC-hexyl-COOHs at the same CNC loadings (2 wt.%) (Figure 3.4, Figure A3.6). The E' of the m-CNC-COOH/SDS stabilized films at 60 °C is 11.2 ± 1.8 MPa (c.f. 17.7 MPa for m-CNC-hexyl-COOH), while the E' of the MxG-CNC-COOH/SDS stabilized films at 60 °C is 12.7 ± 1.6 MPa (c.f. 25.9 MPa for MxG-CNC-hexyl-COOH). It is worthy of note that SEM images of the CNC/SDS films (Figure A3.7) revealed no interconnected structures of the nanofillers. A possible explanation for the difference

in microstructures is that the surface of the monomer droplets is predominantly stabilized with low molecular weight surfactants rather than the CNCs. Therefore, the coalescence and interfusion of latex particles during film formation does not lead to the formation of the honeycomb like network structures compared to the latexes which were covered only with CNCs. It is also possible that the some of the SDS in the formulation coats the CNCs making them more dispersible in the oil phase.

In addition to the mechanical properties, surfactant/CNC formulation may be expected to be more hydrophilic compared to the hexyl-functionalized CNC which will impact the water-swelling behavior of the latex composite films. Indeed, latex films stabilized with CNC-COOH/SDS uptake more water relative to the hexyl-modified CNCs. The equilibrium water uptake is ca. 35 wt.% and 49 wt.% for the latex films stabilized with m-CNC-COOH/SDS and MxG-CNC-COOH/SDS, respectively (Table A3.2), while latex films containing CNC-hexyl-COOH only swell ca. 3 wt.% for either m-CNC-hexyl-COOH or MxG-CNC-hexyl-COOHs. Such a reduction in water uptake offers advantages for the CNC-hexyl-COOH latex films particularly in some coating formulations where water uptake generally leads to a reduction in the film property profile or coating effectiveness.[37,38]

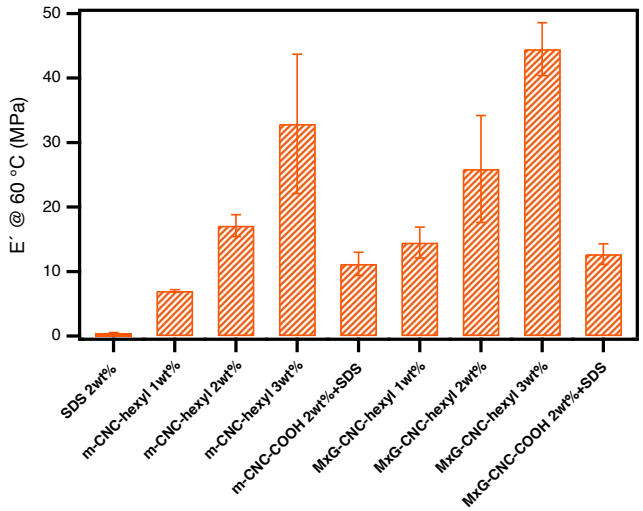

Figure 3.4 Comparison of the storage modulus (*E′*) at 60 °C of as-cast latex composite films stabilized with various type and concentration of stabilizers.

3.4.3 Effect of microstructures on the mechanical properties

Since the above study suggests that the large reinforcement effect of the CNC/latex nanocomposites is attributed to the network structures formed by the latex templating effect. It is of interest to study how the mechanical properties will be affected if the microstructures are altered. To this end, the solution cast films of the latex particles stabilized with alkyl-CNCs were melt-pressed at 90 °C with the goal of disrupting the pre-formed CNC honeycomb structure. The melt-pressed films appear homogeneous without any visible phase separation (Figure A3.8). A slight shrinkage in the film was observed on account of the elasticity of the polymer matrix, and this shrinkage was minimized in films with an increased amount of CNCs. SEM characterization was performed to investigate how the microstructures were affected by melt pressing. As can be seen from the SEM of the cross-sectional areas of the films (Figure 3.5a and b), the honeycomb network structure formed by the CNCs and latex particles has been significantly disrupted by the melt pressing process. The viscoelastic properties of the melt-pressed films were studied using DMA (Table 3.). For the latex films containing only SDS as the stabilizer, the plateau storage modulus at 60 °C increased from 0.48 ± 0.05 MPa to 0.76 MPa after melt pressing. The slight increase in storage modulus is presumably a consequence of the formation of a more compact structure within the films through melt pressing. On the other hand, the plateau storage modulus for the films stabilized with either m-CNC-hexyl-COOH (Figure A3.9) and MxG-CNC-hexyl-COOH (Figure 3.5c) both decreased dramatically as a result of the melt processing. It can be seen from the DMA results that the melt-pressed films containing 1 wt.% m-CNC-hexyl-COOH or MxG-CNC-hexyl-COOH now exhibit similar storage modulus to the film containing SDS, which indicates that the nanofillers (at these loadings) now have little-to-no reinforcement effect in these melt-pressed

latex films. This result supports the hypothesis that the network structure of the CNCs formed by latex templating is key to the strong reinforcement effect observed in the solution-cast latex composite films and a disruption of such network structure leads to a significant decrease in storage modulus of the melt-pressed films.

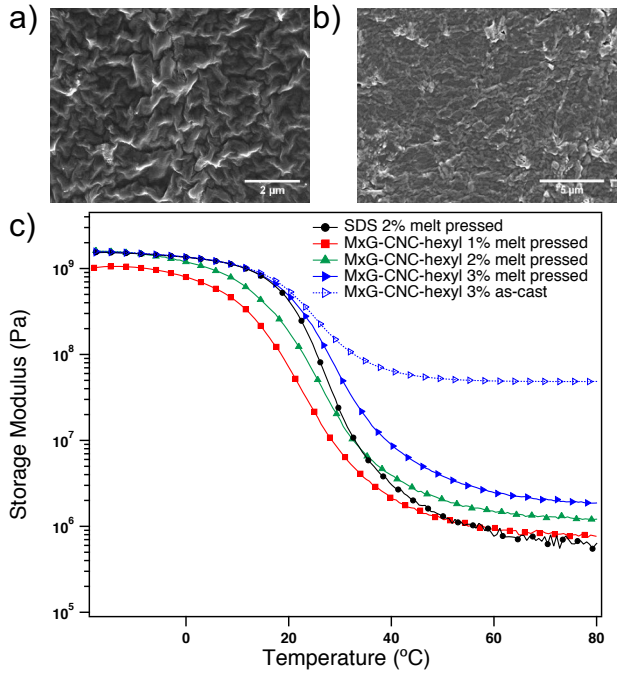

Figure 3.5 SEM images of the cross-sectional areas of melt-pressed latex composite films stabilized using a) 3 wt.% m-CNC-hexyl-COOH and b) 3 wt.% MxG-CNC-hexyl-COOH. c) DMA temperature sweep study of the storage modulus (E') of the latex composite films stabilized with MxG-CNC-hexyl-COOH and SDS after melt pressing. Loss modulus (E'') and tan δ peak are shown in SI (Fig. S10).

3.4.4 Addition of CNC-COOH to the CNC-hexyl-COOH stabilized latexes

For nanocomposites containing rigid nanofillers, the mechanical reinforcement is also a function of the volume fraction of the rigid filler particles, but the relative modulus increase is greatly diminished upon reaching higher filler content. In the case of the alkyl-CNCs latex composite films a significant reinforcement effect is observed even at a relatively low filler content (1-3wt.%).

None-the-less, it was of interest to see whether the network can be further reinforced by increasing the CNC loading in the film. Since the ratio of monomer to aqueous phase is kept at 20:80 (w/w), one way to increase the CNC content relative to the monomer is to increase the CNC concentration in the aqueous phase. However, these hydrophobically functionalized CNCs have reduced dispersibility in the aqueous phase, and the viscosity of the CNC aqueous dispersion also increases rapidly as the CNC concentration increases making it difficult to access stable oil-in-water emulsions at higher CNC content. Therefore, pre-synthesized latex particles stabilized with 3 wt.% of m-CNC-hexyl-COOH or MxG-CNC-hexyl-COOH were mixed with a CNC-COOH aqueous dispersion (10 mg/mL) such that the total amount of CNC-COOH equals ca. 10 wt.% w.r.t. the monomer phase. After stirring the mixtures for 3 hrs, the latex suspensions were cast into composite films with a total CNC weight fraction of 13 wt.%. Both latex composite films contain higher concentration of m-CNC-COOH or MxG-CNC-COOH showed no visible phase separation, however the films were more brittle at room temperature (for example Figure A3.11shows that there is cracking of these films around the cut edges). The mechanical properties of the latex composites were investigated by DMA and the results showed that there is a significant increase in the modulus in the rubbery regime, with a storage modulus E' of 1040 ± 31 MPa and 988 ± 23 MPa at 60 °C for the films stabilized with 13 wt.% m-CNC and 13 wt.% MxG-CNC, respectively (Figure 3.6a). The plateau modulus is more than 2000 times higher than the SDS latex films (without CNCs). It is also worth pointing out that the difference in storage modulus between films stabilized with m-CNCs and MxG-CNCs is not significant, suggesting that in these systems the aspect ratio of individual nanocrystals becomes less important. Similar to the CNC latex films discussed above the storage modulus of these 13 wt.% composite films show a significant decrease in plateau modulus after melt pressing. The E' at 60 °C decreases to 25 ± 7 MPa and 39 ± 14 MPa

for the melt-pressed composites films contain 13 wt.% of m-CNC and MxG-CNC, respectively. The massive decrease in storage modulus is presumably also a consequence of the disruption of the network structures formed within the films as a result of the melt pressing.

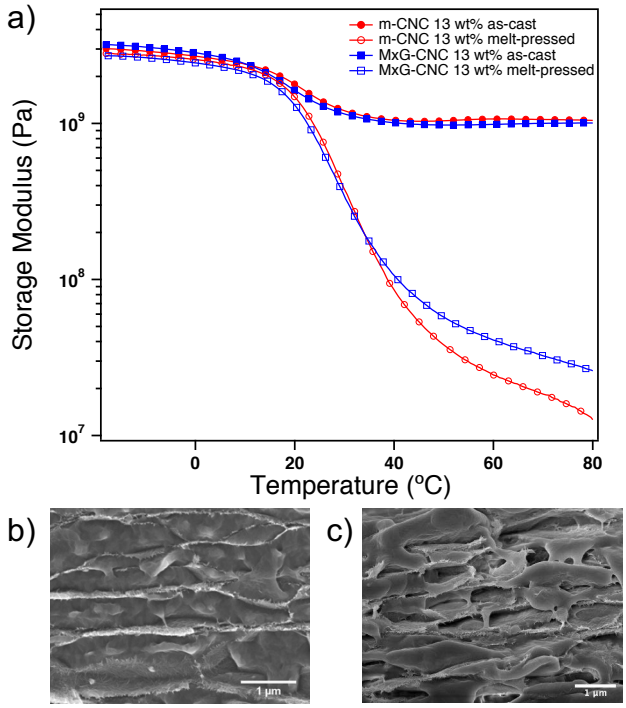

Figure 3.6 a) Comparison between the storage modulus of as-cast and melt-pressed latex composite films stabilized with 13 wt.% total of m-CNCs or MxG-CNCs. Loss modulus (*E″*) and tan δ data are shown in the SI (Fig. S12). SEM image of the cross-sectional areas of latex composite film stabilized with 13 wt.% MxG-CNCs b) as-cast and c) after melt-pressing.

With the goal of understanding the mechanical reinforcement effect, the internal structures of the latex composites stabilized with 13 wt.% of MxG-CNCs was also investigated by SEM (Figure 3.6b). As shown in the SEM image of the cross-sectional area of these films, a more layered microstructure (of what appears to be CNC rich and polymer rich layers) can be observed as opposed to the honeycomb network structure observed in films stabilized with 3 wt.% of MxG-CNC-hexyl-COOH. The lack of any macroscopic phase separation suggests that the polymerized

latex particles stabilized by hexyl functionalized MxG-CNCs and the extra MxG-CNC-COOHs are compatibilized with each other during the ex-situ aqueous mixing process. The higher reinforcement effect is again attributed to the formation of CNC network structures within the composite films by latex templating effect. But in this case, the concentration of CNCs in the interstitial areas (the CNC rich layers observed in SEM) is much higher compared to the network formed within the latex film stabilized with 3 wt% MxG-CNC-hexyl, which resulted in a further enhancement of the film mechanical properties. Furthermore, the network structure could also be disrupted by melt pressing as indicated by the SEM images of the melt-pressed films (Figure 3.6c). This is consistent with the large decrease in storage modulus observed by DMA experiment and is consistent with the previous study that the microstructures formed by the latex particles are crucial for the mechanical reinforcement of the nanocomposites.

3.5 Conclusion

Low molecular weight surfactant free poly(St-*co*-EHA) latex particles with submicron sizes were successfully synthesized by miniemulsion polymerization using hexyl-modified CNCs as stabilizers. These latexes formed films that showed enhanced mechanical properties in the rubber regime relative to the films formed from SDS stabilized latexes even at relative low CNC loadings (1 wt.%). The strong mechanical reinforcement is attributed to the formation of CNC filler networks within the latex composite films as well as better interactions between alkyl-CNCs and polymer matrix on account of the *in-situ* polymerization. The excluded volume of the latex particles results in the formation of a percolating “honeycomb” CNC-rich phase that reinforces the film even at low CNC concentrations. Disruption of this percolating CNC-rich network by melt pressing lead to a significant decrease in mechanical properties of the films. Importantly, these

alkyl-CNC stabilized latexes where shown to form more mechanically robust films that also have lower water uptake than those prepared from corresponding latexes stabilized with a combination of SDS and CNCs, highlighting some key advantages of being able to remove the low moleculaer weight surfactant from the formulation. Finally, it was also shown that the mechanical properties of the latex composite films can be further enhanced by the addition of CNC-COOHs to the pre-synthesized CNC-stabilized latexes. The ability of using alkyl modified CNCs to access latex films without the need of a low molecular weight surfactant to access films with enhanced mechanical properties (even at low CNC loading) and reduced water uptake makes these CNCs an attractive option as a combined green surfactant and reinforcing agent in coating and adhesive applications.

3.6 Appendix

Percolation model

The Percolation model can be used to predict the storage modulus E' of the nanocomposites. This model assumes the rigid filler particles (E'_r) form a percolating network within the soft polymer matrix (E'_s). The level of reinforcement of the CNCs in the nanocomposite is a function of the volume fraction (X_r), aspect ratio (AR) and the modulus of the rigid filler particles (E'_r). According to the percolation model, the modulus of the composite E' can be expressed by:

$$E' = \frac{(1 - 2\psi + \psi X_r)E'_s E'_r + (1 - X_r)\psi {E'_r}^2}{(1 - X_r)E'_r + (X_r - \psi)E'_s}$$

where ψ is the percolation volume fraction of filler particles, which is:

$$\psi = X_r(\frac{X_r - X_c}{1 - X_c})^{0.4}$$

The critical concentration that the network starts to from is called the percolation threshold (X_c), which it is related to the aspect ratio (AR) of the filler particles (X_c = 0.7/AR).

The values used for the prediction of storage modulus of CNC/P(St-*co*-EHA) latex nanocomposites are: modulus of rigid filler E'_r = 3 GPa, modulus of soft polymer matrix E'_s = 0.48 MPa, density of rigid filler ρ=1.49 g/cm^3, density of polymer matrix ρ=1.01 g/cm^3, aspect ratio of m-CNC AR=19 and MxG-CNC AR=65.

Coverage study

The theoretical coverage of CNCs at the particle surface can be calculated by:

$$coverage = \frac{m_p D}{6h\rho V}$$

where m_p is the amount of CNCs absorbed at the interface, D is the average diameter of the latex particles, h is the height of the CNCs (determined by AFM), ρ is the density of the CNCs (1.49 g/cm^3 for both CNCs), and V is the volume of the monomer phase stabilized by CNCs. Assuming all the CNC were absorbed at the interface (which is the ideal case), for m-CNC (h=5.3 nm), the coverage for 1, 2 and 3 wt% based on the average size from DLS are ca. 10, 27 and 34%. For MxG-CNC (h=3.4 nm), the coverage for 1, 2 and 3 wt% are ca. 19%, 38%, 53%. In reality, the coverage number will probably be smaller since not all CNC will be absorbed at the interface.

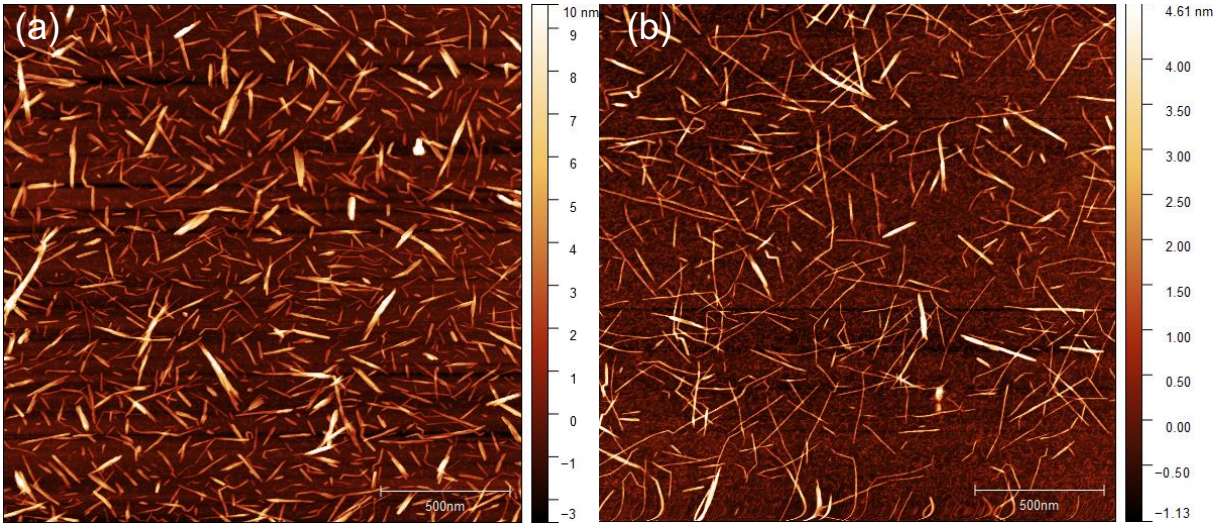

Figure A3.1 AFM height images of a) m-CNC-COOH and b) MxG-CNC-COOH.

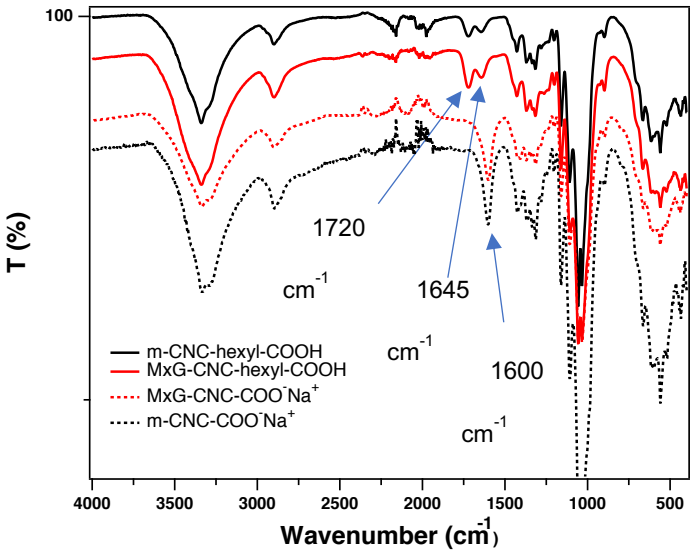

Figure A3.2 FTIR spectra of m-CNC and MxG-CNC after oxidation (m-CNC-COO^-, MxG-CNC-COO^-), and after hydrophobic functionalization (m-CNC-hexyl-COOH, MxG-CNC-hexyl-COOH).

Table A3.1 Elemental analysis and zeta potential study of oxidized m-CNC-COOH and MxG-CNC-COOH, and hydrophobic functionalized m-CNC-hexyl-COOH and MxG-CNC-COOH.

Sample	Elemental Analysis			Zeta Potential
	Carbon (%)	Hydrogen (%)	Nitrogen (%)	(mV)
m-CNC-COOH	41.36	5.64	0.14	-79.7±1.3
MxG-CNC-COOH	41.07	5.68	not found	-91.3±0.8
m-CNC-hexyl-COOH	41.9	5.4	0.75	-55.5±0.8
MxG-CNC-COOH	41.48	5.71	1.03	-55.1±0.8

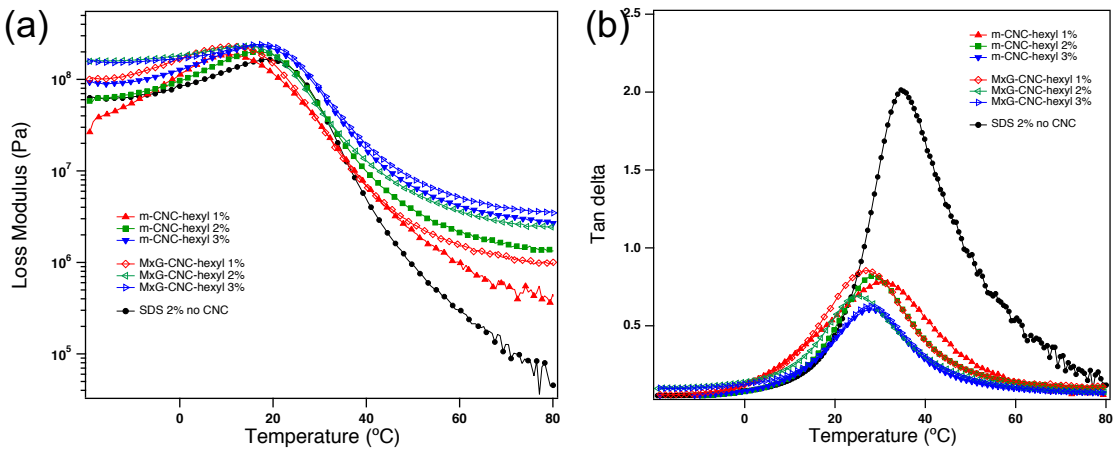

Figure A3.3 DMA temperature sweep study of the a) loss modulus (E'') and b) tan δ of the latex composite films stabilized with different type and concentration of stabilizers.

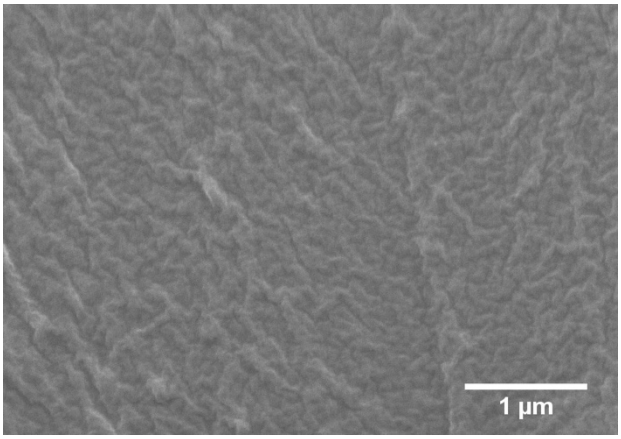

Figure A3.4 SEM images of the cross-sectional areas of latex films stabilized with SDS only.

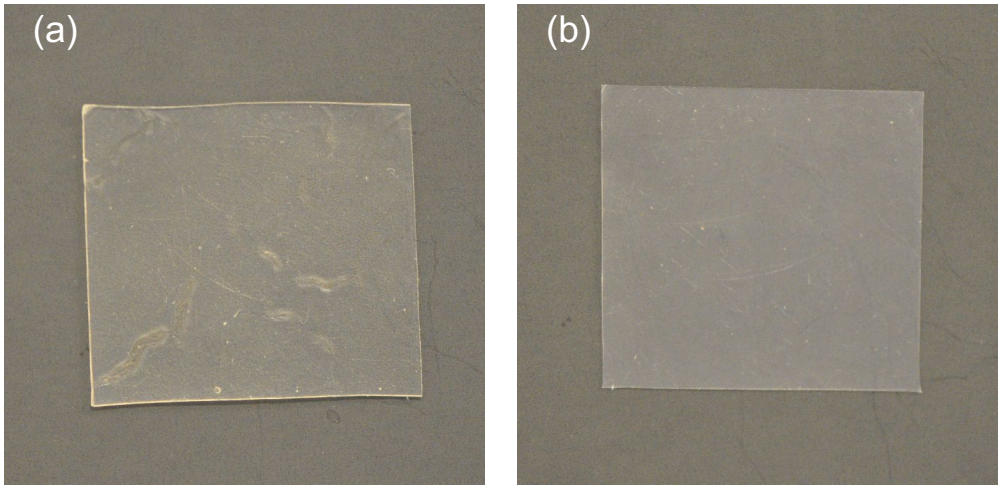

Figure A3.5 Latex composite films stabilized with SDS coated a) m-CNC-COOH and b) MxG-CNC-COOH.

Table A3.2 Comparison of the size of the latex particles and the mechanical properties and water swelling of the latex composite films stabilized with CNC-alkyl-COOH and CNC-COOH/SDS.

Stabilizer	Concentration	SDS	Size (nm)	*E*' at 60 (MPa)	Water Swelling (%)
m-CNC-hexyl-COOH	2wt%	0	590.4±25.3	17.1±1.7	2.9
m-CNC-COOH	2wt%	10 mM	172.9±10.5	11.2±1.8	35
MxG-CNC-hexyl-COOH	2wt%	0	541.0±7.2	25.9±8.3	3.2
MxG-CNC-COOH	2wt%	10 mM	165.6±8.0	12.7±1.6	49

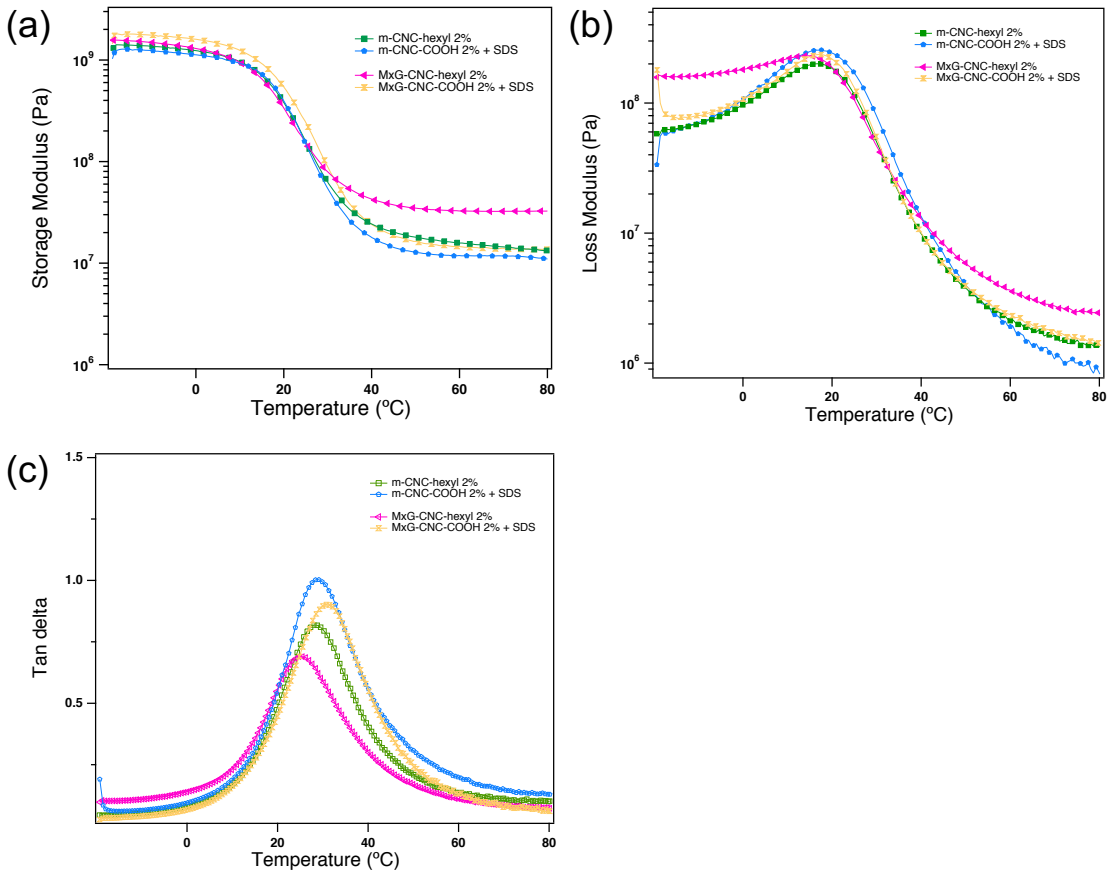

Figure A3.6 DMA temperature sweep study of the a) storage modulus (*E'*), b) loss modulus (*E''*) and c) tan δ of the latex composite films stabilized with SDS/m-CNC-COOH and SDS/MxG-CNC-COOH compared to covalent functionalized CNC-hexyl-COOH.

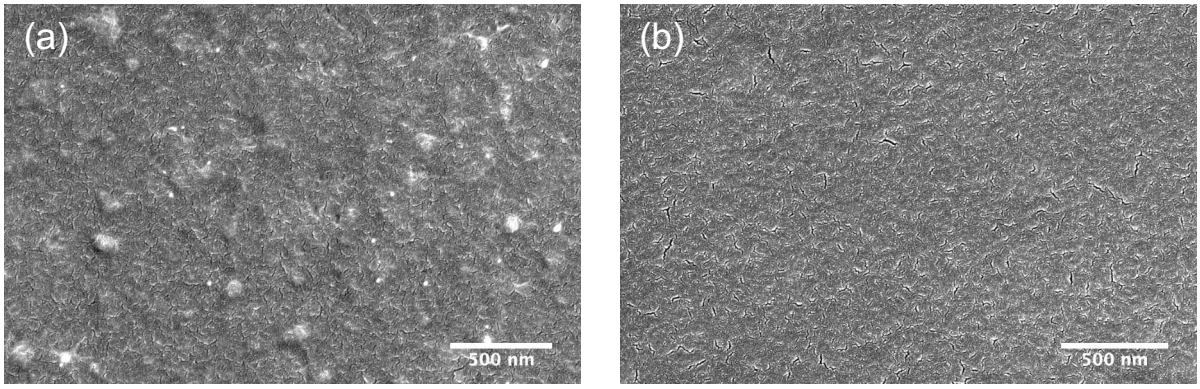

Figure A3.7 SEM images of the cross-sectional areas of latex composite films stabilized using SDS coated a) 2 wt% m-CNC-COOH and b) 2 wt% MxG-CNC-COOH.

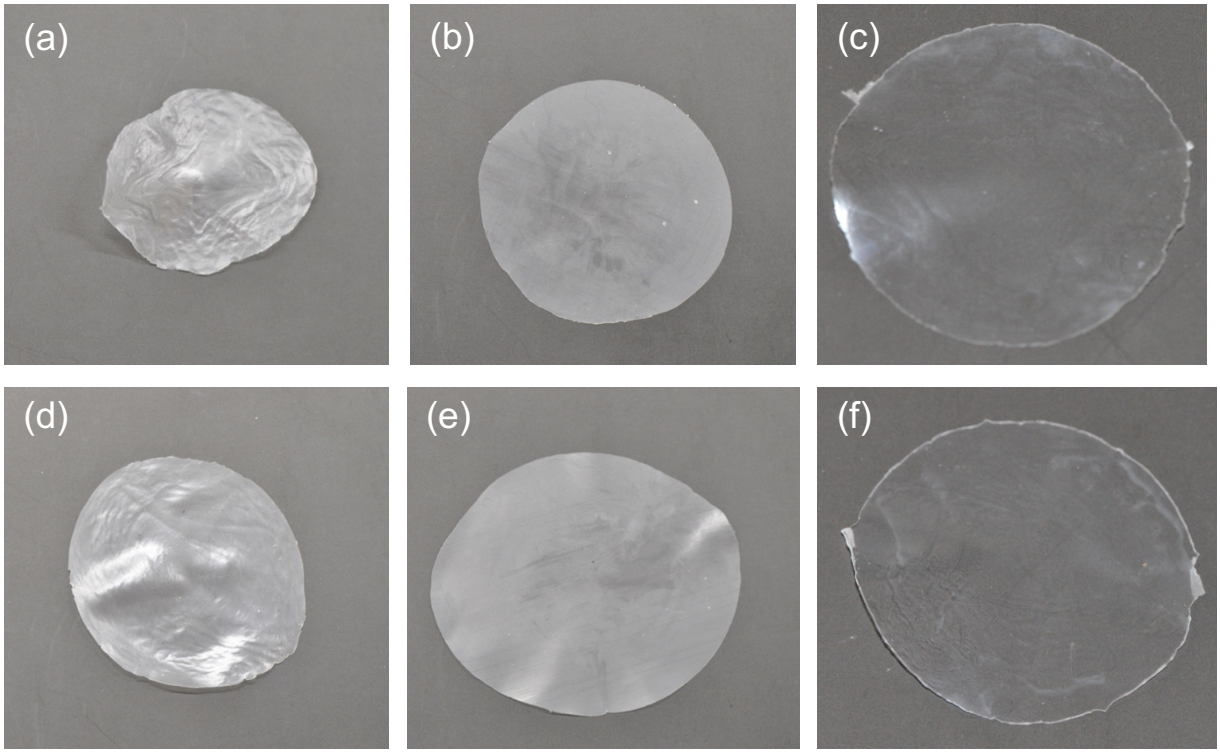

Figure A3.8 Melt-pressed latex nanocomposites stabilized by a) 1 wt%, b) 2wt%, c) 3wt% of m-CNC-hexyl-COOH and d) 1 wt%, e) 2 wt%, f) 3 wt% of MxG-CNC-hexyl-COOH.

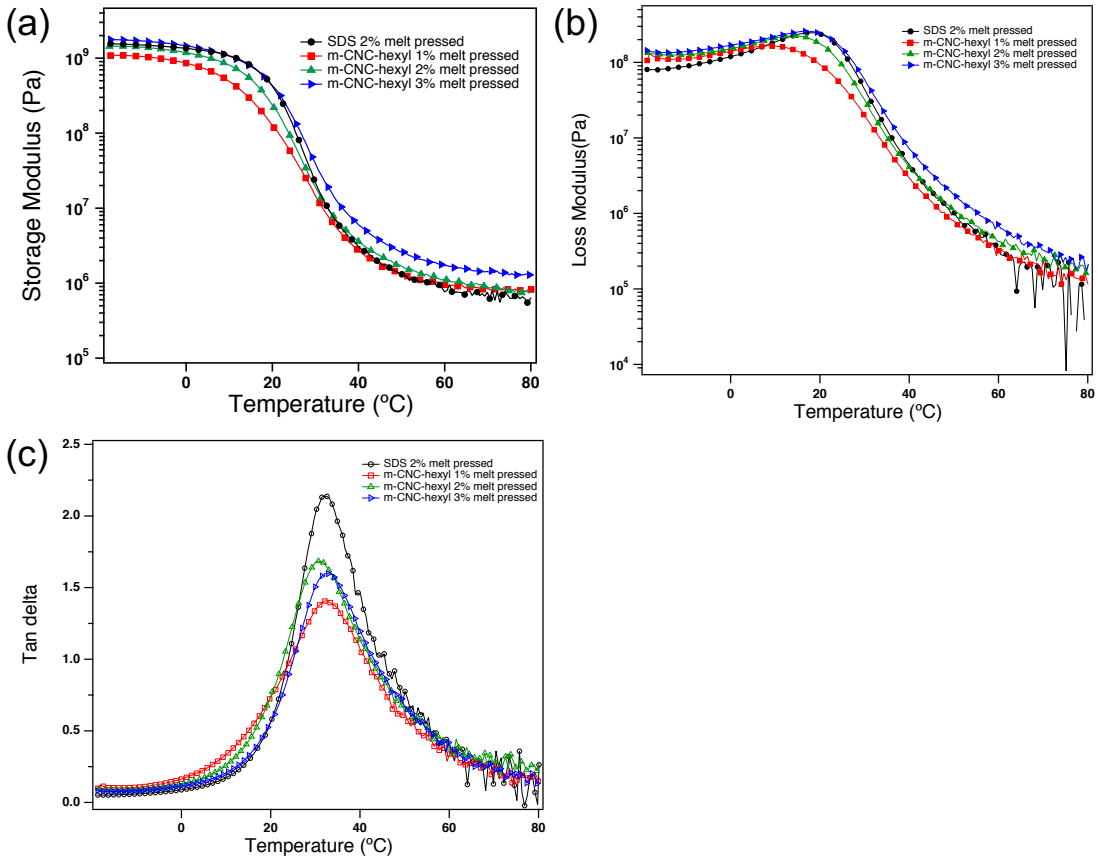

Figure A3.9 DMA temperature sweep study of the a) storage modulus (*E*'), b) loss modulus (*E*'') and c) tan δ of the latex composite films stabilized with SDS or m-CNC-hexyl-COOH after melt.

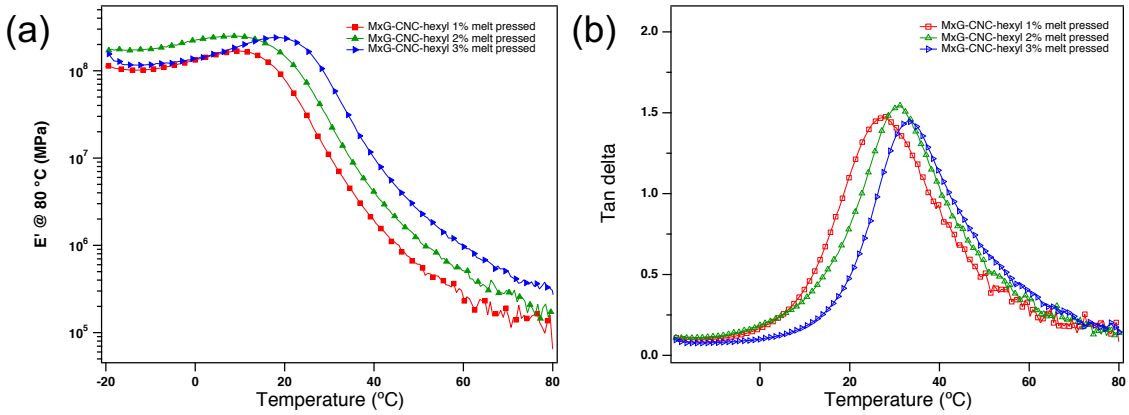

Figure A3.10 DMA temperature sweep study of the a) loss modulus (*E*'') and b) tan δ of the latex composite films stabilized with MxG-CNC-hexyl-COOH after melt pressing.

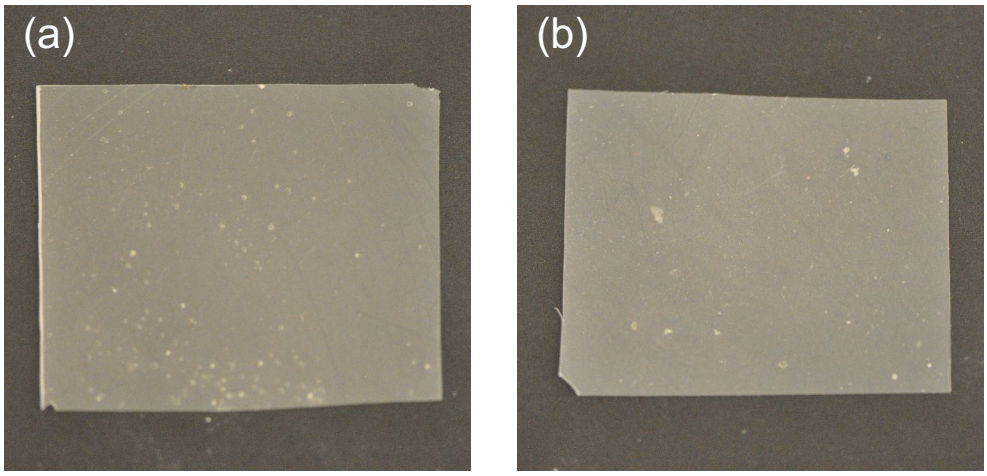

Figure A3.11 Latex composite films containing 13 wt.% (10wt% CNC-COOH and 3 wt.% CNC-hexyl-COOH) of a) m-CNC and b) MxG-CNCs.

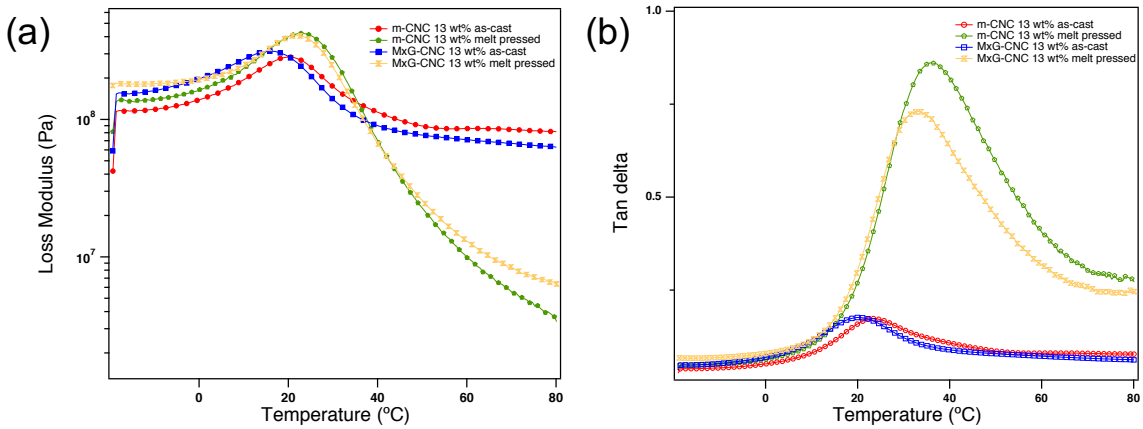

Figure A3.12 DMA temperature sweep study of a) loss modulus (E'') and b) tan δ of the composite films containing 13 wt.% (10wt% CNC-COOH and 3 wt.% CNC-hexyl-COOH) m-CNC and MxG.

3.7 Reference

(1) DeFusco, A. J.; Sehgal, K. C.; Bassett, D. R. Overview of Uses of Polymer Latexes. In *Polymeric Dispersions: Principles and Applications*; Springer Netherlands: Dordrecht, 1997; pp 379–396.

(2) Steward, P. A.; Hearn, J.; Wilkinson, M. C. Overview of Polymer Latex Film Formation and Properties. *Adv. Colloid Interface Sci.* **2000**, *86* (3), 195–267.

(3) Winnik, M. A. Latex Film Formation. *Curr. Opin. Colloid Interface Sci.* **1997**, *2* (2), 192–199.

(4) Xiong, M.; Wu, L.; Zhou, S.; You, B. Preparation and Characterization of Acrylic Latex/Nano-SiO2 Composites. *Polym. Int.* **2002**, *51* (8), 693–698.

(5) Kaboorani, A.; Riedl, B. Nano-Aluminum Oxide as a Reinforcing Material for Thermoplastic Adhesives. *J. Ind. Eng. Chem.* **2012**, *18* (3), 1076–1081.

(6) Zhou, S.; Wu, L.; Xiong, M.; He, Q.; Chen, G. Dispersion and UV-VIS Properties of Nanoparticles in Coatings. *J. Dispers. Sci. Technol.* **2005**, *25* (4), 417–433.

(7) Xiong, M.; Gu, G.; You, B.; Wu, L. Preparation and Characterization of Poly(Styrene Butylacrylate) Latex/Nano-ZnO Nanocomposites. *J. Appl. Polym. Sci.* **2003**, *90* (7), 1923–

(8) Kajtna, J.; Šebenik, U. Microsphere Pressure Sensitive Adhesives—Acrylic Polymer/Montmorillonite Clay Nanocomposite Materials. *Int. J. Adhes. Adhes.* **2009**, *29* (5), 543–550.

(9) Dufresne, A.; Paillet, M.; Putaux, J. L.; Canet, R.; Carmona, F.; Delhaes, P.; Cui, S. Processing and Characterization of Carbon Nanotube/Poly(Styrene-Co-Butyl Acrylate) Nanocomposites. *J. Mater. Sci.* **2002**, *37* (18), 3915–3923.

(10) Ouzas, A.; Niinivaara, E.; Cranston, E. D.; Dubé, M. A. In Situ Semibatch Emulsion Polymerization of 2-Ethyl Hexyl Acrylate/ n -Butyl Acrylate/Methyl Methacrylate/Cellulose Nanocrystal Nanocomposites for Adhesive Applications. *Macromol. React. Eng.* **2018**, *12* (3), 1700068.

(11) Mabrouk, A. Ben; Dufresne, A.; Boufi, S. Cellulose Nanocrystal as Ecofriendly Stabilizer for Emulsion Polymerization and Its Application for Waterborne Adhesive. *Carbohydr. Polym.* **2020**, *229*, 115504.

(12) Trovatti, E.; Oliveira, L.; Freire, C. S. R.; Silvestre, A. J. D.; Pascoal Neto, C.; Cruz Pinto, J. J. C.; Gandini, A. Novel Bacterial Cellulose–Acrylic Resin Nanocomposites. *Compos. Sci. Technol.* **2010**, *70* (7), 1148–1153.

(13) Pu, Y.; Zhang, J.; Elder, T.; Deng, Y.; Gatenholm, P.; Ragauskas, A. J. Investigation into Nanocellulosics versus Acacia Reinforced Acrylic Films. *Compos. Part B Eng.* **2007**, *38* (3), 360–366.

(14) Elmabrouk, A. Ben; Wim, T.; Dufresne, A.; Boufi, S. Preparation of Poly(Styrene- Co - Hexylacrylate)/Cellulose Whiskers Nanocomposites via Miniemulsion Polymerization. *J. Appl. Polym. Sci.* **2009**, *114* (5), 2946–2955.

(15) Dastjerdi, Z.; Cranston, E. D.; Berry, R.; Fraschini, C.; Dubé, M. A. Polymer Nanocomposites for Emulsion-Based Coatings and Adhesives. *Macromol. React. Eng.* **2019**, *13* (2), 1800050.

(16) Dufresne, A. Cellulose Nanomaterials as Green Nanoreinforcements for Polymer Nanocomposites. *Philos. Trans. R. Soc. A* **2018**, *376* (2112), 20170040.

(17) Moon, R. J.; Martini, A.; Nairn, J.; Simonsen, J.; Youngblood, J. Cellulose Nanomaterials Review: Structure, Properties and Nanocomposites. *Chem. Soc. Rev.* **2011**, *40* (7), 3941.

(18) Eichhorn, S. J.; Dufresne, A.; Aranguren, M.; Marcovich, N. E.; Capadona, J. R.; Rowan, S. J.; Weder, C.; Thielemans, W.; Roman, M.; Renneckar, S.; Gindl, W.; Veigel, S.; Keckes, J.; Yano, H.; Abe, K.; Nogi, M.; Nakagaito, A. N.; Mangalam, A.; Simonsen, J.; Benight, A. S.; Bismarck, A.; Berglund, L. A.; Peijs, T. Review: Current International Research into Cellulose Nanofibres and Nanocomposites. *J. Mater. Sci.* **2010**, *45* (1), 1–33.

(19) Habibi, Y.; Lucia, L. A.; Rojas, O. J. Cellulose Nanocrystals: Chemistry, Self-Assembly, and Applications. *Chem. Rev.* **2010**, *110* (6), 3479–3500.

(20) Capadona, J. R.; Shanmuganathan, K.; Tyler, D. J.; Rowan, S. J.; Weder, C. Stimuli-Responsive Polymer Nanocomposites Inspired by the Sea Cucumber Dermis. *Science (80-.).* **2008**, *319* (5868), 1370–1374.

(21) Dagnon, K. L.; Shanmuganathan, K.; Weder, C.; Rowan, S. J. Water-Triggered Modulus Changes of Cellulose Nanofiber Nanocomposites with Hydrophobic Polymer Matrices. *Macromolecules* **2012**, *45* (11), 4707–4715.

(22) Shanmuganathan, K.; Capadona, J. R.; Rowan, S. J.; Weder, C. Biomimetic Mechanically Adaptive Nanocomposites. *Prog. Polym. Sci.* **2010**, *35* (1–2), 212–222.

(23) Jorfi, M.; Roberts, M. N.; Foster, E. J.; Weder, C. Physiologically Responsive, Mechanically Adaptive Bio-Nanocomposites for Biomedical Applications. *ACS Appl. Mater. Interfaces* **2013**, *5* (4), 1517–1526.

(24) Kargarzadeh, H.; Mariano, M.; Huang, J.; Lin, N.; Ahmad, I.; Dufresne, A.; Thomas, S. Recent Developments on Nanocellulose Reinforced Polymer Nanocomposites: A Review. *Polymer*. Elsevier Ltd December 6, 2017, pp 368–393.

(25) Calvino, C.; Macke, N.; Kato, R.; Rowan, S. J. Development, Processing and Applications of Bio-Sourced Cellulose Nanocrystal Composites. *Prog. Polym. Sci.* **2020**, 101221.

(26) Favier, V.; Canova, G. R.; Cavaillé, J. Y.; Chanzy, H.; Dufresne, A.; Gauthier, C. Nanocomposite Materials from Latex and Cellulose Whiskers. *Polym. Adv. Technol.* **1995**, *6* (5), 351–355.

(27) Favier, V.; Chanzy, H.; Cavaillé, J. Y. Polymer Nanocomposites Reinforced by Cellulose Whiskers. *Macromolecules* **1995**, *28* (18), 6365–6367.

(28) Favier, V.; Cavaille, J. Y.; Canova, G. R.; Shrivastava, S. C. Mechanical Percolation in Cellulose Whisker Nanocomposites. *Polym. Eng. Sci.* **1997**, *37* (10), 1732–1739.

(29) Hajji, P.; Cavaillé, J. Y.; Favier, V.; Gauthier, C.; Vigier, G. Tensile Behavior of Nanocomposites from Latex and Cellulose Whiskers. *Polym. Compos.* **1996**, *17* (4), 612–619.

(30) Helbert, W.; Cavaillé, J. Y.; Dufresne, A. Thermoplastic Nanocomposites Filled with Wheat Straw Cellulose Whiskers. Part I: Processing and Mechanical Behavior. *Polym. Compos.* **1996**, *17* (4), 604–611.

(31) Dufresne, A.; Cavaillé, J.-Y.; Helbert, W. Thermoplastic Nanocomposites Filled with Wheat Straw Cellulose Whiskers. Part II: Effect of Processing and Modeling. *Polym. Compos.* **1997**, *18* (2), 198–210.

(32) Dubief, D.; Samain, E.; Dufresne, A. Polysaccharide Microcrystals Reinforced Amorphous Poly(β-Hydroxyoctanoate) Nanocomposite Materials. *Macromolecules* **1999**, *32* (18), 5765–5771.

(33) Annamalai, P. K.; Dagnon, K. L.; Monemian, S.; Foster, E. J.; Rowan, S. J.; Weder, C. Water-Responsive Mechanically Adaptive Nanocomposites Based on Styrene–Butadiene Rubber and Cellulose Nanocrystals—Processing Matters. *ACS Appl. Mater. Interfaces* **2014**, *6* (2), 967–976.

(34) Tkalya, E.; Ghislandi, M.; Thielemans, W.; Van Der Schoot, P.; De With, G.; Koning, C. Cellulose Nanowhiskers Templating in Conductive Polymer Nanocomposites Reduces Electrical Percolation Threshold 5-Fold. *ACS Macro Lett.* **2013**, *2* (2), 157–163.

(35) Limousin, E.; Rafaniello, I.; Schäfer, T.; Ballard, N.; Asua, J. M. Linking Film Structure and Mechanical Properties in Nanocomposite Films Formed from Dispersions of Cellulose Nanocrystals and Acrylic Latexes. *Langmuir* **2020**, *36* (8), 2052–2062.

(36) KEDDIE, J. Film Formation of Latex. *Mater. Sci. Eng. R Reports* **1997**, *21* (3), 101–170.

(37) Gundabala, V. R.; Lei, C.; Ouzineb, K.; Dupont, O.; Keddie, J. L.; F. Routh, A. Lateral Surface Nonuniformities in Drying Latex Films. *AIChE J.* **2008**, *54* (12), 3092–3105.

(38) Yang, Y.-K.; Li, H.; Wang, F. Studies on the Water Resistance of Acrylic Emulsion Pressure-Sensitive Adhesives (PSAs). *J. Adhes. Sci. Technol.* **2003**, *17* (13), 1741–1750.

(39) Limousin, E.; Ballard, N.; Asua, J. M. Synthesis of Cellulose Nanocrystal Armored Latex Particles for Mechanically Strong Nanocomposite Films. *Polym. Chem.* **2019**, *10* (14), 1823–1831.

(40) Errezma, M.; Mabrouk, A. Ben; Magnin, A.; Dufresne, A.; Boufi, S. Surfactant-Free Emulsion Pickering Polymerization Stabilized by Aldehyde-Functionalized Cellulose Nanocrystals. *Carbohydr. Polym.* **2018**, *202* (September), 621–630.

(41) Kalashnikova, I.; Bizot, H.; Cathala, B.; Capron, I. New Pickering Emulsions Stabilized by Bacterial Cellulose Nanocrystals. *Langmuir* **2011**, *27* (12), 7471–7479.

(42) Kalashnikova, I.; Bizot, H.; Bertoncini, P.; Cathala, B.; Capron, I. Cellulosic Nanorods of Various Aspect Ratios for Oil in Water Pickering Emulsions. *Soft Matter* **2013**, *9* (3), 952–959.

(43) Kalashnikova, I.; Bizot, H.; Cathala, B.; Capron, I. Modulation of Cellulose Nanocrystals Amphiphilic Properties to Stabilize Oil/Water Interface. *Biomacromolecules* **2012**, *13* (1), 267–275.

(44) Tang, J.; Lin, N.; Zhang, Z.; Pan, C.; Yu, G. Nanopolysaccharides in Emulsion Stabilization; Springer Singapore, 2019; pp 221–254.

(45) Jiménez Saelices, C.; Capron, I. Design of Pickering Micro- and Nanoemulsions Based on the Structural Characteristics of Nanocelluloses. *Biomacromolecules* **2018**, *19* (2), 460–469.

(46) Jiménez Saelices, C.; Save, M.; Capron, I. Synthesis of Latex Stabilized by Unmodified Cellulose Nanocrystals: The Effect of Monomers on Particle Size. *Polym. Chem.* **2019**, *10* (6), 727–737.

(47) Bai, L.; Lv, S.; Xiang, W.; Huan, S.; McClements, D. J.; Rojas, O. J. Oil-in-Water Pickering Emulsions via Microfluidization with Cellulose Nanocrystals: 1. Formation and Stability. *Food Hydrocoll.* **2019**, *96*, 699–708.

(48) Kedzior, S. A.; Marway, H. S.; Cranston, E. D. Tailoring Cellulose Nanocrystal and Surfactant Behavior in Miniemulsion Polymerization. *Macromolecules* **2017**, *50* (7), 2645–2655.

(49) Kedzior, S. A.; Kiriakou, M.; Niinivaara, E.; Dubé, M. A.; Fraschini, C.; Berry, R. M.; Cranston, E. D. Incorporating Cellulose Nanocrystals into the Core of Polymer Latex Particles via Polymer Grafting. *ACS Macro Lett.* **2018**, *7* (8), 990–996.

(50) Zhang, Y.; Karimkhani, V.; Makowski, B. T.; Samaranayake, G.; Rowan, S. J. Nanoemulsions and Nanolatexes Stabilized by Hydrophobically Functionalized Cellulose

Nanocrystals. *Macromolecules* **2017**, *50* (16), 6032–6042.

(51) Werner, A.; Schmitt, V.; Sèbe, G.; Héroguez, V. Synthesis of Surfactant-Free Micro-and Nanolatexes from Pickering Emulsions Stabilized by Acetylated Cellulose Nanocrystals. *Polym. Chem.* **2017**, *8* (39), 6064–6072.

(52) Tang, C.; Chen, Y.; Luo, J.; Low, M. Y.; Shi, Z.; Tang, J.; Zhang, Z.; Peng, B.; Tam, K. C. Pickering Emulsions Stabilized by Hydrophobically Modified Nanocellulose Containing Various Structural Characteristics. *Cellulose* **2019**, *26* (13–14), 7753–7767.

(53) Zhou, J.; Li, Y.; Li, H.; Yao, H. Cellulose Nanocrystals/Fluorinated Polyacrylate Soap-Free Emulsion Prepared via RAFT-Assisted Pickering Emulsion Polymerization. *Colloids Surfaces B Biointerfaces* **2019**, *177*, 321–328.

(54) Bertsch, P.; Fischer, P. Adsorption and Interfacial Structure of Nanocelluloses at Fluid Interfaces. *Adv. Colloid Interface Sci.* **2020**, *276*, 102089.

(55) Bai, L.; Greca, L. G.; Xiang, W.; Lehtonen, J.; Huan, S.; Nugroho, R. W. N.; Tardy, B. L.; Rojas, O. J. Adsorption and Assembly of Cellulosic and Lignin Colloids at Oil/Water Interfaces. *Langmuir* **2019**, *35* (3), 571–588.

(56) Bai, L.; Xiang, W.; Huan, S.; Rojas, O. J. Formulation and Stabilization of Concentrated Edible Oil-in-Water Emulsions Based on Electrostatic Complexes of a Food-Grade Cationic Surfactant (Ethyl Lauroyl Arginate) and Cellulose Nanocrystals. *Biomacromolecules* **2018**, *19* (5), 1674–1685.

(57) Nigmatullin, R.; Johns, M. A.; Muñoz-García, J. C.; Gabrielli, V.; Schmitt, J.; Angulo, J.; Khimyak, Y. Z.; Scott, J. L.; Edler, K. J.; Eichhorn, S. J. Hydrophobization of Cellulose Nanocrystals for Aqueous Colloidal Suspensions and Gels. *Biomacromolecules* **2020**, acs.biomac.9b01721.

(58) Dastjerdi, Z.; Cranston, E. D.; Dubé, M. A. Synthesis of Poly(n -Butyl Acrylate/Methyl Methacrylate)/CNC Latex Nanocomposites via In Situ Emulsion Polymerization. *Macromol. React. Eng.* **2017**, *11* (6), 1700013.

(59) Dastjerdi, Z.; Cranston, E. D.; Dubé, M. A. Pressure Sensitive Adhesive Property Modification Using Cellulose Nanocrystals. *Int. J. Adhes. Adhes.* **2018**, *81*, 36–42.

(60) Ben Mabrouk, A.; Kaddami, H.; Magnin, A.; Belgacem, M. N.; Dufresne, A.; Boufi, S. Preparation of Nanocomposite Dispersions Based on Cellulose Whiskers and Acrylic Copolymer by Miniemulsion Polymerization: Effect of the Silane Content. *Polym. Eng. Sci.* **2011**, *51* (1), 62–70.

(61) Haaj, S. B.; Thielemans, W.; Magnin, A.; Boufi, S. Starch Nanocrystal Stabilized Pickering Emulsion Polymerization for Nanocomposites with Improved Performance. *ACS Appl. Mater. Interfaces* **2014**, *6* (11), 8263–8273. https://doi.org/10.1021/am501077e.

(62) Cudjoe, E.; Hunsen, M.; Xue, Z.; Way, A. E.; Barrios, E.; Olson, R. A.; Hore, M. J. A.; Rowan, S. J. Miscanthus Giganteus: A Commercially Viable Sustainable Source of Cellulose Nanocrystals. *Carbohydr. Polym.* **2017**, *155*, 230–241.

(63) Kang, K.; Kan, C.; Du, Y.; Liu, D. Synthesis and Properties of Soap-Free Poly(Methyl Methacrylate-Ethyl Acrylate-Methacrylic Acid) Latex Particles Prepared by Seeded Emulsion Polymerization. *Eur. Polym. J.* **2005**, *41* (3), 439–445.

(64) Capadona, J. R.; Shanmuganathan, K.; Trittschuh, S.; Seidel, S.; Rowan, S. J.; Weder, C. Polymer Nanocomposites with Nanowhiskers Isolated from Microcrystalline Cellulose. *Biomacromolecules* **2009**, *10* (4), 712–716.

(65) Yang, H.; Zhang, Y.; Kato, R.; Rowan, S. J. Preparation of Cellulose Nanofibers from Miscanthus x. Giganteus by Ammonium Persulfate Oxidation. *Carbohydr. Polym.* **2019**, *212*, 30–39.

(66) Ouali, N.; Cavaille, J. Y.; Perez, J. Elastic, Viscoelastic and Plastic Behavior of Multiphase Polymer Blends. *Plast. Rubber Compos. Process. Appl.* **1991**, *16* (1), 55–60.

(67) González-Matheus, K.; Leal, G. P.; Asua, J. M. Film Formation from Pickering Stabilized Waterborne Polymer Dispersions. *Polymer (Guildf).* **2015**, *69* (1), 73–82.

(68) Negrete-Herrera, N.; Putaux, J.-L.; David, L.; Haas, F. De; Bourgeat-Lami, E. Polymer/Laponite Composite Latexes: Particle Morphology, Film Microstructure, and Properties. *Macromol. Rapid Commun.* **2007**, *28* (15), 1567–1573.

(69) Bai, L.; Xiang, W.; Huan, S.; Rojas, O. J. Formulation and Stabilization of Concentrated Edible Oil-in-Water Emulsions Based on Electrostatic Complexes of a Food-Grade Cationic Surfactant (Ethyl Lauroyl Arginate) and Cellulose Nanocrystals. *Biomacromolecules* **2018**, *19* (5), 1674–1685.

Chapter 4. Effect of Processing Conditions on the Mechanical Properties of Bio-inspired Mechanical Gradient Nanocomposites.*

4.1 Abstract

Photo-induced thiol-ene crosslinking of allyl-functionalized cellulose nanocrystal (CNC)/polymer nanocomposites allows access to films that mimic the water-enhanced mechanical gradient characteristics of the squid beak. These films are prepared by mixing the functionalized CNCs and polymer in a solvent before solution casting and drying. The photocrosslinking agents are then imbibed into the film before UV exposure. Reported herein are studies aimed at better understanding the effect of the film preparation procedure, film thickness and the conditions under which the UV treatment is carried out. It was found that when the film is heated at a temperature higher than its glass transition temperature (T_g) during the UV irradiation step there is a greater enhancement in the mechanical properties of the films, presumably on account of more efficient crosslinking between the CNC fillers. Moreover, composite films that were compression molded (at 90°C) before the imbibing step displayed lower mechanical properties compared to the as-cast films, which is attributed to phase separation of the CNC fillers and polymer matrix during this additional processing step. Finally, the film thickness was also found to be a critical factor that affects the degree of crosslinking. For example, thinner films (50 μm) displayed a higher wet modulus ca. 130 MPa compared to ca. 80 MPa for the thicker films (150 μm). Understanding the processing conditions allows access to a larger range of mechanical properties which is important for the design of new bio-inspired mechanical gradient nanocomposites.

* This chapter is adapted from: **Zhang, Y.**; Edelbrock, A. N.; Rowan, S. J. *Eur. Polym. J.* **2019**, *115*, 107–114

4.2 Introduction

The rapid development of modern technologies continues to push the demands for materials with improved properties and functionalities. When designing and fabricating high-performance synthetic materials, nature provides ample inspiration[1–5] and natural materials often demonstrate remarkable properties which distinguish them from their synthetic counterparts[6]. To obtain such properties, biological systems have optimized their complex hierarchical structures over multiple length scales[7–10]. One use of these hierarchical structures is to connect materials with different mechanical properties[11–14]. A squid's beak is an ideal example of how nature seamlessly bridges between the stiff tip of the beak (rostrum) and the soft foundation tissue (buccal) that spans 2 orders of magnitude in stiffness[15–17]. Squid beaks are composed of chitin fibers, water and matrix proteins that are chemically crosslinked, where both the relative concentration of each component as well as the degree of crosslinking varies spatially[17]. It is proposed that the hydrophobic, histidine-rich proteins (DgHBPs) form coacervate solutions that diffuse into the chitin-binding protein (DgCBPs) scaffold and induce crosslinking between histidine residues with both 4-methylcatechol and peptidyl catechol moieties (L-DOPA). Near the rostrum, a higher fraction of protein is found with a high crosslink density resulting in high stiffness and less hydration (~15 wt%). Inversely, the buccal region of the beak contains a lower amount of protein and fewer crosslinks yielding a softer material with significantly more water (~ 70 wt%). In dehydrated samples, the difference in modulus between the rostrum and buccal regions is only a factor of 2 times (5 to 10 GPa), indicating that water swelling is critical in defining the mechanical gradient of the squid beak. When hydrated, the chitin-rich soft base swells significantly, while the rostrum's highly-crosslinked network saturated with hydrophobic and H-bonding catechol moieties prevents

significant swelling. This produces an impressive mechanical gradient with a two order of magnitude increase in stiffness across the beak.

Adoption of nature's gradient strategies offers new and interesting ways to design synthetic mechanical gradient materials[2]. These materials can be used as a modulus buffer where stiff therapeutic implant devices are in immediate contact with soft biological tissues, such as glucose sensors for diabetics[18], osseointegrated prosthetic limbs for amputees[19], long term intravascular interfaces[20], as well as biocompatible intracortical microelectrodes[21–23]. There are a few prior studies published on bioinspired mechanical gradient materials. For example, previous reported approaches to lateral gradient materials have controlled the relative concentration of the stiff and soft components, e.g. with different PDMS elastomers[24] or cellulose nanofibrils/polymer mixtures, along the lateral direction of the films[25]. Alternatively, controlling the degree of alignment of carbon nanotubes (CNT), from well-aligned to random, along the films[26] also yields gradient materials. Finally, more akin the squid beak mechanism, gradient films have been developed by varying degree of crosslinking along the film e.g. using catechol-functionalized chitosan with iron oxide nanoparticles[27], chitosan fillers with L-dopa[28], or imidazole-containing polymers with metals ions[29]. Although these synthetic materials all showed mechanical contrasts, they lack facile control of a continuous transition in stiffness, suffer from a small range of mechanical contrast, and/or required special equipment or time-consuming steps to access.

In prior work, Rowan and Weder have developed mechanically dynamic polymer nanocomposites which were inspired by the stimuli-responsive behavior of the inner dermis of the sea cucumber[30]. By embedding cellulose nanocrystals (CNCs) in different polymer matrices, a series of polymer nanocomposites that exhibit water-responsive mechanically adaptable behavior were accessed[31–36]. CNCs are highly crystalline nanofibers, which are approximately 5 to 25 nm

in cross-section, and hundreds of nanometers to microns in length, depending on the biosource they are isolated from[37–41]. It has been proposed that when processed correctly CNCs can form a percolating network within the polymer matrix through strong hydrogen bonding interactions[42], which results in a significant enhancement of the mechanical properties of dry composites. Immersion of these nanocomposites into water allows the materials to switch from stiff to soft, on account of the disengagement of the CNC network (and presumably also reduction of CNC-matrix interactions, depending on the nature of the matrix) via competitive hydrogen bonding between the CNCs and water molecules. Another attractive feature of CNCs is that their surface properties can be tailored for different applications by functionalization of the surface hydroxyl groups[43–58].

Inspired by the squid beak model, previous studies have shown that selective photo-irradiation of an allyl-functionalized CNC/polymer (Poly(vinyl acetate), PVAc)) nanocomposite film embedded with a tetrathiol crosslinker (pentaerythritol tetrakis(3-mercaptopropionate), PTMP) and photoinitiator allow access to water-enhanced mechanical gradient materials (Scheme 4.1)[59]. By introducing crosslinkable functionalities onto the surface of the CNC nanofillers, the original hydrogen bonding interactions can be augmented with covalent crosslinks. The CNC-CNC interactions would then be permanently "switched on" and thus the degree of mechanical softening of the composite materials upon exposure to water could be greatly reduced. As a result formation of a permanent covalent CNC crosslinked network allows access to films with a wet modulus of over 100 MPa, relative to ca. 30 MPa for composites that only use the noncovalent interactions that are disrupted by the presence of water. Furthermore, by utilizing UV-initiated thiol-ene chemistry it was shown that the degree of swelling and the magnitude of the wet modulus (presumably by controlling the amount of crosslinking) could be controlled by irradiation time.

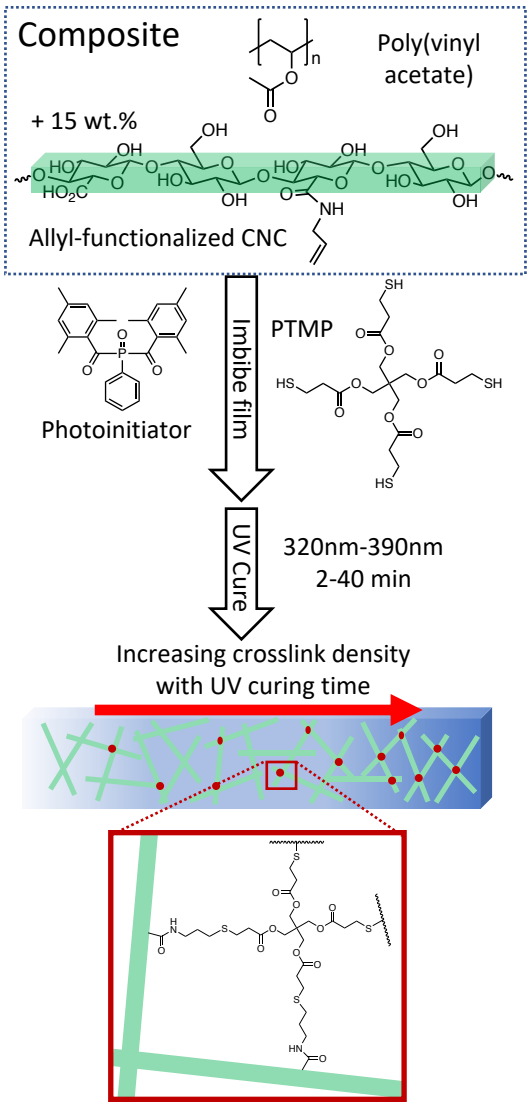

Scheme 4.1 Schematic of the procedure used to access the squid beak mimetic composites and the proposed photo-initiated thiol-ene crosslinking reaction of the CNC nanofillers.

Though polymer nanocomposites with a water-activated mechanical gradient have been successfully achieved, the level of mechanical contrast (E_{stiff}/E_{soft} ca. 5) is still relatively low compared to the mechanical gradient of the squid beak, which ranges from ca. 50 MPa to 5 GPa. Furthermore, during studies following this initial work, it was found that the final wet modulus of the films was very sensitive to a number of processing and film factors which lead to inconsistent results. Specifically, this includes the temperature of the film and the nature of the supporting

substrate during the UV curing step, as well as the how the uncured films are processed and their resulting thickness. The work reported herein was aimed at investigating some of these aspects in more detail with the goal of producing a more robust protocol.

4.3 Experimental Section

Materials

Cellulose nanocrystals were isolated from sea tunicates (*Styela Clava*) that were harvested from floating docks in Warwick Marina (Warwick, RI) and were cleaned and bleached following previously published procedures[34]. NaOCl was received from Alfa Aesar with 14.5% available chlorine. Poly(vinyl acetate) (PVAc) with weight–average molecular weight, M_w=100 000 g/mol, and all the other reagents were purchased from Sigma-Aldrich and used as received.

Synthesis of tCNC-COOH via TEMPO oxidation

Dry, bleached tunicate mantles were hydrolyzed using hydrochloric acid and then oxidized using TEMPO, NaBr and NaOCl to yield tCNC-COOH according to literature procedures[60]. The tCNC-COOHs were titrated using conductometric titration in order to determine the amount of surface carboxylic groups. Briefly, 25 mg of tCNC-COOH was dispersed in 80 ml of DI water by sonication overnight in a Branson CPX sonication bath. 15 µL of concentrated HCl (33 wt%) was added under stirring to drop the pH of the dispersion below 3 and the titration was performed using 0.01 M NaOH solution. The conductivity was plotted against the volume of NaOH consumed and the plateau region was used to determine the carboxylic acid group content.

Synthesis of allyl-functionalized CNCs (tCNC-allyl-COOH)

Allyl functionalization was performed using similar EDC and NHS peptide coupling methods used previously[50] with slight modifications (Scheme 4.2). Oxidized CNCs (200 mg, 0.2 mmol of carboxylic acid moieties) were dispersed in 40 mL of DMF and bath sonicated overnight. 1-Ethyl-3-(3-(dimethylamino)propyl) carbodiimide hydrochloride (EDC) (383.4 mg, 2 mmol, 10 equiv.) was added to the dispersion and the reaction was stirred for 5 min. Then *N*-hydroxysuccinimide (NHS) (230.2 mg, 2 mmol, 10 equiv.) was added and stirred for a further 30 min. Finally, allylamine (228.4 mg, 4 mmol, 20 equiv.) was slowly added and the reaction was allowed to stir for 16 hrs at room temperature. The resulting mixture was precipitated in excess methanol and then centrifuged at 10000 rpm for 10 min. The residual was washed with methanol (3X) and DI water (3X) under successive centrifugation. Functionalized CNCs were re-dispersed in DI water, dialyzed and lyophilized to yield tCNC-allyl-COOH. This ally functionalization was repeated again under the same conditions to enhance the degree of functionalization. The final product was titrated again to determine the residual mount of carboxylic acid groups, and the amount of allyl groups was calculated by the difference in the number of carboxylic acids groups before and after the reaction

Characterization of tCNC-COOH and tCNC-allyl-COOH

Atomic Force Microscopy (AFM). The dimensions of tCNC-COOHs and tCNC-alll-COOHs were measured by AFM. Aqueous suspensions of tCNC-COOHs and tCNC-allyl-COOHs with a concentration of 0.1 mg/mL were drop cast on freshly cleaved mica surface. The samples were imaged in scan assist mode using a Bruker Multimode 8 instrument equipped with a Nanoscope 5 controller. The length and thickness of the CNCs were analyzed using the height image by Gwyddion software.

X-ray Diffraction (XRD). The degree of crystallinity before and after allyl-functionalization was measured by XRD. Lyophilized samples were tightly packed inside plastic washers and were held in place between two pieces of Kapton tape. The XRD patterns were recorded using a SAXSLAB GANESHA 300 XL system with Cu Kα source (λ=0.154 nm) at a voltage of 40 kV and 40 mA power. The crystallinity index (C.I.) was calculated according to the following equation:

$$C.I. = \frac{I_{200} - I_{AM}}{I_{200}} \times 100\% \quad (1)$$

Where I_{200} is the intensity of the (200) reflection and I_{AM} is the intensity at 2θ=18°, corresponding to the minimum between the planes (200) and (110).

X-ray Photoelectron Spectroscopy (XPS). The XPS data were collected using the AXIS Nova spectrometer equipped with a monochromatic Al Kα X-ray source. The Al anode was powered at 10 mA and 15 kV. Instrument base pressure was ca. 1×10^{-10} Torr. For calibration purposes, the binding energies were referenced to C-C/C-H peak in the C 1s signal at 285.0 eV. Lyophilized tCNC-COOH and tCNC-allyl-COOH samples were pressed into pallets and adhered to conductive carbon tape before loading into the instrument.

Elemental Analysis. tCNC-COOH and tCNC-allyl-COOH were wash with 0.1 M HCl to protonate all the carboxylic groups. The samples were then lyophilized, and the carbon, hydrogen and nitrogen contents were measured at Midwest Microlab (Indianapolis, Indiana, USA).

Fabrication of CNC/PVAc nanocomposites

PVAc was dissolved in DMF (50 mg/mL) by stirring for 4 hrs, while tCNC-allyl-COOH was homogeneously dispersed in DMF (3 mg/mL) by ultrasonication. The nanocomposite mixture was prepared by mixing appropriate amounts of the PVAc solution and CNC dispersion and ultrasonicating for 30 min before casting into PTFE dishes. The samples were heated at 60 °C in

a vacuum oven for 5 days to fully remove the DMF. The amount of CNC in the final nanocomposites was set at 15 wt% in this study. Thermogravimetric analysis (TGA) was used to confirm the removal of DMF. The dried nanocomposite films were removed from the PTFE dishes and either used as-cast or were compression molded at 90 °C at 4000 psi for 10 min to yield 150 μm thick films. In the case of the as-cast films, the thickness was controlled by adjusting the amount of CNC/PVAc solutions that were cast into the PTFE dish (diameter 10 cm).

Imbibing Process

The imbibing procedures were adapted from previously published methods with minor modification[59]. CNC/PVAc nanocomposites were cut into rectangular strips with an approximate dimension of 30 mm by 4 mm. Stock solutions of the photoinitiator (Phenylbis(2,4,6-trimethylbenzoyl)phosphie oxide) (2 mM) and crosslinker (pentaerythritol tetrakis(3-mercaptopropionate), PTMP) (10 mM) were prepared by dissolving the reagents in DCM. Then each strip was weighed individually to calculate the amount of allyl groups within the strip based on weight fraction of CNCs and the amount of allyl functionalities on the CNC surface. The required amount of stock solution of photoinitiator (5 mol% of ally groups) and crosslinker (25 mol% of ally groups) were mixed. The imbibing was performed by slowly pipetting the initiator and crosslinker co-solution onto the composite strips until the solution was absorbed. The imbibed films were then placed on PTFE dishes and annealed in a desiccator filled with saturated DCM vapor for 24 hrs in a dark environment. The goal of the solvent annealing step is to ensure a more homogeneous distribution of the photoinitiator and crosslinker within the film. Finally, the strips were dried under reduced pressure at room temperature for 24 hrs to remove any residual DCM. TGA was used to confirm the complete removal of DCM.

Photo-crosslinking procedure

The nanocomposite films were irradiated with a 320-390nm UV light using a Honle Bluepoint UV source at an intensity of 60 mW/cm^2 for different times ranging from 2 to 40 min. During the irradiation procedure the films were supported on different substrates, including an aluminum block, foam block or hot plate. All films were turned over at the midpoint of the exposure time to make sure both sides were exposed with the same amount of UV light. All the films were subsequently soaked in 2-propanol for 2 hrs after irradiation to remove any unreacted crosslinkers. This washing step was repeated twice with fresh 2-propanol before the films were dried in vacuum oven for 24 hrs at room temperature and 48 hrs at 40 °C, respectively.

Water Swelling of Nanocomposites

All films were first weighed to obtain the dry mass after removal from the oven. The films were then placed in vials filled with DI water, and the vials were placed in a temperature-controlled water bath at 37 °C. After 18 hrs the films were removed, gently blotted using filter paper and weighed to obtain the wet mass. The degree of swelling was calculated by:

$$\%\, Swelling = \frac{Wet\ mass - Dry\ mass}{Dry\ mass} \times 100 \qquad (2)$$

Dynamic mechanical analysis (DMA) characterization of nanocomposites

The viscoelastic properties of nanocomposites were analyzed using a RSA-G2 solid analyzer (TA Instrument, DE) equipped with a tension clamp and submersion chamber allowing the measurements to be conducted while the films were immersed in water. The wet modulus of the samples was analyzed using a temperature sweep method from 18 °C to 45 °C at a heating rate of

3 °C /min, with a fixed frequency of 1 Hz and a strain of 0.1%. For characterizing the dry modulus of composite films, only the tension camp was used and the same test procedure was used except for the temperature, which was varied from 0 °C to 90 °C. All the tests were performed in triplicate and the standard deviations were plotted as error bars.

4.4 Results and Discussion

4.4.1 Fabrication of bio-inspired nanocomposites with allyl-functionalized CNCs.

To access allyl-functionalized CNCs, CNCs were first isolated from tunicate mantles using hydrochloric acid hydrolysis. TEMPO mediated oxidation was subsequently performed to oxidize some of the primary OH groups into carboxylic acid moieties. Conductometric titrations on these oxidized CNCs show a carboxylic acid density of 1000 mmol/kg (tCNC-$COOH_{1000}$, where the subscript is the functional group density in mmol/kg). The tCNC-$COOH_{1000}$ were then functionalized with allylamine using standard peptide coupling chemistry (Scheme 4.2). The functionalized CNCs showed a residual carboxylic acid density of 200 mmol/kg as measured by conductometric titration, suggesting that 800 mmol/kg of the carboxylic acid groups were functionalized with allylamine (tCNC-$allyl_{800}$-$COOH_{200}$). FTIR studies of tCNC-$COOH_{1000}$ show a characteristic peak at 1600 cm^{-1} which is associated with the carboxylate moieties. The formation of the amide bond in tCNC-$allyl_{800}$-$COOH_{200}$ is confirmed by the appearance of a new carbonyl peak at 1650 cm^{-1}, while the peak at 1600 cm^{-1} is associated with the residual carboxylate moieties (Figure A4.1). Further verification of the functionalization of the CNCs was obtained by XPS and elemental analysis. XPS spectra of the tCNC-$allyl_{800}$-$COOH_{200}$ sample (Figure A4.2a) shows a signal corresponding to nitrogen (N 1s: 402 eV). Furthermore, after fitting the high-resolution XPS spectra of the C 1s signal using the peak positions reported by Lin and Dufresne that utilized the

same EDC-NHS chemistry[61], a characteristic C-N (286.2 eV) peak is present in the tCNC-allyl$_{800}$-COOH$_{200}$ sample but not in the tCNC-COOH$_{1000}$ starting material (Figure A4.2b and c). Taken together with the elemental analysis results (Table A4.1 in Appendix), which shows a nitrogen content of 0.6% for tCNC-allyl$_{800}$-COOH$_{200,}$ the data is consistent with the successful reaction of allylamine onto the surface of CNCs. The average dimensions of the crystals before and after functionalization were measured using AFM height images (Figure A4.3). The tCNC-COOH$_{1000}$s were found to have an average length of 1186 ± 643 nm and height of 10.2 ± 2.4 nm. The tCNC-allyl$_{800}$-COOH$_{200}$s showed similar dimensions (length 985 ± 454 nm and height 10.3 ± 1.9 nm) confirming that the functionalization did not significantly impact the size of the CNCs and that the tCNC-allyl$_{800}$-COOH200s maintained an aspect ratio of ca. 100. The changes in crystallinity before and after allyl-functionalization were measured by XRD (Figure A4.4). The crystallinity index (C.I.) only changes slightly, from ca. 95.5% to 94% for tCNC-COOH$_{1000}$ and tCNC-allyl$_{800}$-COOH$_{200}$ respectively, confirming the integrity of the cellulose nanocrystals after functionalization.

In the prior studies the effect of irradiation time and the amount of allyl-functionalized CNCs embedded in a poly(vinyl acetate) (PVAc) matrix on the mechanical properties of these photo-crosslinkable nanocomposites was studied[59]. In this work, PVAc nanocomposites containing 15wt% of tCNC-allyl-COOH were prepared in order to study the effect that UV irradiation curing conditions, film processing conditions, as well as film thickness, have on the mechanical properties of the crosslinked composite films. All nanocomposites were fabricated by mixing an appropriate amount of a tCNC-allyl$_{800}$-COOH$_{200}$ dispersion in DMF and a PVAc DMF solution followed by casting and drying in a vacuum oven.

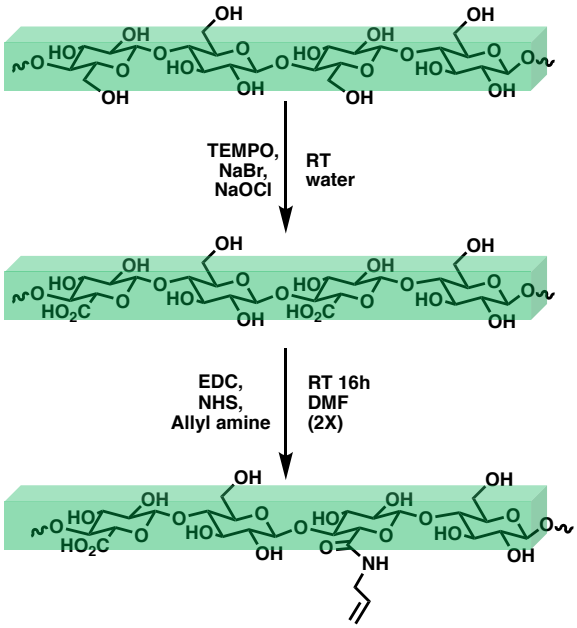

Scheme 4.2 Chemistry used to access the allyl-functionalized CNCs.

4.4.2 Effect of UV irradiation conditions

In order to more precisely control the thickness of the films the dried composites were first compression molded (at 90°C) into a smooth and clear film with thickness around 150 μm, and then imbibed with the photoinitiator and the pentaerythritol tetrakis(3-mercaptopropionate) (PTMP) crosslinker at a 20:20:1 molar ratio of alkene:thiol groups:initiator. The films were then irradiated with UV light (intensity 60 mW/cm^2) for different times ranging from 2 to 40 mins in order to initiate the thiol-ene reaction. It is important to note that the relatively high-intensity UV source can generate heat during the UV irradiation step. Given that the dry composite films have a T_g at ca. 50 °C, as can be seen from the peak of tan δ on the DMA curves (Figure A4.5), it is reasonable to expect that such heating may have an effect on the amount of curing. Thus, initial studies focused on reducing the effect the UV light induced heat by supporting the composite film on an aluminum block which acts as a heat sink to aid dissipation of any heat generated by the UV light. Films were irradiated for varying time periods up to 40 min (20 min each side). After washing

with 2-propanol to remove any residual crosslinker/photoinitiator and drying in a vacuum oven, all films were immersed in water and mechanical testing was conducted on the water swollen films (wet state) after they reached equilibrium swelling. Figure 4.1a shows the temperature dependency of the storage modulus (E') of the nanocomposites films as measured by DMA temperature sweep studies. The wet storage modulus (E') shows a transition at ca. 22 °C for all samples which is attributed to the glass transition temperature (T_g) of the PVAc matrix. It should be noted that the T_g of dry PVAc polymer is around 50 °C, but in the wet state water acts as a plasticizer decreasing the T_g of the polymer matrix. The storage modulus (E') at a temperature higher than T_g (37 °C) was used to evaluate the wet mechanical properties of the films after different UV exposure times. Data in Figure 4.1a shows that the E' increased from 10 MPa for un-irradiated sample to 22 MPa for samples irradiated for 40 min. However, based on the prior work on the 15 wt% tCNC-allyl-COOH/PVAc nanocomposites which showed a wet modulus above 100 MPa, the level of mechanical reinforcement observed in Figure 4.1a was relatively low, presumably on account of a limited degree of covalent crosslinking of the CNC fillers.

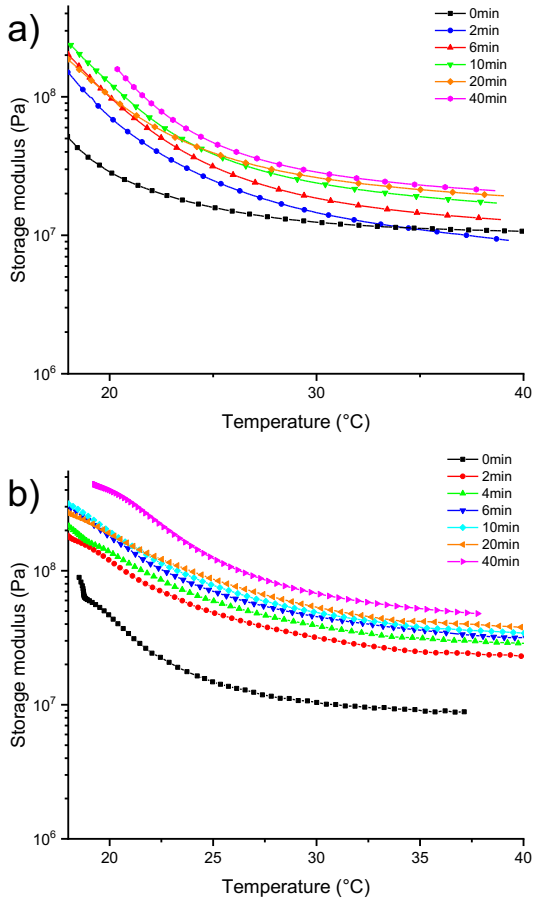

Figure 4.1 Representative DMA temperature sweeps of wet 15wt% tCNC-allyl$_{800}$-COOH$_{200}$/PVAc nanocomposites irradiated on a) aluminum block (heat sink) and b) hotplate set at 60 °C.

One possible reason for this observation is that the UV-initiated thiol-ene reaction is too slow in the bulk film at temperatures lower than the T_g of PVAc polymer matrix (50 °C), on account of the reagents being locally trapped in the glassy polymer matrix. To test this hypothesis, a series of UV curing experiments were carried out under three different conditions: 1) the films were supported on a non-thermally conducting substrate (foam block); 2) the films were pre-swollen with water to lower the T_g of the polymer to around room temperature (22 °C) before being irradiated with UV; and 3) the films were placed on a hot plate set to 60 °C. Figure 4.2a shows the

comparison of wet E' at 37 °C for samples irradiated for 40 min using different conditions. There is no significant difference in the E' (23-25 MPa) of the films supported on either a thermal conducting aluminum substrate or a non-thermal conducting foam substrate, suggesting that under these specific experimental conditions the heat generated by the UV source is not enough to warm up the films to above their T_g. In the case of the water-swollen samples, the temperature at which they are irradiated with UV is now very close to the T_g of the polymer matrix, and as a result, the E' of the crosslinked film increases to 30 MPa. However, the biggest increase in mechanical reinforcement was observed for films supported on the hot plate set to a temperature (60°C) higher than the T_g of the polymer matrix. The wet modulus increased from 10 MPa before irradiation to 50 MPa after irradiating for 40 min (Figure 4.1b). This could be explained by the increase in chain mobility facilitating the diffusion of reagents and resulting in a higher level of crosslinking. A comparison of the E' at 37 °C versus irradiation times for films supported on aluminum or on a 60°C hotplate is shown in Figure 4.2b, which clearly shows that the kinetics of the thiol-ene crosslinking reaction had been improved by heating the films above their T_g during UV irradiation. As a result, the mechanical contrast is significantly improved from E'_{stiff}/E'_{soft} ca. 2 to E'_{stiff}/E'_{soft} ca. 5.

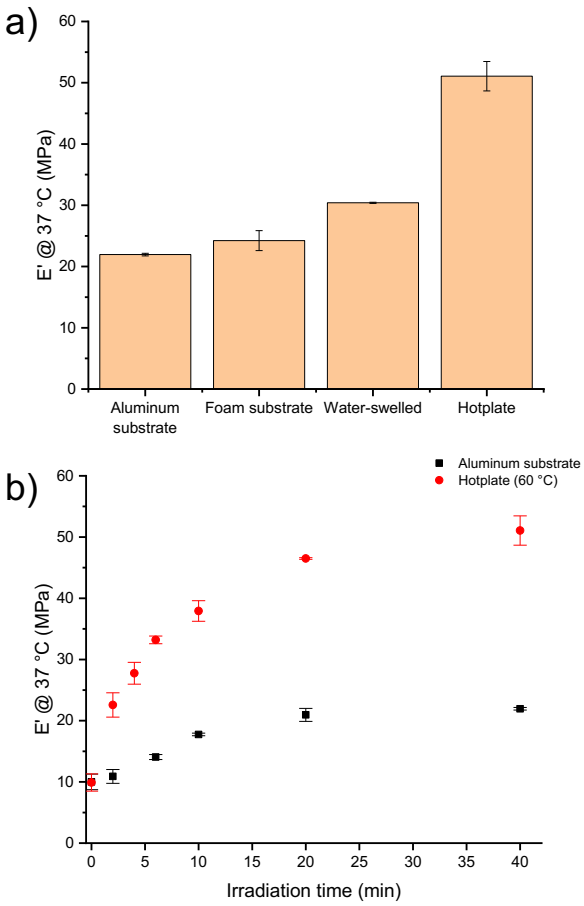

Figure 4.2 Comparison of the wet storage modulus (*E'*) at 37 °C of a) the composite films irradiated for 40 min under different conditions and b) composite films supported on an aluminum substrate or hotplate (at 60 °C) and irradiated for different times ranging from 2-40 min.

4.4.3 Effect of film processing condition

The above studies used tCNC-allyl-COOH/PVAc nanocomposite films that were compression molded before UV curing. Interestingly, while the films appeared smooth and optically clear after melt processing (Figure A4.6), when the films were immersed in water the films appeared slightly inhomogeneous (Figure A4.7). It has been shown that melt processing of CNC composites can induce some phase segregation, and this certainly would be expected to have a negative impact on the mechanical reinforcement of the CNC filler[62] as well as the ability of the light to penetrate

evenly through the wet film. Thus, a new batch of composite films were prepared and were used as-cast (after the films were dried in the vacuum oven) without any compression molding/melt processing. Upon exposure to water, the as-cast films showed more homogeneous swelling relative to the melt processed films (Figure A4.7). Therefore, it is important to study how the different film processing method impacts the mechanical reinforcement of these bio-inspired nanocomposites. It should be noted that the as-cast films should be carefully prepared to ensure they are free of any defects or bubbles, and that the film thickness can be controlled by varying the amount of materials added into the PTFE dish.

As-cast films with a thickness of approximately 150 μm (which matches the thickness of the melt-processed films) were imbibed using the same method as mentioned above. The samples were then placed on a hot plate set at 60 °C and irradiated with UV light at an intensity of 60 mW/cm^2 for times ranging from 2 to 40 mins. As was seen in the prior studies, DMA temperature studies of these films in the wet state (Figure 4.3a) confirm that there is an increase in the wet storage modulus (E') upon UV crosslinking. However, these as-cast crosslinked films show a higher magnitude of mechanical reinforcement relative to the melt-processed films (Figure 4.3b), suggesting that there is an overall improvement in the degree of covalent crosslinking with the more homogeneous as-cast films. It is also important to point out that the degree of crosslinking could be well-controlled by varying the UV irradiation time resulting in a wet E' ranging between ca. 15 MPa and 80 MPa for the least and most crosslinked sample respectively. As hypothesized above, the inhomogeneity after melt processing should not only disrupt the CNC filler network, but could also limit the amount of UV that can penetrate through the film. One way to test this effect is to measure how the UV intensity changes as it passes through the different films. Results showed that the intensity (preset to 60 mW/cm^2) decreased to 45.2 ± 0.8 mW/cm^2 after penetrating

through as-cast films, whereas it dropped to 21.3 ± 0.7 mW/cm^2 for melt-processed films. Considering both films have similar thickness (approximately 150 µm), the results suggest that the inhomogeneity of melt processed films does indeed block more UV light which, in turn, presumably contributes to a lower degree of crosslinking.

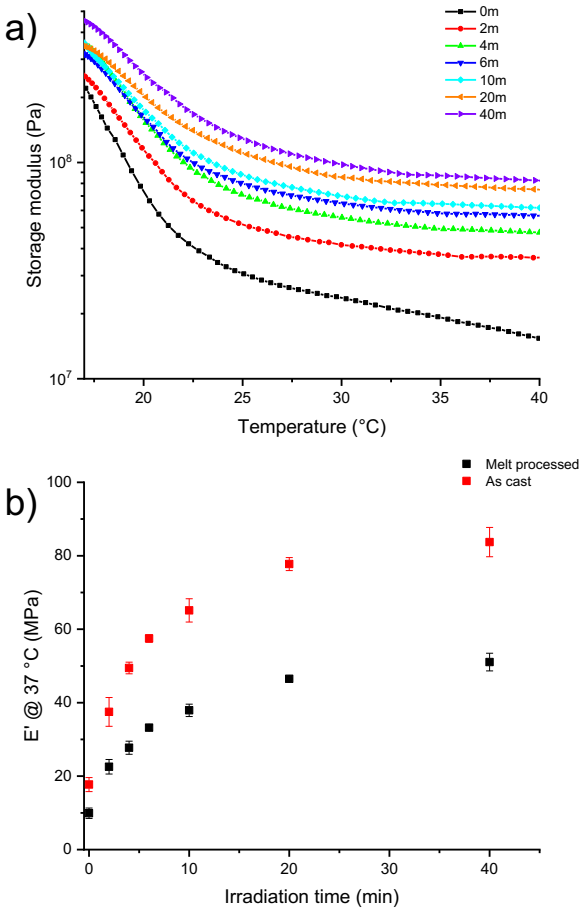

Figure 4.3 a) Representative DMA temperature sweeps of wet as-cast composite films before and after UV irradiation. b) Comparison of the wet storage modulus (E') of melt-processed films (approximately 150 µm) and as-cast films (approximately 150 µm) at 37 °C plotted against irradiation times.

It can be expected that as the degree of crosslinking increases then there should be a decrease in the degree of water swelling. Therefore, the water uptake of both the melt-pressed films and as-cast films after crosslinking were measured, and the equilibrium swelling data versus irradiation time were plotted in Figure 4.4. As expected, the degree of swelling decreased from 60% to 24% after exposure of the as-cast films to UV irradiation, which is much lower than the degree of swelling observed in the cured melt-pressed films (50%), further supporting the fact that a higher degree of crosslinking is observed in the as-cast films. The viscoelastic properties of the crosslinked melt-pressed film and as-cast film in the dry state were also studied (Figure A4.8 Figure A4.9). As expected, unlike the wet films, the storage modulus of the dry films at temperatures higher than T_g of the matrix show only a slight relative increase after covalent crosslinking. Interestingly, comparison of the dry state E' for the as-cast and melt-processed crosslinked films (ca. 730 MPa vs. ca. 520 MPa, respectively) shows that the as-cast film exhibits a higher plateau modulus. Since the dry modulus above the T_g is significantly impacted by the percolating CNC network, this result is also consistent with melt processing resulting in some disruption of the CNC network.

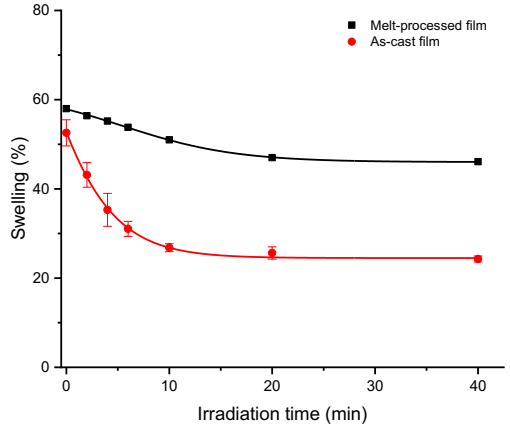

Figure 4.4 Equilibrium swelling data versus irradiation time of 150 μm thick melt-processed and as-cast films.

4.4.4 Effect of film thickness

A key aspect of any photocuring process is the ability of the light to penetrate through the film. In fact, if these films are only irradiated on one side they curl when exposed to water, presumably on account of different degrees of water swelling of the top and bottom surfaces. This can be explained by the limited penetration of the UV light through the composite film resulting in an uneven distribution of crosslinking across the film thickness. The hypothesis is further backed up by measuring the intensity of the UV light that penetrates through the composite films (Figure 4.5), which clearly shows a drop in penetrating UV intensity with increasing composite film thickness. It is worthy of note that a similar study on neat PVAc films (without any CNCs) shows little-to-no effect on UV light penetration irrespective of the film thickness studied (intensity only decrease from 60 mW/cm^2 to 58.3 ± 0.1 mW/cm^2 going from ca. 50 – 150 μm). This suggests that the decrease in UV intensity for the as cast composite films can be attributed to the scattering of UV light by the CNCs. As such, even though the above films are irradiated on both sides, the limited UV penetration depth could still lead to an uneven distribution of crosslinking between the composite film's surface and center. Such an effect should be more pronounced in thicker films. As the original work was carried out on ca. 60 μm films[59] and the above work focused on much thicker 150 μm films, it is important to understand the effect that film thickness has on the wet mechanical properties of the crosslinked materials.

To this end, composite films with approximate thickness of 50 μm, 75 μm and 100 μm were fabricated and used as-cast. These films were imbibed and crosslinked under the same conditions as the 150 μm films in the above study. All the films were then swollen in water, and their wet state storage modulus after irradiation with UV for 40 mins was measured by DMA. Figure 4.5

shows the wet state storage modulus of the films at 37 °C versus film thickness, clearly demonstrating that film thickness does have a significant impact on the wet mechanical properties of these crosslinked films. The wet storage modulus increases from ca. 80 MPa to ca. 130 MPa as the film thickness decreases from 150 μm to 50 μm. This is consistent with the hypothesis that under the same UV irradiation conditions thinner films form a more homogenous covalent crosslinking network through the thickness of the film relative to the thicker films, which in turn results in better overall mechanical properties of the wet films. Even so it is important to note that the 50 μm films are extremely delicate in the wet state making them difficult to handle which was why it was of interest to target the thicker films. The more homogenous networks within thinner films (50 μm) also result in a slight increase in the dry storage modulus (ca. 970 MPa compared with ca. 735 MPa for 150 μm films, Figure A4.10). It is also worthwhile pointing out that there is no significant difference in water swelling for these composite films at the different thickness (between 22%-24%, data not shown here), even though the wet E' show that thinner films have more homogenous crosslinking.

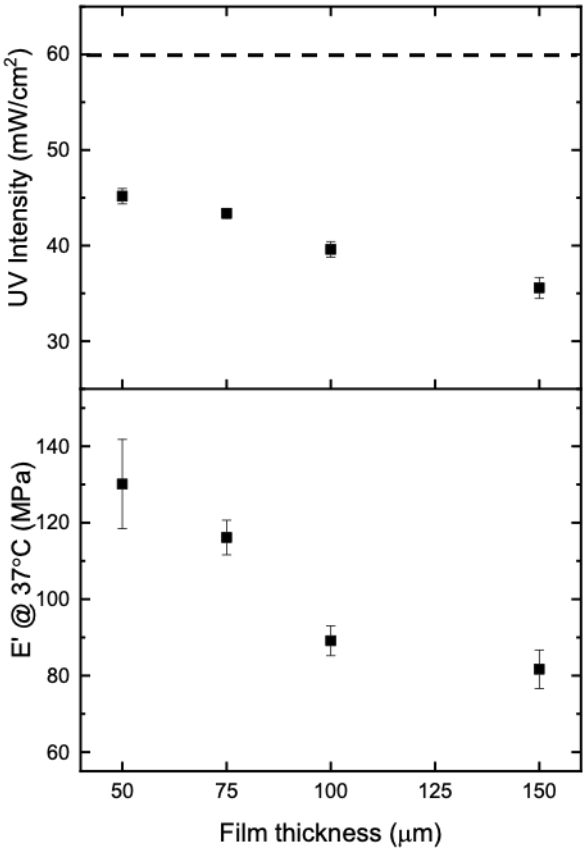

Figure 4.5 UV intensity measured after penetrating through as-cast composite films (contain 15wt% tCNC-allyl-COOH), and a comparison of the wet storage modulus (*E'*) at 37 °C after 40 min UV irradiation versus film thickness. Dash line indicates the original output UV intensity at 60 mW/cm^2.

4.5 Conclusion

Bio-inspired nanocomposites based on allyl-functionalized tunicate CNCs embedded in a PVAc matrix were prepared. The functionalized CNC fillers can be covalently crosslinked using UV initiated thiol-ene chemistry to yield composite films that show tunable mechanical properties upon swelling in water. In order to develop a more reproducible protocol for accessing these films the effects of UV crosslinking conditions, films processing conditions as well as film thickness on the resulting mechanical properties of the films were studied. These conditions were shown to have

a significant impact on the final mechanical properties of crosslinked films. The highest level of mechanical reinforcement in the wet state (E'= 130 MPa at 37 °C) was achieved by using 50 μm thick as-cast films, which were heated at 60 °C during UV irradiation. In these films a mechanical contrast (E'_{stiff}/E'_{soft}) > 7 of the wet films was observed which is slightly higher than observed in the original work (E'_{stiff}/E'_{soft} ca. 5)[59], indicating how the processing conditions can be used to optimize the wet modulus contrast of these materials. Considerations such as these are beneficial for the development of the next generation of squid beak bio-inspired nanocomposites, potentially allowing access to larger mechanical contrasts that more precisely mimic those observed in the squid beak.

4.6 Appendix

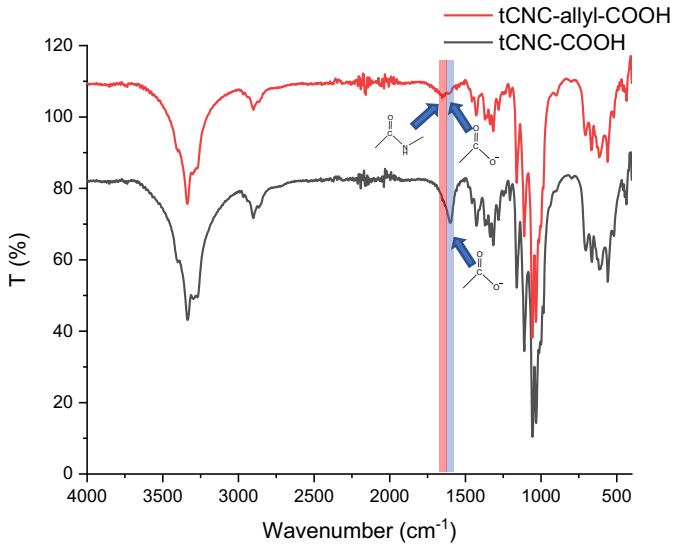

Figure A4.1 FTIR spectra of tCNC-$COOH_{1000}$s and tCNC-$allyl_{800}$-$COOH_{200}$.

Table A4.1 Elemental analysis results of tCNC-$COOH_{1000}$ and tCNC-$allyl_{800}$-$COOH_{200}$.

Samples	Carbon %	Hydrogen %	Nitrogen %
tCNC-$COOH_{1000}$	44.98	6.47	Not found
tCNC-$allyl_{800}$-$COOH_{200}$	45.81	6.34	0.6

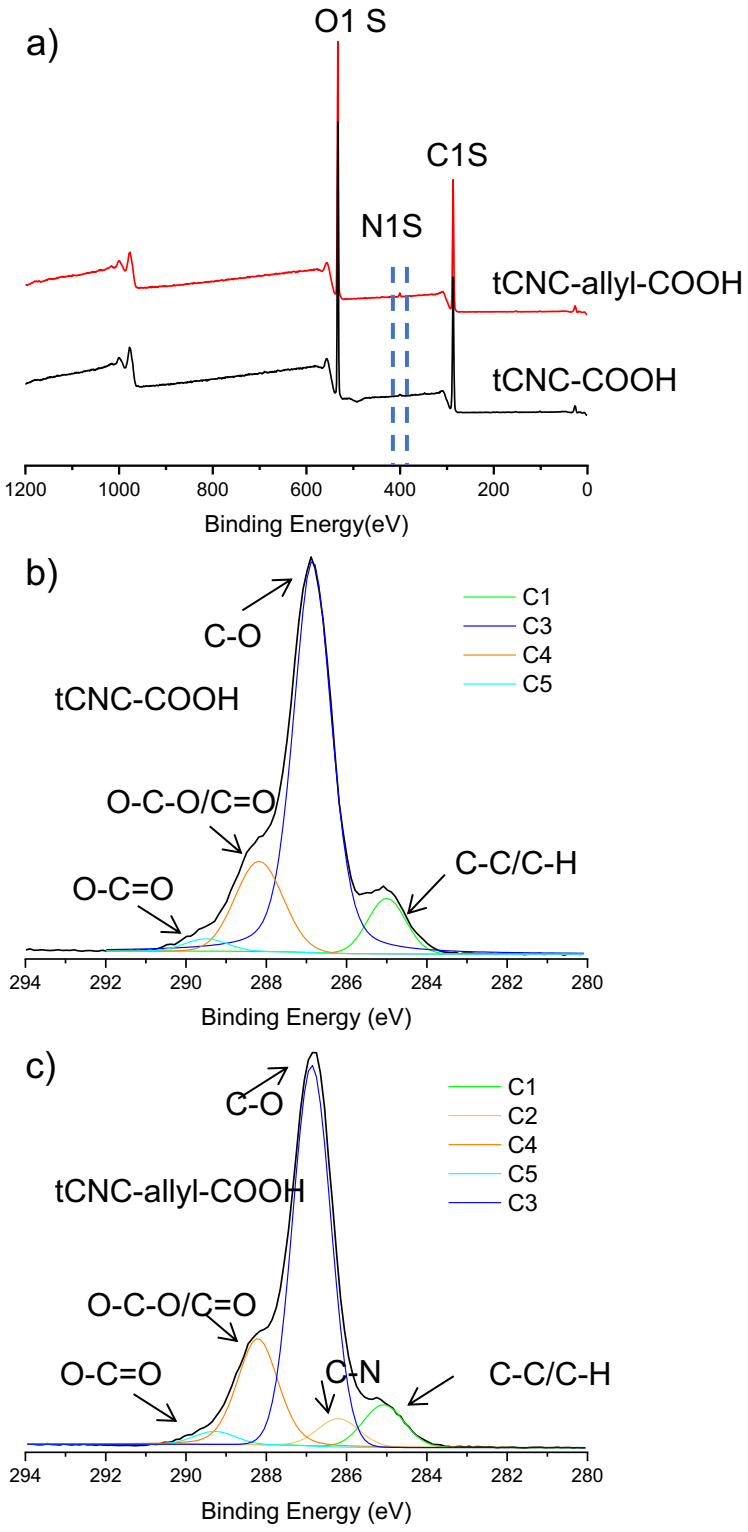

Figure A4.2 a) XPS spectra for tCNC-$COOH_{1000}$ and tCNC-$allyl_{800}$-$COOH_{200}$. And high resolution XPS spectra of the C 1s signal for b) tCNC-$COOH_{1000}$ and c) tCNC-$allyl_{800}$-$COOH_{200}$.

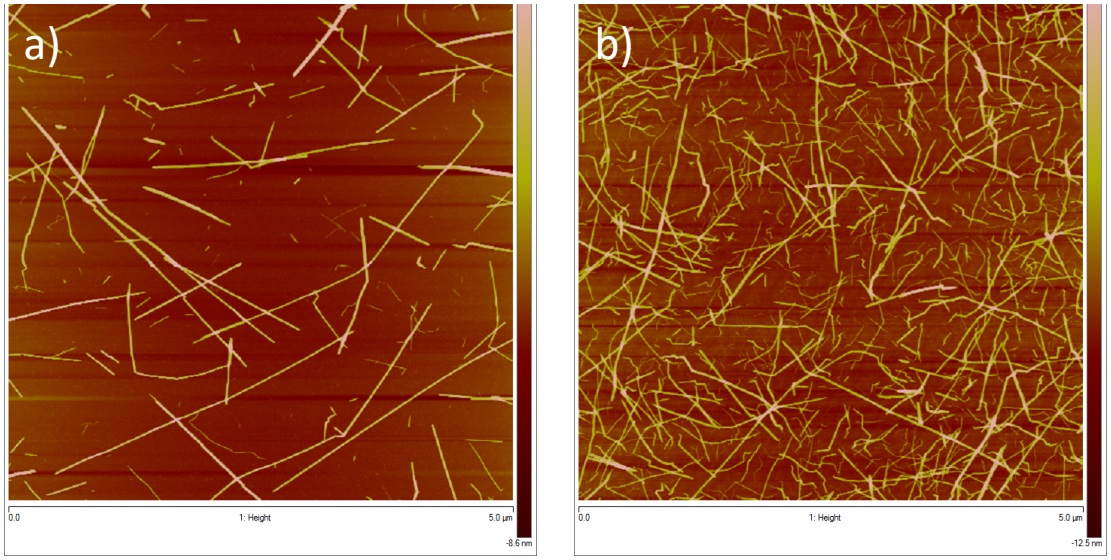

Figure A4.3 AFM height images of a) tCNC-COOH$_{1000}$ and b) tCNC-allyl$_{800}$-COOH$_{200}$.

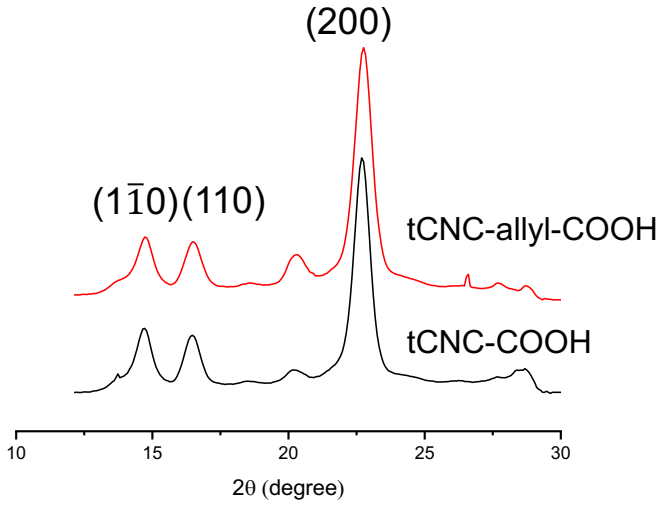

Figure A4.4 X-ray diffraction pattern of tCNC-COOH$_{1000}$ and tCNC-allyl$_{800}$-COOH$_{200}$.

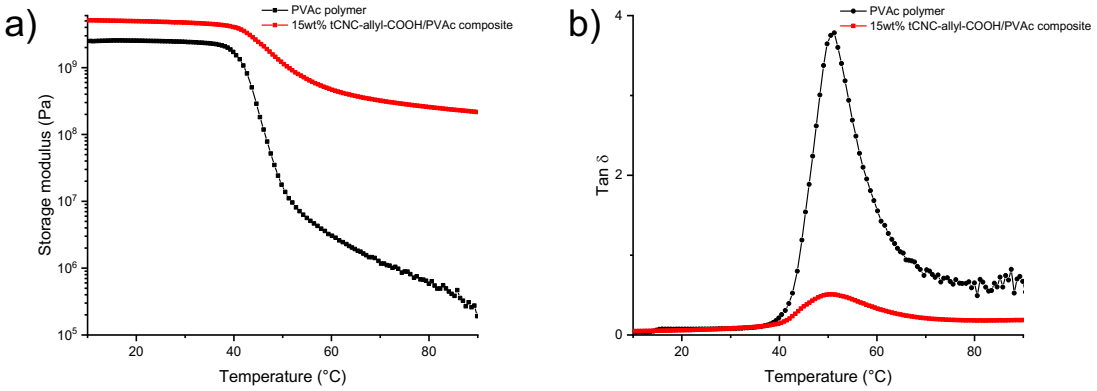

Figure A4.5 Representative DMA temperature sweep curves in the dry state of a) dry storage modulus and b) tan δ for both the neat PVAc polymer matrix and the 15wt% tCNC-allyl-COOH/PVAc composite film.

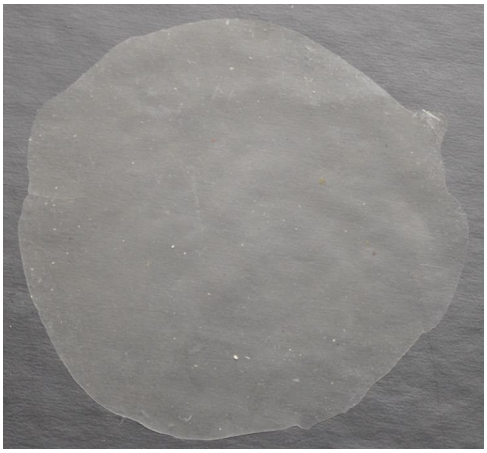

Figure A4.6 Photograph of the 15wt% tCNC-allyl-COOH/PVAc composite film after melt processing.

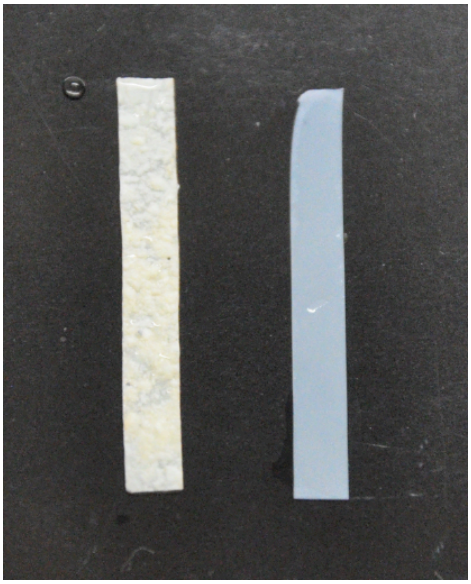

Figure A4.7 Photographs of the melt-processed composite films (left) and as-cast composite films (right) upon exposure to water.

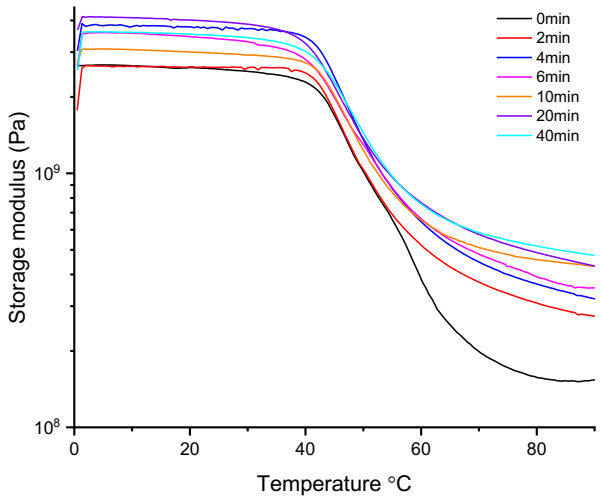

Figure A4.8 Representative DMA temperature sweeps of the 150 µm melt-processed films in the dry state before and after UV irradiation on a hotplate (at 60°C) for times ranging from 2 to 40 min.

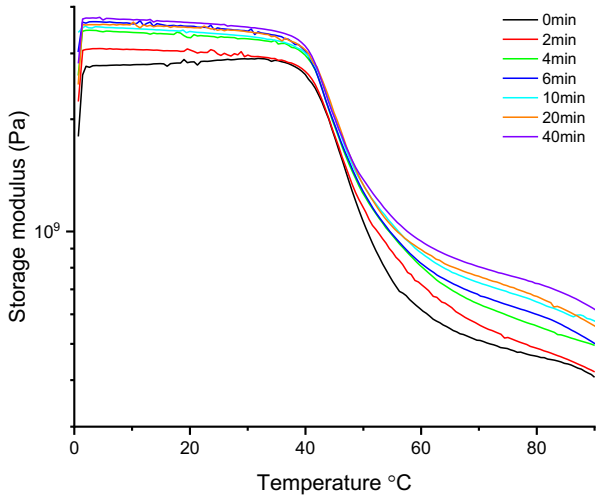

Figure A4.9 Representative DMA temperature sweeps of the 150 µm as-cast composite films in the dry state before and after UV irradiation on a hotplate (at 60°C) for times ranging from 2 to 40 min.

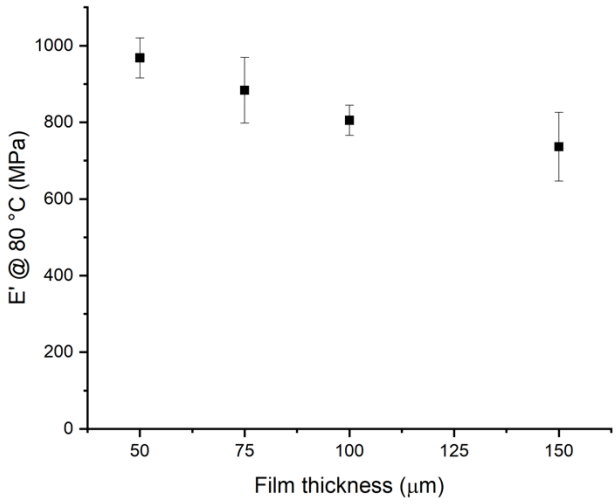

Figure A4.10 Comparison of the dry storage modulus (*E'*) at 80 °C versus film thickness for as-cast films after UV irradiation on a hotplate for 40 min.

Table A4.2 Comparison of the wet storage modulus (E') (as measured by immersion DMA) and the mechanical contrast for films prepared with different conditions and thickness.

		Wet Modulus		
		E' at 37 °C (0 min)	E' at 37 °C (40 min)	E_{stiff}/E_{soft}
Melt-processed (150 μm)		10 MPa	50 MPa	5.2
As-cast	150 μm	17.8 MPa	83 MPa	4.7
	100 μm	16.1 MPa	89 MPa	5.5
	75 μm	19.2 MPa	110 MPa	5.7
	50 μm	Not measured*	130 MPa	7.3**

* Films were too delicate to be measured.

** E_{stiff}/E_{soft} is calculated using the average E' at 37 °C (17.7 MPa) for as-cast films at other thickness.

4.7 Reference

(1) Montero de Espinosa, L.; Meesorn, W.; Moatsou, D.; Weder, C. Bioinspired Polymer Systems with Stimuli-Responsive Mechanical Properties. *Chem. Rev.* **2017**, *117* (20), 12851–12892.

(2) Liu, Z.; Meyers, M. A.; Zhang, Z.; Ritchie, R. O. Functional Gradients and Heterogeneities in Biological Materials: Design Principles, Functions, and Bioinspired Applications. *Prog. Mater. Sci.* **2017**, *88*, 467–498.

(3) Zhang, C.; Mcadams, D. A.; Grunlan, J. C. Nano/Micro-Manufacturing of Bioinspired Materials: A Review of Methods to Mimic Natural Structures. *Adv. Mater.* **2016**, *28* (30), 6292–6321.

(4) Zan, G.; Wu, Q. Biomimetic and Bioinspired Synthesis of Nanomaterials/Nanostructures. *Adv. Mater.* **2016**, *28* (11), 2099–2147.

(5) Wegst, U. G. K.; Bai, H.; Saiz, E.; Tomsia, A. P.; Ritchie, R. O. Bioinspired Structural Materials. *Nat. Mater.* **2015**, *14* (1), 23–36.

(6) Meyers, M. A.; McKittrick, J.; Chen, P.-Y. Structural Biological Materials: Critical Mechanics-Materials Connections. *Science* **2013**, *339* (6121), 773–779.

(7) Chen, P.-Y.; Lin, A. Y. M.; Lin, Y.-S.; Seki, Y.; Stokes, A. G.; Peyras, J.; Olevsky, E. A.; Meyers, M. A.; McKittrick, J. Structure and Mechanical Properties of Selected Biological Materials. *J. Mech. Behav. Biomed. Mater.* **2008**, *1* (3), 208–226.

(8) Yang, W.; Chen, I. H.; Gludovatz, B.; Zimmermann, E. A.; Ritchie, R. O.; Meyers, M. A. Natural Flexible Dermal Armor. *Adv. Mater. Deerfield Beach Fla* **2013**, *25* (1), 31–48.

(9) Ritchie, R. O. Natural Materials: Armoured Oyster Shells. *Nat. Mater.* **2014**, *13* (5), 435–437.

(10) Vukusic, P.; Sambles, J. R. Photonic Structures in Biology. *Nature* **2003**, *424* (6950), 852–855.

(11) Farren, L.; Shayler, S.; Ennos, A. R. The Fracture Properties and Mechanical Design of Human Fingernails. *J. Exp. Biol.* **2004**, *207* (5), 735–741.

(12) Benjamin, M.; Toumi, H.; Ralphs, J. R.; Bydder, G.; Best, T. M.; Milz, S. Where Tendons and Ligaments Meet Bone: Attachment Sites ('Entheses') in Relation to Exercise and/or Mechanical Load. *J. Anat.* **2006**, *208* (4), 471–490.

(13) Lu, H. H.; Thomopoulos, S. Functional Attachment of Soft Tissues to Bone: Development, Healing, and Tissue Engineering. *Annu. Rev. Biomed. Eng.* **2013**, *15* (1), 201–226.

(14) Sun, C.; Waite, J. H. Mapping Chemical Gradients within and along a Fibrous Structural Tissue, Mussel Byssal Threads. *J. Biol. Chem.* **2005**, *280* (47), 39332–39336.

(15) Miserez, A.; Li, Y.; Waite, J. H.; Zok, F. Jumbo Squid Beaks: Inspiration for Design of Robust Organic Composites. *Acta Biomater.* **2007**, *3* (1), 139–149.

(16) Miserez, A.; Schneberk, T.; Sun, C.; Zok, F. W.; Waite, J. H. The Transition from Stiff to Compliant Materials in Squid Beaks. *Science* **2008**, *319* (5871), 1816–1819.

(17) Tan, Y.; Hoon, S.; Guerette, P. A.; Wei, W.; Ghadban, A.; Hao, C.; Miserez, A.; Waite, J. H. Infiltration of Chitin by Protein Coacervates Defines the Squid Beak Mechanical Gradient. *Nat. Chem. Biol.* **2015**, *11* (7), 488–495.

(18) Helton, K. L.; Ratner, B. D.; Wisniewski, N. A. Biomechanics of the Sensor-Tissue Interface—Effects of Motion, Pressure, and Design on Sensor Performance and the Foreign Body Response—Part I: Theoretical Framework. *J. Diabetes Sci. Technol.* **2011**, *5* (3), 632–646.

(19) Fleckman, P.; Olerud, J. E. Models for the Histologic Study of the Skin Interface with Percutaneous Biomaterials. *Biomed. Mater.* **2008**, *3* (3), 034006.

(20) Teichgräber, U. K.; Pfitzmann, R.; Hofmann, H. A. F. Central Venous Port Systems as an Integral Part of Chemotherapy. *Dtsch. Aerzteblatt Online* **2011**.

(21) Capadona, J. R.; Tyler, D. J.; Zorman, C. A.; Rowan, S. J.; Weder, C. Mechanically Adaptive Nanocomposites for Neural Interfacing. *MRS Bull.* **2012**, *37* (6), 581–589.

(22) Harris, J. P.; Hess, A. E.; Rowan, S. J.; Weder, C.; Zorman, C. A.; Tyler, D. J.; Capadona, J. R. *In Vivo* Deployment of Mechanically Adaptive Nanocomposites for Intracortical Microelectrodes. *J. Neural Eng.* **2011**, *8* (4), 046010..

(23) Jorfi, M.; Skousen, J. L.; Weder, C.; Capadona, J. R. Progress towards Biocompatible Intracortical Microelectrodes for Neural Interfacing Applications. *J. Neural Eng.* **2015**, *12* (1), 011001.

(24) Claussen, K. U.; Giesa, R.; Scheibel, T.; Schmidt, H.-W. Learning From Nature: Synthesis and Characterization of Longitudinal Polymer Gradient Materials Inspired by Mussel Byssus Threads. *Macromol. Rapid Commun.* **2012**, *33* (3), 206–211.

(25) Wang, B.; Benitez, A. J.; Lossada, F.; Merindol, R.; Walther, A. Bioinspired Mechanical Gradients in Cellulose Nanofibril/Polymer Nanopapers. *Angew. Chem. Int. Ed.* **2016**, *55* (20), 5966–5970.

(26) Lin, Z.; Gui, X.; Zeng, Z.; Liang, B.; Chen, W.; Liu, M.; Zhu, Y.; Cao, A.; Tang, Z. Biomimetic Carbon Nanotube Films with Gradient Structure and Locally Tunable Mechanical Property. *Adv. Funct. Mater.* **2015**, *25* (46), 7173–7179.

(27) Zvarec, O.; Purushotham, S.; Masic, A.; Ramanujan, R. V.; Miserez, A. Catechol-Functionalized Chitosan/Iron Oxide Nanoparticle Composite Inspired by Mussel Thread Coating and Squid Beak Interfacial Chemistry. *Langmuir* **2013**, *29* (34), 10899–10906.

(28) Zhang, X.; Hassanzadeh, P.; Miyake, T.; Jin, J.; Rolandi, M. Squid Beak Inspired Water Processable Chitosan Composites with Tunable Mechanical Properties. *J. Mater. Chem. B* **2016**, *4* (13), 2273–2279.

(29) Neal, J. A.; Oldenhuis, N. J.; Novitsky, A. L.; Samson, E. M.; Thrift, W. J.; Ragan, R.; Guan, Z. Large Continuous Mechanical Gradient Formation via Metal-Ligand Interactions. *Angew. Chem. Int. Ed.* **2017**, *56* (49), 15575–15579.

(30) Hsu, L.; Weder, C.; Rowan, S. J. Stimuli-Responsive, Mechanically-Adaptive Polymer Nanocomposites. *J. Mater. Chem.* **2011**, *21* (9), 2812–2822.

(31) Capadona, J. R.; Shanmuganathan, K.; Tyler, D. J.; Rowan, S. J.; Weder, C. Stimuli-Responsive Polymer Nanocomposites Inspired by the Sea Cucumber Dermis. *Science* **2008**, *319* (5868), 1370–1374.

(32) Shanmuganathan, K.; Capadona, J. R.; Rowan, S. J.; Weder, C. Bio-Inspired Mechanically-Adaptive Nanocomposites Derived from Cotton Cellulose Whiskers. *J. Mater. Chem.* **2009**, *20* (1), 180–186.

(33) Shanmuganathan, K.; Capadona, J. R.; Rowan, S. J.; Weder, C. Stimuli-Responsive Mechanically Adaptive Polymer Nanocomposites. *ACS Appl. Mater. Interfaces* **2010**, *2* (1), 165–174.

(34) Dagnon, K. L.; Shanmuganathan, K.; Weder, C.; Rowan, S. J. Water-Triggered Modulus Changes of Cellulose Nanofiber Nanocomposites with Hydrophobic Polymer Matrices. *Macromolecules* **2012**, *45* (11), 4707–4715.

(35) Mendez, J.; Annamalai, P. K.; Eichhorn, S. J.; Rusli, R.; Rowan, S. J.; Foster, E. J.; Weder, C. Bioinspired Mechanically Adaptive Polymer Nanocomposites with Water-Activated Shape-Memory Effect. *Macromolecules* **2011**, *44* (17), 6827–6835.

(36) Capadona, J. R.; Shanmuganathan, K.; Trittschuh, S.; Seidel, S.; Rowan, S. J.; Weder, C. Polymer Nanocomposites with Nanowhiskers Isolated from Microcrystalline Cellulose. *Biomacromolecules* **2009**, *10* (4), 712–716.

(37) Moon, R. J.; Martini, A.; Nairn, J.; Simonsen, J.; Youngblood, J. Cellulose Nanomaterials Review: Structure, Properties and Nanocomposites. *Chem. Soc. Rev.* **2011**, *40* (7), 3941–3994.

(38) Eichhorn, S. J.; Dufresne, A.; Aranguren, M.; Marcovich, N. E.; Capadona, J. R.; Rowan, S. J.; Weder, C.; Thielemans, W.; Roman, M.; Renneckar, S.; Gindl, W.; Veigel, S.; Keckes, J.; Yano, H.; Abe, K.; Nogi, M.; Nakagaito, A. N.; Mangalam, A.; Simonsen, J.; Benight,

A. S.; Bismarck, A.; Berglund, L. A.; Peijs, T. Review: Current International Research into Cellulose Nanofibres and Nanocomposites. *J. Mater. Sci.* **2009**, *45* (1), 1.

(39) Habibi, Y.; Lucia, L. A.; Rojas, O. J. Cellulose Nanocrystals: Chemistry, Self-Assembly, and Applications. *Chem. Rev.* **2010**, *110* (6), 3479–3500..

(40) Eichhorn, S. J. Stiff as a Board: Perspectives on the Crystalline Modulus of Cellulose. *ACS Macro Lett.* **2012**, *1* (11), 1237–1239.

(41) Tingaut, P.; Zimmermann, T.; Sèbe, G. Cellulose Nanocrystals and Microfibrillated Cellulose as Building Blocks for the Design of Hierarchical Functional Materials. *J. Mater. Chem.* **2012**, *22* (38), 20105–20111.

(42) Rusli, R.; Shanmuganathan, K.; Rowan, S. J.; Weder, C.; Eichhorn, S. J. Stress Transfer in Cellulose Nanowhisker Composites—Influence of Whisker Aspect Ratio and Surface Charge. *Biomacromolecules* **2011**, *12* (4), 1363–1369.

(43) Eyley, S.; Thielemans, W. Surface Modification of Cellulose Nanocrystals. *Nanoscale* **2014**, *6* (14), 7764–7779.

(44) Lin, N.; Huang, J.; Dufresne, A. Preparation, Properties and Applications of Polysaccharide Nanocrystals in Advanced Functional Nanomaterials: A Review. *Nanoscale* **2012**, *4* (11), 3274–3294.

(45) Wohlhauser, S.; Delepierre, G.; Labet, M.; Morandi, G.; Thielemans, W.; Weder, C.; Zoppe, J. O. Grafting Polymers from Cellulose Nanocrystals: Synthesis, Properties, and Applications. *Macromolecules* **2018**, *51* (16), 6157–6189.

(46) Kedzior, S. A.; Kiriakou, M.; Niinivaara, E.; Dubé, M. A.; Fraschini, C.; Berry, R. M.; Cranston, E. D. Incorporating Cellulose Nanocrystals into the Core of Polymer Latex Particles via Polymer Grafting. *ACS Macro Lett.* **2018**, *7* (8), 990–996.

(47) Malho, J.-M.; Brand, J.; Pecastaings, G.; Ruokolainen, J.; Gröschel, A.; Sèbe, G.; Garanger, E.; Lecommandoux, S. Multifunctional Stimuli-Responsive Cellulose Nanocrystals via Dual Surface Modification with Genetically Engineered Elastin-Like Polypeptides and Poly(Acrylic Acid). *ACS Macro Lett.* **2018**, *7* (6), 646–650.

(48) Wang, Z.; Zhang, Y.; Yuan, L.; Hayat, J.; Trenor, N. M.; Lamm, M. E.; Vlaminck, L.; Billiet, S.; Du Prez, F. E.; Wang, Z.; Tang, C. Biomass Approach toward Robust, Sustainable, Multiple-Shape-Memory Materials. *ACS Macro Lett.* **2016**, *5* (5), 602–606.

(49) Zhang, Y.; Karimkhani, V.; Makowski, B. T.; Samaranayake, G.; Rowan, S. J. Nanoemulsions and Nanolatexes Stabilized by Hydrophobically Functionalized Cellulose Nanocrystals. *Macromolecules* **2017**, *50* (16), 6032–6042.

(50) Way, A. E.; Hsu, L.; Shanmuganathan, K.; Weder, C.; Rowan, S. J. PH-Responsive Cellulose Nanocrystal Gels and Nanocomposites. *ACS Macro Lett.* **2012**, *1* (8), 1001–1006.

(51) Cudjoe, E.; Khani, S.; Way, A. E.; Hore, M. J. A.; Maia, J.; Rowan, S. J. Biomimetic Reversible Heat-Stiffening Polymer Nanocomposites. *ACS Cent. Sci.* **2017**, *3* (8), 886–894.

(52) V. Biyani, M.; Weder, C.; Johan Foster, E. Photoswitchable Nanocomposites Made from Coumarin-Functionalized Cellulose Nanocrystals. *Polym. Chem.* **2014**, *5* (18), 5501–5508.

(53) V. Biyani, M.; Jorfi, M.; Weder, C.; Johan Foster, E. Light-Stimulated Mechanically Switchable, Photopatternable Cellulose Nanocomposites. *Polym. Chem.* **2014**, *5* (19), 5716–5724.

(54) Song, K.; Xu, H.; Xie, K.; Yang, Y. Keratin-Based Biocomposites Reinforced and Cross-Linked with Dual-Functional Cellulose Nanocrystals. *ACS Sustain. Chem. Eng.* **2017**, *5* (7), 5669–5678.

(55) Dash, R.; Foston, M.; Ragauskas, A. J. Improving the Mechanical and Thermal Properties of Gelatin Hydrogels Cross-Linked by Cellulose Nanowhiskers. *Carbohydr. Polym.* **2013**, *91* (2), 638–645.

(56) Girouard, N. M.; Xu, S.; Schueneman, G. T.; Shofner, M. L.; Meredith, J. C. Site-Selective Modification of Cellulose Nanocrystals with Isophorone Diisocyanate and Formation of Polyurethane-CNC Composites. *ACS Appl. Mater. Interfaces* **2016**, *8* (2), 1458–1467.

(57) Shao, C.; Wang, M.; Chang, H.; Xu, F.; Yang, J. A Self-Healing Cellulose Nanocrystal-Poly(Ethylene Glycol) Nanocomposite Hydrogel via Diels–Alder Click Reaction. *ACS Sustain. Chem. Eng.* **2017**, *5* (7), 6167–6174.

(58) Yang, J.; Han, C.-R.; Zhang, X.-M.; Xu, F.; Sun, R.-C. Cellulose Nanocrystals Mechanical Reinforcement in Composite Hydrogels with Multiple Cross-Links: Correlations between Dissipation Properties and Deformation Mechanisms. *Macromolecules* **2014**, *47* (12), 4077–4086.

(59) Fox, J. D.; Capadona, J. R.; Marasco, P. D.; Rowan, S. J. Bioinspired Water-Enhanced Mechanical Gradient Nanocomposite Films That Mimic the Architecture and Properties of the Squid Beak. *J. Am. Chem. Soc.* **2013**, *135* (13), 5167–5174.

(60) Dagnon, K. L.; Way, A. E.; Carson, S. O.; Silva, J.; Maia, J.; Rowan, S. J. Controlling the Rate of Water-Induced Switching in Mechanically Dynamic Cellulose Nanocrystal Composites. *Macromolecules* **2013**, *46* (20), 8203–8212.

(61) Lin, N.; Dufresne, A. Physical and/or Chemical Compatibilization of Extruded Cellulose Nanocrystal Reinforced Polystyrene Nanocomposites. *Macromolecules* **2013**, *46* (14), 5570–5583.

(62) Annamalai, P. K.; Dagnon, K. L.; Monemian, S.; Foster, E. J.; Rowan, S. J.; Weder, C. Water-Responsive Mechanically Adaptive Nanocomposites Based on Styrene–Butadiene Rubber and Cellulose Nanocrystals—Processing Matters. *ACS Appl. Mater. Interfaces* **2014**, *6* (2), 967–976.

Chapter 5. Squid Beak Inspired Crosslinked Cellulose Nanocrystal Composites.*

5.1 Abstract:

Bioinspired crosslinked polymer nanocomposites that mimic the water-enhanced mechanical gradient properties of the squid beak have been prepared by embedding either carboxylic acid- or allyl-functionalized cellulose nanocrystals (CNC) into an alkene-containing polymer matrix (poly(vinyl acetate-*co*-vinyl pentenoate), P(VAc-*co*-VP)). Crosslinking is achieved by imbibing the composite with a tetrathiol crosslinker and carrying out a photo-induced thiol-ene reaction. Central to this study was an investigation on how the placement of crosslinks (i.e. within matrix only or also between the matrix and filler) impacts the wet mechanical properties of these materials. Through crosslinking both the CNCs and matrix it is possible to access larger wet mechanical contrasts upon crosslinking (E'_{stiff}/E'_{soft}=ca. 20) than can be obtained by just crosslinking the matrix alone (where contrast E'_{stiff}/E'_{soft} of up 11 are observed). For example, in nanocomposites fabricated with 15 wt.% of allyl-functionalized tunicate CNCs and P(VAc-*co*-VP) with ca. 30 mole percent of the alkene containing VP units, an increase in the modulus of the wet composite from ca. 14 MPa to ca. 289 MPa at physiological temperature (37 °C) can be observed after UV irradiation. The water swelling of the nanocomposites is greatly reduced in the crosslinked materials as a result of the thiol-ene crosslinking network which also contributes to the wet modulus increase. Given the mechanical turnability and the relatively simple approach which also allows photo-patterning the material properties, these water-activated bio-inspired

* This chapter is adapted from: **Zhang, Y.**; Pon, N.; Awaji, A.; Rowan, S. J. *Biomacromolecules.* Submitted**.**

nanocomposites have potential uses in a broad range of biomedical applications, such as mechanically compliant intracortical microelectrodes.

5.2 Introduction

Polymer nanocomposites that consist of nanosized fillers embedded within a polymer matrix, are frequently utilized in natural systems to create biological materials with a broad range of exceptional physical properties.[1–4] Examples of biological nanocomposites include nacre which demonstrates remarkable toughness,[5] the dermis of the sea cucumber which shows mechanical adaptability when threatened,[6–8] and the club of the mantis shrimp which exhibits exceptional damage tolerance.[9,10] Understanding the mechanism of such biological systems allows for the development of new composites that either directly mimic the function and properties of natural materials or employ nature's design strategies to enhance the performance of synthetic systems.[11–17] Such bio-inspired nanocomposites have already been designed and used in a number of applications, such as structural materials,[18–20] functional coatings,[21] intracortical sensors,[22] and energy harvesting membranes.[23]

The beak of the Humboldt squid is another interesting example of a biological composite. In this case the beak displays a water-enhanced mechanical gradient to seamlessly join the stiff tip of the beak (rostrum) to the squid's soft muscle tissues (buccal).[24,25] The rostrum is one of the stiffest wholly organic materials with an elastic modulus of 5 GPa, and so in order to protect the soft buccal tissues (elastic modulus 50 MPa) from damage a mechanical gradient that spans two orders of magnitude in stiffness is required to allow dissipation of stress.[24] Waite, Zok, Miserez and coworkers have studied this natural nanocomposite in detail and shown that the beak is composed of chitin nanofibers embedded in a protein matrix.[24,25] The excellent mechanical gradient

properties of the beak are achieved by changes in the degree of covalent crosslinking and water hydration between the stiff rostrum and the soft buccal base.[26] Specifically, the beak contains two types of proteins, a family of chitin-binding proteins (DgCBPs) and another family of histidine-rich proteins (DgHBPs).[27–29] The soft buccal region is mainly composed of water-hydrated chitin (ca. 80 wt.% water) with a small percent of DgCBPs. Moving closer to the rostrum region, the water is gradually replaced with hydrophobic DgHBPs, which after crosslinking (via histidine groups and catechol moieties from both low molecular weight and peptidyl catechol compounds) results in a crosslinked protein network that interpenetrates the chitin filler network. The formation of a densely crosslinked protein network as well as the dehydration of the chitin network both play a key role in defining the extraordinary stiffness of the rostrum. It is worth pointing out that in a dehydrated squid beak (i.e. not a natural environment for the squid), the 100-fold mechanical gradient between the rostrum and buccal regions is greatly diminished (modulus ranging from 10 GPa to 5 GPa).

The better understanding of the squid beak (and other examples of mechanical gradient systems in nature) as a material has led to increased interest in new bio-inspired synthetic materials[11,21,30–33] which, for example, could serve as modulus buffers that can bridge soft tissue and stiff implants in some biomedical engineering applications, such as orthopedic implants[34,35] and intracortical microelectrodes.[22,36,37] However, there is still a noticeable gap between the engineered composites and the biological materials with regard to the mechanical contrast and the stiff modulus when the material is wet. Rolandi and coworkers reported the fabrication of chitosan nanocomposites by crosslinking chitosan with L-3,4-dihydrophenyl-alanine (L-dopa) through an oxidation reaction initiated by sodium periodate.[30] The materials demonstrated tunable mechanical properties by varying the amount of L-dopa. However, the gradient and stiff modulus in these hydrated samples

is relatively low (elastic modulus from 26 MPa to 55 MPa) compared to the squid beak bio-model. To-date-the largest mechanical contrast observed in synthetic materials has been reported by Guan and co-workers who, inspired by the jaw of the polychaete worm, used imidazole-containing polymer networks crosslinked by metal ions.[31] The degree of crosslinking was controlled by varying the concentration of metal ions which resulted in a gradient that spans across 0.5 to 100 MPa in dry low T_g films.

In prior work, we have reported bio-inspired mechanically-adaptive polymer nanocomposites that have been designed to mimic the hydration-enhanced mechanical gradient behavior of the squid beak.[38,39] By embedding allyl-functionalized cellulose nanocrystals (CNC) into a poly(vinyl acetate) (PVAc) matrix along with a tetrathiol crosslinker (pentaerythritol tetrakis(3-mercaptopropionate), PETMP), the CNC fillers can be covalent crosslinked via photo-induced thiol-ene chemistry, and the degree of crosslinking can be controlled by UV irradiation exposure which allows access to films with mechanical gradient properties. In the dry state, hydrogen bonding interactions between the CNC fillers and between the filler and matrix result in a significant increase in the mechanical properties of the composites. However, in the hydrated state, the modulus of the uncrosslinked composites drops dramatically (to < 20 MPa) on account of disruption of the hydrogen bonding between the CNC (and CNCs and matrix) by the water molecule as well as water plasticization of the polymer matrix. However, covalent crosslinking between the CNCs reduces the degree of water softening yielding a wet modulus of ca.130 MPa at maximum degree of crosslinking. As such, it was possible to obtain water-activated mechanical gradients with a wet modulus contrast, E'_{stiff}/E'_{soft}, of ca. 7 between crosslinked and uncrosslinked materials.[39]

While this initial study showed that it was possible to access water-activated mechanical gradients in CNC composites, the wet mechanical contrast achieved in these first-generation bio-inspired nanocomposites is still far away from the gradient observed in squid beak materials (E'_{stiff}/E'_{soft} ca. 7 vs 100). For many applications it is important to be able to access modulus gradients that span across larger mechanical contrasts while at the same time being able to access stiffer wet films (larger E'_{stiff}). As such it is of interest to investigate different approaches in materials design and/or crosslinking strategies to further improve this class of bio-inspired nanocomposites. One possible route is to introduce matrix-matrix and CNC-matrix crosslinks (which have been shown to improve the mechanical stiffness of CNC-based nanocomposites[40–42]) instead of the CNC-CNC only crosslinks used in the prior study. In fact, the impressive wet stiffness in the rostrum area of the squid beak is achieved through a densely crosslinked protein matrix. Furthermore, a much higher mol% of alkene crosslinking groups can be incorporated into the matrix than is possible through functionalization of the nanofiller which should result in much higher degrees of crosslinking and therefore wet stiffness. As such, reported herein are investigations of two types of thiol-ene crosslinkable CNC nanocomposites, one where crosslinking occurs primarily within the polymer matrix and one where crosslinking can occur between matrix and CNCs (in addition to within the matrix and between the CNCs themselves). The goal here is to better mimic the wet mechanical contrast of the squid beak and develop a better understanding of this class of bioinspired composites. In addition, the possibility of photo-patterning of these nanocomposites is explored to access water-activated shape-changing films.

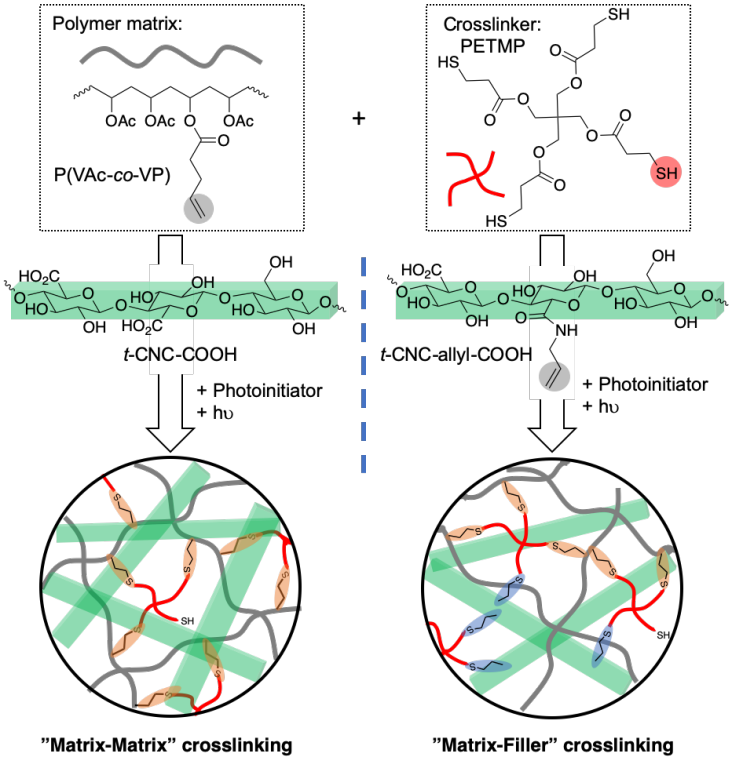

Scheme 5.1 Schematic of the preparation of bio-inspired nanocomposites based on matrix-matrix crosslink and matrix-filler crosslink approaches.

5.3 Experimental Section

Materials

Oxalyl chloride, 4-(dimethylamino)pyridine (DMAP), 4-pentenoic acid, triethylamine phenylbis(2,4,6-trimethylbenzoyl)phosphine oxide (BAPO), pentaerythritol tetrakis(3-mercaptopropionate) (PETMP), Poly(vinyl acetate) (PVAc, M_w=100 000 g/mol) were purchased from Sigma-Aldrich and used as received. Hydrochloric acid, sodium bicarbonate, and all the other solvents were purchased from Fisher Scientific and used without further purification. TEMPO-oxidized cellulose nanocrystals (*t*-CNC-COOH) with a charge density of 1000 mmol/kg, allyl-functionalized cellulose nanocrystals (*t*-CNC-allyl-COOH) with an allyl functionality of 800

mmol/kg and a residual charge density of 200 mmol/kg were obtained from sea tunicate mantles using the procedures published in previous work.[38,39]

Synthesis of Poly(vinyl acetate-co-vinyl alcohol) P(VAc-co-VA)

P(VAc-*co*-VA) copolymers were prepared by partial hydrolysis of PVAc under acidic conditions. PVAc (15g, Mw=100 000 g/mol) dissolved in a 9:1 (v/v) methanol/water mixture (250 mL) was heated to 50 °C for 1 hr. 12M HCl is added to the reaction mixture until the concentration of the HCl is 0.2M and the hydrolysis reaction was carried out for 2, 4 or 6 hrs at 50 °C. After the reaction, the solution was concentrated to ca. 50 mL and precipitated in excess DI water. The product was rinsed with DI water, re-dissolved in 50 mL of methanol and re-precipitated in water. The degree of hydrolysis of the P(VAc-*co*-VA_x) (where x is 10, 21 or 29 corresponding to the mole fraction of VA units) was calculated via ^{1}H NMR peak integration (see Appendix).

Synthesis of 4-pentenoyl chloride

To a solution of 4-pentenoic acid (10.01 g, 100 mmol) in 150 mL of anhydrous dichloromethane (DCM) was added oxalyl chloride (13.96 g, 110 mmol) and one drop of anhydrous dimethylformamide (DMF). The reaction was stirred for 6 hrs at room temperature. Excess solvent was fully removed by rotary evaporation at 40 °C. The resulting 4-pentenoyl chloride product was confirmed by NMR (Figure A5.3) and used without further purification (yield 95%).

Synthesis of Poly(vinyl acetate-co-vinyl pentenoate) P(VAc-co-VP)

Sample procedure for the synthesis of P(VAc-*co*-VP_{10}) copolymer: P(VAc-*co*-VA_{10}) (5 g, 6.11 mmol of OH groups) was dissolved in 200 mL of anhydrous tetrahydrofuran (THF). DMAP (0.07

g, 0.61 mmol) and triethylamine (3.09 g, 30.56 mmol) were dissolved in anhydrous THF separately and transferred to the reaction under argon. The reaction vessel was placed in an ice bath and cooled before 4-pentenoyl chloride (1.45 g, 12.23 mmol) in 25 mL of THF was added dropwise over 30 mins. The reaction was then allowed to continue for 3 hrs at room temperature followed by 16 hrs at 60 °C. The THF was fully removed by rotary evaporation, and the products were re-dissolved in ethyl acetate (EtOAc). The mixture was washed with saturated sodium bicarbonate solution (five times), followed with 0.1 M HCl solution (five times), and finally with DI water (five times). The product was further purified by dissolving in THF and passing through a silica packed column. Finally, the purified polymer was precipitated in hexane and dried in a vacuum oven. ^{1}H NMR spectra of the copolymer in $CDCl_3$ is shown in Figure A5.4. A new peak appeared between 5.6-5.9 ppm corresponding to the alkene group's internal proton (-CH=CH_2) in the VP units. The mole fraction of VP units was characterized by NMR integration (see Appendix). Similar procedures were carried out for the synthesis of P(VAc-*co*-VP_{22}) and P(VAc-*co*-VP_{30}) by using P(VAc-*co*-VA_{21}) (5 g, 12.89 mmol of OH) and P(VAc-*co*-VA_{29}) (5 g, 20.44 mmol of OH), respectively. The isolated yield of the esterification reactions was all above ca. 75 %.

Fabrication of t-CNC/P(VAc-co-VP) nanocomposites

t-CNC-COOH/P(VAc-*co*-VP_x) and *t*-CNC-allyl-COOH/P(VAc-*co*-VP_x) nanocomposites with different mole percent VP were prepared by solution casting from DMF. For a target nanocomposite containing 15 wt.% of CNC fillers, 510 mg of P(VAc-*co*-VP_x) (x=10, 22, 30) was dissolved in DMF at 50 mg/mL by stirring at room temperature for 4 hrs, and 90 mg of *t*-CNC-COOH or *t*-CNC-allyl-COOH was homogeneously dispersed in DMF at 3 mg/mL via ultrasonication for 30 mins. The nanocomposites were prepared by mixing the polymer solution

with the CNC dispersion, and submitting to ultrasonication for ca. 30 min before casting into a PTFE dish (diameter 12 cm). The solvent was fully removed in a vacuum oven at 60 °C for 5 days. Thermogravimetric analysis (TGA) was used to confirm the removal of DMF. The dried nanocomposite films were removed from the PTFE dishes and used as-cast without any melt processing.

Imbibing Process

Dried nanocomposite films were cut into rectangular strips with approximate dimensions of 30 mm by 4 mm. Stock solutions of the photoinitiator (Phenylbis(2,4,6-trimethylbenzoyl)phosphine oxide, BAPO) (5 mM) and crosslinker (pentaerythritol tetrakis(3-mercaptopropionate), PETMP) (50 mM) were prepared by dissolving the reagents in DCM separately. The exact volume of stock solution of initiator and crosslinker were measured (initiator - 5 mol% with respect to alkene groups and crosslinker - 25 mol% with respect to alkene groups, calculated with reference to the molar amount of total alkene groups from both CNCs and polymer matrix) and combined, and the co-solution was slowly and evenly pipetted onto the film until the solution was absorbed. The imbibed films were then supported on a PTFE dish and annealed in saturated DCM vapor for 24 hrs with the exclusion of light, with the goal of ensuring a more homogeneous distribution of the photoinitiators and crosslinkers within the film. Finally, the film strips were carefully dried in a dark environment under reduced pressure for 24 hrs to remove any residual DCM.

Photo crosslinking process

UV-induced thiol-ene crosslinking was performed using a Honle Bluepoint UV source with an intensity of 60 mW/cm^2 measured in the wavelength interval 320 nm to 390 nm. Composite films

supported on a piece of Teflon film were placed on a hot plate set at 60 °C before being irradiated for different times ranging from 2 to 40 min. Each sample was turned over at half of the exposure time to expose both sides to the UV irradiation. The irradiated films were soaked in 2-propanol immediately after exposure in order to remove any unreacted initiator and crosslinker. The 2-propanol was refreshed three times during a 24 hr soaking period. Finally, the samples were removed from 2-propanol and allowed to dry in a well-ventilated hood overnight before the removal of any residual solvent under reduced pressure at 40 °C for 48 hrs.

Characterization

Nuclear Magnetic Resonance (NMR) Spectroscopy. ^{1}H NMR measurements were performed using a Bruker Avance II 500 spectrometer operating at 500 MHz. Spectra are collected at room temperature with a minimum of 16 scans. Spectra were calibrated to the residual solvent peak of $CDCl_3$ (7.26 ppm ^{1}H NMR). Data were treated with MNova software.

Fourier Transform Infrared Spectroscopy (FTIR). FTIR studies of nanocomposite films were performed using a Shimadzu IRTracer-100 FTIR spectrometer. Film samples were placed directly on the ATR crystal, and the spectra were collected in transmission mode between 400 to 4000 cm-1 with a resolution of 4 cm^{-1}.

Differential scanning calorimetry (DSC). DSC measurements were performed using a TA Instruments Discovery DSC 2500. All samples were first heated to 100 °C and cooled down to -20 °C at a rate of 10 °C min^{-1}. And then the samples were heated back up again from -20 °C to 100 °C at a rate of 10 °C min^{-1}. The second heating cycle was used for data analysis.

Water swelling. Swelling tests were performed by placing the composite samples into vials filled with DI water and left in a water bath at 45 °C for 48 hrs. The degree of swelling was calculated by:

$$\%swelling = \frac{wet\ mass - dry\ mass}{dry\ mass} \times 100$$

Dynamic mechanical analysis (DMA). The viscoelastic properties of nanocomposites were analyzed using a RSA-G2 solid analyzer (TA Instrument, DE) equipped with a tension clamp and a submersion chamber. Dynamic temperature sweep measurements were performed with a fixed frequency of 1 Hz, a strain of 0.1%, a preload force of 0.1 N, and 125% force track. For characterizing the dry modulus of the composite films, the tension clamp was used and the modulus was measured while the temperature increased from 0 °C to 100 °C at a heating rate of 3 °C min^{-1}. The wet modulus was measured using the submersion chamber which allows the measurements to be conducted while the films were fully immersed in water during the tests. The temperature of the water was increased from 17 °C to 50 °C at a heating rate of 3 °C min^{-1}. It is worth pointing out that in the case of the submersion test, all samples were pre-swollen in water for 48 hrs before the test. All the DMA tests were performed in triplicate and the standard deviations were plotted as error bars.

5.4 Results and Discussion

5.4.1 Synthesis and characterization of P(VAc-*co*-VP)

As the initial work discussed above focused on using poly(vinyl acetate), PVAc, as the polymer matrix it was decided to target poly(vinyl acetate-*co*-vinyl pentenoate) (PVAc-*co*-VP), with various amounts of vinyl pentanoate repeat units, as the thiol-ene crosslinkable matrix. As such, commercially-available PVAc was partially hydrolyzed to poly(vinyl acetate-*co*-vinyl alcohol)

(P(VAc-*co*-VA)) using acidic conditions as it has been reported that this allows for good control of the degree of hydrolysis and results in a copolymer whose VA repeat units are randomly distributed along the polymer backbone.[43,44] The degree of hydrolysis was controlled by varying the reaction time to target copolymers with ca. 10 mol%, 20 mol% and 30 mol% of VA units.[45] The final degree of hydrolysis was estimated by ^{1}H NMR (Figure A5.1**)** to be 10%, 21% and 29% for PVAc hydrolyzed for 2 hr, 4 hr, and 6 hr, respectively (Table A5.1). Furthermore, after partial hydrolysis of PVAc, a new peak appeared in the FTIR spectra at 3300 cm^{-1} corresponding to the -OH groups of the P(VAc-*co*-VA) copolymer (Figure A5.2).

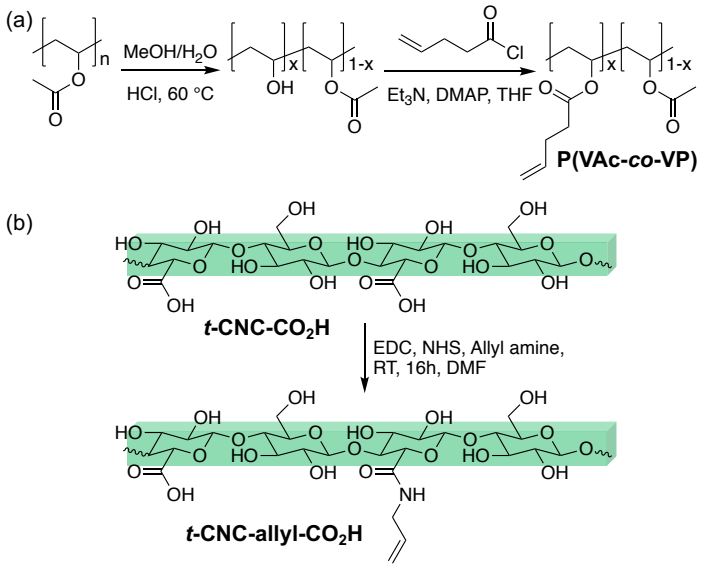

Scheme 5.2 The synthesis of a) poly(vinyl acetate-*co*-vinyl pentenoate), P(VAc-*co*-VP), in two steps from poly(vinyl acetate), PVAc and b) allyl-functionalized CNCs (*t*-CNC-allyl-COOH) from carboxylic acid-functionalized CNCs (*t*-CNC-COOH).

Poly(vinyl acetate-*co*-vinyl pentenoate) (P(VAc-*co*-VP)) copolymers were then prepared by the esterification of the hydroxyl groups of the different P(VAc-*co*-VA)s with 4-pentenoyl chloride. The molar fraction of VP units on the polymer can be calculated via ^{1}H NMR (Figure A5.4) to be

ca. 10 , 22 and 30 %, as shown in Table A5.2 Calculation of the ratio of VP:VAc units and the measured and predicted T_g of the P(VAc-*co*-VP) copolymers.(P(VAc-*co*-VP_x), where x, which corresponds to the mole fraction percent of VP units, is 10, 22 or 30). Conversion of the VA units to VP units was also confirmed by FTIR (Figure A5.2), as the -OH peak at 3300 cm^{-1} disappeared after esterification reaction and new peaks at 920 cm^{-1} (=C-H) and 1647 cm^{-1} (C=C) appear.

The glass transition temperature (T_g) of the copolymers was investigated by DSC. All P(VAc-*co*-VP_x) copolymers showed a single glass transition temperature that decreases with increasing percentage of VP units (Figure A5.5). The measured T_g's are close to the values calculated via the Fox equation (Table A5.2), consistent with a random distribution of VP units along the polymer backbone.

5.4.2 Nanocomposites with only crosslinked polymer matrix

As mentioned above prior work on the first-generation of these bioinspired composites focused on understanding the effect of only crosslinking the CNC nanofiller.[38,39] However, crosslinking of the protein matrix is a critical feature of the squid beak bio-model.[24] In addition, the placement of the alkene moiety in the matrix polymer dramatically increases the potential number of crosslinking sites in the composite. For example, in the first generation 15 wt.% *t*-CNC-allyl-COOH/PVAc composites the amount of alkene units in the film corresponds to ca. 0.12×10^{-3} mmol/mg. However, the use of the P(VAc-*co*-VP_x) matrix with 15 wt.% *t*-CNC-COOH results in composites that contain an order of magnitude higher concentration of alkene moieties, namely 0.94×10^{-3} mmol/mg, 1.99×10^{-3} mmol/mg and 2.60×10^{-3} mmol/mg alkene moieties for x = 10, 22 and 30, respectively. Thus, a series of materials were prepared to examine how crosslinking only the matrix with these much higher levels of potential crosslinking sites would impact the properties

of these bioinspired synthetic films. To this end, *t*-CNC-COOHs (with no alkene units attached) were embedded into the three different P(VAc-*co*-VP_x) copolymer matrices. These nanocomposites were fabricated by mixing a DMF solution of the polymer and a dispersion of the *t*-CNC-COOHs in DMF. After solution casting and solvent evaporation, optically clear composite films with a thickness between 100 and 120 μm were obtained. In the prior studies it was shown that melt processing of the CNC composites can induce phase segregation which disrupts the CNC filler network and negatively impacts the mechanical properties.[39] Therefore, all the composite films fabricated in this study were used as-cast without any melt processing. The nanocomposites were subsequently imbibed with a tetra-thiol crosslinker, pentaerythritol tetrakis(3-mercaptopropionate) (PETMP), and a photo-initiator, phenylbis(2,4,6-trimethylbenzoyl)phosphine oxide (BAPO), in order to form thiol-ene crosslinks upon UV irradiation. It is worth pointing out that in each composite sample the imbibed amount of PETMP crosslinker was adjusted based on the total amount of alkene groups within the polymer matrix to maintain a constant 1:1 thiol to alkene mole ratio. Exposure of these films to UV irradiation results in crosslinking, which was initially confirmed upon sonicating both UV exposed and unexposed films in DMF; the UV unexposed films dissolve while the exposed films remain intact (Figure A5.6).

A key advantage of using the UV-induced thiol-ene crosslinking approach is that it is possible to control the degree of crosslinking by the amount of exposure to UV irradiation.[46,47] As such the imbibed P(VAc-*co*-VP_x)/*t*-CNC-COOH films (where x = 10, 22 or 30 wt.%) were irradiated with UV light (60 mW/cm^2) for times ranging from 2 min to 40 min. Prior studies have shown that the CNCs can scatter the UV light limiting its penetration depth through the composite films during the photocuring process.[39] Thus, to ensure a more even distribution of UV exposure through the

film's thickness the samples were irradiated on both sides (films were flipped at the halfway point of exposure). Finally, the irradiated samples were swollen in 2-propanol for 24 hrs to remove unreacted initiator and crosslinker before being dried under reduced pressure for further characterization. A control sample (unexposed to UV light) was also prepared by directly washing the imbibed composite strip in 2-propanol followed by the same drying procedures.

The thermomechanical properties of these bio-inspired nanocomposites were characterized by dynamic mechanical analysis (DMA) in both dry and wet states. Representative DMA temperature sweep curves showing the temperature dependency of storage modulus (E') and tan δ of P(VAc-*co*-VP_{30})/*t*-CNC-COOH nanocomposites in the dry state before and after UV irradiation are shown in Figure 5.1a. The storage modulus exhibits a transition between 30-60 ℃, attributed to the glass transition temperature, T_g, of the P(VAc-*co*-VP) matrix and a rubbery plateau at higher temperatures. After UV irradiation, a shift of the tan δ peak to higher temperatures as the exposure time increases can be observed. For example, the tan δ peak of unexposed P(VAc-*co*-VP_{30})/*t*-CNC-COOH nanocomposites increased from ca. 43 ℃ to ca. 58℃ after 40 min UV irradiation (Table 5.1), consistent with covalent crosslinking of the polymer matrix.[48] Similar behavior is also observed in the P(VAc-*co*-VP_{10})/*t*-CNC-COOH and P(VAc-*co*-VP_{22})/*t*-CNC-COOH nanocomposites (Figure A5.7). It is worthy of note that in the first-generation of these bio-inspired nanocomposites in which crosslinking only occurs between the CNCs, there is no change in the T_g of the PVAc matrix after UV irradiation.[38,39]

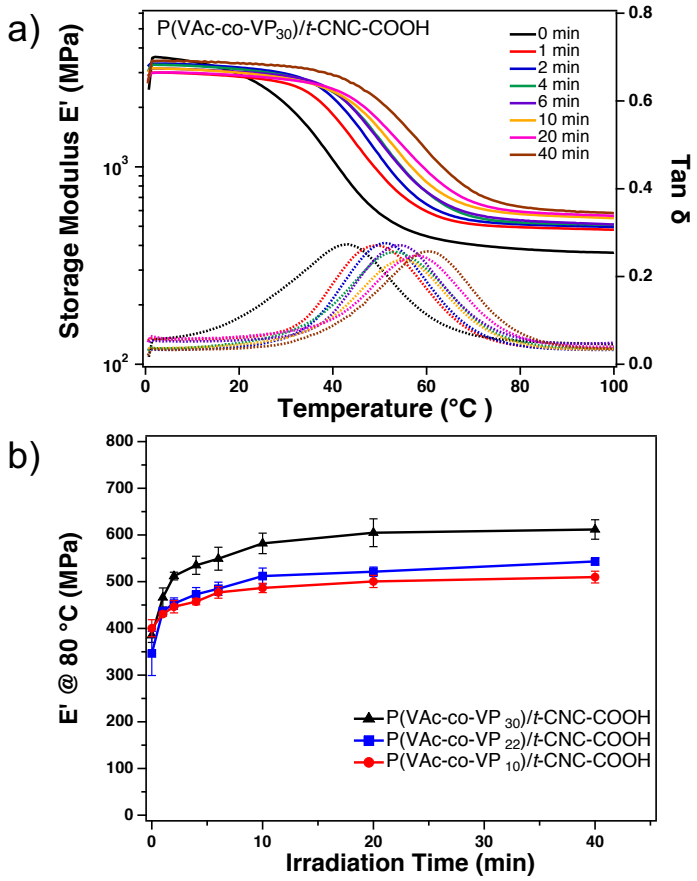

Figure 5.1 a) Representative DMA temperature sweep study of P(VAc-*co*-VP$_{30}$)/*t*-CNC-COOH nanocomposites in the dry state before and after UV irradiation. b) Storage modulus, *E′*, at 80 °C of various P(VAc-*co*-VP)/*t*-CNC-COOH nanocomposites after different UV irradiation times. (DMA conditions: heating rate 3 °C/min, frequency 1 Hz, strain 0.1 %.)

The formation of covalent networks within the P(VAc-*co*-VP)/*t*-CNC-COOH nanocomposites can be further demonstrated by the increase in plateau storage modulus (*E′*) after 2-40 min of UV irradiation. The plateau *E′* at 80 °C (ca. 20 °C higher than the highest T_g) were obtained from the DMA temperature sweep curves and used to evaluate the effect of UV irradiation condition on the mechanical properties. As can be seen from Figure 5.1b, all the nanocomposites showed an increase in *E′* (80 °C) with longer irradiation times. The composite samples fabricated using P(VAc-*co*-VP$_{30}$) demonstrate the highest plateau *E′* (>600 MPa) after 40 min irradiation (Table

5.1), consistent with a higher level of crosslinking in this material. In all samples there is a relatively small contrast in dry plateau storage modulus at 80 ℃ between uncrosslinked (0 min, E'_{soft}) and crosslinked samples (40 min, E'_{stiff}). For example, P(VAc-co-VP_{30})/*t*-CNC-COOH nanocomposites have a E'_{stiff}/E'_{soft}=1.6, slightly lower than the first-generation bioinspired nanocomposites based on filler-filler crosslinks (E'_{stiff}/E'_{soft} =2).

Table 5.1 Summary of the thermal mechanical property of P(VAc-co-VP_{30})/*t*-CNC-COOH in both dry and wet state at different UV irradiation times.[a]

	P(VAc-co-VP_{30})/*t*-CNC-COOH				
Irradiation time (min)	Dry E' at 80 ℃ MPa	Dry T_g ℃	Wet E' at 50 ℃ MPa	Wet T_g ℃	Water swelling %
0	385 ± 15	43.4 ± 1.1	13 ± 5	--	86 ± 3.5
1	466 ± 20	51.2 ± 2.4	83 ± 5	25.4 ± 0.6	7 ± 2
2	512 ± 8	51.6 ± 0.6	101 ± 7	27.9 ± 0.7	6.5 ± 1
4	535 ± 19	52.0 ± 1.9	120 ± 10	28.1 ± 0.4	6 ± 0.9
6	549 ± 25	53.2 ± 2.3	130 ± 8	28.6 ± 0.3	5.8 ± 0.9
10	582 ± 22	54.0 ± 4.1	136 ± 7	29.3 ± 0.9	5.6 ± 1.0
20	605 ± 30	55.3 ± 2.6	143 ± 12	29.7 ± 0.2	5.5 ± 1.0
40	612 ± 21	57.6 ± 3.4	145 ± 14	30.2 ± 0.2	5.3 ± 0.7

[a]All data are based on DMA experiments.

Of course, as it relates to the squid beak bio-model, what is more important for this class of materials is the mechanical properties of the wet composite films. In the wet state, a similar trend

of increasing T_g and plateau modulus is observed after exposure to UV light for 2-40 mins as can be seen from the representative DMA temperature sweep studies of the P(VAc-co-VP_{30})/*t*-CNC-COOH nanocomposites (Figure 5.2a). All the composite samples were pre-swollen in water until equilibrium swelling was reached before testing, and the DMA characterization was carried out in a submersion chamber. Compared to the dry films, a clear shift of the tan δ peak to lower temperatures can be observed in the wet materials, which is attributed to the water plasticization of the polymer matrix. For example, while the T_g for the unexposed P(VAc-*co*-VP_{30})/*t*-CNC-COOH composites in the wet state is too low to be obtained from the DMA study, the T_g of the irradiated nanocomposite increased to ca. 30℃ after 40 min UV irradiation. This result is consistent with the successful crosslinking within the polymer matrix and is further supported by the fact the increase in T_g is related to the amount of alkene moieties within the nanocomposite; the P(VAc-*co*-VP_{22}) and P(VAc-*co*-VP_{10}) nanocomposites show a T_g increase from ca. 17 to 28 ℃ and from ca. 20 to 22 ℃ after 40 min UV irradiation, respectively (Figure A5.8).

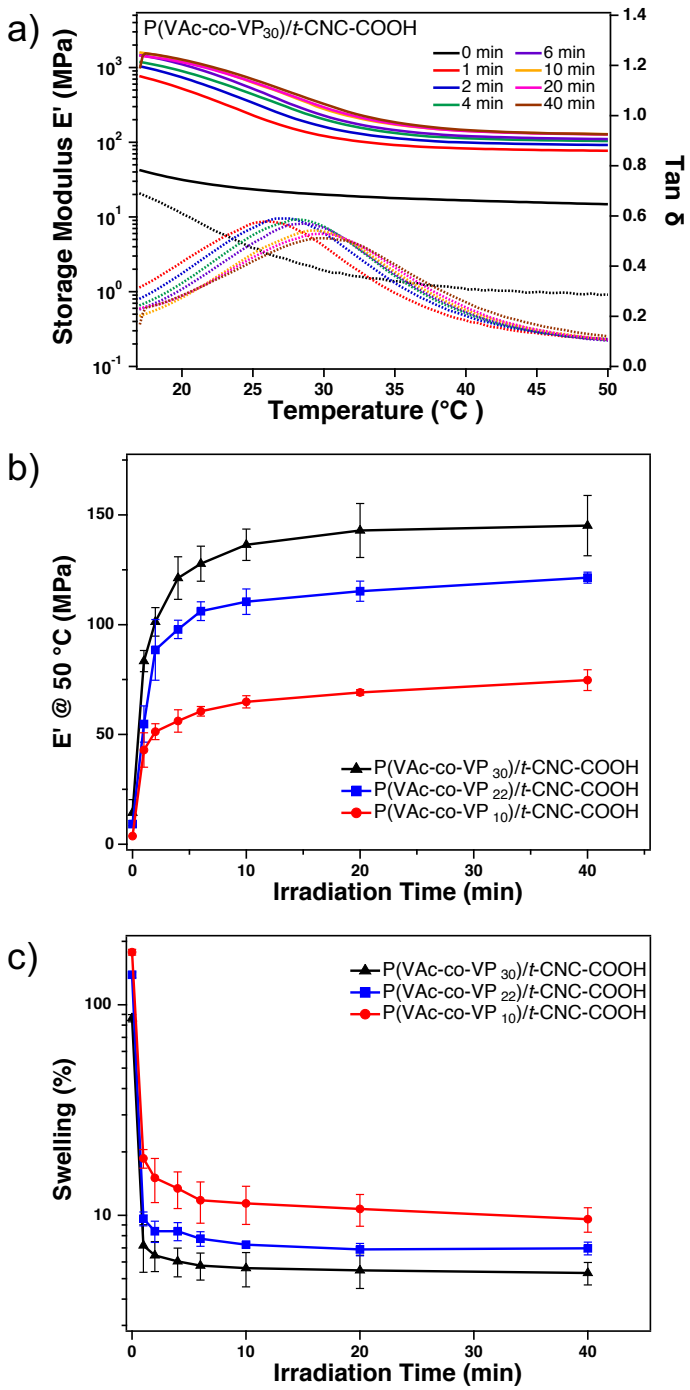

Figure 5.2 a) Representative DMA temperature sweeps of P(VAc-*co*-VP$_{30}$)/*t*-CNC-COOH nanocomposites in the wet state before and after UV irradiation. b) Storage modulus, *E′*, at 50 °C and c) equilibrium water swelling of various P(VAc-*co*-VP)/*t*-CNC-COOH nanocomposites after different UV irradiation times. (DMA conditions: heating rate 3 °C/min, frequency 1 Hz, strain 0.1 %.)

Importantly, the wet plateau E' can be controlled by varying the UV irradiation time as well as the amount of crosslinkable groups in the matrix (Figure 5.2b). For the P(VAc-*co*-VP_{30})/*t*-CNC-COOH nanocomposites, samples irradiated for 40 min show a wet plateau E' of 145 MPa and in this material the wet modulus contrast, E'_{stiff}/E'_{soft}, between the irradiated and unexposed films is ca. 11. This compares to a contrast of ca. 7 with the PVAc/*t*-CNC-allyl nanocomposites, where crosslinking is predominantly occurring between the CNCs.[39]

Interestingly, the wet mechanical contrast does not change significantly in the composites that have a lower amount of alkene groups in the polymer matrix. Wet contrast values of ca. 12 and 13 are observed with the P(VAc-*co*-VP_{10}) and P(VAc-*co*-VP_{22}) composites, respectively. Although of course in these materials the maximum wet modulus is lower at 75 MPa for P(VAc-*co*-VP_{10}) and 121 MPa for P(VAc-*co*-VP_{22}) (Table S3, S4). A possible explanation is that while the wet E'_{stiff} is larger in the P(VAc-*co*-VP_{30}) composites on account of a higher crosslink density, the higher mole percent of VP units increases the hydrophobicity of the matrix which limits the E'_{soft} of the unexposed materials in the wet state (which is 5.4, 9.2, 13.4 MPa for the P(VAc-*co*-VP_x) composites where x = 10, 22 and 30 respectively). This increased hydrophobicity of the crosslinked matrix is seen in the degree of water swelling of the different composite systems (Figure 5.2c). The unexposed P(VAc-*co*-VP_{10}) nanocomposites with the lease amount of VP moieties shows the highest amount of water uptake, ca. 180 wt.%. Water swelling significantly decreases for the composites based on P(VAc-*co*-VP_{22}) (ca. 140 wt.%) and P(VAc-*co*-VP_{30}) (ca. 85 wt.%). All the composite samples displayed a dramatic decrease in water uptake after UV irradiation which is again consistent with the formation of thiol-ene crosslinked networks. It is worthwhile noting that the water uptake for all these composite samples after 40 min of irradiation is between 5 to 10 wt.%, which is significantly lower than is observed for the first-generation bio-

inspired crosslinked nanocomposites based on PVAc/*t*-CNC-allyl-COOH, whose swelling was greater than 20 wt.%.[39]

5.4.3 Nanocomposites fabricated by crosslinking both the polymer matrix and CNC fillers

The above data shows that it is possible to access bio-inspired, controlled wet modulus nanocomposites, with mechanical contrast >10 and stiff wet modulus > 140 MPa, by crosslinking of the matrix. It was therefore of interest to investigate if the wet mechanical properties of the CNC based nanocomposites can be further enhanced by introducing crosslinking between the matrix and the CNCs, as well as within the matrix and between the CNCs. To this end, nanocomposites were fabricated using allyl-functionalized CNCs (*t*-CNC-allyl-COOH) as fillers embedded in the P(VAc-*co*-VP_x) copolymer matrices investigated above. It is important to note that the addition of the allyl-CNCs further increases the number of crosslinking sites in the composite, as discussed above 15 wt.% *t*-CNC-allyl-COOH contributes to 0.12×10^{-3} mmol/kg of alkene moieties in the nanocomposites. A comparison of the total alkene content (in mmol/mg) of the different nanocomposites is summarized in Table 5.2. Films were cast and imbibed under the same conditions as described previously with the amount of PETMP crosslinkers adjusted based on the total amount of alkene units (on both the *t*-CNC-allyl-COOH nanofillers (800 mmol/kg) and the P(VAc-*co*-VP) matrix) to maintain a 1:1 thiol to alkene molar ratio. Covalent thiol-ene networks between the CNCs and the polymer matrix were formed by irradiating the composite films with UV light using the same conditions as discussed above (60 mW/cm^2, 2-40 min). Similar to the nanocomposites made with *t*-CNC-COOH, the successful crosslinking was initially confirmed by DMF solubility tests using unexposed and crosslinked P(VAc-*co*-VP_{30})/*t*-CNC-allyl-COOH nanocomposites (Figure A5.9). Consistent with crosslinking, the sample irritated for 40 min

remained intact after swelling and sonication in DMF, as compared to the unexposed showing a complete dissolution in DMF.

Table 5.2 Comparison of the content of alkene moieties in nanocomposites.

Sample	Crosslink type	Filler Content	[alkene] from CNC	[alkene] from polymer	Total [alkene]
		wt.%	mmol/mg	mmol/mg	mmol/mg
PVAc/*t*-CNC-allyl	Filler-Filler	15	0.12×10^{-3}	0	0.12×10^{-3}
P(VAc-*co*-VP_{10})/*t*-CNC-COOH	Matrix-Matrix	15	0	0.94×10^{-3}	0.94×10^{-3}
P(VAc-*co*-VP_{22})/*t*-CNC-COOH	Matrix-Matrix	15	0	1.99×10^{-3}	1.99×10^{-3}
P(VAc-*co*-VP_{30})/*t*-CNC-COOH	Matrix-Matrix	15	0	2.60×10^{-3}	2.60×10^{-3}
P(VAc-*co*-VP_{10})/*t*-CNC-allyl-COOH	Matrix-Filler	15	0.12×10^{-3}	0.94×10^{-3}	1.06×10^{-3}
P(VAc-*co*-VP_{22})/*t*-CNC-allyl-COOH	Matrix-Filler	15	0.12×10^{-3}	1.99×10^{-3}	2.11×10^{-3}
P(VAc-*co*-VP_{30})/*t*-CNC-allyl-COOH	Matrix-Filler	15	0.12×10^{-3}	2.60×10^{-3}	2.72×10^{-3}

DMA temperature sweep studies of P(VAc-*co*-VP_{30})/*t*-CNC-allyl-COOH nanocomposites before and after UV irradiation in the dry state are shown in Figure 5.3a. In the dry state, the general shapes of the storage modulus (*E'*) and tan δ curves of the P(VAc-co-VP)/*t*-CNC-allyl-COOH films are similar to the composites containing the *t*-CNC-COOH fillers. A shift of the tan δ peak to higher temperatures (38.0 ℃ to 54.5 ℃) and an increase of the plateau storage modulus (337 MPa to 686 MPa at 80 ℃) of the samples irradiated for 40 min can be observed (Table 5.3). It is worthy of note that both the tan δ peak (38.0 ℃) and plateau modulus (337 MPa) for unexposed P(VAc-*co*-VP_{30})/*t*-CNC-allyl-COOH films are lower relative to P(VAc-*co*-VP_{30})/*t*-CNC-COOH composite films (43.4 ℃ and 385 MPa), possibly on account of reduced filler-filler and filler-matrix (hydrogen bonding) interactions that occur as a result of the functionalization the CNCs surface with allyl groups.

After irradiation for 40 min, the plateau modulus for P(VAc-co-VP_{30})/*t*-CNC-allyl-COOH nanocomposite increased to ca. 686 ± 18 MPa, which is slightly improved compared to P(VAc-co-VP_{30})/*t*-CNC-COOH (ca. 612 ± 21 MPa). The result is presumably a consequence of the additional degree of crosslinking between the filler and matrix, as well as between CNC fillers.

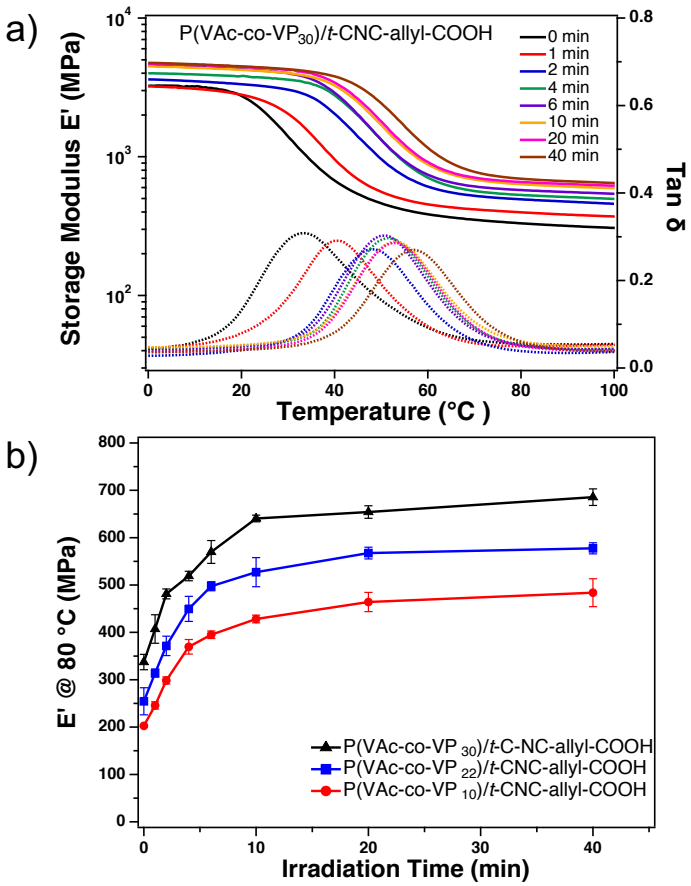

Figure 5.3 a) Representative DMA temperature sweep study of P(VAc-*co*-VP$_{30}$)/*t*-CNC-allyl-COOH nanocomposites in the dry state before and after UV irradiation. b) Storage modulus *E'* at 80 °C of various P(VAc-*co*-VP)/*t*-CNC-allyl-COOH nanocomposites at different UV irradiation times. (DMA conditions: heating rate 3 °C/min, frequency 1 Hz, strain 0.1 %.)

As mentioned in the study above, the wet mechanical properties of these films are of more interest given the squid beak exhibits its mechanical gradient in wet conditions. A representative submersion DMA curve of P(VAc-co-VP$_{30}$)/*t*-CNC-allyl-COOH sample is shown in Figure 5.4a (DMA curves of P(VAc-co-VP$_{22}$)/*t*-CNC-allyl-COOH and P(VAc-co-VP$_{10}$)/*t*-CNC-allyl-COOH are shown in Figure A5.11). Relative to the nanocomposites with covalent crosslinks only within the matrix, the introduction of the additional matrix-filler/filler-filler crosslinks yields an increase in both the T_g as well as plateau modulus after UV irradiation. For example, the T_g of P(VAc-co-VP$_{30}$)/*t*-CNC-allyl-COOH increased to ca. 34 °C after 40 min UV irradiation (cf. ca. 30 °C for

P(VAc-co-VP_{30})/*t*-CNC-COOH), while the plateau E' increased to ca. 200 MPa at 50 °C (cf. ca. 130 MPa for P(VAc-co-VP_{30})/*t*-CNC-COOH at 50 °C). As a result, the wet modulus contrast before and after UV irradiation is improved (E'_{stiff}/E'_{soft}=ca. 16) for P(VAc-co-VP_{30})/*t*-CNC-allyl-COOH nanocomposites. The same trend can also be observed in the other two nanocomposites with matrices containing lower mole fraction of pendant alkene groups (Figure 5.4b). The wet plateau E' arose from 9 MPa to 126 MPa for P(VAc-*co*-VP_{22})/*t*-CNC-allyl-COOH (E'_{stiff}/E'_{soft}=ca. 14) before and after UV irradiation, while the contrast for P(VAc-*co*-VP_{10})/*t*-CNC-allyl-COOH is from 5 MPa to 80 MPa with a E'_{stiff}/E'_{soft} of ca. 15. Using the combination of the allyl-functionalized CNC with the alkene-containing polymer matrix does result in an increase in the wet plateau modulus of the highly crosslinked materials (E'_{stiff}), but, akin to what is observed for the P(VAc-co-VP)/*t*-CNC-COOH nanocomposites, the overall contrast is limited by a slightly higher E'_{soft} of the unexposed materials on account of the increased hydrophobicity of both the filler and matrix.

The equilibrium water swelling of the nanocomposite films containing crosslinks between matrix and filler before and after UV irradiation are shown in Figure 5.4c. As expected, the equilibrium water uptake drops dramatically as the UV irradiation time increases which is consistent with the formation of covalent crosslinks. The equilibrium water uptake for these allyl-functionalized CNC composites is decreased to 4-7 % relative to the 5-10 % for films containing CNC-COOHs, which is presumably the consequence of the more hydrophobic (allyl) moieties on the CNCs surface.

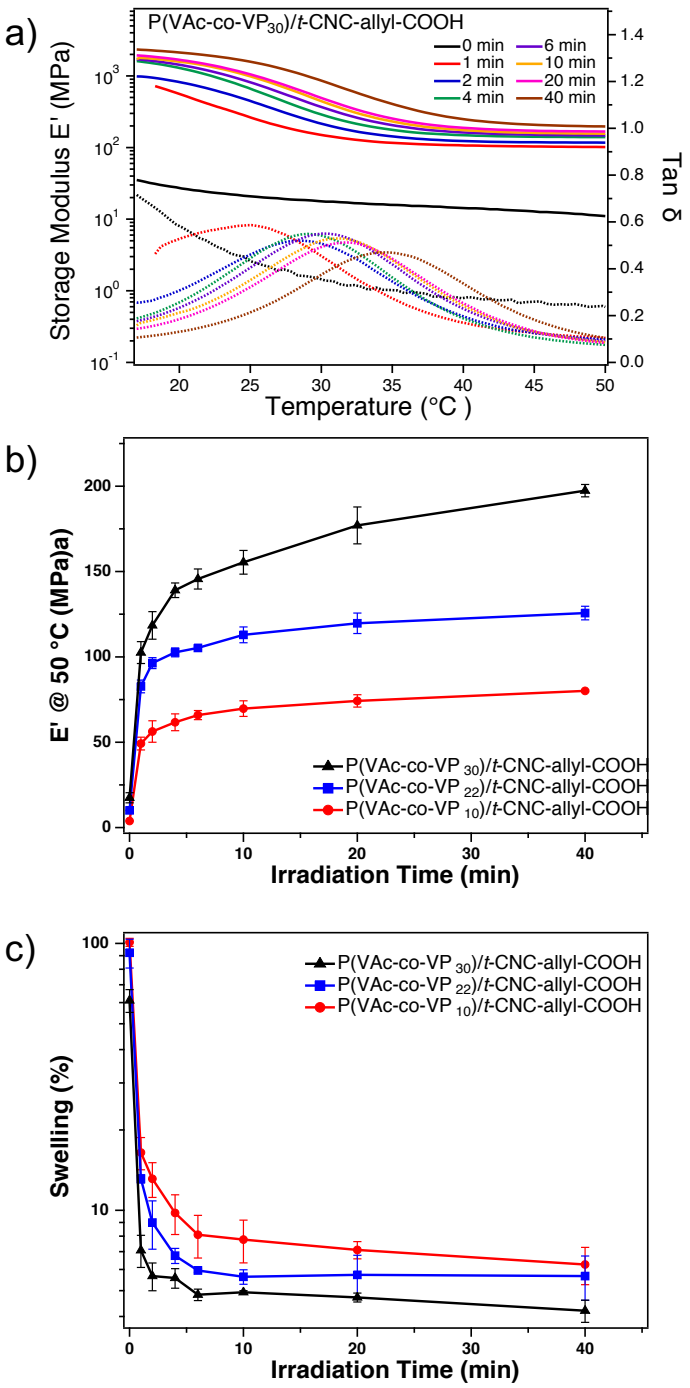

Figure 5.4 a) Representative DMA temperature sweeps of P(VAc-*co*-VP$_{30}$)/*t*-CNC-allyl-COOH nanocomposites in the wet state before and after UV irradiation. b) Storage modulus *E'* at 50 °C and c) equilibrium water swelling of various P(VAc-*co*-VP)/*t*-CNC-allyl-COOH nanocomposites at different UV irradiation times. (DMA conditions: heating rate 3 °C/min, frequency 1 Hz, strain 0.1 %.)

While the above-mentioned mechanical contrasts are all calculated based on the modulus in the plateau region at 50 °C, it is worthwhile pointing out that at physiological temperature (37 °C) the modulus contrast (E'_{stiff}/E'_{soft}) is ca. 20 with a tunable E' between 14 MPa and 289 MPa depending on the degree of irradiation. Such bio-inspired nanocomposites with improved wet modulus contrast could facilitate the design of novel intracortical microelectrodes.[22,36,37]

Table 5.3 Summary of the thermal mechanical property of P(VAc-co-VP_{30})/*t*-CNC-allyl-COOH in both dry and wet state at different UV irradiation times.[a]

	P(VAc-co-VP_{30})/*t*-CNC-allyl-COOH				
Irradiation time (min)	Dry E' at 80 °C MPa	Dry T_g °C	Wet E' at 50 °C MPa	Wet T_g °C	Water swelling %
0	337 ± 16	38.0 ± 5.8	12.7 ± 4		61.2 ± 6.0
1	407 ± 30	42.8 ± 4.8	103 ± 6	26.0 ± 1.2	7.1 ± 1.0
2	481 ± 10	47.2 ± 3.4	118 ± 8	28.1 ± 1.0	5.7 ± 0.7
4	519 ± 10	48.6 ± 3.6	139 ± 4	29.2 ± 0.5	5.6 ± 0.5
6	570 ± 24	49.7 ± 2.6	146 ± 6	30.1 ± 0.4	4.8 ± 0.2
10	641 ± 7	50.3 ± 3.9	155 ± 7	30.9 ± 1.5	4.9 ± 0.1
20	654 ± 13	51.7 ± 1.3	177 ± 11	33.3 ± 1.1	4.7 ± 0.2
40	686 ± 18	54.5 ± 2.1	197 ± 4	33.5 ± 1.1	4.2 ± 0.4

[a]All data are based on DMA experiments.

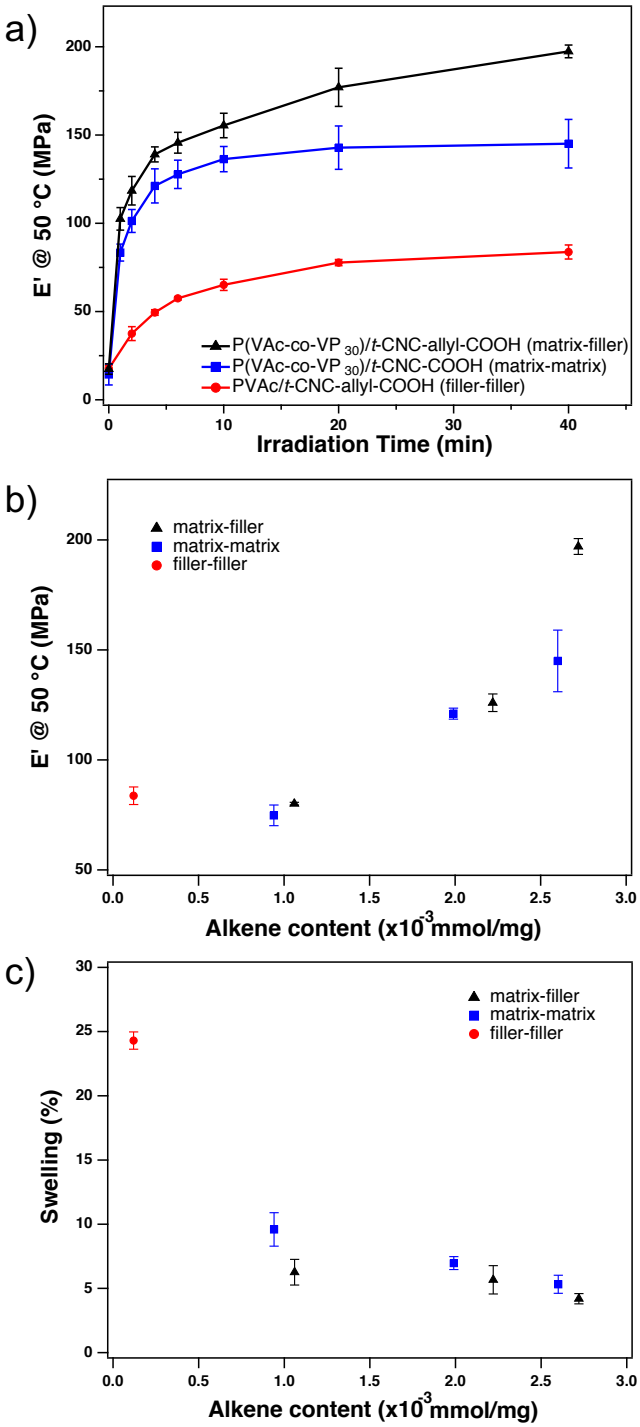

Figure 5.5 a) Comparison of the wet storage modulus E' at 50 °C of PVAc/t-CNC-allyl-COOH,39 of P(VAc-co-VP30)/t-CNC-COOH and of P(VAc-co-VP30)/t-CNC-allyl-COOH. b) Comparison of the wet storage modulus E' and c) degree of swelling at 50 °C of the different 15wt.% CNC bio-inspired nanocomposites with filler-filler crosslinking (PVAc/t-CNC-allyl-COOH), matrix-matrix crosslinking (P(VAc-co-VPx)/t-CNC-COOH, x = 10, 22, 30) and matrix-filler (P(VAc-co-VPx)/t-CNC-allyl-COOH, x = 10, 22, 30) in the pre-crosslinked films.

Figure 5.5a compares the wet storage modulus vs irradiation time for the three classes of CNC-based nanocomposites that differ in both the degree and type of crosslinking (between the CNCs, within the matrix or crosslinking of the matrix and CNCs). The data demonstrate that nanocomposites containing matrix-fillers crosslinks (and the higher degree of crosslinking) show higher plateau E' after UV irradiation compared to composites containing only matrix-matrix or filler-filler crosslinks. Of course the P(VAc-*co*-VP_{30}) nanocomposites contain a much higher content of alkene moieties relative to the PVAc based materials (CNC-CNC crosslinks only) (Table 2). Therefore, the lower wet modulus in the filler-only crosslink material is presumably a consequence of the limited number of crosslinking sites within the nanocomposites. For comparison, Figure 5.5b and c show the wet modulus (E') and degree of water swelling (after the maximum amount of UV exposure) versus the alkene moiety content in the pre-crosslinked films for the six films reported in this study and the previously reported PVAc/*t*-CNC-allyl-COOH. As would be expected in general the higher the alkene content the higher the wet modulus and lower degree of swelling after crosslinking. While it is difficult to draw too many other conclusions from this data it is worthwhile pointing that, even though the total alkene content in P(VAc-*co*-VP_{30})/*t-CNC*-allyl-COOH (matrix-filler) is only slightly higher than P(VAc-*co*-VP_{30})/*t-CNC*-COOH (matrix-matrix) (ca. 4.6 mol% increase), the wet mechanical properties show ca. 36% increase in the wet E'_{stiff} for these highly crosslinked samples.

5.4.4 Photo-patterning of bio-inspired nanocomposites

One advantage of using a photo-induced crosslinking approach is the ability to photo-pattern the materials using a pre-designed photomask. For example, Kumacheva and coworkers have shown

the fabrication of a 3D shape transformation hydrogel by controlling the shrinkage and elastic modulus within different regions of the material using photopatterning.[49] They showed that a hydrogel sheet containing alternating stripe patterns of different crosslinked poly(NIPAm)/poly(AMPS) can transform into a 3D helical shape when placed in hot water or a NaCl solution on account of the variation in the degree of water swelling between the exposed and unexposed regions. In addition, they showed that the pitch of the helix is proportional to the tilt (tan θ) of the stripes. Thus, to examine if these bioinspired nanocomposite films had a similar capability they were photo-patterned using a mask. A P(VAc-*co*-VP_{30})/*t*-CNC-allyl-COOH nanocomposite film (30 mm x 4 mm) was chosen as an example and was irradiated with UV using a photomask for 20 min on only one side of the sample. The photomask contains alternating dark and transparent strips that are 1 mm in width, and are tilted at a given angle to the long axis of the film (either 30° or 60°) (Figure 5.6a). This procedure aims to transfer the strip patterns to the nanocomposites to create alternating crosslinked (under transparent mask areas) and uncrosslinked regions (under dark mask areas) with different mechanical properties and degrees of swelling. After UV irradiation, the composite samples were placed in DCM, and the film transformed into a helical 3D structure within a few minutes (Figure 5.6b and c). The shape transformation is presumably a result of the difference in swelling between the crosslinked and uncrosslinked regions. Consistent with the work of Kumacheva[49] the morphology of helix did depend on the angle of the pattern, with a more compacted helical structure formed at a smaller angle (30°). It can be expected that with the use of nanofabrication equipment and a properly designed and fabricated photomask, more complex patterns and shapes can be fabricated which broadens the application of these bio-inspired nanocomposites.

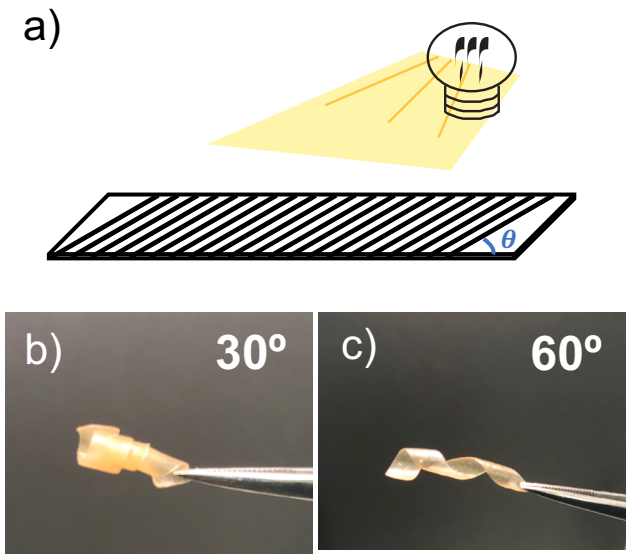

Figure 5.6 a) Schematic representation of the photomasks. b) and c) Photos of the P(VAc-*co*-VP_{30})/*t*-CNC-allyl-COOH nanocomposites after irradiation under a photomask and swelled in DCM for 5 min. The labels on b and c show the angle of the strip patters to the long axis.

5.5 Conclusion

Building on our previous squid beak inspired nanocomposites prepared with allyl-functionalized CNCs embedded in a PVAc matrix, a next-generation of bioinspired nanocomposites have been prepared and investigated using a crosslinkable alkene-containing poly(vinyl acetate-*co*-vinyl pentenoate) P(VAc-*co*-VP) copolymer matrix. Both P(VAc-*co*-VP)/*t*-CNC-COOH and P(VAc-*co*-VP)/*t*-CNC-allyl-COOH nanocomposites were prepared, and the materials can be covalently crosslinked using photo-induced thiol-ene chemistry to yield composite films. By using a polymer matrix with pendant alkene groups, the covalent network formed by photo-induced thiol-ene chemistry can be further extended to include matrix-matrix and matrix-filler crosslinks, which improves both the wet stiffness and wet modulus contrast of the nanocomposite films compared to the first-generation filler only crosslinked composite films. Specifically, nanocomposites composed of 15 wt.% *t*-CNC-allyl-COOH and P(VAc-*co*-VP_{30}) (matrix-filler crosslinks) with ca.

30 mol% of alkene-containing repeat units exhibited a wet storage modulus at 50 °C that is tunable between 13 MPa (uncrosslinked) and 197 MPa after 40 min of UV crosslinking (E'_{stiff}/E'_{soft}=ca. 16). The contrast in wet modulus is slightly higher relative to the matrix crosslinked nanocomposites containing 15 wt.% *t*-CNC-COOH and P(VAc-*co*-VP_{30}) which have a E'_{stiff}/E'_{soft}=ca. 11 (13 MPa to 145 MPa). It is also worthwhile pointing out that at physiological temperature (37 °C), the wet composites of *t*-CNC-allyl-COOH and P(VAc-*co*-VP_{30}) (matrix-filler crosslink) demonstrate an even larger modulus contrast at E'_{stiff}/E'_{soft}=ca. 20 (between 289 MPa and 14 MPa) which is much higher relative to what was obtained in the original work (E'_{stiff}/E'_{soft}=ca. 7).[39] Preliminary studies on the photopatterning of these composite films have shown that it is also possible to control the mechanical properties and swelling behavior within different regions of the materials by using a photomask, which opens the door to fabrication of these materials with complex shapes or even with spatial mechanical gradients.

5.6 Appendix

NMR of Poly(vinyl acetate-co-vinyl alcohol) P(VAc-co-VA).

Commercially-available PVAc was partially hydrolyzed to access the poly(vinyl acetate-*co*-vinyl alcohol) P(VAc-*co*-VA) copolymer using acidic conditions (see experimental section for more details). The resonance peaks between 1.4-1.9 ppm correspond to the methylene protons (A, C), the peaks between 1.9-2.2 ppm correspond to the methyl protons (E), and the peaks between 4.7-5.2 ppm correspond to the methine protons (B) of VAc unit. However, the methine proton peaks of VA unit were too small to be observed. Based on the ^{1}H NMR, the molar fraction of VAc can be calculated by the integration of methine peak of VAc (B) or by the integration of methyl peak of VAc (E) (Table A5.1).

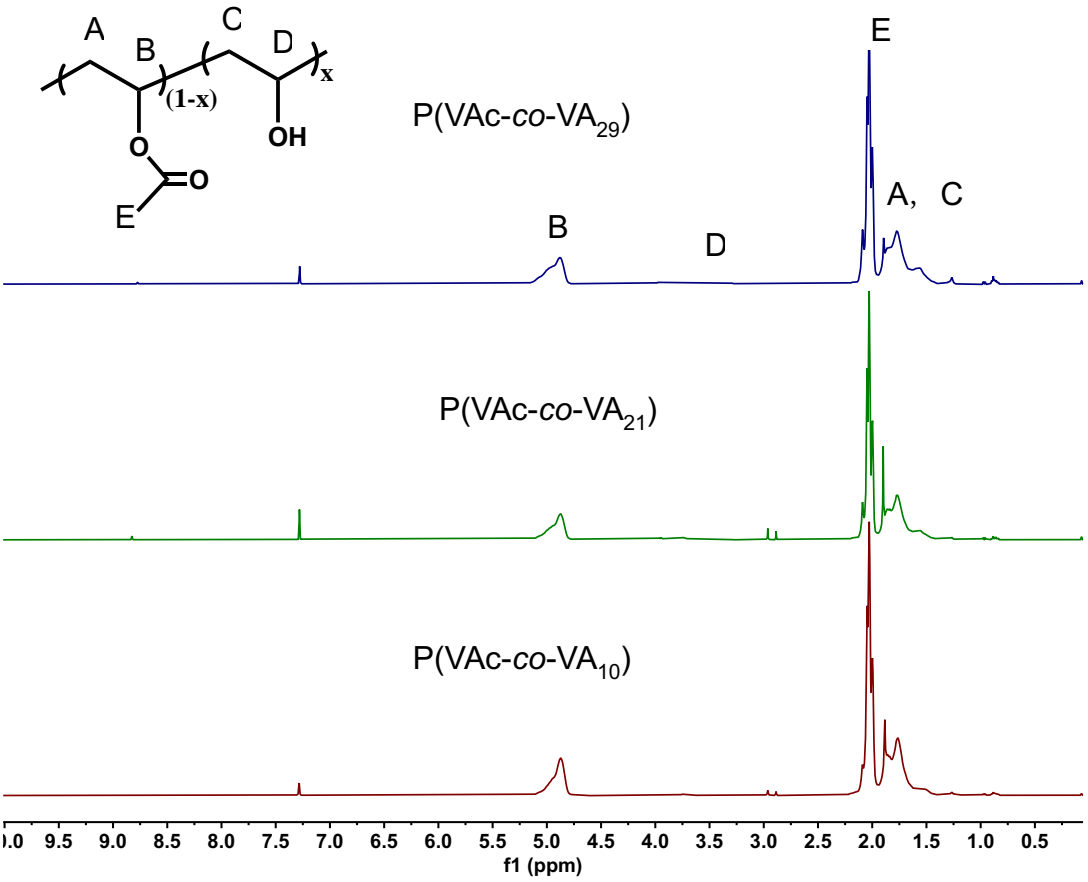

Figure A5.1 ^{1}H NMR (500 MHz, $CDCl_3$) spectra of the different poly(vinyl acetate-*co*-vinyl alcohol) P(VAc-*co*-VA) copolymers.

Table A5.1 Degree of hydrolysis for P(VAc-*co*-VA) copolymer.

Sample	Hydrolysis Time (h)	Degree of Hydrolysis (VA)		Average
		$1-\frac{2B}{A+C}$	$1-\frac{2E}{3(A+C)}$	
P(VAc-*co*-VA$_{10}$)	2	0.12	0.08	0.10
P(VAc-*co*-VA$_{21}$)	4	0.22	0.19	0.21
P(VAc-*co*-VA$_{29}$)	6	0.29	0.28	0.29

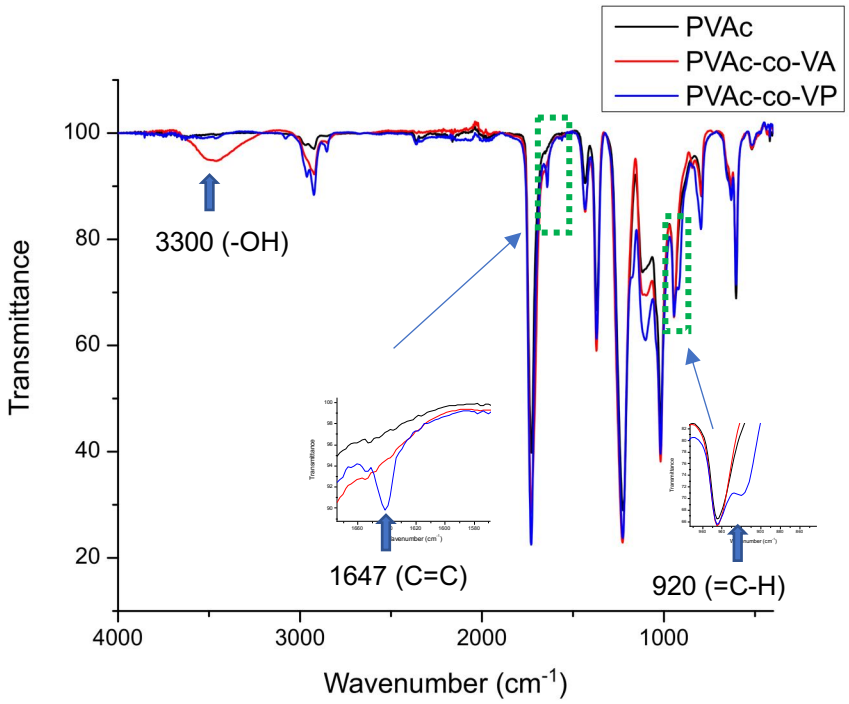

Figure A5.2 FTIR of PVAc, P(VAc-*co*-VA) and P(VAc-*co*-VP).

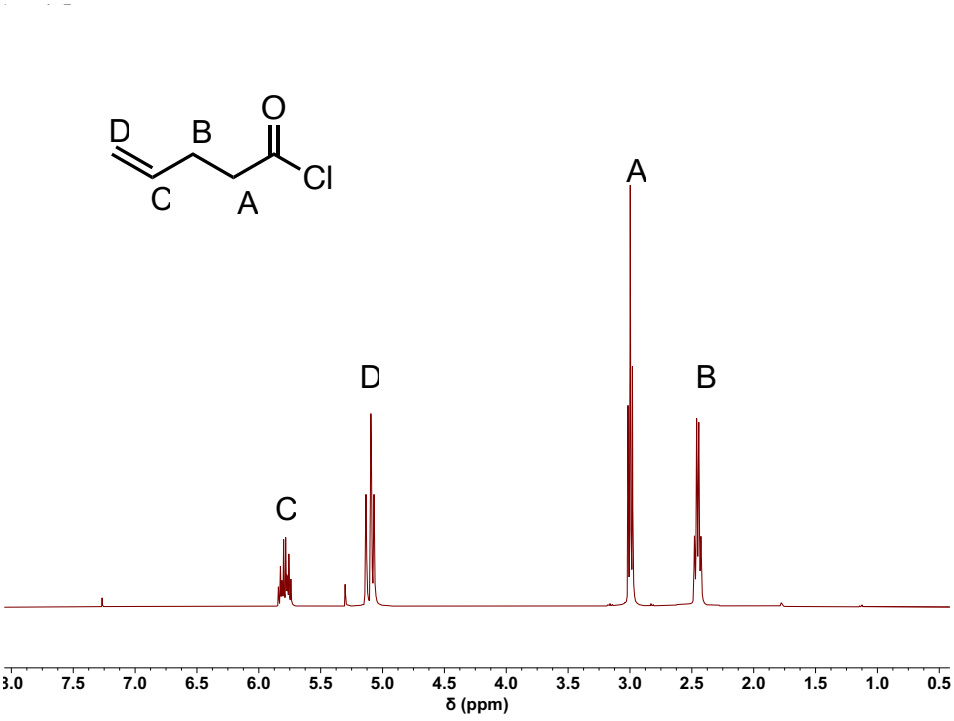

Figure A5.3 ^{1}H NMR (500 MHz, $CDCl_3$) spectra of 4-pentenoyl chloride.

[1]H NMR of Poly(vinyl acetate-co-vinyl pentenoate) P(VAc-co-VP).

Poly(vinyl acetate-*co*-vinyl pentenoate) (P(VAc-*co*-VP)) copolymer with pendant alkene groups was prepared by the esterification of P(VAc-*co*-VA) with 4-pentenoyl chloride. The new peaks between 5.6-5.9 ppm correspond to proton (G) on the alkene group of the VP unit. The molar fraction of VP as well as the residual amount of VAc can be calculated via peak integrations, as shown in Table A5.2.

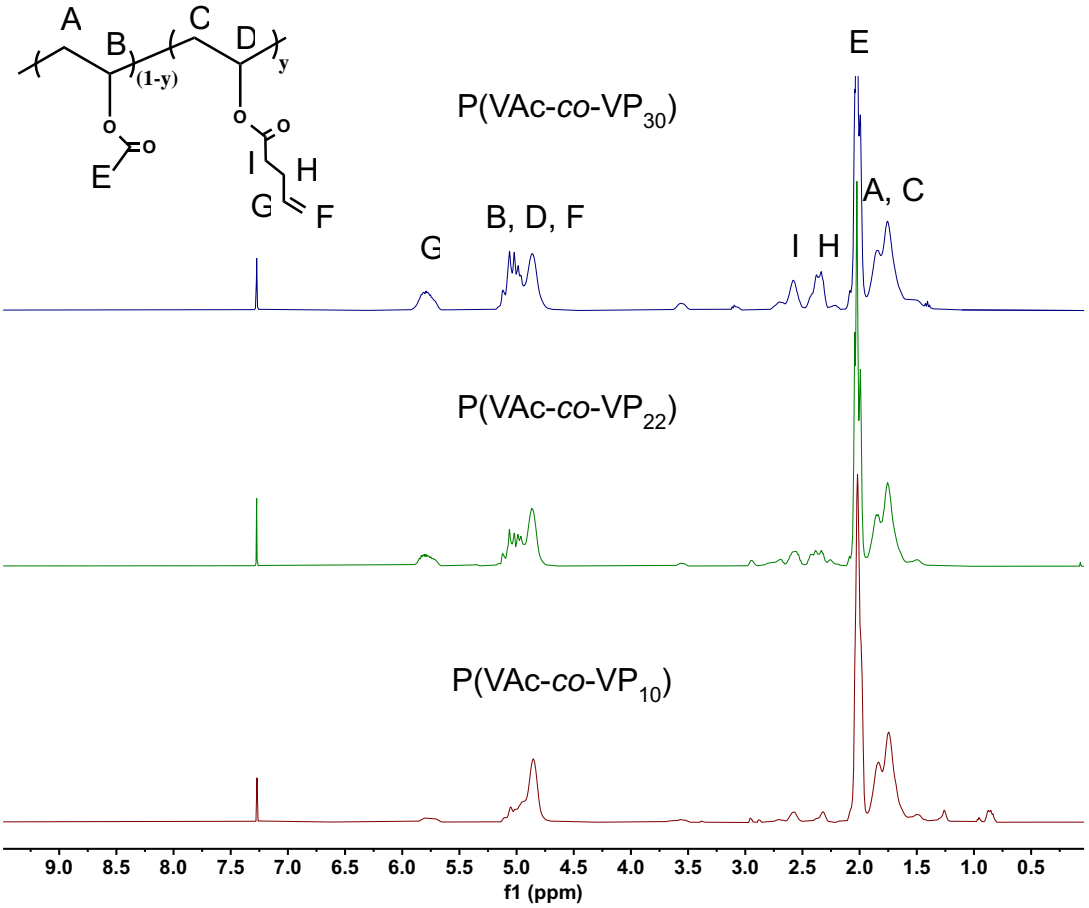

Figure A5.4 ^{1}H NMR (500 MHz, $CDCl_3$) spectra of the different poly(vinyl acetate-co-vinyl pentenoate) (P(VAc-*co*-VP)) copolymers.

Table A5.2 Calculation of the ratio of VP:VAc units and the measured and predicted T_g of the P(VAc-*co*-VP) copolymers.

Sample	VP $\frac{2G}{A+C}$	Residual VAc $\frac{2E}{3(A+C)}$	T_g (°C)	
			Measured	Predicted
P(VAc-*co*-VP_{10})	0.10	0.87	33.2	30.9
P(VAc-*co*-VP_{22})	0.22	0.79	22.8	21.4
P(VAc-*co*-VP_{30})	0.30	0.70	17.6	13.2

Estimation of the glass transition temperature of P(VAc-co-VP) copolymer.

The T_g of P(VAc-*co*-VP) copolymer was estimated by the Fox equation:

$$\frac{1}{T_g} = \frac{w_1}{T_{g,1}} + \frac{w_2}{T_{g,2}}$$

Where w_1 and w_2 are the weight fraction of poly(vinyl acetate) and poly(vinyl pentanoate), respectively. And $T_{g,1}$ and $T_{g,2}$ are the glass transition temperature of polyvinyl acetate (315 K) and polyvinyl pentanoate (248 K), respectively. Both $T_{g,1}$ and $T_{g,2}$ are acquired from Polymer Properties Database.

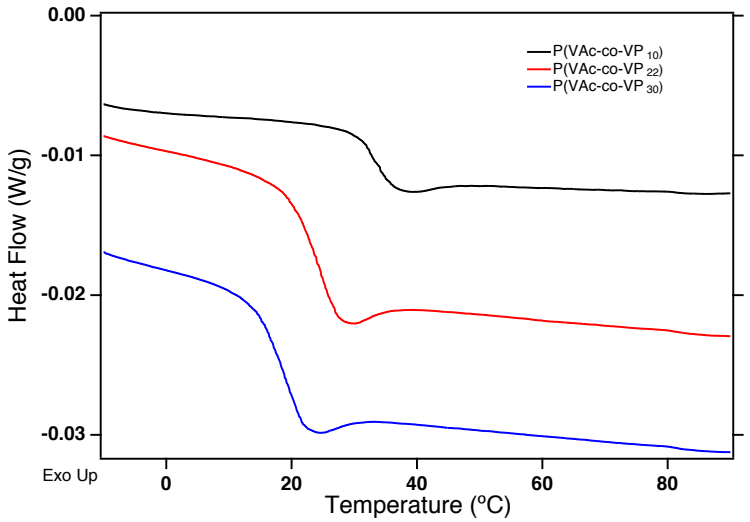

Figure A5.5 DSC of P(VAc-*co*-VP) copolymers with various content of VP units.

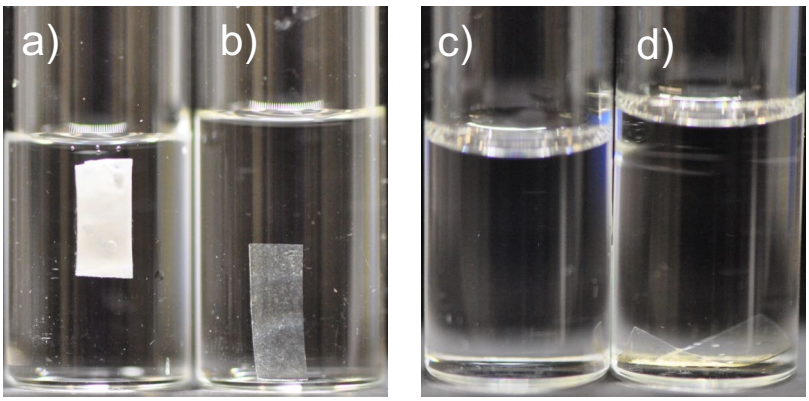

Figure A5.6 Pictures of unexposed (a, c) and UV-irradiated (b, d) /P(VAc-co-VP30)/ t-CNC -COOH nanocomposites after immersion in DMF for 24 hrs (a, b) followed by sonication for 6 hrs (c, d). Sample shown in b and d was irradiated with UV light for 40 min.

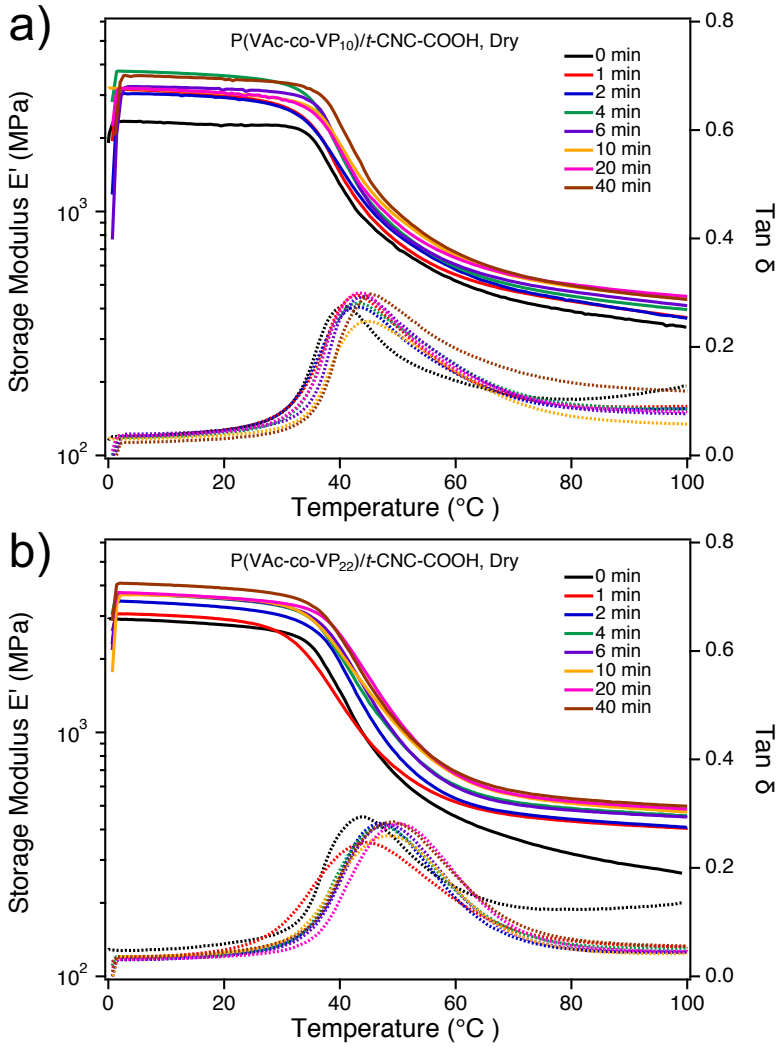

Figure A5.7 Representative DMA temperature sweep study of a) P(VAc-*co*-VP_{10})/*t*-CNC-COOH and b) P(VAc-*co*-VP_{22})/*t*-CNC-COOH nanocomposites in the dry state before and after UV irradiation. (DMA conditions: heating rate 3 °C/min, frequency 1 Hz, strain 0.1 %.)

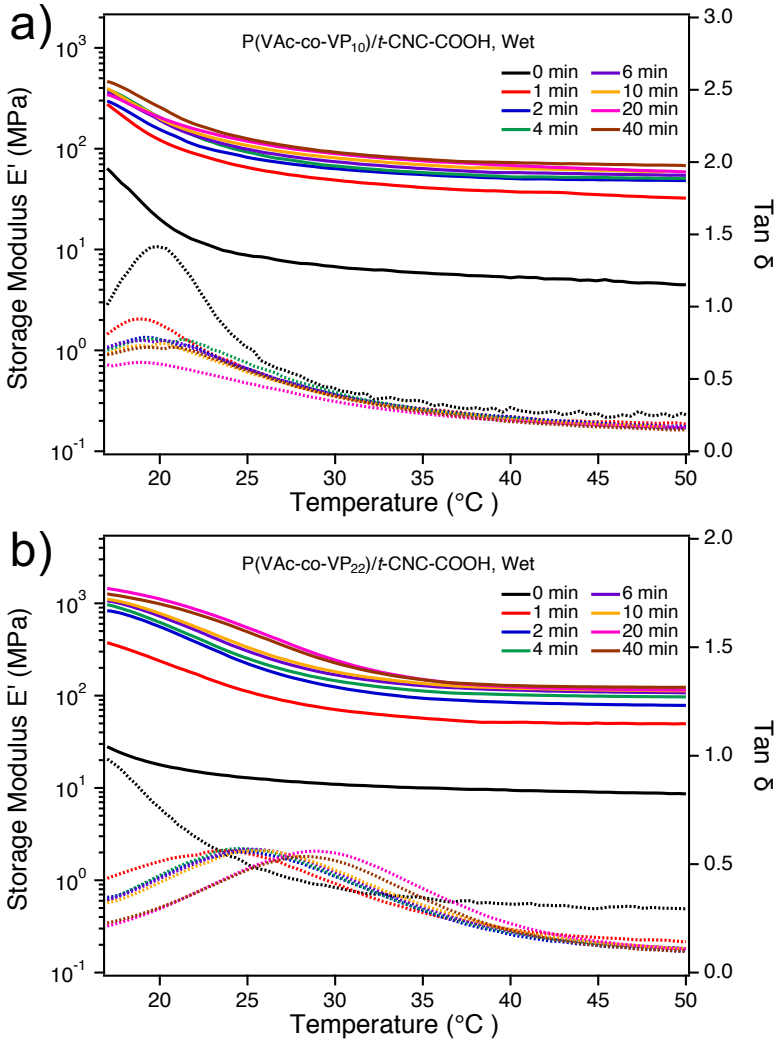

Figure A5.8 Representative DMA temperature sweeps of a) P(VAc-*co*-VP_{10})/*t*-CNC-COOH and b) P(VAc-*co*-VP_{22})/*t*-CNC-COOH nanocomposites in the wet state before and after UV irradiation. (DMA conditions: heating rate 3 °C/min, frequency 1 Hz, strain 0.1 %.)

Table A5.3 Summary of the thermal mechanical property of P(VAc-co-VP_{10})/ *t*-CNC-COOH in both the dry and wet state after different UV irradiation times.

	P(VAc-co-VP_{10})/ *t*-CNC-COOH				
Irradiation time (min)	Dry E' at 80 ℃ MPa	Dry T_g ℃	Wet E' at 50 ℃ MPa	Wet T_g ℃	Water swelling %
0	400 ± 18	40.2 ± 0.8	5.4	19.9	177
1	431 ± 5	42.5 ± 1.3	43 ± 8	20.4 ± 1.5	18 ± 2
2	446 ± 13	41.9 ± 1.5	51 ± 4	20.4 ± 1.4	15 ± 4
4	457 ± 7	43.9 ± 0.6	56 ± 5	20.5 ± 1.3	13 ± 3
6	477 ± 12	43.5 ± 1.0	61 ± 2	20.3 ± 1.5	12 ± 3
10	487 ± 10	43.8 ± 1.0	65 ± 3	21.3 ± 1.5	11 ± 2
20	501 ± 13	44.3 ± 1.1	69 ± 1	21.1 ± 2.4	11 ± 2
40	510 ± 13	44.9 ± 0.9	75 ± 5	21.8 ± 1.7	10 ± 1

Table A5.4 Summary of the thermal mechanical properties of P(VAc-co-VP_{22})/ *t*-CNC-COOH in both the dry and wet state after different UV irradiation times.

	P(VAc-co-VP_{20})/ *t*-CNC-COOH				
Irradiation time (min)	Dry E' at 80 ℃ MPa	Dry T_g ℃	Wet E' at 50 ℃ MPa	Wet T_g ℃	Water swelling %
0	346 ± 47	42.7 ± 1.5	9.2 ± 0.5	17.0 ± 0.0	139 ± 4
1	437 ± 7	45.5 ± 1.3	55 ± 8	23.3 ± 0.6	10 ± 1
2	453 ± 12	47.6 ± 1.0	89 ± 14	24.2 ± 0.2	8.4 ± 1.0
4	473 ± 15	47. 7 ± 3.3	98 ± 4	25.2 ± 0.3	8.4 ± 0.8
6	485 ± 14	48.5 ± 2.2	106 ± 4	25.8 ± 0.8	7.7 ± 0.6
10	512 ± 17	49.2 ± 3.0	110 ± 6	26.4 ± 0.8	7.3 ± 0.2
20	521 ± 10	50.6 ± 3.0	115 ± 5	27.5 ± 1.1	6.9 ± 0.5
40	543 ± 8	50.7 ± 2.9	121 ± 5	28.3 ± 0.5	7.0 ± 0.5

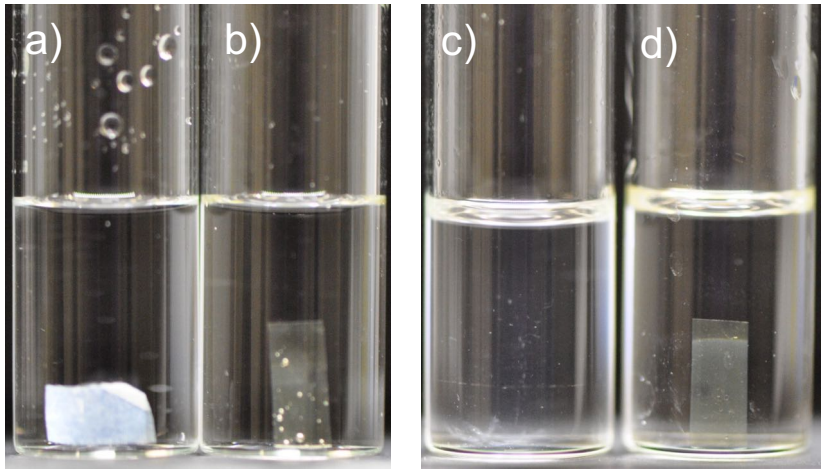

Figure A5.9 Pictures of unexposed (a, c) and UV-irradiated (b, d) /P(VAc-*co*-VP_{30})/ *t*-CNC-allyl-COOH composites after immersion in DMF for 24 hrs (a, b) and after sonication for 6 hrs (c, d). Sample shown in b and d was irradiated to UV light for 40 min.

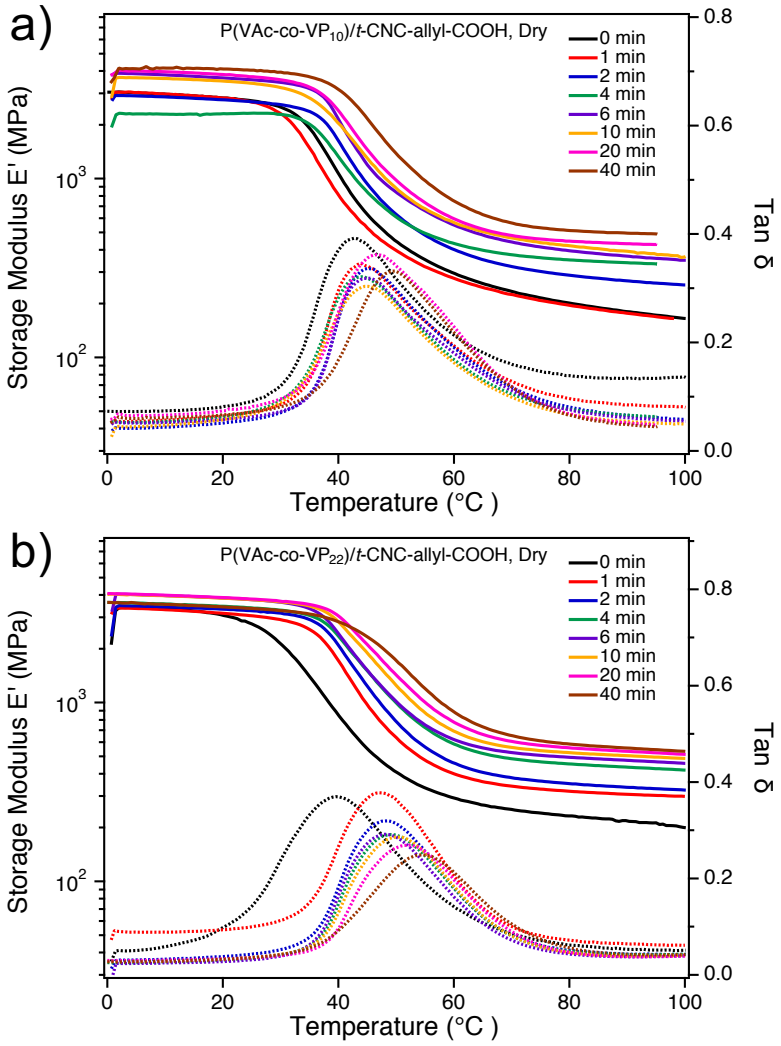

Figure A5.10 Representative DMA temperature sweep study of a) P(VAc-*co*-VP_{10})/*t*-CNC-allyl-COOH and b) (VAc-*co*-VP_{22})/*t*-CNC-allyl-COOH nanocomposites in the dry state before and after UV irradiation. (DMA conditions: heating rate 3 °C/min, frequency 1 Hz, strain 0.1 %.)

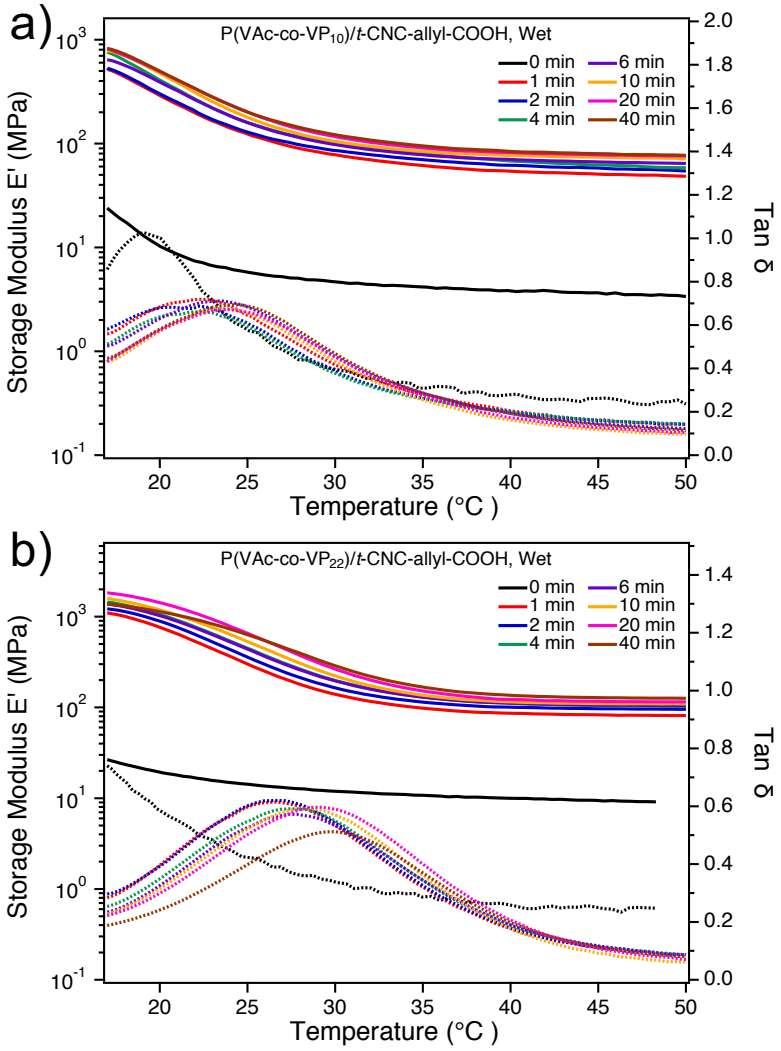

Figure A5.11 Representative DMA temperature sweeps of a) P(VAc-*co*-VP_{10})/*t*-CNC-allyl-COOH and b) (VAc-*co*-VP_{22})/*t*-CNC-allyl-COOH nanocomposites in the wet state before and after UV irradiation. (DMA conditions: heating rate 3 °C/min, frequency 1 Hz, strain 0.1 %.)

Table A5.5 Summary of the thermal mechanical properties of P(VAc-co-VP_{10})/*t*-CNC-allyl-COOH in both the dry and wet state after different UV irradiation times.

	P(VAc-co-VP_{10})/ *t*-CNC-allyl-COOH				
Irradiation time (min)	Dry E' at 80 °C MPa	Dry T_g °C	Wet E' at 50 °C MPa	Wet T_g °C	Water swelling %
0	202 ± 3	41.9 ± 2.2	5.3 ± 0.1	19.5	101 ± 4
1	246 ± 8	44.8 ± 1.5	49 ± 4	22.9 ± 0.9	17 ± 2
2	298 ± 8	45.2 ± 0.9	56 ± 6	23.1 ± 0.4	13 ± 2
4	370 ± 15	44.8 ± 1.8	62 ± 5	23.4 ± 0.3	10 ± 2
6	395 ± 8	45.7 ± 1.2	66 ± 3	23.0 ± 0.7	8 ± 2
10	428 ± 8	45.3 ± 2.0	70 ± 5	23.4 ± 0.6	8 ± 1
20	464 ± 20	46.6 ± 1.0	74 ± 4	23.5 ± 0.5	7 ± 1
40	484 ± 29	47.3 ± 3.0	80 ± 1	24.5 ± 0.3	6 ± 1

Table A5.6 Summary of the thermal mechanical properties of P(VAc-co-VP_{22})/*t*-CNC-allyl-COOH in both the dry and wet state after different UV irradiation times.

	P(VAc-co-VP_{20})/ *t*-CNC-allyl-COOH				
Irradiation time (min)	Dry E' at 80 °C MPa	Dry T_g °C	Wet E' at 50 °C MPa	Wet T_g °C	Water swelling %
0	254 ± 29	35.9 ± 3.7	9.2 ± 0.1	17.1 ± 0.6	92 ± 11
1	314 ± 8.5	45.1 ± 4.2	83 ± 4	26.4 ± 0.3	13 ± 0.5
2	371 ± 21	47.7 ± 1.7	96 ± 3	26.9 ± 0.2	9 ± 2
4	450 ± 27	48.6 ± 0.9	102 ± 3	27.4 ± 0.3	7 ± 0.5
6	497 ± 10	48.0 ± 0.1	105 ± 1	28.1 ± 0.4	6.0 ± 0.1
10	527 ± 31	49.5 ± 0.5	113 ± 5	28.5 ± 0.3	5.6 ± 0.4
20	568 ± 12	51.0 ± 1.0	120 ± 6.0	29.1 ± 0.4	5.7 ± 1.1
40	578 ± 12	54.2 ± 1.4	126 ± 4.0	29.9 ± 0.7	5.7 ± 1.1

5.7 Reference

(1) Dunlop, J. W. C.; Fratzl, P. Biological Composites. *Annu. Rev. Mater. Res.* **2010**, *40* (1), 1–24.

(2) Vincent, J. F. V. Biomimetic Materials. *J. Mater. Res.* **2008**, *23* (12), 3140–3147.

(3) Wegst, U. G. K.; Ashby, M. F. The Mechanical Efficiency of Natural Materials. *Philos. Mag.* **2004**, *84* (21), 2167–2186.

(4) Chen, P. Y.; McKittrick, J.; Meyers, M. A. Biological Materials: Functional Adaptations and Bioinspired Designs. *Progress in Materials Science*. Elsevier Ltd November 1, 2012, pp 1492–1704.

(5) Sun, J.; Bhushan, B. Hierarchical Structure and Mechanical Properties of Nacre: A Review. *RSC Adv.* **2012**, *2* (20), 7617.

(6) Motokawa, T.; Tsuchi, A. Dynamic Mechanical Properties of Body-Wall Dermis in Various Mechanical States and Their Implications for the Behavior of Sea Cucumbers. *Biol. Bull.* **2003**, *205* (3), 261–275.

(7) Koob, T. J.; Koob-Emunds, M. M.; Trotter, J. A. Cell-Derived Stiffening and Plasticizing Factors in Sea Cucumber (Cucumaria Frondosa) Dermis. *J. Exp. Biol.* **1999**, *202* (17), 2291–2301.

(8) Szulgit, G. K.; Shadwick, R. E. Dynamic Mechanical Characterization of a Mutable Collagenous Tissue: Response of Sea Cucumber Dermis to Cell Lysis and Dermal Extracts. *J. Exp. Biol.* **2000**, *203* (10), 1539–1550.

(9) Weaver, J. C.; Milliron, G. W.; Miserez, A.; Evans-Lutterodt, K.; Herrera, S.; Gallana, I.; Mershon, W. J.; Swanson, B.; Zavattieri, P.; DiMasi, E.; Kisailus, D. The Stomatopod Dactyl Club: A Formidable Damage-Tolerant Biological Hammer. *Science.* **2012**, *336* (6086), 1275–1280.

(10) Amini, S.; Tadayon, M.; Idapalapati, S.; Miserez, A. The Role of Quasi-Plasticity in the Extreme Contact Damage Tolerance of the Stomatopod Dactyl Club. *Nat. Mater.* **2015**, *14* (9), 943–950.

(11) Zhao, Y.; Cao, J.; Zhang, Y.; Peng, H. Gradually Crosslinking Carbon Nanotube Array in Mimicking the Beak of Giant Squid for Compression-Sensing Supercapacitor. *Adv. Funct. Mater.* **2019**, 1902971.

(12) Bai, J.; Shi, Z.; Yin, J.; Tian, M.; Qu, R. Shape Reconfiguration of a Biomimetic Elastic Membrane with a Switchable Janus Structure. *Adv. Funct. Mater.* **2018**, *28* (29), 1800939.

(13) Zhao, Z.; Fang, R.; Rong, Q.; Liu, M. Bioinspired Nanocomposite Hydrogels with Highly Ordered Structures. *Adv. Mater.* **2017**, *29* (45), 1703045.

(14) Thompson, C. B.; Chatterjee, S.; Korley, L. S. T. J. Gradient Supramolecular Interactions and Tunable Mechanics in Polychaete Jaw Inspired Semi-Interpenetrating Networks. *Eur. Polym. J.* **2019**, *116*, 201–209.

(15) Montero de Espinosa, L.; Meesorn, W.; Moatsou, D.; Weder, C. Bioinspired Polymer Systems with Stimuli-Responsive Mechanical Properties. *Chem. Rev.* **2017**, *117* (20),

12851–12892.

(16) Wegst, U. G. K.; Bai, H.; Saiz, E.; Tomsia, A. P.; Ritchie, R. O. Bioinspired Structural Materials. *Nat. Mater.* **2015**, *14* (1), 23–36.

(17) Zhang, C.; Mcadams, D. A.; Grunlan, J. C. Nano/Micro-Manufacturing of Bioinspired Materials: A Review of Methods to Mimic Natural Structures. *Adv. Mater.* **2016**, *28* (30), 6292–6321.

(18) Zhou, B. L. Bio-Inspired Study of Structural Materials. In *Materials Science and Engineering C*; Elsevier, 2000; Vol. 11, pp 13–18.

(19) Zhao, H.; Yang, Z.; Guo, L. Nacre-Inspired Composites with Different Macroscopic Dimensions: Strategies for Improved Mechanical Performance and Applications. *NPG Asia Materials*. Nature Publishing Group April 1, 2018, pp 1–22.

(20) Ortiz, C.; Boyce, M. C. MATERIALS SCIENCE: Bioinspired Structural Materials. *Science (80-.).* **2008**, *319* (5866), 1053–1054.

(21) Wang, Z.; Wang, K.; Huang, H.; Cui, X.; Shi, X.; Ma, X.; Li, B.; Zhang, Z.; Tang, X.; Chiang, M. Y. M. Bioinspired Wear-Resistant and Ultradurable Functional Gradient Coatings. *Small* **2018**, *14* (41), 1802717.

(22) Nguyen, J. K.; Park, D. J.; Skousen, J. L.; Hess-Dunning, A. E.; Tyler, D. J.; Rowan, S. J.; Weder, C.; Capadona, J. R. Mechanically-Compliant Intracortical Implants Reduce the Neuroinflammatory Response. *J. Neural Eng.* **2014**, *11* (5), 056014.

(23) Chen, C.; Liu, D.; He, L.; Qin, S.; Wang, J.; Razal, J. M.; Kotov, N. A.; Lei, W. Bio-Inspired Nanocomposite Membranes for Osmotic Energy Harvesting. *Joule* **2020**, *4* (1), 247–261.

(24) Miserez, A.; Schneberk, T.; Sun, C.; Zok, F. W.; Waite, J. H. The Transition from Stiff to Compliant Materials in Squid Beaks. *Science (80-.).* **2008**, *319* (5871), 1816–1819.

(25) Miserez, A.; Li, Y.; Waite, J. H.; Zok, F. Jumbo Squid Beaks: Inspiration for Design of Robust Organic Composites. *Acta Biomater.* **2007**, *3* (1), 139–149.

(26) Miserez, A.; Rubin, D.; Waite, J. H. Cross-Linking Chemistry of Squid Beak. *J. Biol. Chem.* **2010**, *285* (49), 38115–38124.

(27) Cai, H.; Gabryelczyk, B.; Manimekalai, M. S. S.; Grüber, G.; Salentinig, S.; Miserez, A. Self-Coacervation of Modular Squid Beak Proteins – a Comparative Study. *Soft Matter* **2017**, *13* (42), 7740–7752..

(28) Tan, Y.; Hoon, S.; Guerette, P. A.; Wei, W.; Ghadban, A.; Hao, C.; Miserez, A.; Waite, J. H. Infiltration of Chitin by Protein Coacervates Defines the Squid Beak Mechanical Gradient. *Nat. Chem. Biol.* **2015**, *11* (7), 488–495.

(29) Zvarec, O.; Purushotham, S.; Masic, A.; Ramanujan, R. V.; Miserez, A. Catechol-Functionalized Chitosan/Iron Oxide Nanoparticle Composite Inspired by Mussel Thread Coating and Squid Beak Interfacial Chemistry. *Langmuir* **2013**, *29* (34), 10899–10906.

(30) Zhang, X.; Hassanzadeh, P.; Miyake, T.; Jin, J.; Rolandi, M. Squid Beak Inspired Water Processable Chitosan Composites with Tunable Mechanical Properties. *J. Mater. Chem. B* **2016**, *4* (13), 2273–2279.

(31) Neal, J. A.; Oldenhuis, N. J.; Novitsky, A. L.; Samson, E. M.; Thrift, W. J.; Ragan, R.; Guan,

Z. Large Continuous Mechanical Gradient Formation via Metal-Ligand Interactions. *Angew. Chemie Int. Ed.* **2017**, *56* (49), 15575–15579.

(32) Claussen, K. U.; Giesa, R.; Schmidt, H.-W. Longitudinal Polymer Gradient Materials Based on Crosslinked Polymers. *Polymer (Guildf).* **2014**, *55* (1), 29–38.

(33) Wang, D.; Zhang, H.; Guo, J.; Cheng, B.; Cao, Y.; Lu, S.; Zhao, N.; Xu, J. Biomimetic Gradient Polymers with Enhanced Damping Capacities. *Macromol. Rapid Commun.* **2016**, *37* (7), 655–661.

(34) Fleckman, P.; Olerud, J. E. Models for the Histologic Study of the Skin Interface with Percutaneous Biomaterials. *Biomed. Mater.* **2008**, *3* (3), 034006.

(35) Lu, H. H.; Thomopoulos, S. Functional Attachment of Soft Tissues to Bone: Development, Healing, and Tissue Engineering. *Annu. Rev. Biomed. Eng.* **2013**, *15* (1), 201–226.

(36) Jorfi, M.; Skousen, J. L.; Weder, C.; Capadona, J. R. Progress towards Biocompatible Intracortical Microelectrodes for Neural Interfacing Applications. *Journal of Neural Engineering*. IOP Publishing February 1, 2015, p 011001.

(37) Shoffstall, A. J.; Capadona, J. R. Bioinspired Materials and Systems for Neural Interfacing. *Current Opinion in Biomedical Engineering*. Elsevier B.V. June 1, 2018, pp 110–119.

(38) Fox, J. D.; Capadona, J. R.; Marasco, P. D.; Rowan, S. J. Bioinspired Water-Enhanced Mechanical Gradient Nanocomposite Films That Mimic the Architecture and Properties of the Squid Beak. *J. Am. Chem. Soc.* **2013**, *135* (13), 5167–5174.

(39) Zhang, Y.; Edelbrock, A. N.; Rowan, S. J. Effect of Processing Conditions on the Mechanical Properties of Bio-Inspired Mechanical Gradient Nanocomposites. *Eur. Polym. J.* **2019**, *115*, 107–114.

(40) Biyani, M. V.; Jorfi, M.; Weder, C.; Foster, E. J. Light-Stimulated Mechanically Switchable, Photopatternable Cellulose Nanocomposites. *Polym. Chem.* **2014**, *5* (19), 5716–5724.

(41) Parambath Kanoth, B.; Claudino, M.; Johansson, M.; Berglund, L. A.; Zhou, Q. Biocomposites from Natural Rubber: Synergistic Effects of Functionalized Cellulose Nanocrystals as Both Reinforcing and Cross-Linking Agents via Free-Radical Thiol-Ene Chemistry. *ACS Appl. Mater. Interfaces* **2015**, *7* (30), 16303–16310.

(42) Blanchard, R.; Ogunsona, E. O.; Hojabr, S.; Berry, R.; Mekonnen, T. H. Synergistic Cross-Linking and Reinforcing Enhancement of Rubber Latex with Cellulose Nanocrystals for Glove Applications. *ACS Appl. Polym. Mater.* **2020**, *2* (2), 887–898.

(43) Park, J. W.; Im, S. S. Miscibility and Morphology in Blends of Poly(L-Lactic Acid) and Poly(Vinyl Acetate-Co-Vinyl Alcohol). *Polymer (Guildf).* **2003**, *44* (15), 4341–4354.

(44) Isasi, J. R.; Cesteros, L. C.; Katime, I. Hydrogen Bonding and Sequence Distribution in Poly(Vinyl Acetate-Co-Vinyl Alcohol) Copolymers. *Macromolecules* **1994**, *27* (8), 2200–2205.

(45) Ding, N.; Shentu, B.; Pan, P.; Shan, G.; Bao, Y.; Weng, Z. Synthesis and Crystallization of Poly(Vinyl Acetate)- g -Poly(l -Lactide) Graft Copolymer with Controllable Graft Density. *Ind. Eng. Chem. Res.* **2013**, *52* (36), 12897–12905.

(46) An, S. Y.; Lee, D. G.; Hwang, J. W.; Kim, K. N.; Nam, J. H.; Jung, H. W.; Noh, S. M.; Oh,

J. K. Photo-Induced Thiol-Ene Polysulfide-Crosslinked Materials with Tunable Thermal and Mechanical Properties. *J. Polym. Sci. Part A Polym. Chem.* **2014**, *52* (21), 3060–3068.

(47) Wiley, K. L.; Ovadia, E. M.; Calo, C. J.; Huber, R. E.; Kloxin, A. M. Rate-Based Approach for Controlling the Mechanical Properties of "thiol-Ene" Hydrogels Formed with Visible Light. *Polym. Chem.* **2019**, *10* (32), 4428–4440.

(48) Menard, K. P.; Menard, N. Dynamic Mechanical Analysis. In *Encyclopedia of Analytical Chemistry*; John Wiley & Sons, Ltd: Chichester, UK, 2017; pp 1–25.

(49) Wu, Z. L.; Moshe, M.; Greener, J.; Therien-Aubin, H.; Nie, Z.; Sharon, E.; Kumacheva, E. Three-Dimensional Shape Transformations of Hydrogel Sheets Induced by Small-Scale Modulation of Internal Stresses. *Nat. Commun.* **2013**, *4* (1).

Chapter 6. Bio-inspired Mechanical Adaptive Nanocomposite with Large Modulus Gradient.

6.1 Introduction:

Evolution of biological systems has led to a great variety of biomaterials that display a wide range of remarkable properties that have designed to overcome specific challenges.[1–3] Among these properties, mechanical gradients are commonly utilized by nature to provide a smooth transition between tissues with significantly different mechanical properties and are critical at minimizing interfacial damage.[4,5] These gradients are generally achieved by varying the local chemical compositions of different components (chemical gradient),[6–9] or controlling the orientation, arrangement, and distribution of the building blocks (structural gradient).[10–14] Mimicking the gradient structures offers new opportunities for scientists to develop synthetic composite materials that can address a number of issues, such as increasing distribution of mechanical stress at interface, improving connection of mechanical dissimilar components and reducing contact deformation and damage.[15–18] These bioinspired composite materials are particularly valuable for biomedical applications where stiff implants are commonly in close contact with soft tissues.[19–22]

The potential of developing synthetic composite materials with mechanical gradient properties has been well illustrated in the recent literature. Composite films with layered or lateral mechanical gradients have been prepared using a segmented fabrication process in which the mechanical properties of each segment are varied.[23–26] For example, Raghhavan and co-workers recently reported the preparation of hybrid hydrogels containing mechanically distinct zones of polydimethylacrylamide with a 100-fold difference in shear modulus between stiff and soft zones

as controlled by varying the concentrations of laponite (LAP) and silane crosslinkers in the hydrogel formaulation.[26] However, only non-continuous gradients can be achieved using this approach. Other reports have focused on the fabrication of a smooth transition in mechanical properties, such as those that include controlling the degree of alignment of carbon nanotube (CNT) along the lateral direction,[27,28] varying the concentration of nanofillers through magnetic field,[29,30] and controlling the degree of chemical crosslinking within the films.[31–36] It should be noted that many of these materials suffer from only a small contrast in mechanical properties (around 1 order of magnitude), and/or required special equipment and process to fabricate. There is an interesting work reported by Guan and co-workers on the preparation of mechanical gradient materials using metal-ligand crosslinks which resulted in a continuous gradient that span over a 200-fold difference in stiffness.[35] However, the process relies on pulling the samples through a metal ion solution with a syringe pump over two days to create the mechanical gradients, which is time-consuming for large scale material synthesis and lacks the versatility to allow access to complex gradient structures within the materials.

In prior work, we have reported the fabrication of polymer nanocomposites with water-enhanced mechanical gradient properties that have been inspired by the beak of Humboldt squid.[37–39] The squid beak is an interesting biocomposite that consists exclusively of chitin, proteins and water.[40] Unlike other biomodels which utilize biomineralization,[41,42] metal ion crosslinking[43] or protein halogenation,[44] the extraordinary stiffness gradient that spans two order of magnitude between the soft buccal base (elastic modulus 50 MPa) and stiff rostrum (elastic modulus 5 GPa) is achieved by varying the level of hydration and degree of covalent crosslinking of the protein matrix along the gradient.[9,45,46] To mimic such gradient properties, a synthetic analogue consisting of allyl-functionalized cellulose nanocrystals (CNC) embedded into poly(vinyl acetate-*co*-vinyl-

pentenoate) (PVAc-*co*-VP) polymer matrix along with a tetrathiol crosslinker (pentaerythritol tetrakis(3-mercaptopropionate), PETMP) have been prepared.[39] The degree of crosslinking between the CNC fillers and the polymer matrix was controlled by photo-induced thiol-ene chemistry which yield materials with tunable mechanical properties. In the dry state, the CNC fillers can form a strong percolating network and good filler-matrix interactions through hydrogen bonding interactions, resulting in significant mechanical reinforcement of the nanocomposites and as such only a small increase in modulus is observed after crosslinking. However, the modulus of the uncrosslinked materials drops dramatically upon exposure to water on account of the water plasticization effect of the polymer matrix and a disruption of the hydrogen bonding between the CNCs (and CNCs and matrix). The hydration-induced softening is greatly reduced with increase in the degree of covalent crosslinking allowing access to stiff wet film with a modulus of 289 MPa at 37 ℃ and a 20 times difference in wet modulus (E'_{stiff}/E'_{soft} ca.20) between stiff (crosslinked) and soft (uncrosslinked) materials.

It is worth pointing out that the PVAc-*co*-VP/tCNC-allyl-COOH based nanocomposites still suffer from a relatively low modulus contrast as compared to what is achieved in the other synthetic materials and the squid beak biomodel. The use of ally-functionalization of the CNCs along with that addition of the vinyl-pentenoate repeat unit on the matrix backbone resulted in more hydrophobic films that showed greatly reduced water uptake. As such the uncrosslinked films of these more hydrophobic materials show limited water swelling and resulted in films with a higher "soft state" modulus which limits the overall mechanical contrast that can be achieved. To address these issues and further optimize the wet mechanical gradient of this class of bioinspired composites, reported herein are the design and preparation of our next-generation bio-inspired nanocomposites based on carboxylic acid functionalized tCNC-COOH and partially hydrolyzed

poly(vinyl acetate-*co*-vinyl alcohol) (PVAc-*co*-VA) matrix. A commercially available glycoluril-based crosslinker (1,3,4,6-tetrakis(methoxymethyl)glycoluril, TMMGU) was utilized and the covalent crosslinking between the crosslinker with the hydroxyl groups from both the CNCs and polymer matrix was initiated by a photoacid generator (PAG). Using poly(vinyl acetate-*co*-vinyl alcohol) (PVAc-*co*-VA) as matrix can decrease the modulus in the soft uncrosslinked materials as a result of the strong hydrophilicity of the polymer which then further enlarge the modulus contrast between the stiff and soft regions. The aim of this study is to have a better understanding of how the UV irradiation conditions and the hydroxyl content influence the mechanical properties of the PVAc-*co*-VA/tCNC-COOH nanocomposite in both dry and wet states. The potential of accessing continuous mechanical gradients and programming complex gradient by photo-patterning process have also been investigated.

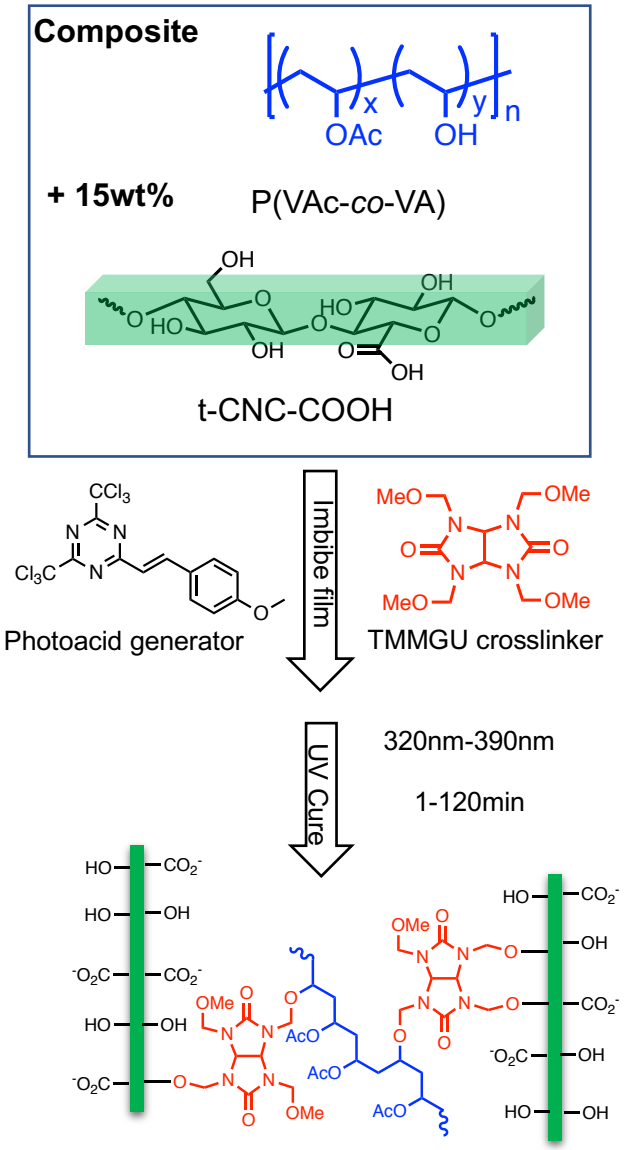

Scheme 6.1 Schematic of the preparation of bio-inspired nanocomposites based on P(VAc-*co*-VA) and tCNC-COOH, and the proposed photo-initiated crosslinking reactions between the polymer matrix and CNC filler.

6.2 Experimental Section

Materials

1,3,4,6-Tetrakis(methoxymethyl)glycoluril (TMMGU) crosslinker was purchased from TCI Chemical. The photoacid generator (PAG) 2-(4-Methoxystyryl)-4,6-bis(trichloromethyl)-1,3,5-

triazine was purchased from Sigma-Aldrich. All the other solvents were purchased from Fisher Scientific. TEMPO-oxidized cellulose nanocrystals (tCNC-COOH) with a charge density of 1000 mmol/kg were obtained from sea tunicate mantles using the procedures published in previous work.[37] Poly(vinyl acetate-*co*-vinyl alcohol) P(VAc-*co*-VA) copolymers with various degrees of hydrolysis were synthesized and characterized in previous work.[39]

Fabrication of P(VAc-co-VA) films and P(VAc-co-VA)/tCNC-COOH nanocomposites

P(VAc-*co*-VA) copolymer films were prepared by compression molding between two PTFE supporting sheets at 90 °C and 4000 psi for 10 min using a Carver laboratory press. A transparent film with thickness between 100 and 150 μm was obtained.

P(VAc-*co*-VA)/tCNC-COOH nanocomposites were fabricated by solution casting from DMF. tCNC-COOH was dispersed in DMF at a concentration of 3 mg/mL via sonication overnight in a bath sonicator follower by ultrasonication for 30 mins using a Branson SFX 550 Sonifier. P(VAc-*co*-VA) was dissolved in DMF at a concentration of 50 mg/mL by stirring for 4 hrs. The appropriate amount of tCNC-COOH dispersion and P(VAc-*co*-VA) solution were combined to yield 15 wt.% of CNC in the final composite films and ultrasonicated for 30 min before casting into PTFE dishes. The mixtures were dried in a vacuum oven at 60 °C for 5 days to fully remove the DMF. The dried nanocomposite films were removed from the PTFE dishes and used as-cast without any melt processing. Thermogravimetric analysis (TGA) was used to confirm the removal of DMF.

Imbibing process

Nanocomposites were cut into rectangular samples with dimensions of 30 x 4 mm. Stock solutions of the photoacid generator (PAG) 2-(4-Methoxystyryl)-4,6-bis(trichloromethyl)-1,3,5-triazine (5 mM) and crosslinker (1,3,4,6-Tetrakis(methoxymethyl)glycoluril, TMMGU) (50 mM) were prepared by dissolving the reagents in THF separately. The required amount of PAG (2 mol% of OH groups) and TMMGU crosslinker (25 mol% of OH groups to give a 1:1 methoxy to OH ratio) was calculated based on the molar amount of total hydroxyl groups from both the polymer matrix and CNC fillers (surface hydroxyl groups ca. 1800 mmol/kg). Composite films were supported on PTFE dishes, and the exact volume of stock solution and PAG and crosslinker were evenly pipetted onto the film until the solution was absorbed. The samples were then annealed in saturated THF vapor for 24 hrs to ensure a more homogeneous distribution of the PAG and crosslinkers within the sample. Finally, the samples were removed from THF vapor and dried in a dark environment under reduced pressure for 48 hrs.

UV curing process

The crosslinking reaction was performed by irradiating the imbibed samples using a Honle Bluepoint UV source (320-390 nm) with an intensity of 40 mW/cm^2 for times ranging from 1 to 120 min. All films were irradiated on both sides by flipping the samples at the midpoint of the reaction to endure a more homogeneous distribution of crosslinking throughout the thickness of the film. The irradiated nanocomposites were then soaked in 2-propanol for 24hrs with the goal of removing any unreacted species. The solution was exchanged twice with fresh 2-propanol during this washing step. Finally, the films were removed and dried in a well-ventilated fume hood for 24 hrs before being placed in a vacuum oven for 48 hrs at 40 °C to remove any residual solvent.

Characterization

Differential scanning calorimetry (DSC). DSC measurements were performed using a TA Instruments Discovery 2500 DSC. All samples were first heated to 100 °C and cooled down to 0 °C at a rate of 10 °C min^{-1}. And then the samples were heated back up again from 0 °C to 100 °C at a rate of 10 °C min^{-1}. The second heating cycle was used for data analysis.

Dynamic mechanical analysis (DMA). The viscoelastic properties of nanocomposites were analyzed using a RSA-G2 solid analyzer (TA Instrument, DE) equipped with a tension clamp and a submersion chamber. Dynamic temperature sweep measurements were performed with a fixed frequency of 1 Hz, a strain of 0.1%, a preload force of 0.1 N, and a 125% force track. For characterizing the dry modulus of the composite films, only the tension camp was used and the storage modulus, loss modulus as well as tan δ were measured while the temperature increased from 0 °C to 100 °C at a heating rate of 3 °C min^{-1}. In the case of wet properties, all samples were first pre-swollen in water for 48 hrs and the characterizations were performed using the submersion chamber which allows the measurements to be conducted while the films were fully immersed in water. The temperature of the water was heated from 17 °C to 50 °C at a rate of 3 °C min^{-1} while the wet mechanical properties were being measured.

Water swelling. Dry composite samples were weighed to obtain the dry mass before immersing into DI water for 48 hrs at 45 °C. The samples were then removed, gently blotted using filter paper, and weighed again to obtain the wet mass. The degree of swelling can be calculated by:

$$\%swelling = \frac{wet\ mass - dry\ mass}{dry\ mass} \times 100$$

6.3 Results and Discussion

6.3.1 UV-initiated crosslink of P(VAc-*co*-VA) copolymer matrix

Poly(vinyl acetate-*co*-vinyl alcohol) P(VAc-*co*-VA_x) copolymers, where x is the mole percent of VA, were prepared by partial hydrolysis of PVAc under acidic conditions.[39] A series of P(VAc-*co*-VA_x) copolymers with different mole percent of VA units (x=10, 21, 29) were prepared with the goal of controlling the amount of crosslinkable groups as well as optimizing the hydrophilicity of the polymer. UV-initiated crosslinking reaction was first carried out on the copolymer films (without any CNC filler) to demonstrate the possibility of forming covalent crosslink networks with the TMMGU crosslinker. To this end, P(VAc-*co*-VA_{10}), P(VAc-*co*-VA_{21}) and P(VAc-*co*-VA_{29}) were imbibed with the TMMGU crosslinking units and photoacid generator (PAG) and at a mole ratio of OH : TMMGU: PAG = 100: 25 : 2, such that there is a mole ratio of one hydroxyl moiety on the polymer per one methoxymethyl moiety (on the TMMGU crosslinker) . The imbibed films were irradiated with 320-390 nm UV at an intensity of 40 mW/cm^2 for 240 s. After washing in 2-propanol to remove residual crosslinkers followed by drying at 40 °C under vacuum, the thermomechanical properties of the films were characterized by dynamic mechanical analysis (DMA).

DMA temperature sweep studies of dry P(VAc-*co*-VA_{21}) and P(VAc-*co*-VA_{29}) copolymer films before and after UV irradiation were shown in Figure 6.1a. In the glassy regime, the dry P(VAc-*co*-VA) films showed similar storage modulus (E') between 2.7 and 3 GPa (measured at 20 °C) before and after UV irradiation. However, at higher temperatures, a rubbery plateau can be observed for films after UV irradiation, consistent with the formation of a crosslink network. The storage modulus (E') in the rubbery regime (measured at 80 °C) also increased from 0.7 MPa to 5.8 MPa for P(VAc-*co*-VA_{21}), and from 0.9 MPa to 12.6 MPa for P(VAc-*co*-VA_{29}) as a result of

the UV-initiated crosslinking. The higher plateau E' for P(VAc-*co*-VA$_{29}$) films indicates that the dry mechanical properties in the rubber regime are affected by the hydroxyl content within the polymer. The successful formation of covalent crosslink networks can be further backed up by the increase in glass transition temperatures T_g as measured by the peak of the tan δ curve since the covalent interactions can potentially hinder the polymer chain movements.[47] The T_g increased from 54 °C to 67 °C for P(VAc-*co*-VA$_{21}$) after UV irradiation, while the irradiated P(VAc-*co*-VA$_{29}$) film exhibited an even higher T_g at 80 °C.

It is worth pointing out that the tan δ curve of P(VAc-*co*-VA$_{21}$) and P(VAc-*co*-VA$_{29}$) showed similar peaks at ca. 54 °C, which is inconsistent with the fact that higher content of hydroxyl groups could form hydrogen bonding interactions which increase the T_g. DSC analysis was then performed on the as-synthesized copolymers, and the results revealed that increasing hydroxyl contents indeed lead to an increase in T_g (Figure A6.1).

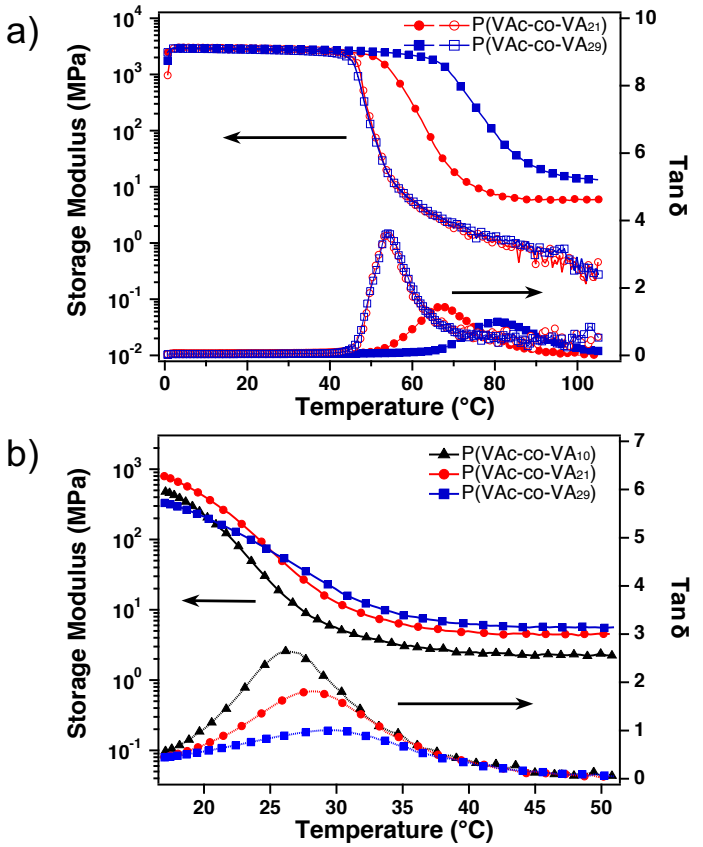

Figure 6.1 DMA temperature sweep study of P(VAc-*co*-VA) film before (open symbol) and after UV irradiation (close symbol) in both a) dry and b) wet state. (DMA condition: heating rate 3 °C/min, frequency 1 Hz, strain 0.1 %.)

The thermal-mechanical properties of wet films as measured by submersion DMA were shown in Figure 6.1b. Characterization of the non-irradiated polymer films was not carried out since the samples disintegrated in water during initial swelling on account for the strong hydrophilic nature of these films. For irradiated films, the formation of covalent networks between the hydroxyl groups successfully prevented the samples from disintegrating in water. A clear shift of the peak of tan δ to lower temperature (26-30 °C) can be observed as opposed to the dry films which is likely a consequence of the water plasticization the copolymers. It can also be observed that P(VAc-*co*-VA$_{29}$) films with the highest content of VA units exhibited the highest T_g after UV irradiation. The plateau modulus (E') of the wet crosslinked films (measured at 37 °C) also

increased systematically from 2.9 MPa to 5.9 MPa as the VA content increased from 10 to 29 mol percent. The DMA results indicated that the wet mechanical properties are affected by both the hydrophilic nature of the polymer as well as the degree of covalent crosslinking. However, the plateau moduli of the crosslinked polymer films are relatively low in both dry and wet states which could limit their applications as functional materials. A possible route to further improve the mechanical properties of the materials is to employ a polymer nanocomposite structure, which is also commonly observed in biological systems.

6.3.2 Crosslink of P(VAc-*co*-VA)/tCNC-COOH nanocomposites

Having proved that covalent crosslinked networks can be successfully formed in the P(VAc-*co*-VA) copolymer upon UV irradiation using PAGs and TMMGU crosslinkers, the next step was to utilize this crosslinking process to prepare P(VAc-*co*-VA)/tCNC-COOH nanocomposites with tunable mechanical properties. This was achieved using composite films containing 15 wt% of tCNC-COOH embedded into P(VAc-*co*-VA) polymer matrix which was imbibed with PAGs and TMMGU crosslinkers as described previously. The amount of TMMGU was adjusted with respect to the total hydroxyl groups from both the copolymer matrix and the surface hydroxyl groups from the CNC fillers (ca. 1800 mmol//kg calculated based on the crystal dimensions of tunicate CNC, 1000 out of the 1800 mmol/kg hydroxyl groups have been oxidized into carboxylate groups).[48,49] The total hydroxyl and carboxylate groups from CNCs correspond to ca. 0.27×10^{-3} mmol/mg based on the weight of the nanocomposites, as opposed to the hydroxyl content from the P(VAc-*co*-VA_x) matrix which equals to 1.22×10^{-3} mmol/mg, 2.58×10^{-3} mmol/mg and 4.09×10^{-3} mmol/mg for x = 10, 21 and 29, respectively. The imbibed composite samples were irradiated with UV light on both

sides for times ranging from 1 to 120 min with the goal of controlling the degree of crosslinking with the composites.

Mechanical properties of these nanocomposites in both dry and wet states were characterized by DMA and the effect of irradiation time on the tunability of storage modulus examined. The temperature dependency of the storage modulus (E') and tan δ of nanocomposites with various content of hydroxyl groups after UV irradiation in the dry state are shown in Figure 6.2 and Figure A6.3. The DMA curves clearly show that UV irradiation leads to a change of the thermal-mechanical properties of the nanocomposites which is consistent with the formation of covalent crosslink networks, namely increasing the T_g (peak of tan δ) and the plateau modulus (E') at temperatures higher than T_g. Specifically, the peak of tan δ shifted to a higher temperature with the time of UV irradiation which is consistent with an increasing degree of crosslinking within the films. The result is also in agreement with our previous work on nanocomposites crosslinked by thiol-ene chemistry, where an increase T_g was observed with an increase degree of covalent crosslinking between the polymer matrix as well as between matrix and fillers.[39] The relative increase in T_g before and after UV irradiation was also impacted by the VA content in the P(VAc-*co*-VA) matrix. For example, nanocomposites containing P(VAc-*co*-VA_{21}) exhibited an increase of T_g from 50 °C to 60 °C after 120 min UV irradiation as opposed to P(VAc-*co*-VA_{29}) which had a T_g of 62 °C under the same irradiation time. The slightly higher T_g is consistent with the expected increase in the degree of crosslinking within the P(VAc-*co*-VA_{29}) nanocomposites.

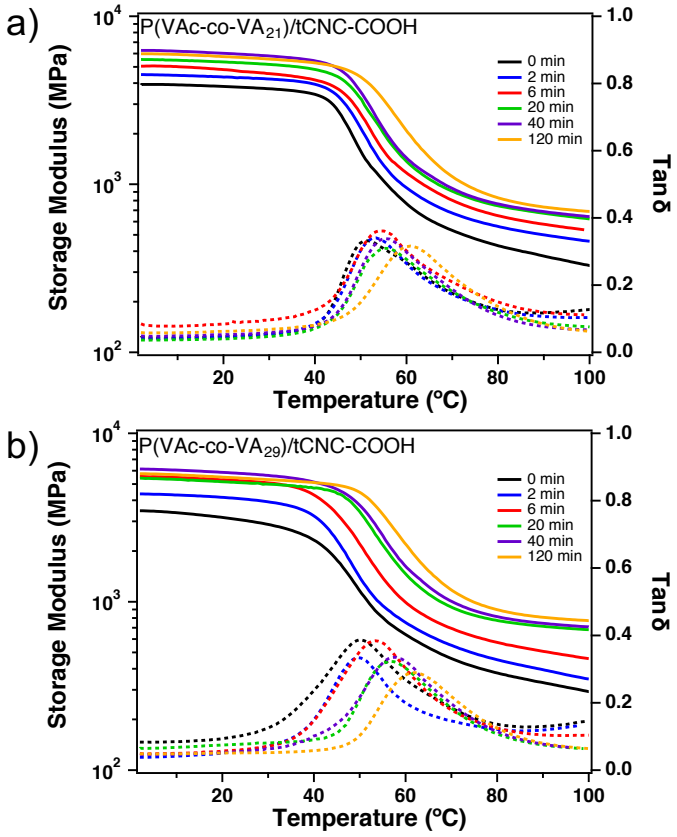

Figure 6.2 Representative DMA temperature sweep study of a) P(VAc-*co*-VA_{21})/tCNC-COOH and b) P(VAc-*co*-VA_{29})/tCNC-COOH nanocomposites in the dry state before and after UV irradiation (full DMA data with more time points is shown in Figure S2).

In addition to the increase in T_g, the plateau modulus (E') in the rubbery regime also increases after UV irradiation. Figure 6.3 plots the plateau modulus (E') (measured at 80 °C) of the composite samples versus UV irradiation time. As can be seen from the graph, the modulus of dry films can be well-controlled by varying the time of UV irradiation. Comparison of the dry E' before (0 min, E'_{soft}) and after UV irradiation (120 min, E'_{stiff}) demonstrate a relatively small increase in the plateau modulus as a result of the formation of covalent crosslink network. For example, the plateau modulus (E') of the P(VAc-*co*-VA_{29})/tCNC-COOH nanocomposites increased from ca. 380 MPa to ca. 890 MPa after 120 min of irradiation which shows a mechanical contrast (E'_{stiff}/ E'_{soft}) of ca. 2.3. Nanocomposites with lower content of VA units display a smaller mechanical

contrast of ca. 2.0 and 1.7 for P(VAc-*co*-VA$_{21}$) (*E′* increased from ca. 420 MPa to 840 MPa) and ca. 1.7 for P(VAc-*co*-VA$_{10}$) (*E'* increased from ca. 450 MPa to 760 MPa), respectively. The result is consistent with the above study on covalently crosslinking the polymer only which exhibited a small increase in plateau storage modulus. However, in the CNC nanocomposites, the mechanical properties are dramatically enhanced as a result of the strong hydrogen bonding interactions between the polymer matrix and the CNC fillers as well as between CNC fillers in addition to the matrix-matrix interactions. The plateau modulus was further improved after UV initiated crosslink reaction on account for the additional covalent bonds formed along with the noncovalent networks.

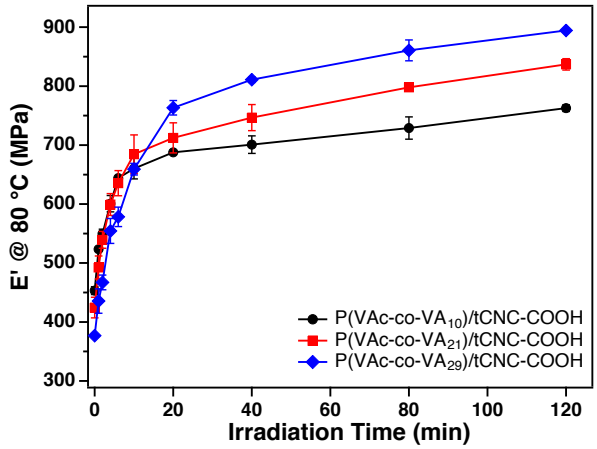

Figure 6.3 Plateau storage modulus *E′* at 80 °C of various P(VAc-*co*-VA)/tCNC-COOH nanocomposites at different UV irradiation times.

The covalent crosslink networks also promote changes to the mechanical properties of the wet nanocomposites in a similar trend as compared to the dry crosslinked films. As can be seen from the DMA temperature sweep studies of the water-swollen samples before and after UV irradiations (Figure 6.4 and Figure A6.5), both the peak of tan δ and plateau storage modulus (*E′*) of the wet films increased with the time of UV irradiation. However, the T_g of the wet nanocomposites are

much lower than the dry materials and only the T_g of nanocomposites irradiated longer than 80 min can be detected within the temperature range (16-50 °C) of the submersion DMA test. The relatively low T_g for less-crosslinked samples is attributed to the water swelling of the composite and plasticization of the polymer matrix as a result of the strong hydrophilic nature of the material. The increased T_g of the wet composite films to ca. 20-22 °C after 80-120 min of UV irradiation is presumably due to the covalent crosslink network formed within materials, as can be observed from the decreasing in the degree of water swelling.

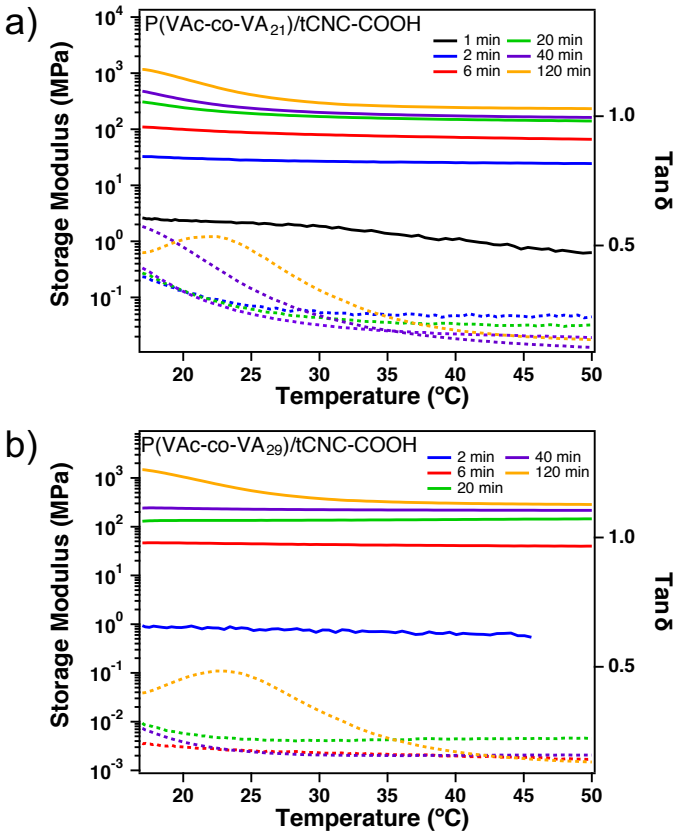

Figure 6.4 Representative DMA temperature sweep study of a) P(VAc-*co*-VA$_{21}$)/tCNC-COOH and b) P(VAc-*co*-VA$_{29}$)/tCNC-COOH nanocomposites in the wet state before and after UV irradiation (full DMA data with more time points is shown in Figure S2).

The equilibrium water uptake and plateau storage modulus (measured at 37 °C) of various P(VAc-*co*-VA)/tCNC-COOH composite samples as an effect of UV irradiation time is plotted in Figure 6.5a. The results reveal that the water uptake is governed by both the VA content and the length of irradiation which is consistent with the above study on the copolymer only films. For instance, P(VAc-*co*-VA_{10})/tCNC-COOH with the lowest mole percent of VA exhibits an equilibrium water uptake of 140 % before UV irradiation, which decreases to 14 % for the samples irradiated at 120 min. Nanocomposites with a higher content of hydroxyl units display a much larger water uptake at 174 % and 250 % for P(VAc-*co*-VA_{21}) and P(VAc-*co*-VA_{29}) based composites that were irradiated at 1 min, respectively. The swelling decreases dramatically with the time of UV irradiation and reaches a minimum swelling between 7-8 % in the highly crosslinked samples (120 min). It is important to note that the non-irradiated nanocomposites swelled extensively in water and the films disintegrate preventing the collection of swelling and DMA data.

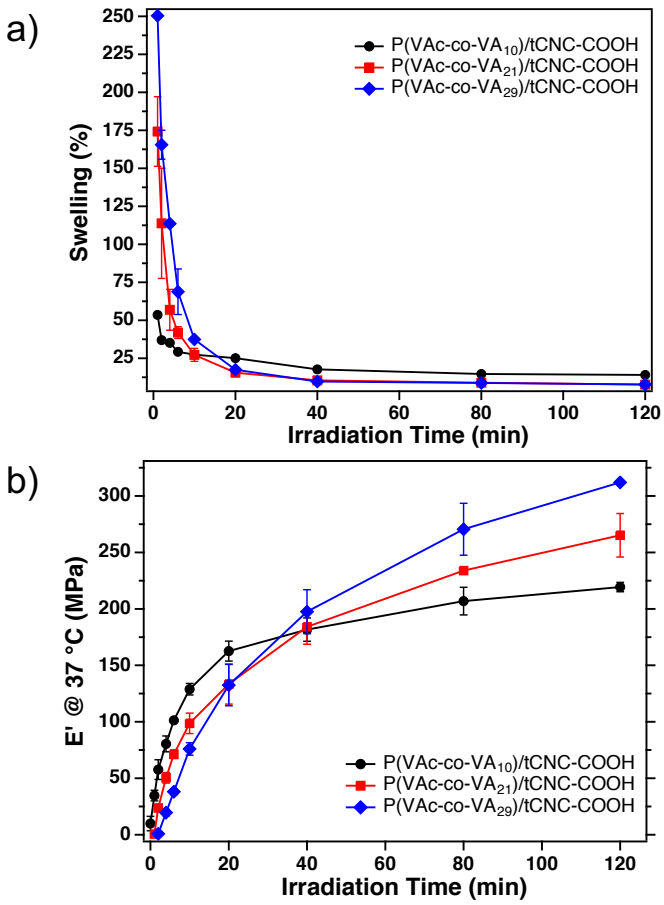

Figure 6.5 a) Equilibrium water swelling and b) b) wet storage modulus *E′* at 37 °C of various P(VAc-*co*-VA)/tCNC-COOH nanocomposites at different UV irradiation times.

The DMA results in Figure 6.5b demonstrate that the wet plateau modulus of the swollen nanocomposite after UV irradiation is inversely proportional to the degree of water uptake. This is in agreement with the water being able to disrupt the hydrogen bonding interactions in the uncrosslinked materials as opposed to the dry films, while in the crosslinked composites the covalent network formed between matrix-matrix and between matrix-filler drives water molecules out of the crosslinked region which stiffens the material. The wet plateau modulus of P(VAc-*co*-VA_{10})/tCNC-COOH nanocomposite increased from ca. 10 MPa to 219 MPa after UV irradiation, which is a modulus contrast of ca. 22 between stiff and soft materials. This number is higher

relative to the bio-inspired nanocomposites crosslinked via thiol-ene chemistry in prior studies which has a maximum contrast ratio of 20.[39] Furthermore, for P(VAc-*co*-VA_{21}) and P(VAc-*co*-VA_{29}) based composites, which exhibit a larger degree of aqueous swelling (>150 %), a plateau modulus < 1 MPa is obtained. The modulus gradually increased with the time of UV irradiation until a maximum modulus > 250 MPa is obtained after 80-120 min of irradiation. Comparison of the wet modulus before and after UV irradiation now shows a modulus contrast that is over two orders of magnitude. Specifically, P(VAc-*co*-VA_{21})/tCNC-COOH nanocomposites possessed a modulus change from 0.6 MPa (E'_{soft}, 1 min) to 265 MPa (E'_{stiff}, 120 min) with a modulus contrast E'_{stiff}/E'_{soft} that is over 400. P(VAc-*co*-VA_{29})/tCNC-COOH nanocomposites with a slightly higher content of hydroxyl groups exhibited a similar modulus contrast (E'_{stiff}/E'_{soft}=ca. 390) with a wet modulus that is tunable between 0.8 MPa (E'_{soft}, 2 min) and 312 MPa (E'_{stiff}, 120 min). Films irradiated for only 1 min were too soft to be accurately measured by DMA on account of the large degree of water swelling (ca. 250 %). To the best of our knowledge, a 400-fold difference in storage modulus between soft and stiff regions represents the largest modulus gradients ever seen in a bioinspired synthetic material. In fact, the modulus gradient obtained in these materials is larger than the squid beak bio-model which exhibits a contrast ratio of ca. 100 (50 MPa to 5 GPa) in the wet state.

6.3.3 Mechanical gradient nanocomposites fabricated by photo-patterning.

After establishing a relationship between the time of UV irradiation and the mechanical properties of the nanocomposites using individual samples, it is of interest to further investigate the preparation of nanocomposites with a continuous modulus gradient within a single piece of material. We have shown in previous work that nanocomposites based on thiol-ene crosslink can

be photo-patterned using a printed mask under UV irradiation which allow access to programmed gradients within the samples.[39] Therefore, the same process was utilized here to first evaluate the feasibility of patterning the P(VAc-*co*-VA)/tCNC-COOH nanocomposites with a mask. The photomask was prepared by direct printing the patterns on a transparent acetate sheet using an inject printer. The pattern contains alternating dark and transparent strips that are 1 mm in width and are tilted at 45° angle with respect to the long axis (Figure 6.6a). P(VAc-*co*-VA_{21})/tCNC-COOH nanocomposites film which displays the largest modulus contrast were chosen as an example for this study. The film (30 mm x 4 mm) was first irradiate for 1 min (30s each side) without a mask to prevent the less crosslinked region from falling apart in water. The sample was then placed under the printed photomask and further irradiated for 10 min on only one side of the sample with the goal of creating highly crosslinked (under transparent mask areas) and less crosslinked (under dark mask areas) regions with different modulus and water swelling that are adjacent to each other. As can be seen from the photo of the irradiated sample after 2-propanol washing and drying, the pattern on the mask has been successfully transferred to the composite sample with alternating clear and yellow strips which corresponds to less crosslinked (transparent) and highly crosslinked materials (yellow) (Figure 6.6b). The yellow color is attributed to the decomposition of PAGs which is also an indication of the degree of crosslinking reaction. Immersion of the patterned sample into water results in a transformation from planar to a helical structure after a few hours (Figure 6.6c). The result is proven to be an effect of the difference in modulus and water swelling degree between the neighboring regions which leads to a macroscopic shape change of the film.

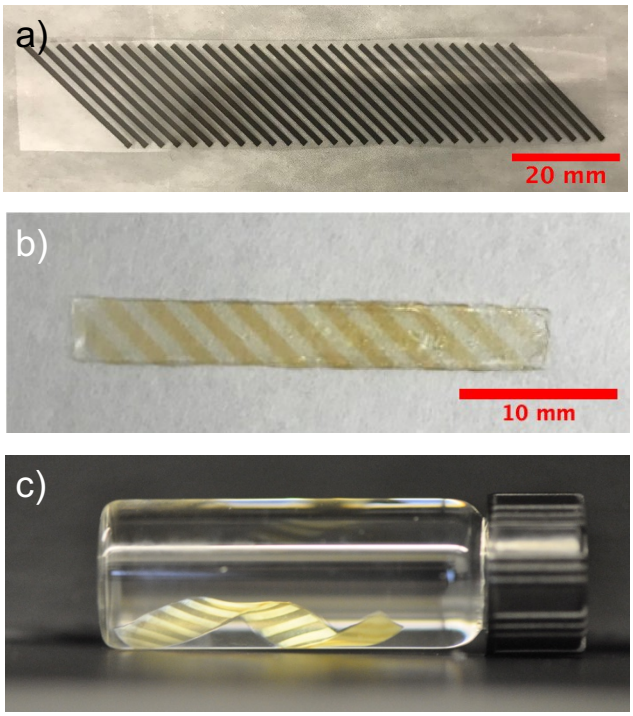

Figure 6.6 a) Photograph of the printed photomask with alternating dark and transparent strips. b) P(VAc-*co*-VA$_{21}$)/tCNC-COOH nanocomposite sample (30 mm x 4 mm) after 10 min UV irradiation using the mask. c) Photograph of photo-patterned P(VAc-*co*-VA$_{21}$)/tCNC-COOH nanocomposite sample after immersion in water for 6 hrs.

The photo-patterning process can also be used to easily fabricate composite films with a continuous gradient. A photomask with a linear grayscale pattern that seamlessly transits from transparent to black was prepared as shown in Figure 6.7a. The goal is to gradually decrease the UV intensities that penetrate through the photomask from the transparent side to the black side. A piece of P(VAc-*co*-VA$_{21}$)/tCNC-COOH nanocomposite sample (30 mm x 4 mm) were irradiated for 10 min under the photomask. After irradiation, the sample was carefully washed in 2-propanol to remove the residual PAG and crosslinkers. As excepted, a clear transition from dark yellow to light yellow to transparent from the left end to the right end of the sample can be observed, which is consistent with the direction of the grayscale pattern (transparent to black) from the photomask (Figure 6.7b). The result is also in agreement with a decrease in the degree of crosslinking within

the materials from the dark yellow side to the transparent side. As we learned from the above studies, the storage modulus of the nanocomposites is directly related to the degree of crosslinking. Therefore, it is assumed that the sample film which was irradiated using the grayscale mask resulted in a continuous modulus gradient. More detailed characterizations of the modulus at different locations of the sample need to be carried out to further verify the machinal gradient, possibly by indentation study. The printed photomask is utilized here as a proof-of-concept purpose, the approach can be easily adapted into photolithography process for the fabrication of devices with much smaller size and complex features for biomedical applications.

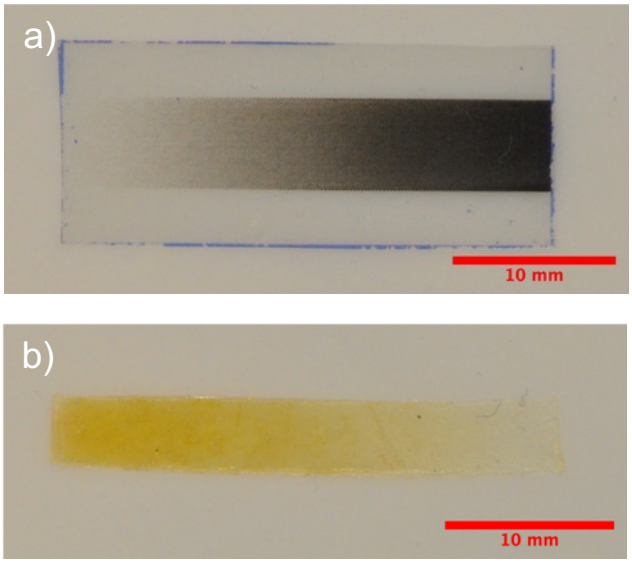

Figure 6.7 a) Photograph of the printed grayscale photomask. b) P(VAc-*co*-VA_{21})/tCNC-COOH nanocomposite sample (30 mm x 4 mm) after 10 min UV irradiation using the grayscale mask.

6.4 Conclusion

In this study, we have shown the preparation of bio-inspired nanocomposites with tunable mechanical properties based on P(VAc-*co*-VA) copolymer matrix and oxidized tCNC-COOH nanofillers. Covalent crosslink networks can be formed between the polymer matrix and the CNC

fillers which leads to an increase in storage modulus in both dry and wet films after UV irradiation as well as a decrease in water swelling. The new nanocomposite offers several key advantages as compared to the original one based on thiol-ene chemistry. Firstly, the PVAc-*co*-VA polymer matrix is more hydrophilic as opposed to the alkene-containing PVAc-*co*-VP, as such the wet modulus of the less crosslinked samples (E'_{soft}) can be further decreased on account of a higher degree of water uptake. Moreover, the surface of CNC is rich in hydroxyl groups, using hydroxyl based crosslinking chemistry results in a higher number of crosslinking sites from the CNC nanofillers which further improves the wet modulus in the highly crosslinked samples (E'_{stiff}). As a result, the nanocomposites demonstrated a modulus contrast over 2 order of magnitude ($E'_{stiff}/E'_{soft} > 400$) upon swelling in water which is higher than the contrast observed in the squid beak biomodel (E'_{stiff}/E'_{soft} ca. 100). In addition, studies on photo-patterning of the nanocomposites demonstrated that complex mechanical gradients can be easily programmed into the materials using specifically designed photomasks. The large tunability in wet modulus as well as the ability to control the modulus using a simple photo-patterning process makes these bio-inspired nanocomposites attractive to be used as the substrate for the fabrication of implantable devices, such as intracortical microelectrode. Future studies on using photolithography process to design and fabricate prototype devices based on the nanocomposites with much more complex modulus gradients and smaller feature sizes will be carried out.

6.5 Appendix

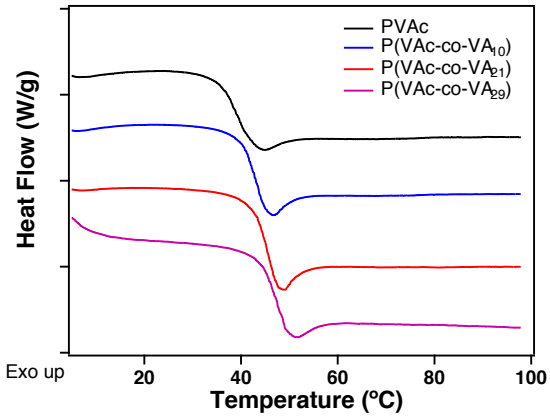

Figure A6.1 DSC study of P(VAc-*co*-VA) copolymer with various content of VA units.

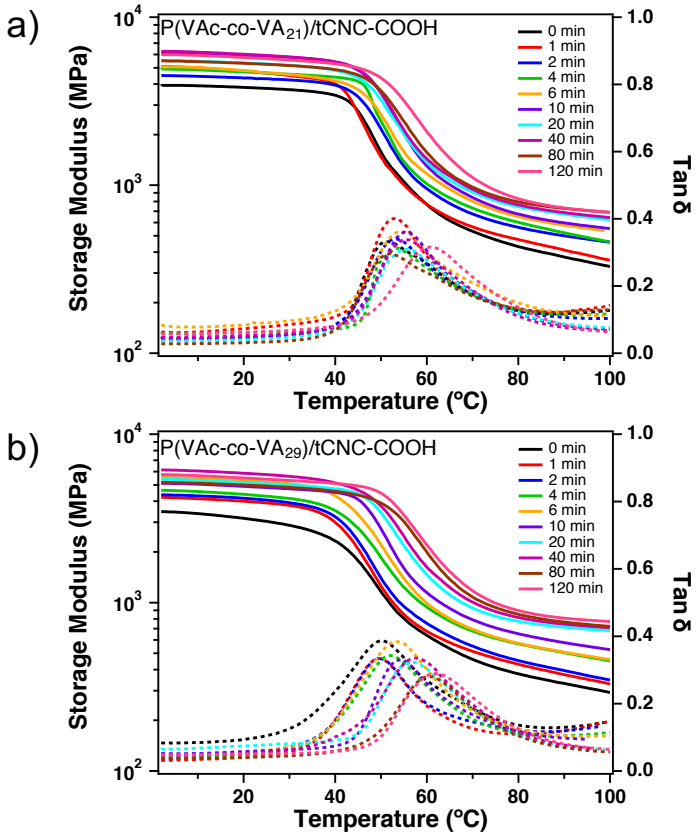

Figure A6.2 Representative DMA temperature sweep study of a) P(VAc-*co*-VA$_{21}$)/tCNC-COOH and b) P(VAc-*co*-VA$_{29}$)/tCNC-COOH nanocomposites in the wet state before and after UV irradiation.

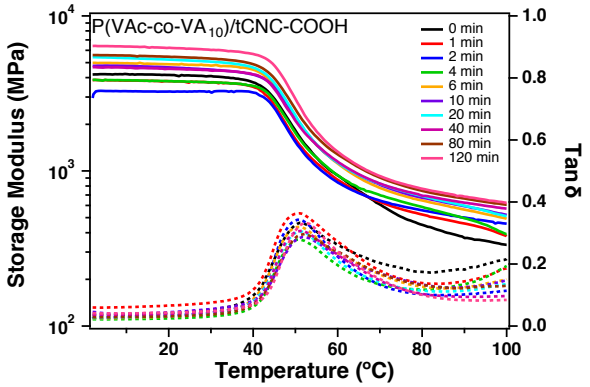

Figure A6.3 Representative DMA temperature sweep study of P(VAc-*co*-VA$_{10}$)/tCNC-COOH nanocomposites in the dry state before and after UV irradiation.

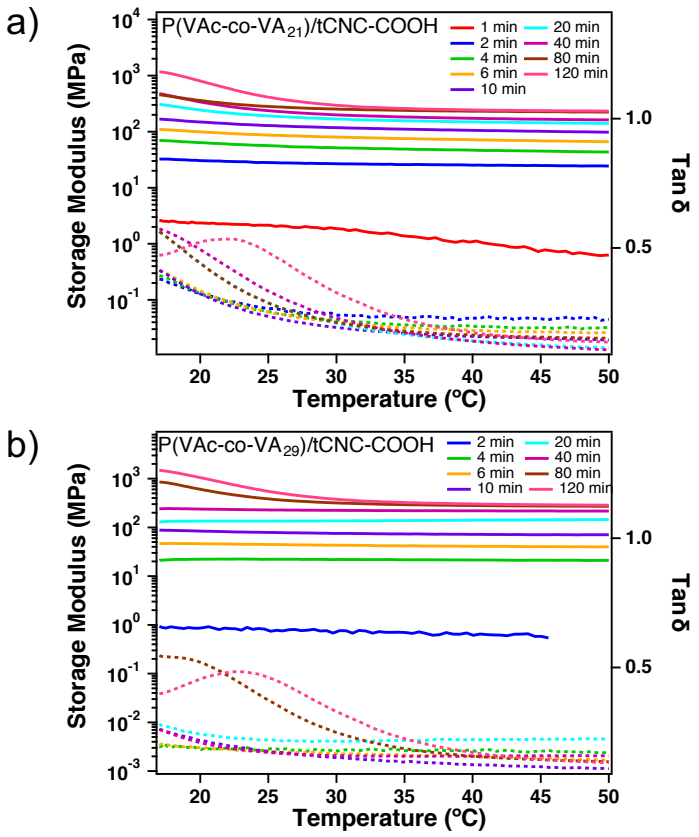

Figure A6.4 Representative DMA temperature sweep study of a) P(VAc-*co*-VA$_{21}$)/tCNC-COOH and b) P(VAc-*co*-VA$_{29}$)/tCNC-COOH nanocomposites in the wet state before and after UV irradiation.

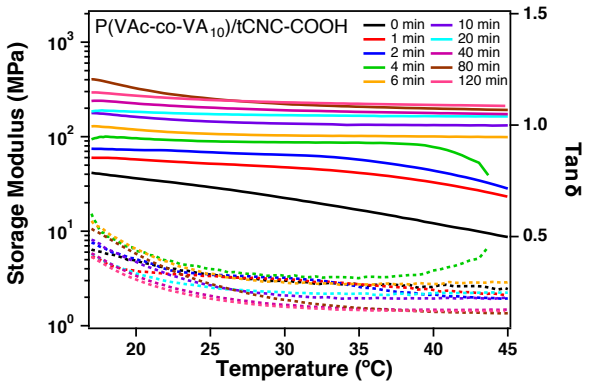

Figure A6.5 Representative DMA temperature sweep study of P(VAc-*co*-VA_{10})/tCNC-COOH nanocomposites in the wet state before and after UV irradiation.

Table A6.1 Summary of the thermal mechanical property of P(VAc-co-VP)/tCNC-COOH in both dry and wet state at different UV irradiation times.

	P(VAc-co-VA_{10})/tCNC-COOH		
Irradiation time (min)	Dry E' at 80 °C MPa	Wet E' at 37 °C MPa	Water swelling %
0	453.29 ± 6.66	9.85 ± 6.43	
1	523.41 ± 0.90	34.64 ± 4.64	53.60
2	549.50 ± 7.91	57.73 ± 8.73	37.00
4	600.62 ± 13.93	80.40 ± 7.07	35.20
6	644.00	101.26 ± 1.65	29.30
10	660.18 ± 17.54	128.84 ± 5.14	27.40
20	687.72	162.63 ± 8.86	25.10
40	700.82 ± 14.87	181.61 ± 10.31	17.75
80	729.02 ± 18.82	206.85 ± 12.20	14.70
120	762.66 ± 5.70	219.31 ± 4.16	14.10

Table A6.1 Summary of the thermal mechanical property of P(VAc-co-VP)/tCNC-COOH in both dry and wet state at different UV irradiation times.

	P(VAc-co-VA$_{21}$)/tCNC-COOH		
Irradiation time (min)	Dry E' at 80 °C MPa	Wet E' at 37 °C MPa	Water swelling %
0	424.45 ± 17.50		
1	492.51 ± 19.45	0.61 ± 0.54	174.23 ± 22.93
2	539.37 ± 14.21	23.70 ± 2.97	113.85 ± 36.27
4	599.32 ± 18.47	50.40 ± 4.70	56.90 ± 13.45
6	635.50 ± 21.31	71.33 ± 3.85	41.95 ± 3.89
10	684.56 ± 32.77	98.60 ± 9.04	27.23 ± 4.29
20	712.30 ±25.44	133.42 ± 17.74	15.53 ±2.57
40	746.66 ± 22.05	184.12 ± 15.42	10.50 ± 1.06
80	797.83	233.95 ± 2.90	8.95 ± 0.64
120	836.83 ± 9.57	265.15 ±19.30	7.70

	P(VAc-co-VA$_{29}$)/tCNC-COOH		
Irradiation time (min)	Dry E' at 80 °C MPa	Wet E' at 37 °C MPa	Water swelling %
0	376.79		
1	435.51 ± 20.74		250.40
2	467.13 ± 12.56	0.81 ± 0.28	165.55 ± 9.55
4	554.48 ± 21.11	19.63 ± 2.72	113.60
6	578.35 ± 16.42	38.13 ± 2.69	68.8 ± 14.99
10	659.08 ± 9.93	76.03 ± 5.57	37.40
20	763.28 ± 12.23	132.44 ±18.28	17.5 ± 0.42
40	811.07 ± 4.65	197.50 ± 19.49	9.75 ± 0.78
80	860.71 ± 17.68	270.49 ± 23.02	8.80
120	894.35	312.06	7.80

6.6 Reference

(1) Chen, P. Y.; Lin, A. Y. M.; Lin, Y. S.; Seki, Y.; Stokes, A. G.; Peyras, J.; Olevsky, E. A.; Meyers, M. A.; McKittrick, J. Structure and Mechanical Properties of Selected Biological Materials. *J. Mech. Behav. Biomed. Mater.* **2008**, *1* (3), 208–226.

(2) Meyers, M. A.; McKittrick, J.; Chen, P.-Y. Structural Biological Materials: Critical Mechanics-Materials Connections. *Science* **2013**, *339* (6121), 773–779.

(3) Wegst, U. G. K.; Ashby, M. F. The Mechanical Efficiency of Natural Materials. *Philos. Mag.* **2004**, *84* (21), 2167–2186.

(4) Benjamin, M.; Toumi, H.; Ralphs, J. R.; Bydder, G.; Best, T. M.; Milz, S. Where Tendons and Ligaments Meet Bone: Attachment Sites ('entheses') in Relation to Exercise and/or Mechanical Load. *J. Anat.* **2006**, *208* (4), 471–490.

(5) Lu, H. H.; Thomopoulos, S. Functional Attachment of Soft Tissues to Bone: Development, Healing, and Tissue Engineering. *Annu. Rev. Biomed. Eng.* **2013**, *15* (1), 201–226.

(6) Bruet, B. J. F.; Song, J.; Boyce, M. C.; Ortiz, C. Materials Design Principles of Ancient Fish Armour. *Nat. Mater.* **2008**, *7* (9), 748–756.

(7) Broomell, C. C.; Chase, S. F.; Laue, T.; Waite, J. H. Cutting Edge Structural Protein from the Jaws of Nereis Virens. *Biomacromolecules* **2008**, *9* (6), 1669–1677.

(8) Degtyar, E.; Harrington, M. J.; Politi, Y.; Fratzl, P. The Mechanical Role of Metal Ions in Biogenic Protein-Based Materials. *Angew. Chemie Int. Ed.* **2014**, *53* (45), 12026–12044.

(9) Miserez, A.; Schneberk, T.; Sun, C.; Zok, F. W.; Waite, J. H. The Transition from Stiff to Compliant Materials in Squid Beaks. *Science (80-.).* **2008**, *319* (5871), 1816–1819.

(10) Färber, J.; Lichtenegger, H. C.; Reiterer, A.; Stanzl-Tschegg, S.; Fratzl, P. Cellulose Microfibril Angles in a Spruce Branch and Mechanical Implications. *J. Mater. Sci.* **2001**, *36* (21), 5087–5092.

(11) Raabe, D.; Sachs, C.; Romano, P. The Crustacean Exoskeleton as an Example of a Structurally and Mechanically Graded Biological Nanocomposite Material. *Acta Mater.* **2005**, *53* (15), 4281–4292.

(12) Dawson, C.; Vincent, J. F. V.; Rocca, A.-M. How Pine Cones Open. *Nature* **1997**, *390* (6661), 668–668.

(13) Jiao, D.; Liu, Z. Q.; Qu, R. T.; Zhang, Z. F. Anisotropic Mechanical Behaviors and Their Structural Dependences of Crossed-Lamellar Structure in a Bivalve Shell. *Mater. Sci. Eng. C* **2016**, *59*, 828–837.

(14) Fratzl, P.; Barth, F. G. Biomaterial Systems for Mechanosensing and Actuation. *Nature* **2009**, *462* (7272), 442–448.

(15) Suresh, S. Graded Materials for Resistance to Contact Deformation and Damage. *Science.* **2001**, *292* (5526), 2447–2451.

(16) Chen, P.-Y.; McKittrick, J.; Meyers, M. A. Biological Materials: Functional Adaptations and Bioinspired Designs. *Prog. Mater. Sci.* **2012**, *57* (8), 1492–1704.

(17) Zhang, C.; Mcadams, D. A.; Grunlan, J. C. Nano/Micro-Manufacturing of Bioinspired Materials: A Review of Methods to Mimic Natural Structures. *Adv. Mater.* **2016**, *28* (30), 6292–6321.

(18) Liu, Z.; Meyers, M. A.; Zhang, Z.; Ritchie, R. O. Functional Gradients and Heterogeneities in Biological Materials: Design Principles, Functions, and Bioinspired Applications. *Prog. Mater. Sci.* **2017**, *88*, 467–498.

(19) Shoffstall, A. J.; Capadona, J. R. Bioinspired Materials and Systems for Neural Interfacing. *Current Opinion in Biomedical Engineering*. Elsevier B.V. June 1, 2018, pp 110–119.

(20) Jorfi, M.; Skousen, J. L.; Weder, C.; Capadona, J. R. Progress towards Biocompatible Intracortical Microelectrodes for Neural Interfacing Applications. *Journal of Neural Engineering*. IOP Publishing February 1, 2015, p 011001.

(21) Nguyen, J. K.; Park, D. J.; Skousen, J. L.; Hess-Dunning, A. E.; Tyler, D. J.; Rowan, S. J.; Weder, C.; Capadona, J. R. Mechanically-Compliant Intracortical Implants Reduce the Neuroinflammatory Response. *J. Neural Eng.* **2014**, *11* (5), 056014.

(22) Helton, K. L.; Ratner, B. D.; Wisniewski, N. A. Biomechanics of the Sensor-Tissue Interface—Effects of Motion, Pressure, and Design on Sensor Performance and the Foreign Body Response—Part I: Theoretical Framework. *J. Diabetes Sci. Technol.* **2011**, *5* (3), 632–646.

(23) Wang, D.; Zhang, H.; Guo, J.; Cheng, B.; Cao, Y.; Lu, S.; Zhao, N.; Xu, J. Biomimetic Gradient Polymers with Enhanced Damping Capacities. *Macromol. Rapid Commun.* **2016**, *37* (7), 655–661.

(24) Natterodt, J. C.; Meesorn, W.; Zoppe, J. O.; Weder, C. Functionally Graded Polyurethane/Cellulose Nanocrystal Composites. *Macromol. Mater. Eng.* **2018**, *303* (6), 1700661.

(25) Wang, B.; Benitez, A. J.; Lossada, F.; Merindol, R.; Walther, A. Bioinspired Mechanical Gradients in Cellulose Nanofibril/Polymer Nanopapers. *Angew. Chemie* **2016**, *128* (20), 6070–6074.

(26) Gharazi, S.; Zarket, B. C.; DeMella, K. C.; Raghavan, S. R. Nature-Inspired Hydrogels with

Soft and Stiff Zones That Exhibit a 100-Fold Difference in Elastic Modulus. *ACS Appl. Mater. Interfaces* **2018**, *10* (40), 34664–34673.

(27) Zhao, Y.; Cao, J.; Zhang, Y.; Peng, H. Gradually Crosslinking Carbon Nanotube Array in Mimicking the Beak of Giant Squid for Compression-Sensing Supercapacitor. *Adv. Funct. Mater.* **2019**, 1902971.

(28) Lin, Z.; Gui, X.; Zeng, Z.; Liang, B.; Chen, W.; Liu, M.; Zhu, Y.; Cao, A.; Tang, Z. Biomimetic Carbon Nanotube Films with Gradient Structure and Locally Tunable Mechanical Property. *Adv. Funct. Mater.* **2015**, *25* (46), 7173–7179.

(29) Wang, Z.; Wang, K.; Huang, H.; Cui, X.; Shi, X.; Ma, X.; Li, B.; Zhang, Z.; Tang, X.; Chiang, M. Y. M. Bioinspired Wear-Resistant and Ultradurable Functional Gradient Coatings. *Small* **2018**, *14* (41), 1802717.

(30) Wang, Z.; Shi, X.; Huang, H.; Yao, C.; Xie, W.; Huang, C.; Gu, P.; Ma, X.; Zhang, Z.; Chen, L.-Q. Magnetically Actuated Functional Gradient Nanocomposites for Strong and Ultra-Durable Biomimetic Interfaces/Surfaces. *Mater. Horizons* **2017**, *4* (5), 869–877.

(31) Wang, Y.-Q.; Wang, Y.; Zhang, H.-F.; Zhang, L.-Q. A Novel Approach to Prepare a Gradient Polymer with a Wide Damping Temperature Range by In-Situ Chemical Modification of Rubber During Vulcanization. *Macromol. Rapid Commun.* **2006**, *27* (14), 1162–1167.

(32) Claussen, K. U.; Giesa, R.; Schmidt, H.-W. Longitudinal Polymer Gradient Materials Based on Crosslinked Polymers. *Polymer (Guildf).* **2014**, *55* (1), 29–38.

(33) Zhang, X.; Hassanzadeh, P.; Miyake, T.; Jin, J.; Rolandi, M. Squid Beak Inspired Water Processable Chitosan Composites with Tunable Mechanical Properties. *J. Mater. Chem. B* **2016**, *4* (13), 2273–2279.

(34) Zvarec, O.; Purushotham, S.; Masic, A.; Ramanujan, R. V.; Miserez, A. Catechol-Functionalized Chitosan/Iron Oxide Nanoparticle Composite Inspired by Mussel Thread Coating and Squid Beak Interfacial Chemistry. *Langmuir* **2013**, *29* (34), 10899–10906.

(35) Neal, J. A.; Oldenhuis, N. J.; Novitsky, A. L.; Samson, E. M.; Thrift, W. J.; Ragan, R.; Guan, Z. Large Continuous Mechanical Gradient Formation via Metal-Ligand Interactions. *Angew. Chemie Int. Ed.* **2017**, *56* (49), 15575–15579.

(36) Karabanova, L. V.; Mikhalovsky, S. V.; Lloyd, A. W.; Boiteux, G.; Sergeeva, L. M.; Novikova, T. I.; Lutsyk, E. D.; Meikle, S. Gradient Semi-Interpenetrating Polymer Networks Based on Polyurethane and Poly(Vinyl Pyrrolidone). *J. Mater. Chem.* **2005**, *15* (4), 499.

(37) Zhang, Y.; Edelbrock, A. N.; Rowan, S. J. Effect of Processing Conditions on the Mechanical Properties of Bio-Inspired Mechanical Gradient Nanocomposites. *Eur. Polym.*

J. **2019**, *115*, 107–114.

(38) Fox, J. D.; Capadona, J. R.; Marasco, P. D.; Rowan, S. J. Bioinspired Water-Enhanced Mechanical Gradient Nanocomposite Films That Mimic the Architecture and Properties of the Squid Beak. *J. Am. Chem. Soc.* **2013**, *135* (13), 5167–5174.

(39) Zhang, Y.; Pon, N.; Awaji, A.; Rowan, S. J. Squid Beak Inspired Crosslinked Cellulose Nanocrystal Composites. *Biomacromolecules Submitted*.

(40) Miserez, A.; Li, Y.; Waite, J. H.; Zok, F. Jumbo Squid Beaks: Inspiration for Design of Robust Organic Composites. *Acta Biomater.* **2007**, *3* (1), 139–149.

(41) Weaver, J. C.; Wang, Q.; Miserez, A.; Tantuccio, A.; Stromberg, R.; Bozhilov, K. N.; Maxwell, P.; Nay, R.; Heier, S. T.; DiMasi, E.; Kisailus, D. Analysis of an Ultra Hard Magnetic Biomineral in Chiton Radular Teeth. *Mater. Today* **2010**, *13* (1–2), 42–52.

(42) Kamat, S.; Su, X.; Ballarini, R.; Heuer, A. H. Structural Basis for the Fracture Toughness of the Shell of the Conch Strombus Gigas. *Nature* **2000**, *405* (6790), 1036–1040.

(43) Lichtenegger, H. C. High Abrasion Resistance with Sparse Mineralization: Copper Biomineral in Worm Jaws. *Science (80-.).* **2002**, *298* (5592), 389–392.

(44) Khan, R. K.; Stoimenov, P. K.; Mates, T. E.; Waite, J. H.; Stucky, G. D. Exploring Gradients of Halogens and Zinc in the Surface and Subsurface of Nereis Jaws. *Langmuir* **2006**, *22* (20), 8465–8471.

(45) Miserez, A.; Rubin, D.; Waite, J. H. Cross-Linking Chemistry of Squid Beak. *J. Biol. Chem.* **2010**, *285* (49), 38115–38124.

(46) Tan, Y.; Hoon, S.; Guerette, P. A.; Wei, W.; Ghadban, A.; Hao, C.; Miserez, A.; Waite, J. H. Infiltration of Chitin by Protein Coacervates Defines the Squid Beak Mechanical Gradient. *Nat. Chem. Biol.* **2015**, *11* (7), 488–495.

(47) Menard, K. P.; Menard, N. Dynamic Mechanical Analysis. In *Encyclopedia of Analytical Chemistry*; John Wiley & Sons, Ltd: Chichester, UK, 2017; pp 1–25.

(48) Eyley, S.; Thielemans, W. Surface Modification of Cellulose Nanocrystals. *Nanoscale* **2014**, *6* (14), 7764–7779.

(49) Okita, Y.; Saito, T.; Isogai, A. Entire Surface Oxidation of Various Cellulose Microfibrils by TEMPO-Mediated Oxidation. *Biomacromolecules* **2010**, *11* (6), 1696–1700.